Long-term monitoring of existing wind turbine towers and fatigue performance of UHPFRC under compressive stresses

PAR

Christophe Thierry LORAUX

ÉCOLE POLYTECHNIQUE
FÉDÉRALE DE LAUSANNE

Suisse
2018

À mon pépé,
qui m'a appris tout ce que l'on ne trouve pas dans les livres.
C.L.

Abstract

An increasing number of onshore wind turbines in Europe will reach the end of their relatively short service duration, currently limited to 20 years by the design codes. Many owners already wish to extend the service duration of their turbines as it can increase the returns on investment of existing projects. Recently published recommendations require the coupled visual inspection and complex aero-elastic models for the safety verification of aging turbines. Despite the complexity of the available wind turbine simulation tools, lack of cooperation from turbine manufacturers leaves researchers no choice but to use generic models and safety factors covering the significant uncertainties related to the estimated structure geometry and control system of wind turbines. Although such structures are subject to heavy loading, the site-specific wind conditions are likely to be below the design assumptions, and the effective fatigue loading endured by the structural components of the wind turbines is lower than initially planned.

Wind turbines are poorly instrumented structures, and some data can be accessed from the Supervisory Control And Data Acquisition (SCADA) system. It provides environmental and operational parameters that can be a complement to expensive meteorological masts. Many researches start focusing on the use of the SCADA data in combination with vibration-based condition monitoring with the aim to capture the structural dynamics and to provide damage detection methods. These methods however still lack accuracy and rely on numerical models that are subject to uncertainties. The direct monitoring of the wind loading effects on the structure can overcome many limitations and provide accurate data on the fatigue loading. Direct measurement of the mechanical loading through conventional strain gauges is, however, only used over short periods for the certification of new turbines or the calibration of new measurement sensors.

This thesis aims to develop a robust and economical setup for the long-term monitoring of wind turbine towers that can be combined with the SCADA data and operated by wind farm owners. The proposed methodology for the measurement of the tower deformation provides solutions concerning the temperature and long-term effects on the strain gauges. This setup was found particularly stable over the three years of continuous high-frequency measurements and provided a realistic examination of the wind loading and wind-induced fatigue loading. Extreme events and accidental loads were recorded during the extended measurement period, and extreme values theory was used for the safety verification at ultimate limit state. Recommendations are provided on sufficient monitoring duration.

The fatigue damage and extreme acting forces were found to be highly dependent on seasonal effects, with a majority of the damage produced during few high-wind storms, mainly occurring in winter. A complete year of measurement was found to be sufficient for the extrapolation of extreme loading events. Based on these results, recommendations are given to the owner to improve the management of the wind farm during storms, thereby allowing to decide between full power production and increased risk of damage.

An approach for the calculation of the effective fatigue loading over the turbine service duration is presented. Monitored data, in combination with the SCADA data, are used to estimate the endured fatigue load spectrum. The calculated damage for various operating conditions and

wind condition is correlated with the SCADA data available since the commissioning and all along the turbine service period. The estimated remaining service duration takes into account the changing wind conditions by correctly taking into account the variable annual frequency of storms. Results show that the monitored turbine tower could be safely extended significantly beyond the 20-year design limit.

Another approach for the extension of the service duration of future towers is the use of Ultra-High Performance Fibre Reinforced Cement-based Composites (UHPFRC). UHPFRC is a high-strength cementitious material reinforced with a high amount of fine steel fibres. It exhibits high mechanical properties with compressive strength above 150 MPa and tensile strength above 7 MPa and excellent durability properties thanks to an optimised dense matrix. The objective of the experimental campaign was to study the fatigue resistance of thermally cured UHPFRC under compressive stresses. Constant amplitudes uniaxial compressive fatigue tests were conducted on thin UHPFRC plates under high fatigue stresses and very high number of cycles. The fatigue endurance limit of UHPFRC under compressive stresses at 10 million cycles was determined to be around 65 % of the ultimate limit strength. UHPFRC is found to be particularly suited for offshore turbines support structures as it could overcome the severe durability concerns of steel corrosion and allow for a more economical and durable solution for both onshore and offshore wind turbines.

Résumé

Un nombre croissant d'éolienne terrestres en Europe atteindront prochainement la fin de leur relativement courte durée de service, actuellement limitée à 20 ans par les codes de conception. De nombreux propriétaires souhaitent déjà prolonger la durée de service de leurs éoliennes car cela peut augmenter le retour sur investissement des projets existants. Les recommandations récemment publiées exigent une inspection visuelle couplée et des simulations aéro-élastiques complexes pour la vérification de la sécurité des éoliennes vieillissantes. Malgré la complexité des outils de simulation d'éoliennes disponibles, le manque de coopération des constructeurs de d'éoliennes ne laisse d'autre choix aux chercheurs que d'utiliser des modèles génériques et des facteurs de sécurité couvrant les incertitudes multiples liées à l'estimation de la géométrie de la structure et du système de contrôle des éoliennes. Bien que ces structures soient soumises à des forces élevées, il est très probable que les conditions de vent propres à chaque site soient inférieures aux hypothèses de conception, et que la sollicitation de fatigue effectivement endurées par les éléments structurels des éoliennes soit inférieure à celle initialement prévue.

Les éoliennes sont des structures équipées de relativement peu de capteurs et certaines de ces données peuvent être consultées à partir du système d'acquisition et de contrôle des données (SCADA). Il fournit des paramètres environnementaux et opérationnels qui peuvent être une alternative aux coûteux mâts météorologiques. De plus en plus de recherches commencent à se concentrer sur l'utilisation des données SCADA en combinaison avec la surveillance de l'état vibratoire de la structure dans le but de capturer son comportement dynamique et de fournir des méthodes de détection des dommages. Cependant, ces méthodes manquent encore de précision et reposent sur des simulations numériques soumis à des incertitudes de modélisation. La surveillance directe des effets de la pression du vent sur la structure peut surmonter de nombreuses limitations et fournir des données précises sur la sollicitation de fatigue. La mesure directe des efforts mécaniques à l'aide de jauges de contraintes conventionnelles n'est toutefois utilisée que sur de courtes périodes pour la certification de nouvelles éoliennes ou l'étalonnage de nouveaux capteurs de mesure.

Le présent projet de recherche vise à développer un system robuste et économique pour la surveillance à long terme des tours d'éoliennes pouvant être combinées avec les données SCADA et exploitées par les propriétaires de parcs éoliens. La méthodologie proposée pour la mesure des déformations de la tour a fourni des solutions concernant la température et les effets à long terme sur les jauges de contrainte. Cette configuration s'est avérée particulièrement stable durant les trois années de mesure continue à haute fréquence et a fourni un examen réaliste des forces et de la sollicitation de fatigue induites par le vent. Des événements extrêmes et des charges accidentelles ont été enregistrés pendant la période de mesure prolongée, et la théorie des valeurs extrêmes a été utilisée pour la vérification de la sécurité à l'état limite ultime. Des recommandations sont fournies sur la durée nécessaire de surveillance.

L'endommagement causé par les sollicitations de fatigue et les forces extrêmes dépendent fortement de variations saisonnières, la majorité du dommage étant causés par quelques orages violents, principalement en hiver. Une année complète de mesure s'est révélée suffisante pour la prédiction des valeurs extrêmes. Sur la base de ces résultats, des recommandations sont

données au propriétaire pour améliorer la gestion de son parc éolien pendant les tempêtes, lui permettant ainsi de décider entre la pleine production d'énergie et le risque accru de dommages.

Une approche pour le calcul de la sollicitation effective de fatigue sur la durée de service de l'éolienne est présentée. Les données mesurées combinées avec les données SCADA sont utilisées pour estimer le spectre de sollicitations de fatigue enduré par la structure. Le dommage calculé pour différentes conditions de vent et de fonctionnement sont corrélés avec les données SCADA disponibles depuis la mise en service puis tout au long de la période d'utilisation de l'éolienne. La durée de service restante estimée tient compte de l'évolution des conditions de vent en prenant correctement en compte la fréquence annuelle variable des tempêtes. Les résultats montrent que la durée de service de la tour surveillée pourrait être étendue de façon significative au-delà de la limite de conception de 20 ans.

Une autre approche pour l'extension de la durée de service des futures tours est l'utilisation de Béton Fibré Ultra-Performant (BFUP). Le BFUP est un matériau cimentaire à haute résistance renforcé avec une grande quantité de courtes fibres d'acier. Il présente des propriétés mécaniques élevées avec une résistance à la compression supérieure à 150 MPa et une résistance à la traction supérieure à 7 MPa et d'excellentes propriétés de durabilité grâce à une matrice dense et optimisée. L'objectif de la campagne expérimentale est d'étudier la résistance à la fatigue du BFUP durci thermiquement sous des contraintes de compression. Des essais de fatigue en compression uniaxiale à amplitudes constantes ont été effectués sur des plaques minces en BFUP, sous des contraintes de fatigue élevées et à un très grand nombre de cycles. La limite d'endurance à la fatigue du BFUP à 10 millions de cycles sous des contraintes de compression a été déterminée comme étant à 65 % de la résistance ultime. Le BFUP est particulièrement adapté aux mâts d'éoliennes offshore, car il pourrait surmonter les graves problèmes de durabilité liés à la corrosion de l'acier et serait une solution plus économique et durable pour les éoliennes terrestres et offshore.

Mots clés: Éoliennes existantes, sécurité structurale, sollicitation de fatigue, suivi à long terme, théorie des valeurs extrêmes, Ciment Fibré Ultra-Performant (CFUP), comportement en fatigue en compression.

Foreword

Since wind turbines typically are planned to be in service only for 20 years, structural engineers have to devise methods to extend the service duration of the structural components (tower and foundation) of existing wind turbines. Extension of the service duration of wind turbines, after eventual renewal of the nacelle and blades, can increase the return on investment of existing installations and improve sustainability. In order to examine the structural safety of structural components of wind turbines, in particular towers, and given the fact that the site-specific wind conditions are likely to be below the design assumptions, the effective fatigue loading endured by the structural components may be significantly lower than initially assumed.

In his doctoral thesis, Christophe Loraux developed a robust and economical setup for the long-term monitoring of the structural behaviour of wind turbine towers subjected to wind loading. The obtained data were combined with the Supervisory Control And Data Acquisition (SCADA) data as obtained from the wind turbine owner. Data from this monitoring campaign was used to examine the fatigue safety of the monitored tower and to forecast realistic fatigue duration. In addition, the fatigue behaviour under compressive stresses of UHPFRC, a novel material to build high WT towers, was investigated as a second approach to improve the fatigue resistance of WT towers.

The doctoral thesis by Christophe Loraux provides new knowledge towards more accurate structural engineering methods for the safety verification of existing structures and in particular of WT towers. The way how structural engineers deal with existing structures has a significant socio-economic impact because of the high monetary value of the built infrastructure. The goal is to "get more out of an existing structure". This thesis contributes to this ambitious goal.

With his doctoral thesis, Christophe Loraux provides the proof of his capabilities to conduct a significant research and to solve complex questions by applying engineering sciences. The present thesis delivers results and findings that are useful and applicable for wind turbine towers.

In the name of the whole team of MCS, I thank him for his thorough investment to the thesis topic as well as for his professional skills and personal qualities.

Lausanne, January 2018

Professor Eugen Brühwiler

Remerciements

Je souhaite tout d'abord remercier sincèrement le Professeur Eugen Brühwiler de m'avoir donné l'opportunité de réaliser cette thèse. Je souhaite également le remercier de m'avoir partagé ses connaissances et ses visions sur le BFUP et sur le monitoring d'ouvrage, qui me semblent être les deux éléments permettant la gestion durable des infrastructures de génie civil dans un futur proche.

Je souhaite également remercier le comité de thèse composé du Professeur Anton Schleiss (président du jury) de l'EPFL, du Professeur Christian Große de l'Université Technique de Munich, du Professeur Alain Nussbaumer de l'EPFL et du Professeur Cornelius Oesterlee de la Haute Ecole Spécialisée Bernoise. Je leur suis très reconnaissant de leurs commentaires qui m'ont aidé à améliorer la version finale de ma thèse.

Je souhaite remercier le Dr. Emmanuel Denarié pour son aide tout au long ces quatre années, et je le remercie encore une fois pour ce magnifique projet de Master sur le phare de la Jument, qui a été le point de départ de cette thèse. Je remercie également au sein de ce laboratoire Christine Benoit qui m'a aidé au tout début de ma thèse, Florence Grandjean pour sa bonne humeur constante et son soutien dans les tâches administratives, et Hamid Sadouki pour sa connaissance des éléments finis.

Ce projet n'aurait pas été possible sans l'immense compétence des techniciens du groupe d'ingénierie des structures, notamment Gilles Guignet et Gérald Rouge pour l'installation du monitoring ; ainsi que Frédérique Dubugnon, Serge Despont et évidemment Sylvain Demierre pour les essais au laboratoire.

Le monitoring de l'éolienne a été possible avec le soutien des Forces Motrices Bernoises (BKW Energie AG), je remercie principalement Renato Lang et son successeur Johannes Vogel ; ainsi que leurs techniciens durant les phases de câblage des capteurs. Egalement un énorme merci à Pierre Berger de Juvent SA pour son enthousiasme et sa disponibilité tout au long de ces trois années de mesures.

Cette recherche a été financée par le projet EuroTech Wind et supervisée par le Dr. Gregor Giebel, que je remercie pour l'organisation et les réunions informelles. Je remercie tous les doctorants de ce projet, et tout particulièrement mon collègue et ami Christian Geiss, avec qui j'ai pu beaucoup échanger et eu l'occasion de faire un magnifique périple dans le Jura !

Je remercie évidemment tous mes collègues du MCS pendant cette période. Un grand merci au Dr. Mark Treacy et Dr. Basil Grigoriou pour les nombreuses discussions sur le monitoring et leur aide précieuse à mes débuts et au Dr. Tohru Makita, Dr. Maléna Bastien Masse et Dr. Marina Rocha pour m'avoir partagé leurs connaissances. Un grand merci à mes collègues arrivés durant la deuxième partie de ma thèse et qui ont redonné un nouveau souffle au groupe : Amir Hajiesmaeili, Mohamed Hafiz et Gianni Shen ainsi que Bartek Sawicki et Imane Bayane, et mon dernier collègue de bureau Philippe Schiltz !

Je remercie mes collègues et amis de la volée Génie Civil 2013 qui ont effectué leur doctorat en même temps que moi, leur soutien tout au long de ce projet a été précieux, un grand merci

au Dr. Yves Reuland, à Fabian Barras, Davide Wüthrich et Martin Garcia. Je remercie également Paul Mayencourt, Jagoda Cupać et Alexander Wolhoff, pour leur collaboration sur divers projets qui ont enrichie mon doctorat. Un grand merci également à tous mes collègues et amis des laboratoires LSMS et SuNMIL avec qui j'ai passé beaucoup de temps.

Je remercie infiniment mes parents, Christine et Marc, qui m'ont toujours soutenu et encouragé durant mes études, Guillaume qui a suivi cette thèse de très loin, et mes grands-parents qui ont également toujours été là pour moi.

Ma chère Pelin, cette thèse est aussi la tienne, car tu as su m'accompagner pendant les moments les plus merveilleux mais aussi les plus difficiles de ce doctorat tout en te consacrant à ta propre thèse. Merci pour ton incroyable patience et ton immense soutien durant cette dernière année, je n'aurais pas pu le faire sans toi. *Seni Seviyorum.*

Lausanne, Janvier 2018

Christophe Loraux

Table of contents

List of figures

xviii

List of tables

List of abbreviations

BMM	Block Maxima Method
CDF	Cumulative density function
CI	Confidence Interval
DAU	Data acquisition units
DEL	Damage Equivalent Load
EV	Extreme values
FA	Fore-aft
FEM	Finite Element Model
GEVD	Generalized Extreme Value Distribution
GPD	Generalized Pareto Distribution
LVDT	Linear Variable Differential Transducers
MLE	Maximum likelihood estimates
MSE	Mean squared error
MWD	Main wind direction
O&M	Operation and Maintenance
pdf	Probability density function
POT	Peak-over-threshold
PSD	Power Spectral Density
SCADA	Supervisory Control And Data Acquisition
SEV	Standard Extreme Variate
SHM	Structural Health Monitoring
S-level	Solicitation level
SS	Side-to-side
SWD	Secondary wind direction
TI	Turbulence Intensity
UHPFRC	Ultra-High Performance Fibre Reinforced Cement-based Composites
WT	Wind turbine

1 Introduction

1.1 Motivation and context

An increasing number of onshore wind turbines (WT) in Europe will reach the end of their service duration, currently limited to 20 years by the design codes (IEC 61400-1 2005). By the end of 2020, it is estimated that 28 % of the installed wind turbines will be older than 15 years (EWEA 2016). Nowadays wind turbine operators who have owned turbines for several years wish to extend the service duration of their wind farms and are confronted with complex decisions including technical, economical, and legal aspects. The current approach for assessing the remaining service duration of existing wind turbines is based on a combined visual inspection and renewed fatigue calculation. However, the effective fatigue loading endured by the structural components of the wind turbines is likely to be much below design assumptions provided by current codes (Heilmann et al. 2014).

The monitoring of onshore and offshore wind turbines is becoming an increasing interest in the development of advanced numerical models for both wind farm scale and wind turbine scale providing more and more understanding of such structures. However, this still requires a significant amount of simulation time. Despite the increasing accuracy of such simulation tools, uncertainties remain large and numerous due to the incredibly complex interaction between the structure and its surrounding. This is why current research focuses on developing new systems of measurement for both actions (such as incoming wind characteristics on the wind turbine) and action effects on different structural components of the turbine (namely the blades, the tower and the foundation). Wind and sea state must be considered together in the case of offshore turbines.

International standards provide guidelines and recommendations for the certification of new wind turbines based on short-term measurements of mechanical loads where the objective is to validate the design calculations. Those short-term measurements which are performed by manufacturers of wind turbines often remain private and are therefore not used to improve numerical models. Monitoring of existing wind turbines for the extension of the service duration also remains a challenge because it requires many data that are not always available or reliable.
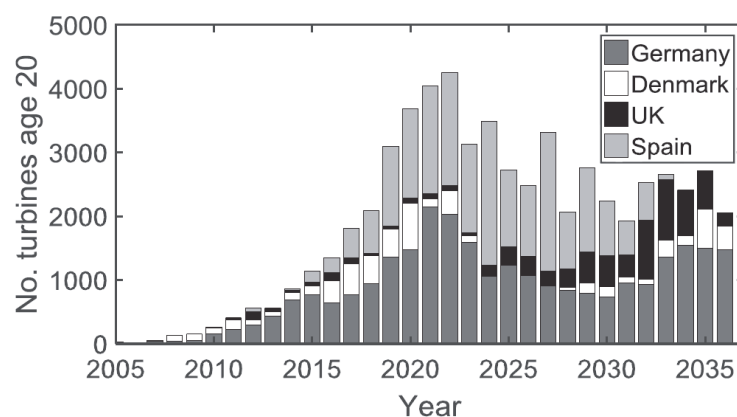
Figure 1-1. Number of onshore wind turbines reaching 20-year of service duration annually in Denmark, Germany, Spain, and the UK (Ziegler et al. 2018).

1

Regarding new turbine concepts, the vast majority of the research is now focused on offshore wind turbines as the wind conditions yield higher and more constant power production. New concepts include floating wind turbines, but the material used for towers and foundations are either steel (for floating and monopiles) or conventional concrete for shallow water foundation. As a result, the totality of offshore wind turbines is designed with materials that are known to be profoundly impacted by severe and aggressive environmental conditions. Moreover, Operation and Maintenance (O&M) are estimated to be 5 to 10 times more expensive for offshore than for onshore (Van Bussel and Zaayer 2001).

Another approach for more economical and sustainable wind turbines is the use of novel materials, such as Ultra High-Performance Fiber Reinforced Cement Composite (UHPFRC) as a drastic improvement to the cost and durability of offshore turbines.

1.2 Structural monitoring for service duration extension of wind turbines

Structural Health Monitoring (SHM) for wind turbine aims to ensure the detection, the localization, and quantification of damage, all well as its prediction. This monitoring approach is used in a wild range of structures, applications, and sensors to evaluate specific components of the rotor or the entire structure (e.g., vibration-based monitoring of the tower + rotor system). Overviews of various methods and techniques for wind turbines are available (Beganovic and Söffker 2016; Martinez-Luengo, Kolios, and Wang 2016; Wymore et al. 2015). SHM can provide the structural behavior of a structure and reduce the uncertainties of prediction models.
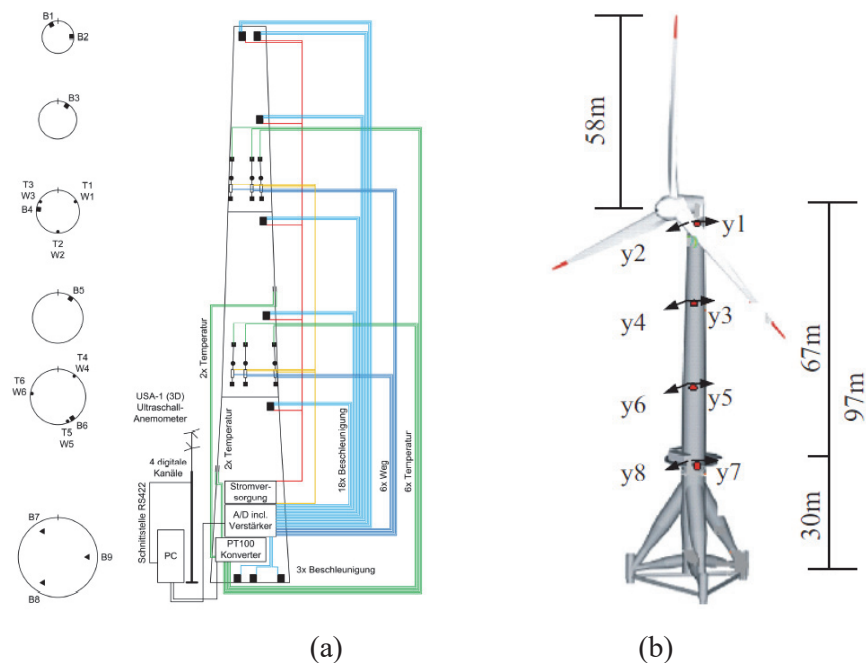
Figure 1-2. Examples of monitoring system based on (a) displacement transducer (LVDT's) (Lachmann 2014) and (b) accelerometers for the onshore testing of the offshore Areva Multibrid M5000 (Hu et al. 2015a)

2

A comprehensive and long-term monitoring campaign was conducted on a small-scale 500 MW turbine (Figure 1-2(a)) (Lachmann 2014; Smarsly, Hartmann, and Law 2013) and revealed a relatively long remaining service duration based on fatigue calculation. In Portugal, a 2.1 MW turbine Wind Class III IEC2a, 80 m tall, was heavily instrumented with accelerometers and strain gauges within the research project HISTWIN (High strength steel towers for wind turbines) (Rebelo, Veljkovic, Silva, et al. 2012). A total of 96 strain channels were installed on the tower walls and inside bolts. Intensive vibration and resonance studies were performed on the M5000 Multibride prototype from Areva (Figure 1-2(b)) (Rohrmann, Thöns, and Rücker 2010; Hu et al. 2015a, 2015b). This prototype was also used as a reference for the monitoring based condition assessment of offshore turbine support structures(Thöns 2011). More recently, a monitoring system based on accelerometers and strain measurement was deployed on a 3.0 MW hybrid turbine located in south Germany (Botz et al. 2016). The goal is to study the connection between the concrete and the steel in detail. An abundant amount of vibration measurements and operational modal analysis were also performed, occasionally employing wireless sensors to capture the dynamics of the structures (Häckell and Rolfes 2013; Iliopoulos et al. 2014; Lu, Peng, and Kuo 2014).

To evaluate the remaining service duration and fatigue analysis, a recent study focused on two offshore Vestas V112-3MW (Weijtens et al. 2016), and the fatigue calculation was performed on two leading turbines of the wind farm with the final goal of estimating the fatigue progression in the wind farm. Another trend in the fatigue load estimation is the use of accelerometers in combination with high-frequency Supervisory Control And Data Acquisition (SCADA) data to predict the wind loads. This method of virtual sensing is promising for calculating stresses in inaccessible locations (such as the mud line in offshore monopiles) despite the calibration and uncertainties of the wind turbine sensors. The effect of wake from neighboring wind turbines on the remaining fatigue life of the main components of a wind turbine was also addressed using short-term measurements on Vestas V66 located in north Germany (Karlina-Barber, Mechler, and Nitschke 2016). It results from this study that the method based on short-term load measurement was not sufficient and too dependent on the distribution of wind speed frequencies. In these studies, results were normalized due to confidentiality of the turbine geometry. Figure 1-3 shows the proposed alternative method combining temporary strain measurements with the use of SCADA data for the extension of the service duration of turbine towers.
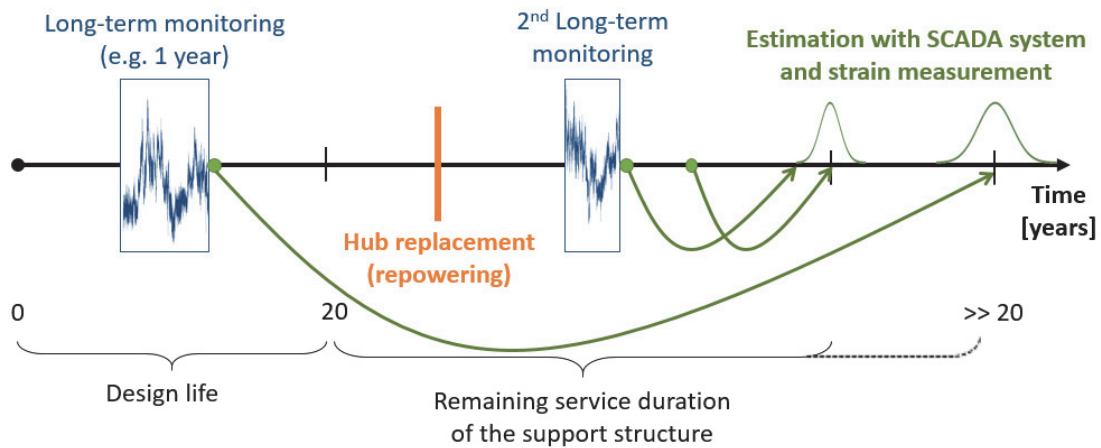
Figure 1-3. Proposed method for extension of service duration of the wind turbine support structure based on the use of long-term monitoring of strain, operational, and environmental data.

1.3 UHPFRC for turbine towers

UHPFRC stands for Ultra High Performance Fiber Reinforced Cement Composite and is a high-strength cementitious material characterized by a very dense matrix reinforced with 3-9% by volume of fine steel fibres. The compact matrix has almost zero capillary pores that make the UHPFRC highly impermeable to gases and liquid solutions. The cracking behavior of the material is controlled by fine fibre reinforcement and it gives UHPFRC its high strength, strain-hardening behavior, ductility, and fracture energy properties.

The use of Ultra High Performance Fiber Reinforced Cement Composite (UHPFRC) for the design of wind turbines towers will be a significant evolution compared to the conventional steel or concrete. Despite being now heavily used (in Switzerland) to increase the load capacity and the durability of existing bridges, it is still not used for onshore nor offshore but only suggested in some studies. Recently, some conceptual designs have been proposed, and some preliminary results employing these designs were shared. The concepts for UHPFRC tower are similar: a combination of UHPFRC precast elements with a segmental construction method. The tower is prestressed from the foundation to the tower top.

A comparison on the 69.07 m tower fixed on a prestressed concrete gravity shaft from the STRABAG Serial System was performed between actual steel structure and UHPFRC walls of 100 mm to 200 mm thicknesses (Werner et al. 2013). The properties of UHPFRC used in this project were DUCTAL FM Grey, formulation 2GM2.0 from Lafarge. The analysis was limited to the verification of the first eigenfrequency of this structure. Another segmental design was studied at Service Limit State (SLS) and Ultimate Limit State (ULS) with a finite element model (Jammes, Cespedes, and Resplendino 2013). This research focused on a 120 m UHPFRC tower, with a bottom diameter of 8.0 m and a top diameter of 4.0 m. The wall thickness linear decreases from 120 mm at the foundation to 60 mm at the top. The vibration analysis was not performed in this case. Finally, a new concept with UHPC was proposed regarding transportation issues

(Sritharan and Schmitz 2013). This design combines columns and panels, and in this study three different connections were tested.

The use of UHPFRC for turbine tower can emerge only if turbine manufacturers realize the high potential of this material, especially for the harsh environment of offshore wind turbines. Additionally, they also need to be convinced that UHPFRC can withstand the 10^8 to 10^9 load cycles that structural components of wind turbines typically experience over their service duration.

1.4   Objectives of the thesis

Despite the relatively simple structure of the wind turbine tower, the modeling of the complex interactions between the blades and the surrounding environment by means of aero-elastic simulations leads to high uncertainties. The turbines used in this simulation are mostly generic models that approximate the tower geometry and the control system settings since such information is often confidential. The direct measurement of wind effects on the support structure reduces the uncertainties regarding the dynamic behavior of the turbine, the environmental conditions, and the operational conditions.

The overall aim of the thesis is to develop approaches for the extensions of the service duration of existing and future wind turbine towers. Fatigue safety verification of the existing towers is based on a realistic examination of wind action effect obtained from direct monitoring. For the future tower, the fatigue behavior and fatigue strength of Ultra High Performance Fibre Reinforced Cement Composite (UHPFRC) under compression is investigated.

The main objectives of this thesis are summarized as follow:

1. Develop and install a long-term monitoring system on an existing wind turbine located in the biggest wind farm of Switzerland. The system must be economic and robust. The calibration procedures must not affect the power production of the turbine and not require any intervention from the owner during the measurement period.
2. Development of a methodology for data treatment and processing of the large datasets with the investigation of measurement errors inherent to long-term measurement resulting from drift and temperature effects. The measured signals will be synchronized with data from the SCADA system.
3. Investigate the effective fatigue loading and the remaining service duration of a critical connection detail of the tower.
4. Investigate the current approaches and propose an alternative for the extrapolation of extreme values of wind load effects from measured data and wind speed from the SCADA system with the study of the impact of the monitoring period and durations on the estimates.
5. Investigate the fatigue behavior and fatigue strength of UHPFRC plates subject to a high number of cycles and provide recommendations for the use of UHPFRC for future wind turbine towers.

The final goal is to provide a framework for the fatigue verification of an existing wind turbine by focusing on the monitoring approach from direct monitored data in combination with

environmental and operational data from the SCADA system rather than simulations on generic turbine models. Meanwhile, results from the testing campaign on UHPFRC plates should provide recommendations for the future design of wind turbine towers in UHPFRC.

1.5 Scope of the thesis

Many recent studies on wind turbines focus on either short-term measurements or vibration-detection of damage methods using accelerometers. For research, studying a specific problem such as the effect of wake between neighboring turbines, the effect of rotor misalignment or rotor imbalance, or the development of new measurement systems, only a small set of data which goes from few hours to few weeks of measurement is required. SHM using accelerometers even reduces these measurements to just a few minutes per hours. Because of the highly variable nature of the wind and the non-linear response of the turbine to the wind loads, this work will focus on high frequency and continuous measurements to adequately capture both the seasonal effects and very particular events such as the tower response to wind gusts and accidental loads resulting from a fault. This research will use existing monitoring system previously developed in the MCS Laboratory (Treacy 2014; Grigoriou 2015) rather than focusing on the development of new sensors or measurement techniques.

The tensile fatigue behavior of UHPFRC was previously studied in combination with steel rebars, and no research was performed regarding the compressive fatigue behavior. Limited tests on ultra-high performance concrete are not applicable for UHPFRC. The testing campaign aims to provide a first set of data regarding the compressive fatigue behavior of UHPFRC under a very high number of cycles for its application to the domain of wind turbines.

1.6 Methodology and structure of the thesis

This thesis follows the process that was necessary for the implementation of long-term monitoring of an existing wind turbine for the realistic examination of the endured wind load and wind fatigue loads.

Chapter 2 describes the upstream work necessary for the understanding of the studied structure and for the planning of an efficient monitoring system with the use of the data available from the SCADA system. The monitoring system is described in details and the limitations encountered by traditional mechanical loads measurement setups are addressed.

Chapter 3 presents the measured wind loads and wind fatigue loads. It shows the influence of environmental and operational effects on the results. The verification for the fatigue safety from direct strain measurement is presented.

Chapter 4 presents the results from statistical load extrapolations performed on monitored data using continuous measurements and addresses, in particular, the effect of the measurement period and duration on the extrapolated values.

Chapter 5 presents a method for the reconstruction of the fatigue damage endured by the wind turbine base on long-term measurement and simultaneous recording of environmental and operational data through the SCADA system.

Chapter 6 presents the results of the testing campaign on the UHPFRC and addresses the fatigue performance of UHPFRC plates under compressive stresses.

Finally, chapter 7 provides conclusions on the work and suggests future work.

2 Design of a Wind Turbine monitoring system for long-term measurement of wind loads and fatigue loads

2.1 Introduction

The number of turbines reaching the end of the service duration is increasing every year and will soon represent an important part of the total installed turbines. A large number of owners wishes to extend the service duration of their turbines and go beyond the design limit of 20 years. Performing new numerical simulations for the fatigue safety verification with state-of-art aero-simulation tools is still limited. Many safety factors are necessary to compensate the significant uncertainties of the models that not necessarily conclude in a possible extension of the service duration. SHM methods based on vibrations, on the other hand, can be used for the detection of the damages of some critical components but still cannot directly estimate the remaining service duration since it cannot quantify the fatigue damage of the tower. Direct monitoring of the strain could overcome those difficulties and limitations by providing to the owners of wind turbines a realistic estimation of the endured loads.

The objective of this chapter is to provide an experimental setup that can provide reliable information regarding wind forces and wind fatigue damage on the tower structure of wind turbines. Such monitoring system must be able to capture the mechanical loads acting on the structure and should take into account the environmental and operating data already available through the SCADA.

This work is based on the long-term measurement of a 2.0MW Vestas V90 wind turbine located on the biggest wind farm of Switzerland (Mont-Crosin, BE) and mainly relies on conventional strain gauges for the direct extraction of the strains induced during the power production of the turbine. This work covers and answers the following points:

- Design of a robust and economical monitoring setup for long-term measurement of mechanical loads and its synchronization with environmental and operational data provided by the SCADA system;
- Evaluation of the uncertainties and errors generated by current short-term mechanical load setup;
- Quantification of the long-term effects on the measurement system;
- The impact the environmental and operational parameters on the tower behavior.

The data collected and presented in this chapter is the foundation for work presented in later chapters by providing a reliable set of wind-induced strains data used for the estimation of extreme values and fatigue damage.

2.2 Turbine characteristics and site description

This study is based on the monitoring of the n°10 2.0MW V90 wind turbine manufactured by the Vestas Company. The wind turbine is currently owned by JUVENT SA and operated by BKW Energy AG. At the time of the installation of the monitoring setup in October 2014, the automatic export of the environmental and operational parameters was available on this specific turbine. The owners of this wind turbine were already involved with research done at Swiss

Federal Institute of Technology in Lausanne (EPFL) by the Electromagnetic Compatibility Laboratory (EMC) (Smorgonskii 2016) and at Swiss Federal Institute of Technology in Zurich (ETHZ). The Laboratory for Energy Conversion (LEC) performed a recent study on the measurement of tower deflection (Zendehbad, Chokani, and Abhari 2017).

This turbine was installed in 2010 during the first repowering plan of this wind farm. A second repowering has been achieved in 2017 with the installation of four new V112 Vestas turbines to increase the production from 50 to 70 GWh per year. The V90 is a common (by its rotor size, height, and tower type) onshore wind energy converter for low wind speed regions and its design is a good representation of the commonly installed turbines in Europe during the 2000-2010 decade. The Vestas company alone installed more than 19'000 units of the 2.0-3.0 MW platforms in the world (and 26 only in Switzerland). Thus, despite not being the last state-of-the-art multi-megawatt turbine of 6.0 MW and more installed on offshore wind farms, this turbine is the perfect case to study for onshore wind turbines reaching their mid-service life and soon the end of their design service duration of 20 years.

2.2.1   Turbine characteristics

The V90 wind turbine is a 3-bladed upwind turbine with a rotor diameter of 90 m (swept area of 6362 m^2) and a generator rated at 2.0 MW. This model was particularly designed for regions with modest wind conditions since it is optimized for low to medium winds and low turbulence. The turbine operates at variable speeds from 8.8 to 14.9 rpm with a pitch control system. The pitch system works as the primary brake system by pitching the blade to an angle of 24° to 89°, causing the rotor to idle. An additional mechanical disk brake is located on the high-speed shaft of the gearbox and is only used as a parking brake. The 44 m blades are made of fiberglass reinforced epoxy and carbon fibres and weight approximately 6.75 tons each. The support structure is a 95 m tall conical S355 (according to EN 100024) steel mast bolted to a concrete foundation. It is composed of four tower segments bolted together. The diameter varies from 4.20 m at the base to 2.70 m at the top. The total weight of the tower is approximately 205 tons. The generation of electrical power increases gradually for wind speed from V_{in} = 4.0 m/s to V_{rated} = 13 m/s and is stable up to V_{out} = 21 m/s. Above this cut-off wind speed, the blades are pitched to avoid any potential damage caused by storms. The nacelle is oriented automatically during power production to maximize the power output and reduce the risks of nacelle misalignment. The yawing speed is about 0.41°/s (*i.e.*, 15 minutes for a full rotation of 360°). The turbine hub is equipped with an ultrasonic wind sensor and data including the rotor speed, the blade pitch, and the nacelle orientation are also collected. Table 2-1 summarizes the main turbine characteristics (Vestas 2010).

Table 2-1. Technical specification of the Vestas V90.

General		Rotor	
Rated power	2000 kW	Diameter	90 m
Design lifetime	20 years	Number of blades	3
Cut-in wind speed	4 m/s	Low rotation speed	8.8 rpm
Rated wind speed	13 m/s	Rated rotation speed	14.9 rpm
Cut-out wind speed	20 m/s	Blade weight	6750 kg
Tower		Support foundation	
Type	Conical tubular	Geometry	Circular
Material	S355	Material	Reinforced concrete
Hub height	95 m		

Manufacturers of wind turbines do not provide the fabrication drawings. Therefore, geometrical properties of the tower are measured in situ, as the exact wall thickness and tower diameter at the locations of strain gauges are necessary to calculate the stresses and bending moments. The internal diameter is measured with a laser telemeter along the tower height at the level of the radial welds between each plate. The height of the plates is also measured for each segments using a graduated tape. For the first tubular segment, the diameter is constant, and plates are about 3.0 m tall. Segments 2 to 4 are conical tubes with an internal diameter varying from 4.11 to 2.46 m, and plates are in average 2.85 m tall.

The thickness of plate is more complicated to measure in-situ and requires the use of an ultrasonic device (PCE-TG 200 2017). This operation is performed for almost every 32 plates along the tower height. Wall thickness varies from 42 mm at the bottom (at the entrance platform) to 12 mm at the top. This measurement campaign is particularly crucial for the creation of the finite element model of the tower and for the realistic examination of the wind forces. In-situ measured data are presented in Figure 2-1 below.
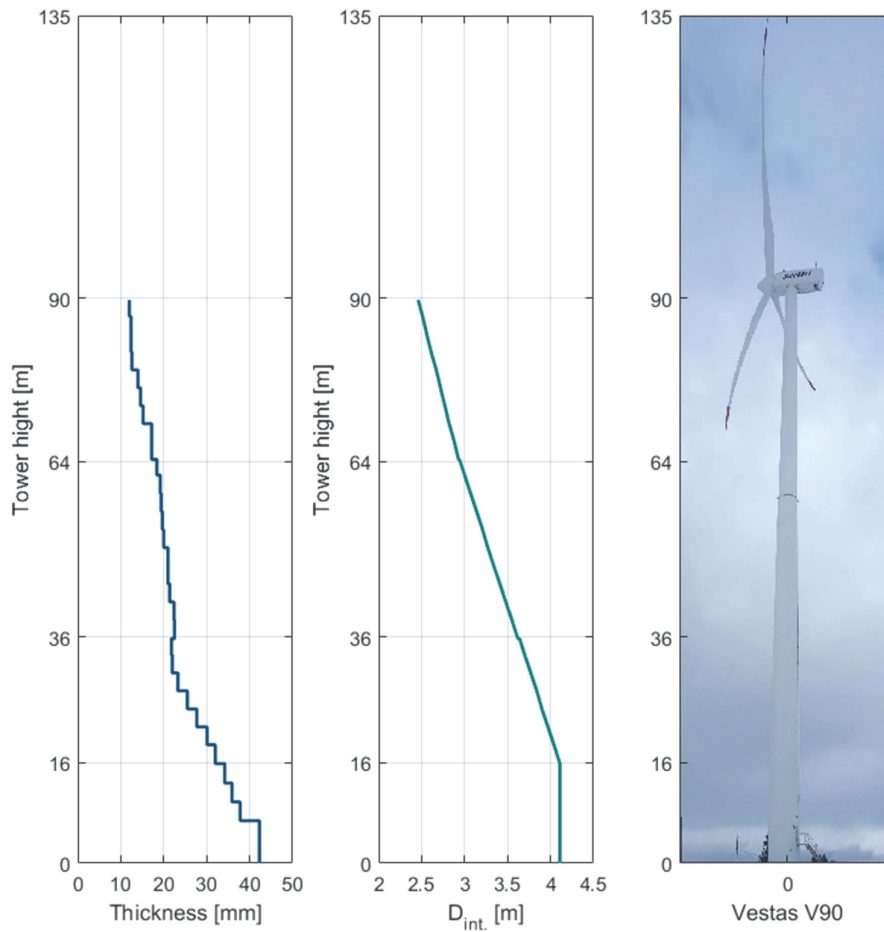
Figure 2-1. Wall thicknesses and internal diameters of the tower measured in-situ

2.2.2   Site description

Juvent SA wind farm is located in the complex topography of the Jura Mountain, in western Switzerland. Figure 2-2(a) shows the implantation of the 16 wind turbines of the wind farm as well as the annual average wind speed at 100 m (OFEN 2016) with an uncertainty of +/- 0.5 m/s. The turbine n°10 is indicated with the yellow cycle. Turbines are installed on the Mont-Crosin crest along the St-Imier valley that follows the WSW-ENE direction at an altitude varying from 1100 m to 1250 m (1235 m a.s.l for Turbine n°10). One can also note that this area is subject to icing. The Swiss Federal Office of Energy (OFEN) points that one can expect between 10 to 20 days of icing per year. Icing can reduce the aerodynamics of the blades and lead to production losses. Mass imbalance resulting from the added weight can also increase loads and fatigue of the structure. Thus, wind turbines are shut down for safety reasons during icing periods.
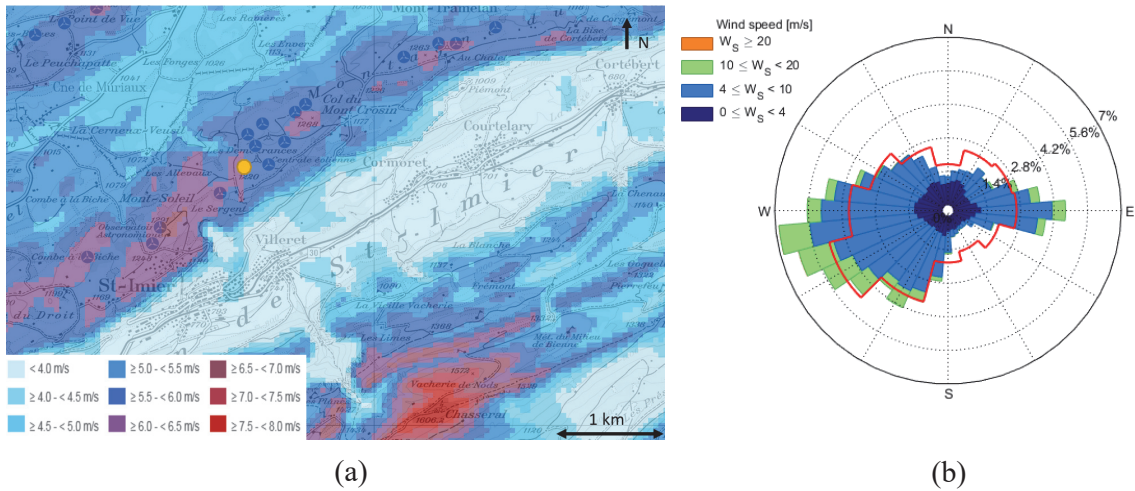
Figure 2-2. Layout of the Juvent SA wind farm located in the Swiss Jura mountains- St-Imier, Bern, Switzerland. (a) Modeled annual average wind speed of 100 m (+/- 0.5 m/s); the turbine n°10 is shown by the yellow dot. (b) Wind rose based on SCADA data and compared with the modeled annual average direction at 100 m by the OFEN, shown with the red line.

The wind rose (Figure 2-2(b)) obtained with the measured wind direction of the ultrasonic anemometer of the wind turbine n°10 reveals two preferential wind direction. The main wind direction (MWD) is relatively spread out between West and South-West and merely corresponds to the leading regional wind called "Vent". The secondary wind direction (SWD) is a narrow band along the East direction referring to the wind called "Bise".

Finally, the local wind speed distribution (regardless of the wind direction) can be established using the measured 10-minute average wind speed at hub height provided by the SCADA system. The histogram, which was acquired using the wind speed recorded by the sonic anemometer of the turbine n°10 from January 2012 to April 2017 is indicated in Figure 2-3. A Weibull distribution was fitted (green curve) and the Weibull distribution provided by the OFEN at the turbine location (brown curve) are presented for comparison. The fitted Weibull distribution based on in-situ measurement tends to underestimate low to medium wind speed whereas the modeled Weibull distribution minimizes the low to medium wind speed even more. The modeled Weibull distribution also overestimates the high wind speed considerably (see Figure 2-3). These differences between in-situ measurement and design distribution - usually a Weibull distribution with shape parameter k = 2 and scale parameter $\lambda = \sqrt{2}\sigma$ (thus being a Rayleigh distribution) – often result in discrepancies between measured and calculated wind loading and wind fatigue loading. Nonetheless, the Gamma distribution gives a better fit for the measured wind speeds at hub height. This distribution with shape parameter $\alpha = 3.96$ and scale parameter $\beta = 1.47$ (obtained using the maximum likelihood method) will be used later to estimate the 50 years return of wind speed near turbine n°10.

13
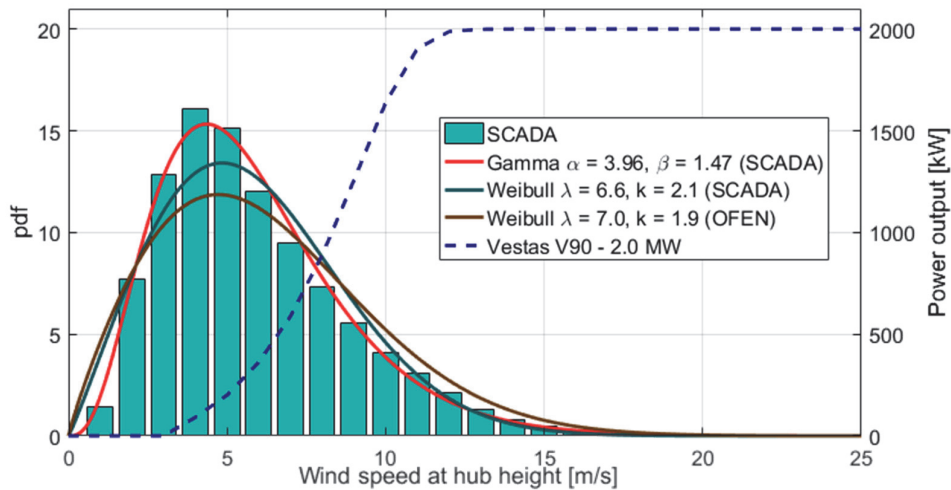
Figure 2-3. pdf distribution of the 10-minutes average of the wind speed at hub height (from the SCADA system of the turbine n°10) and theoretical power output curve of the Vestas V90 – 2.0 MW.

2.3 Environmental and operational data

The use of the SCADA data is becoming more and more important since it provides useful information regarding the turbine operation and the wind conditions. As mentioned earlier, this specific turbine was selected because of the available SCADA data. At that time, however, only the 10-minute values of the following datasets were available: minimum, maximum, average, and standard deviation of the wind speed in addition to 10-minute average wind orientation, hub temperature, rotor rotational speed, pitch angles of blades, the nacelle orientation, and the power output. As of today, new wind turbines are automatically equipped with a SCADA system and provide information at a much higher resolution of 1 Hz.

The environmental and operational data and the statistical analysis collected from December 2014 to April 2017 from the SCADA system of the turbine n°10 are shown in Figure 2-4 and Figure 2-5, respectively. The annual temperature variation is displayed in Figure 2-4(a). A minimum temperature of -11°C was recorded in January 2017 and a maximum of 31°C in July 2015.The variation of other environmental parameters and the corresponding histogram plots are presented in Figure 2-4(b-g). Figure 2-4(b) indicates the 10-minute average wind speed, with a maximum average recorded at 23.4 m/s. The annual variation can also be observed with relatively higher wind speed in winter seasons. The maximum wind speed recorded is 39.6 m/s (143 km/h) on January 12th, 2017. One should note that the SCADA system sometimes stops recording parameters during power outages, which happens mainly during the most violent storms. Figure 2-4(d-e) shows the wind direction where the two main directions are identified along the West for the MWD and East for the SWD. The calculation of the absolute wind direction (wind angle from 0° to 180°) leads to only one main absolute wind direction, along with the West-East direction. This wind configuration is more unfavorable than if two main wind directions do not coincide. The wind forces and wind fatigue forces will most of the time act along the same axe, with 31 % of the time in a 30° sector (along West-East) and 50 % of

the time in a 54° sector (i.e., only 15 % of the circumference). The turbulence intensity (TI) showed in Figure 2-4(f-g) is derived from the SCADA data and is defined as the ratio between the standard deviation and the mean wind speed in the same time interval:

$$TI = \frac{\sigma_{v_{hub}}}{v_{hub}} \qquad (2\text{-}1)$$

The measured annual average turbulence intensity is 16.1 % when the average TI is approximately 15.1% and 17.9 % for speed ranging from the cut-in wind speed V_{in} to the rated wind speed V_{rated} and from V_{rated} to the cut-out wind speed V_{out}, respectively. However, the situations below rated wind speed represent 57.2 % of the time against only 2.0 % for full power production; the rest of the time – 40.8 % – being below cut-in speed.

One should use environmental SCADA data cautiously due to several reasons mentioned below. The sonic anemometer situated at the top of the nacelle is subject to interference with the rotor, while the blades passing in front of it can perturb the wind flow and thus lead to lower wind speeds and higher TI (Noppe, Weijtjens, and Devriendt 2015). The tower vibrations can also bias the measurement from the sonic anemometer, as the fast deflection of the tower can influence the wind speed measurement. Over a period of 10 minutes, such effects (*i.e.,* wind gusts of few seconds) may not be so significant, and comparison with similar turbines can be made as the anemometer is situated at the same location. For a more in-depth study of the wind speed and the turbulence intensity, and if the wind farm size can warrant the investment, the erection of a meteorological mast could provide more precise data.
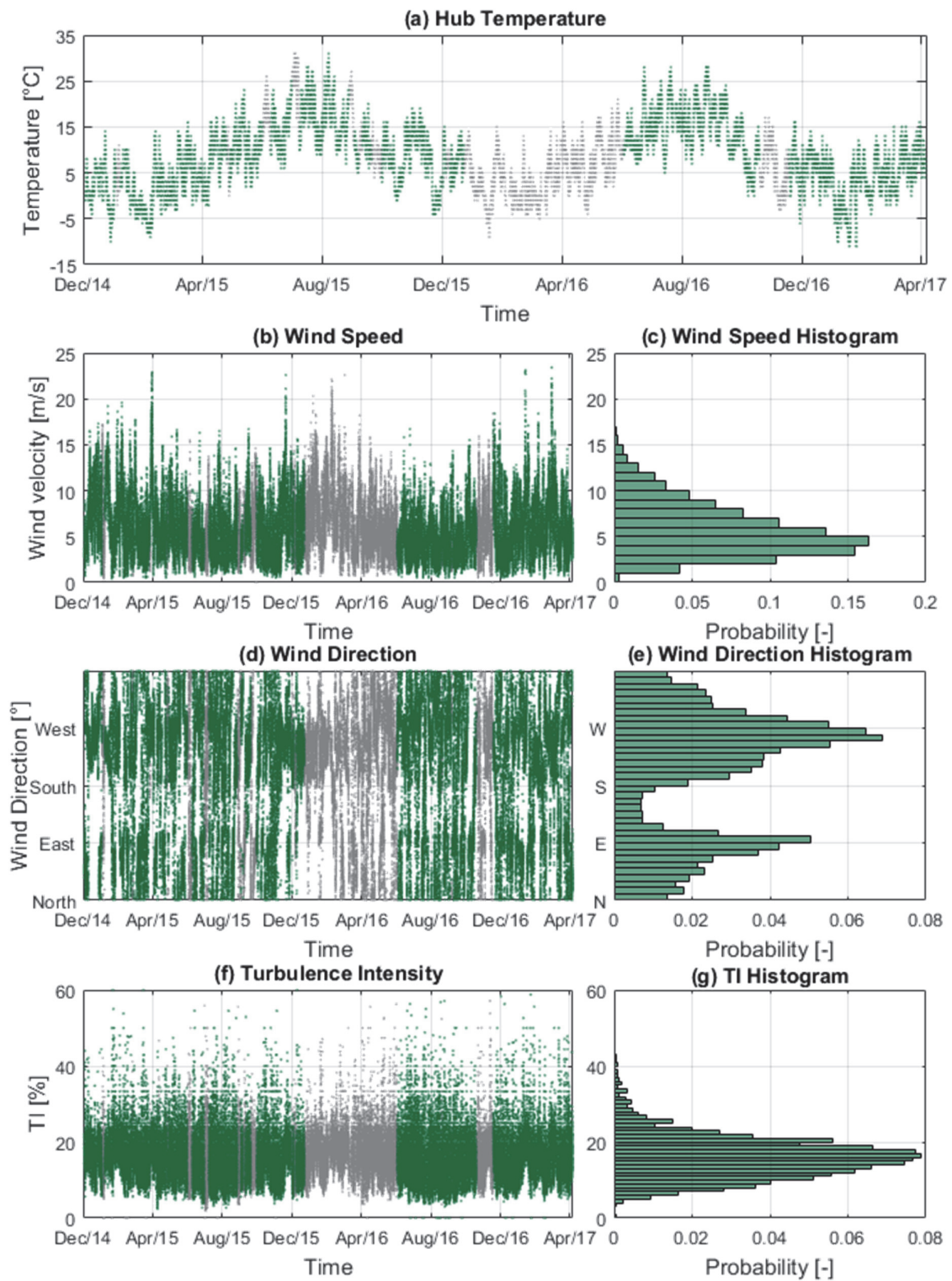
Figure 2-4. Environmental data and corresponding statistical analysis from December 2014 to April 2017 for the turbine n°10.

Figure 2-5 provides the variation of the operational data and its statistical analysis. Only time series with values of power output above 100 kW are considered as production periods. The idle/shut-down periods with low wind speed and no production represent 40 % of the time again. The blade pitch angle in Figure 2-5(c-d) varies from 0° to 15° with a nominal value of -2.0° below rated wind speed. The blades are pitched at an angle of 24° during the idle position of the rotor, and a value above 86 % for the blade pitch signifies that the turbine is parked. Finally, Figure 2-5(e-f) shows the rotor speed. To avoid any excitation frequencies generated by the rotor frequency (1P) and the blade passing frequency (3P), the rotor speed is quickly increased from 2.5 to 8.8 rpm and reach the rated speed of 14.9 rpm. During the idle time of the turbine, the rotor speed varies freely from 0 to 2.5 rpm.
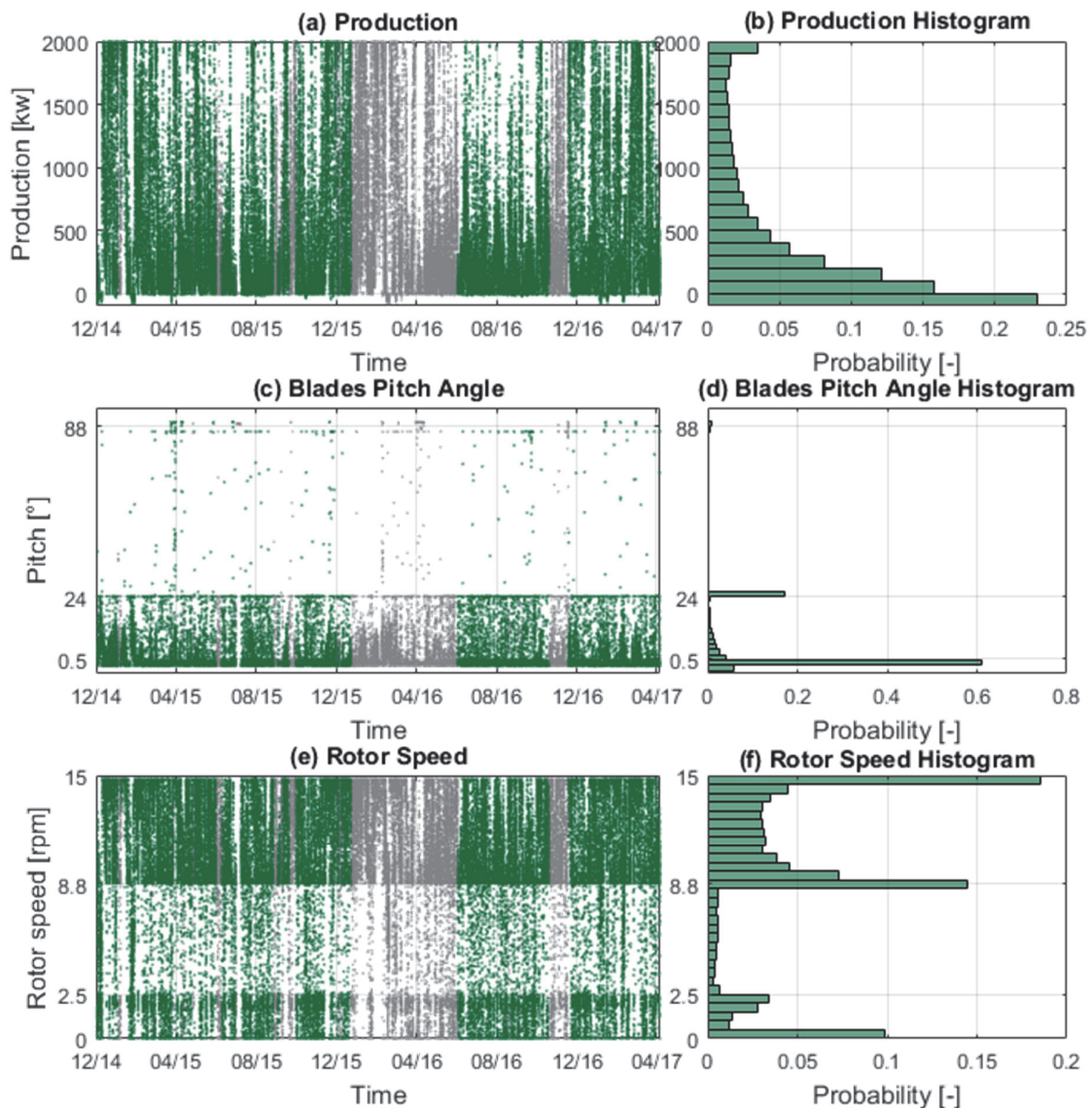
Figure 2-5. Operational data and corresponding statistical analysis from December 2014 to April 2017 for the turbine n°10.

2.3.1 Wind condition

The 95 m Vestas V90 is designed for the wind class IEC IIIA according to the International Electrotechnical Commission standards (IEC 61400-1 2005). It indicates the following assumptions that are made for the design: low (III) annual average wind speed and higher turbulence intensity (A). Three parameters characterize the turbine classes: the 50-year return wind 10-minute average V_{ref}, the annual average wind speed V_{ave}, and the characteristic turbulence intensity for $V_{hub} = 15$ m/s in which V_{hub} is the 10-minute average wind speed at hub height.

For the specific location of the turbine n°10, one can compute the in-situ wind condition with the measured wind speed and compare with the design values. The 50-year return wind 10' average V_{ref} is extrapolated from the fitted Gamma distribution (Figure 2-3). The probability of exceedance of a particular wind speed V observed during a 10-minute period is simply calculated with:

$$P(V_{hub} > V) = 1 - \Gamma(V; \alpha, \beta) \tag{2-2}$$

where $\Gamma(V; \alpha, \beta)$ is the cumulative distribution function (CDF) of the Gamma distribution.

To estimate the empirical probability that any wind speed V_{hub} will exceed the wind speed level V_{50}, wind speeds are ranked in ascending order ($V_{1,hub} > \cdots > V_{i,hub} > \cdots > V_{N,hub}$), where N is the total number of measured 10-minute series. The probability that any V_{hub} will exceed the wind speed V can be determined using the Weibull plotting position with:

$$P(V_{hub} > V) = \frac{i}{N + 1} \qquad\qquad i = 1, 2, \dots, N \tag{2-3}$$

The probability of exceeding the 50-year return wind speed in any given 10-minute period is:

$$P(V_{hub} > V_{50}) = \frac{1}{50 \cdot 365.25 \cdot 24 \cdot 6} = 3.8 \cdot 10^{-7}. \tag{2-4}$$

From the SCADA data, the site-specific wind conditions are established, and parameters are summarized in Table 2-2 below.

Table 2-2. Wind conditions for onshore turbines with site-specific parameters obtained from the SCADA data from December 2014 to April 2017 for the turbine n°10

Wind turbine class	I	II	III	Site-specific	Remarks
Wind	high	medium	low		
V_{ref} [m/s]	50	42.5	37.5	32.9	50-year return wind 10-minute average
V_{ave} [m/s]	10	8.5	7.5	5.8	Annual average wind speed
Category	A	B	C	Site-specific	Remarks
Turbulence Intensity	higher	moderate	lower		
I_{15} [%]	18.0	16.0	14.5	17.9	Characteristic turbulence intensity for $V_{hub} = 15$ m/s

Such information indicates that the specific wind condition in the studied wind farm is clearly below the lowest wind turbine class. The reference and the average wind speed at hub height are 12.3 % and 22.7 % smaller than the design value of the low wind class III, respectively. The turbulence intensity is the same for $V_{hub} = 15$ m/s, with respect to category A.

2.3.2 Clustering of operating condition

As seen in Figure 2-4, environmental factors vary a lot, especially the wind speed distribution that can change yearly based on stronger and weaker wind years. To consider these variations for a safe and reliable estimation of the future service duration of a wind turbine support structure, the measured data are coupled with operational and environmental data provided by the SCADA system, as these data are available since the WT installation.

In recent years, the use of the data from the SCADA system has become a widespread method in wind turbines and related studies, as it provides a broad set of relevant information especially for Condition Monitoring and Structural Health Monitoring (Hu et al. 2015b; Dai et al. 2017; Iliopoulos et al. 2016; Noppe et al. 2016a; Spiridonakos et al. 2015; Schlechtingen and Santos 2014) . It is also used for fault and failure detection (Sun et al. 2016; Zaher et al. 2009) and performance assessment of wind farms (Mittelmeier, Blodau, and Kühn 2017). These approaches rely mainly on the neuronal network and learning algorithms.

The clustering method used here relies on the statistical analysis conducted on the SCADA data collected from December 2014 to April 2017 and is presented in Figure 2-5 and Figure 2-6. Employing environmental (wind speed and turbulence intensity) and operational data (power production, rotor speed, and pitch angle) the 10-minute series are clustered into different loading categories, *e.g.*, normal operation, normal operation plus fault (fault in pitch control, for example, resulting in under power production) or icing on blades.

The algorithm makes a first pass on the SCADA to identify all the abnormal situations that do not generate power, and with a second pass power production category is identified.

Table 2-3 resumes the various defined load cases and turbine conditions that will be used in upcoming chapters. During this period, the WT produced energy during 63.4 % of the time (or 233 days/year). Start-up and shutdown periods also account for 13 % of the time, and the icing on the blades occurred about nine days/year.

Table 2-3. Clustering of 10-minute time series.

Operating condition	Load case	12/2014 - 04/2017		yearly average
		# 10' series	%	# days
Normal power production	1.1	50748	58.3	213
Over power production	1.2	1181	1.36	5.0
Under power production	1.3	3031	3.48	12.7
Power production with pitch fault	1.4	420	0.48	1.8
Start-up/Stop ($v = v_{in}$)	2	11387	13.1	47.8
Start-up/Stop ($v_{in} < v \leq v_{rated}$)	3	342	0.39	1.4
Parked ($v \leq v_{rated}$)	4.1	836	0.96	3.5
Parked ($v > v_{rated}$)	4.2	218	0.25	0.9
Idling	4.3	14846	17.1	62.3
Emergency shut-down	5	72	0.08	0.3
Icing of blades	6	2078	2.39	8.7
No SCADA	7	1817	2.09	7.6
		86976	100	365
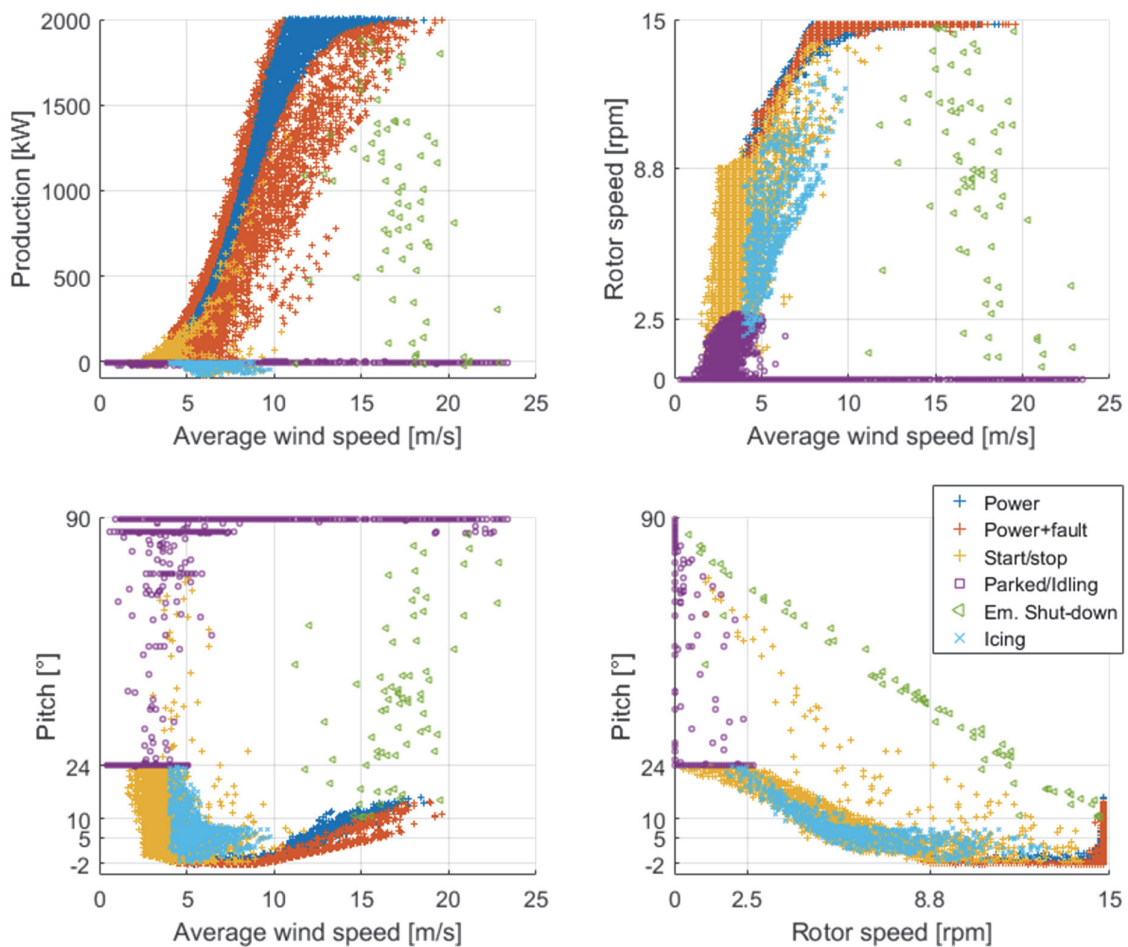
Figure 2-6. Relation between environmental and operational factors

As seen in Figure 2-6, various operating conditions are captured with the clustering algorithm. One can easily recognize specific patterns. Parked or idling situations are characterized with a blade pitch angle of respectively 90° and 24° and a rotor speed of 0.0 or varying from 0.0 to 2.5 rpm, and is always associated with a negative power output (the WT draw some current from the grid for its own operation). The icing on the blade is characterized by a stronger negative power output (up to -100 kW) and lower than average rotor speed. This behavior is the result of multiples start/stop sequences during the 10-minute periods, as the vibrations of the tower quickly reach the emergency shutdown threshold. Emergency shutdowns during storms are clearly visible on every plot, as both the rotor speed and the pitch angle rapidly decrease from their rated values to their parked values. For standard operation (*i.e.,* power production), the theoretical power production curve is used to separate 10' series between normal production and out-of-range production. An underproduction situation is often characterized by a lower-than-average pitch angle, clearly visible on the Average wind speed – Pitch graph.

2.4 Detailed Finite Element model of the Vestas V90 tower

Thanks to the measurements of plate thickness performed over the height of the tower (Figure 2-1), a detailed finite element model (FEM) is developed using DIANA 10 software. The tower is modeled in 3D using quadratics quadrilateral curved shell elements (CQ40S). The door opening and its dimensions are included into the model (Figure 2-7(a)). The nacelle mass is modeled as a lumped mass attached to the tower top segment with rigid springs (Figure 2-7 (b)). The tower connection to the foundation is considered rigid as no valid information could be found on a probable foundation stiffness.

(a)   (b)
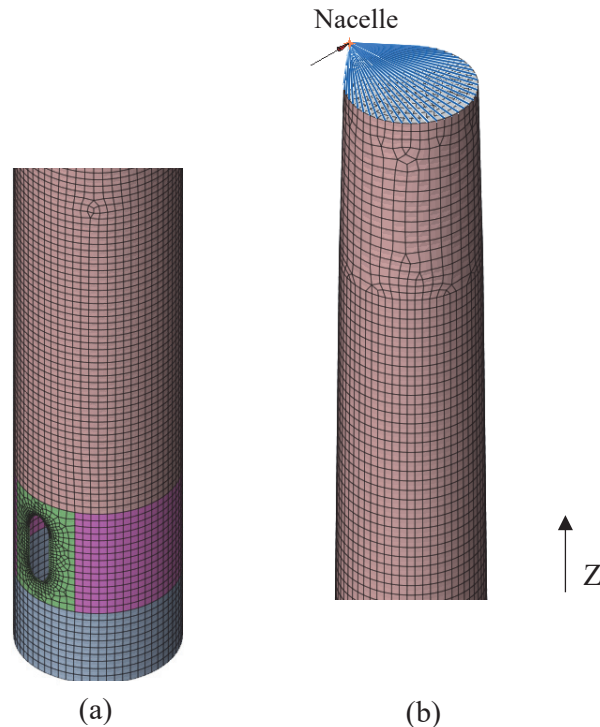
Figure 2-7. Finite element model used for structural analysis: (a) bottom segment with the door opening and (b) nacelle lumped mass.

The model was used to determine the stress distribution over the tower height and localize the maximum stress location. The final longitudinal stress distribution σ_{zz} resulting from a quasi-static tower top thrust load is presented in Figure 2-8(a) below. Figure 2-8(b) shows the stress measured at the bottom section (7.8 m from tower foundation) and at 36 m, close to the junction between the tube #2 and #3 during few hours of rated wind speed. The longitudinal stress between tube #2 and #3 is found to be 1.56 times the stress measured at the bottom section when the ratio measured with strain gauges is 1.59. The relation is linear, which confirms that the stress measured at the bottom section can be used to evaluate the fatigue at the critical location.
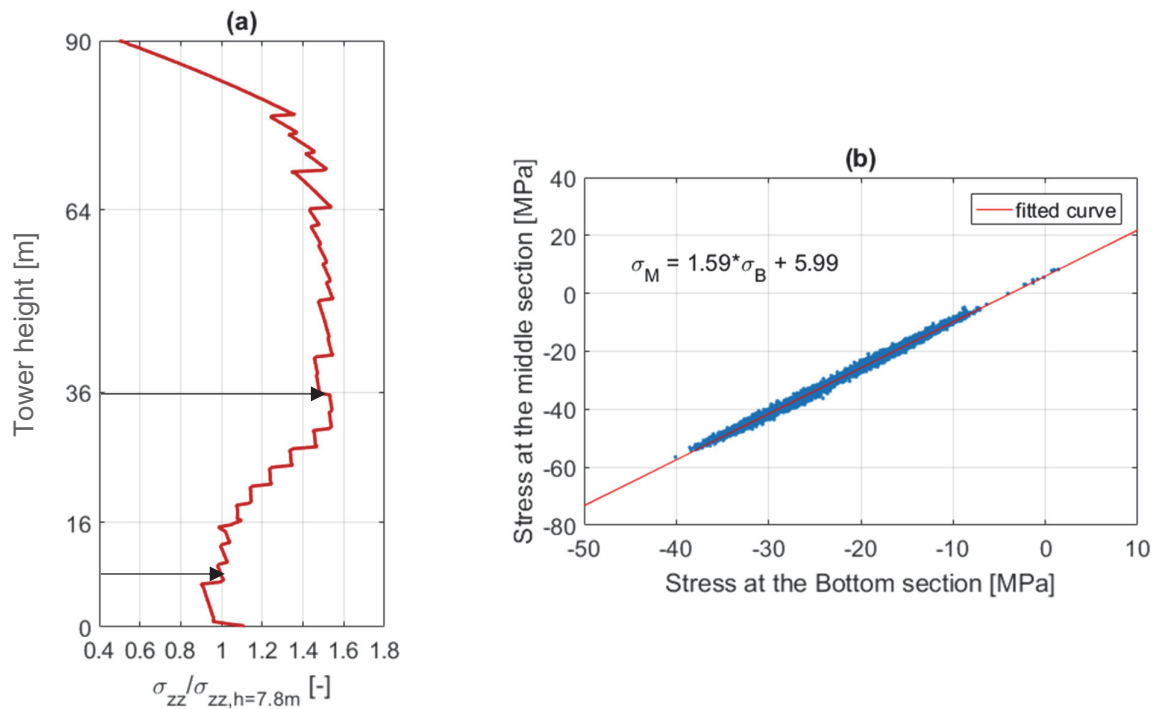
Figure 2-8. (a) Stress distribution normalized to the stress calculated at 7.8 m from the foundation (bottom section measurement) and (b) correlation between stress measured at the bottom section (reference section) and at the junction between tube #2 and #3.

2.5   Monitoring system

The monitoring system developed for this study features strain gauges on the tower walls, temperature and humidity sensors, and accelerometers. It was particularly designed to be robust, since the first goal was to measure strains continuously for one year, and then it could be extended up to 3 years. This system was also designed in a way that sensors could be added and removed without problems. In total, three sections of the tower were instrumented with strain gauges and temperature sensors, and accelerometers were installed in the nacelle and at the tower top (just below the yaw system).

Finally, the following set of sensors were installed:

- 8 linear strain gauges and 2 rosettes strain gauges
- 11 temperature sensors
- 3 accelerometers
- 1 humidity sensor

In addition, the data acquisition system was composed of the following equipment:

- 3 data acquisition units (DAU)
- 1 synchronization unit
- 1 router and 1 switch
- 1 data storage PC

All sensors were connected to the DAU using double shielded cables, and the link between the DAU placed on the tower top and main synchronization unit at the bottom is performed using a single 100 m long optical cable. Schematics of the complete monitoring system is presented in Figure 2-9, and the data acquisition equipment and its installation are displayed in Figure 2-10.

The first set of sensors was installed in October 2014 on the level of the first platform above the entrance, at 7.80 m higher from the tower foundation. The second set of sensors was installed soon after on the tower top platform, at about 87.2 m higher from the foundation. The installation of the equipment and the strain gauges required one day of work for each monitored section with the help of two technicians. A year later, two extra strain gauges were added at the junction between the 2nd and the 3rd tower segments and connected to the bottom DAU. The FEM with the precise geometry of the tower (instead of a simple linear interpolation between the tower bottom and top sections) revealed that the highest stresses are situated (see the stress distribution over the tower height in Figure 2-8(a)) along the 2nd and 3rd tower segments, with a maximum stress at the junction between tube #2 and #3, 36 m from the foundation. Only two strain gauges were installed there since just a small amount of data was needed to perform the check, and full temperature compensation was not required.

During the first year of measurement strain and acceleration were recorded at 50 Hz, which lead to about 500 Mb of data per day. After the 1st year, the strain gauges and accelerometers situated at the tower top were removed. The acquisition frequency was also reduced to 20 Hz as it was demonstrated that no data was lost compared to the initial frequency of 50 Hz. To date, the monitoring has required only 110 Mb of disc space per day with the reduced monitoring set-up. Table 2-4 summarizes the installed sensors and measurement frequencies. The data presented in the thesis results from a total of 604 days of measurement.

Table 2-4. Summary of installed sensors

Section	Sensors			1st year	2nd year +
	Type	Type	#	Sampling rate [Hz]	
Bottom	Linear SG	1-LY61-6/120	3	50	20
	Rosette SG	1-RY101-6/120	1	50	20
	Temperature	Pt100	5	1	1
Middle	Linear SG	1-LY61-6/120	2	-	20
	Temperature	Pt100	2	-	1
Top	Linear SG	1-LY61-6/120	3	50	-
	Rosette SG	1-RY101-6/120	1	50	-
	Temperature	Pt100	4	1	-
	Humidity		1	1	-
Tower-Nacelle connection	Accelerometers	HBM B12 200m/s2	3	50	-
			25		
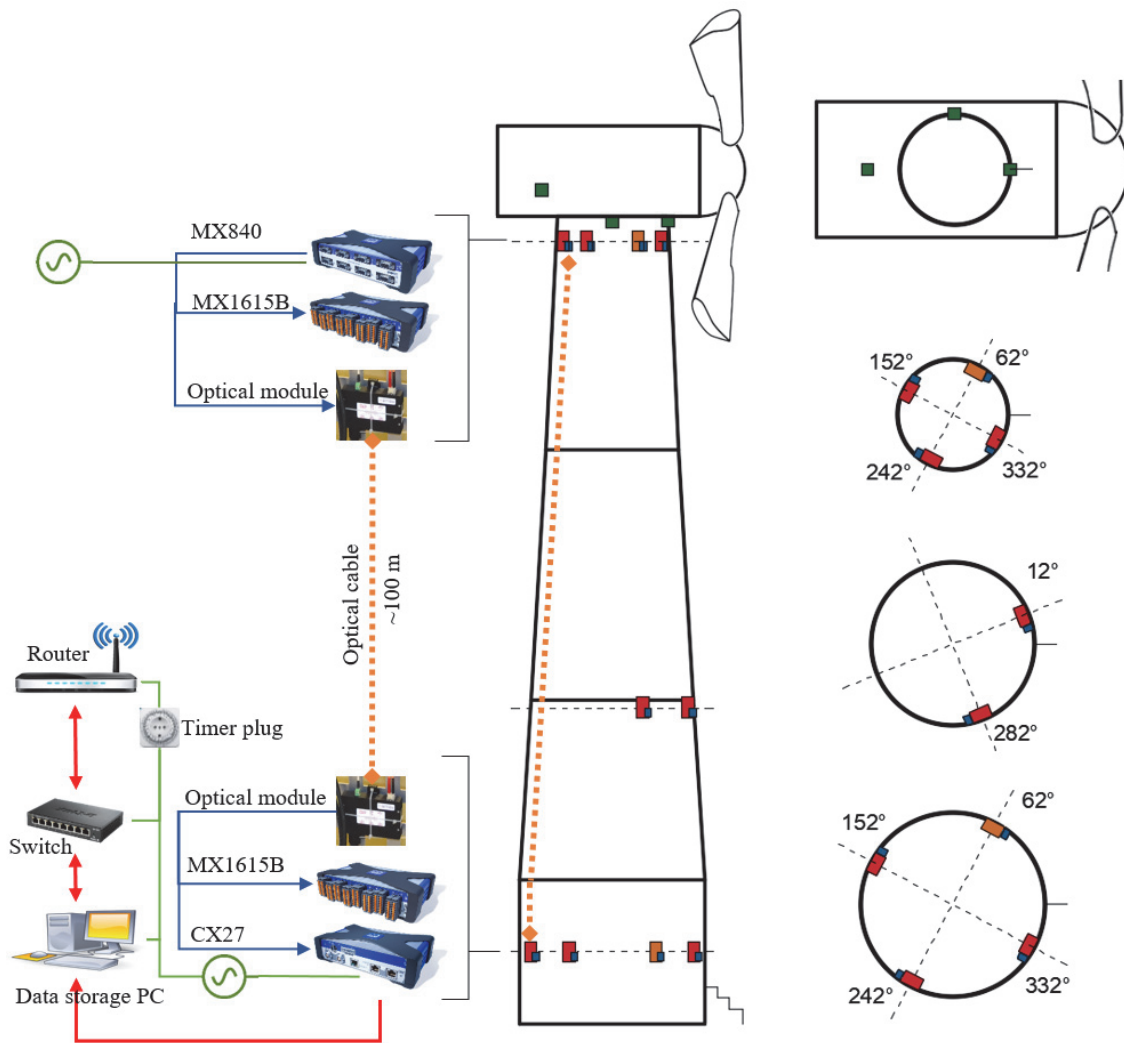
Figure 2-9. Schematic of the WT n°10 monitoring system. The blue, red, orange, and green markers are respectively Pt100 temperature sensors, linear strain gauges, rosette strain gauges, and accelerometers.

2.6   Data Acquisition equipment

The monitoring system mostly relies on HBM QuantumX modules as they proved their suitability for long-term measurements under severe conditions of temperature, relative humidity (RH), and dust (Treacy 2014; Grigoriou 2015). In the turbine tower, high RH and possibly very low temperature were the main concern, especially in winter times where negative temperature is often expected.

Figure 2-10(a) shows the main installation on the bottom platform. The elevator protection grid was found to be a convenient support for main units as they are properly secured; the computer, the router, and the switch were stored in a Polystyrene box to prevent freezing. The firstly installed computer (MacMini with HDD) was later replaced by an aluminum case, fanless NUC with an SSD that was found much more reliable and robust. For short outage and lightning protection, the computer was connected to a UPS. Remote control of the system was available through a 3G connection and the Teamviewer software; the router was plugged into a timer, to ensure the daily restart of the connection. An external antenna was needed as no signal can be detected inside the tower and it was fixed outside above the door, alongside with an external temperature sensor (Figure 2-10(b)).
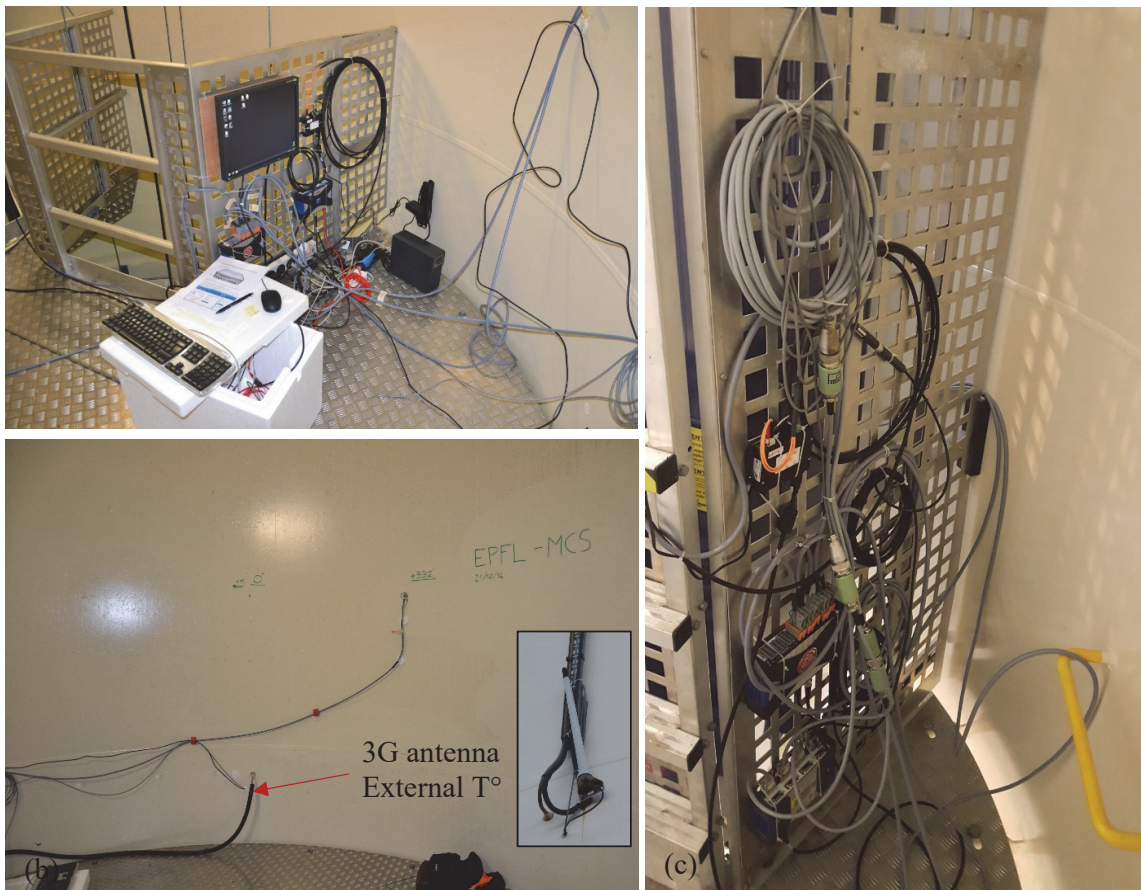
Figure 2-10. Images of the monitoring system (a) data acquisition equipment on the first platform (b) wiring of the strain gauges and temperature sensors (c) data acquisition equipment on tower top platform.

On the bottom platform level, strain gauges and temperature signals were connected to a 16 channels MX1615B module. This device was connected to the computer through a CX27 synchronization module. On the tower top platform (Figure 2-10(c)) accelerometers and the humidity sensor were connected to an 8 channels MX840 module, strain gauges and temperature sensors to an MX1615B module. The two measurement sections being distant by 80 meters from each other, employing a centralized data acquisition system would require hundreds of meters of shielded cables and thus would increase the monitoring budget and the installation time. Finally, a single 100 m optical cable was installed with one optical module on each side to convert the electrical signal. This solution decreased the risk of electromagnetic disturbance generated by the high voltage power cable coming from the turbine generator (Krug and Lewke 2009).

2.7   Strain gauge configuration

Strain gauges are very sensitive sensors that can directly measure strain, but many factors can easily distort the measurements. To ensure the proper measurement of the strain variations in the tower over an extended period, all potential sources of error must be carefully identified, and the monitoring setup must be designed accordingly.

The most frequent source of error is the temperature. The electrical resistance of the strain gauge changes with the deformation but also changes with temperature, as well as the gauge factor of a single gauge system which is defined as:

$$\frac{\Delta R}{R} = GF \cdot \epsilon = GF \cdot \frac{\Delta L}{L} = GF \cdot \frac{\sigma}{E} \qquad (2\text{-}5)$$

where $\Delta R/R$ is the relative change in the gauge resistance (VTI n.d.). Temperature effects on the gauge response can be in the magnitude of the measured strain (Vishay 2007), thus must be corrected and compensated. Most of the strain gauges are already compensated for temperature; the specific alloy used to fabricate the gauge is designed in a way that the resistance of the gauge itself cancels out the thermal expansion of the tested specimen (Keil 1988). However a, small difference remains and compensation curves provided by the gauge manufacturer must be used to eliminate this effect. In this project, the following equation is provided by the gauge manufacturer Hottinger Baldwin Messtechnik (HBM):

$$\varepsilon_{T/O} = -22.6 + 2.42 \cdot T - 7.35 \cdot 10^{-2} \cdot T^2 - 2.99 \cdot 10^{-4} \cdot T^3 \pm 0.3 \cdot (T - 20) \; \mu\epsilon/°C \quad (2\text{-}6)$$

Equation (2-6) is the thermal output of the installed linear strain gauges on the tower, compensated for steel with a thermal expansion coefficient of $\alpha = 10.8 \cdot 10^{-6} \; K^{-1}$. Deviation in the thermal output between different gauges from the same production batch is possible and is in the range of ±0.3·(T-20) µε/°C, as shown in Figure 2-11(a). Temperature (and humidity) may also affect the zero reference of the measurement. Thermal drift is caused by microstructural changes in the measurement grid and the glue used to attach the gauges is also altered by temperature and humidity (Hoffmann 1989). For long measurement periods, one must also consider the fatigue of the gauge itself. The alternating strain acting on the gauge induces a remaining zero point error and can end in the failure of the gauge for either very high

number of cycles or very high alternating strains. However, when type LY61-6/120 of strain gauges (6 mm, 120 ohm linear strain gauge) glued with the X 60 adhesive and used, the numbers of cycles to failure seem to be way above 10 million cycles for relatively large alternating cycles of ± 1'000 με (HBM n.d.).
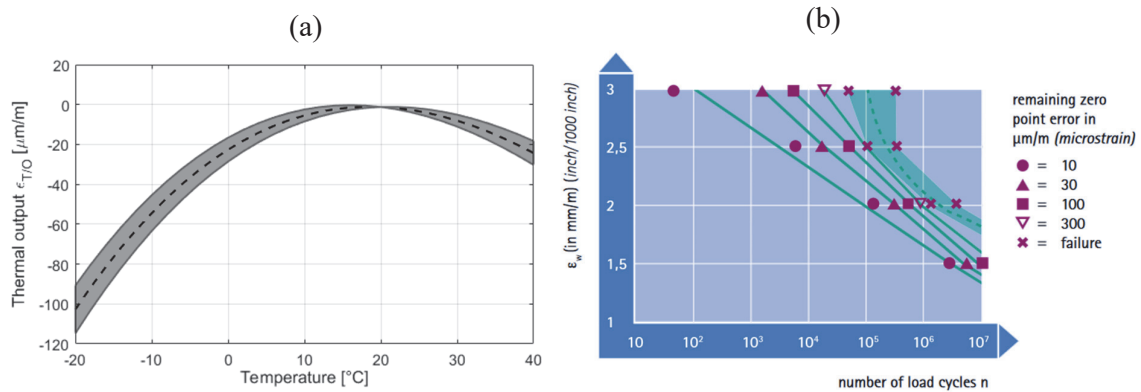
Figure 2-11. (a) Example of thermal output compensation curve for linear strain gauges and possible spread within the same production batch. (b) Example diagram of the fatigue life vs stress amplitude of strain gauges (HBM n.d.).

One must also consider the thin steel tower walls that quickly react to the local heating of the sun. This effect can also influence the measured strains, as the temperature gradient becomes highly non-linear. For any unrestrained section, the free strain is:

$$\varepsilon_{n,T} = \alpha T_0 - \alpha \frac{\Delta T}{h} y \tag{2-7}$$

where T_0 is the uniform temperature change in the material, ΔT being the temperature difference between the bottom and top surfaces, and h the section height. For a circular section that is evaluated on the internal surface, equation 2.7 becomes:

$$\varepsilon_{\theta,T,free} = \alpha T_0 - \alpha \frac{\Delta T}{D_i} R_i \cos(\theta + \beta) \tag{2-8}$$

where β is the axis orientation along which the ΔT is the maximum. Figure 2-12(a) represents the measured temperature along the tower circumference at the bottom location (red curve) with the corresponding linear profile (black curve) fitted with Equation (2-8), in which $\beta = 96.8°$ and $\Delta T = 8.4\,°C$.

The strain gauges are already compensated for temperature effect. Thus, the signal must not change with the free deformation of the section. However, with a non-linear temperature gradient, the signal is disturbed by strains resulting from the differences in temperature between the linear and the non-linear profiles. The strain gauges will then "overcompensate" or "undercompensate" the temperature. This effect is clearly visible in Figure 2-12(c), and the difference is displayed with the red curve on Figure 2-12(d). This results in an alternation of positive and negative strains that are actually an indirect measurement of self-equilibrated stresses that develop because of the restrained situation. The thermal stresses are small (up to 3-4 MPa), and of no interest in this study, however, the strains must be corrected as it will

influence the mechanical stress calculation. The thermal response of the gauges can be expressed as:

$$\varepsilon_{\theta,T,gauge} = \begin{cases} 0 & linear\ T°\ gradient \\ \alpha\left(T_0 - \dfrac{\Delta T}{2}\cos(\theta + \beta)\right) - \alpha T(\theta) & non-linear\ T°\ gradient \end{cases} \quad (2\text{-}9)$$

And the temperature induced stresses:

$$\sigma_{\theta,T,gauge} = E\alpha \cdot \left(T_0 - \frac{\Delta T}{2}\cos(\theta + \beta) - T(\theta)\right) \quad (2\text{-}10)$$
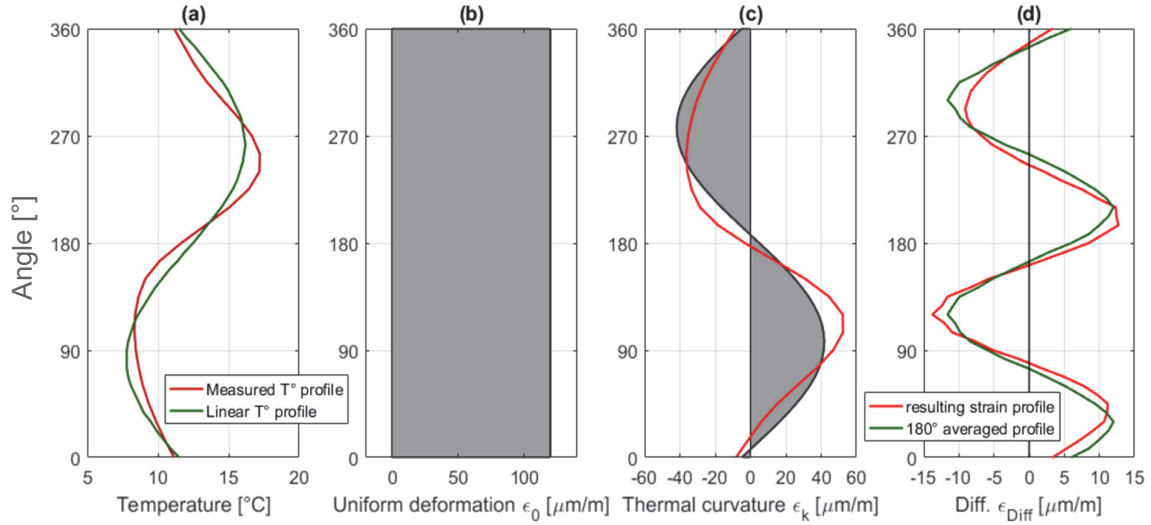
Figure 2-12. Example of temperature and longitudinal thermal strains distributions along a circular steel section. The grey plots correspond to a linear temperature profile when the red curves represent an example of a non-linear temperature gradient.

The calculation of these artificial strains requires values of the temperatures in multiple locations around the section for a reliable estimation of the different parameters. However, one can take benefit from the approximate 90° phase between alternative peaks by taking the average of similar values at 180°. The green curve on Figure 2-12(d) is resulting from the average opposite strains. The remaining strain is about ± 3 µm/m, which is approximately 4.5 times less than the value shown in that example. The equation below resumes the strains and the potential sources of errors resulting from the measurement with a strain gauge:

$$\begin{aligned} \varepsilon_{tot,gauge} &= \varepsilon_{mech}(wind, nacelle\ masse\ imbalance) \\ &+ \varepsilon_{T/O}(Temperature) \\ &+ \varepsilon_{T°}(non-linear\ T°) \\ &+ \varepsilon_{drift}(time, RH, T°, fatigue, \dots) \end{aligned} \quad (2\text{-}11)$$

Mechanical strains ε_{mech} are resulting from bending moments caused by the nacelle mass imbalance and the thrust force of the wind on the rotor, and follow the expression below:

$$\varepsilon_{mech,\theta} = -\varepsilon_{mech,\theta+180°} \quad (2\text{-}12)$$

Drift caused by long-term effects and fatigue of the gauge is supposed to be similar for two opposite gauges (as the same stress amplitudes occur for both gauges).Therefore, gauges installed the same day, under the same temperature and relative humidity, and aging under the same conditions are expected to be affected the same way. Thus, the following hypothesis is considered valid:

$$\varepsilon_{drift,\theta} = \varepsilon_{drift,\theta+180°} \qquad (2\text{-}13)$$

Finally, strains induced by non-linear temperature profiles are assumed following:

$$\varepsilon_{T°,\theta} \cong \varepsilon_{T°,\theta+180°} \qquad (2\text{-}14)$$

Based on these considerations, the measurement system must contain a set of four strain gauges along the perimeter equally spaced every 90°. Along each strain gauge, a temperature sensor is required for the thermal compensation. The remaining parasite strains appearing when the sun heats the structure are removed by average the sum of the opposite strain gauges. In addition, this configuration offers a more robust system, as some perturbations of the signal on one gauge can be avoided as the opposite gauge take the relay.
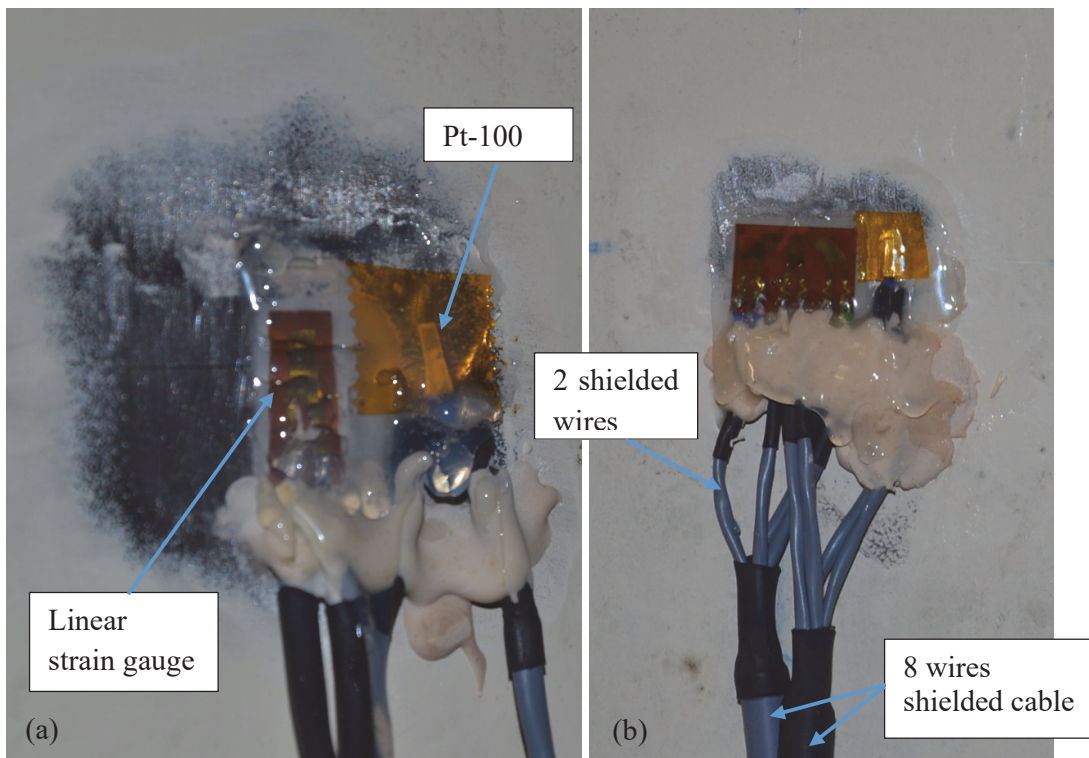
Figure 2-13. (a) Longitudinal strain gauge with Pt-100 temperature sensor. (b) Rosette with Pt-100 temperature sensor

Figure 2-13(a) represents the typical linear strain gauge with its temperature sensor Pt-100. The tower mast was carefully prepared before the gluing of the gauge. The protective painting was removed locally, and the steel was finely sanded before cleaning the remaining dust and oil with an alcohol to ensure a perfect bonding of the gauge. Sensors were protected against

humidity with a silicone gel. Strain gauges were connected in a ¼ bridge configuration with a regulated 4-wire circuit, according to patented Kreuzer circuit of HBM. This ensures no temperature effects on the cable, as the change in electrical resistivity of the cables due to temperature is adequately compensated. Double shielded cables with 8 wires were used for each pair of sensors. Each cable – no matter the distance from the DAU to the measurement location – is of the same length to eliminate the potential disparity.

2.8 Strain signal extraction

To get the final two strain signals at 90°, the following steps were performed. Measured strain signals were denoted ε_θ, with $\theta = 62°, 152°, 242°, 332°$ in which the angles refer to the door axis.

1) The thermal output of each raw signal was subtracted:

$$\varepsilon_\theta = \varepsilon_{\theta,raw} - \varepsilon_{\theta,\frac{T}{O}}(T(\theta)) \qquad for\ \theta = 62, 152, 242, 332° \qquad (2\text{-}15)$$

2) Opposite signals were averaged for both sensor axis, and a smoothing of the signal was performed using a centered moving average by sliding a window of length N along the signal. A 10-minute window was found appropriate in this case (N = 12'000 for a signal at 20 Hz).

$$\varepsilon_{\theta,\theta+180} = \frac{\varepsilon_\theta + \varepsilon_{\theta+180}}{2} \qquad for\ \theta = 62, 152° \qquad (2\text{-}16)$$

$$\bar{\varepsilon}_{\theta,\theta+180,i} = \frac{1}{N+1} \sum_{k=i-N/2}^{k=i+N/2} \varepsilon_{\theta,\theta+180,k} \qquad for\ N-n > i > n \qquad (2\text{-}17)$$

3) The corrected signal was obtained by simply using the equation:

$$\varepsilon_\theta = \varepsilon_\theta - \bar{\varepsilon}_{\theta,\theta+180} \qquad for\ \theta = 62, 152° \qquad (2\text{-}18)$$

4) Finally, the strain signal needed to be zeroed. This procedure is called the calibration check in the International Electrotechnical Commission standards for the measurement of mechanical loads on wind turbines (IEC 61400-13 2001). This requires yawing the nacelle through 360° below cut-in wind speed. The eccentricity of the nacelle and rotor mass generate a sinusoidal signal, and the mean of this signal represent the zero point.

This signal extraction procedure can be automatized in the data acquisition software Catman provided by HBM. However, it was preferred to record each strain gauge individually, perform the temperature and drift compensation in a second step to ensure no error that could make the data invalid.

2.8.1 Daily temperature effect

February 25th of 2017 is selected and showed in Figure 2-14 to illustrate the daily temperature effects on the measurements. This day illustrates many wind turbine conditions since periods of power production alternated with turbine idling (when the pitch angle is equal to 24° and

wind speed below the cut-in speed). At around 12:00, the wind turbine performed an automatic 360° rotation. This operation was necessary as the main power cable between the nacelle and the tower needs to be untwisted. Usually, the turbine control system operates this operation below the cut-in wind speed, but a rotation may be required during high wind speed, causing more damage to the turbine as it has to break and pitch the blade up to 88°. Figure 2-14(a) shows the four strain signals measured at the bottom section and zeroed during the nacelle rotation. The opposite signals seemed similar during production, however, the strain signals during idling were completely biased. The average of the two opposite signals are plotted in Figure 2-15(a). The thermal output, as the temperature change from -5.5°C to +5.8°C, is relatively small (about 20 με) and follows the average temperature. Once removed, the effect of the non-linear temperature takes place with a sudden change at about 8 am when the sun rises and starts heating the East side of the tower (at 332°). The path of the sun can be followed on Figure 2-14(b); sensors at 242° are oriented south as they are heated during the whole day and reach the highest temperature whereas sensor at 152° slightly is heated just before sunsets.
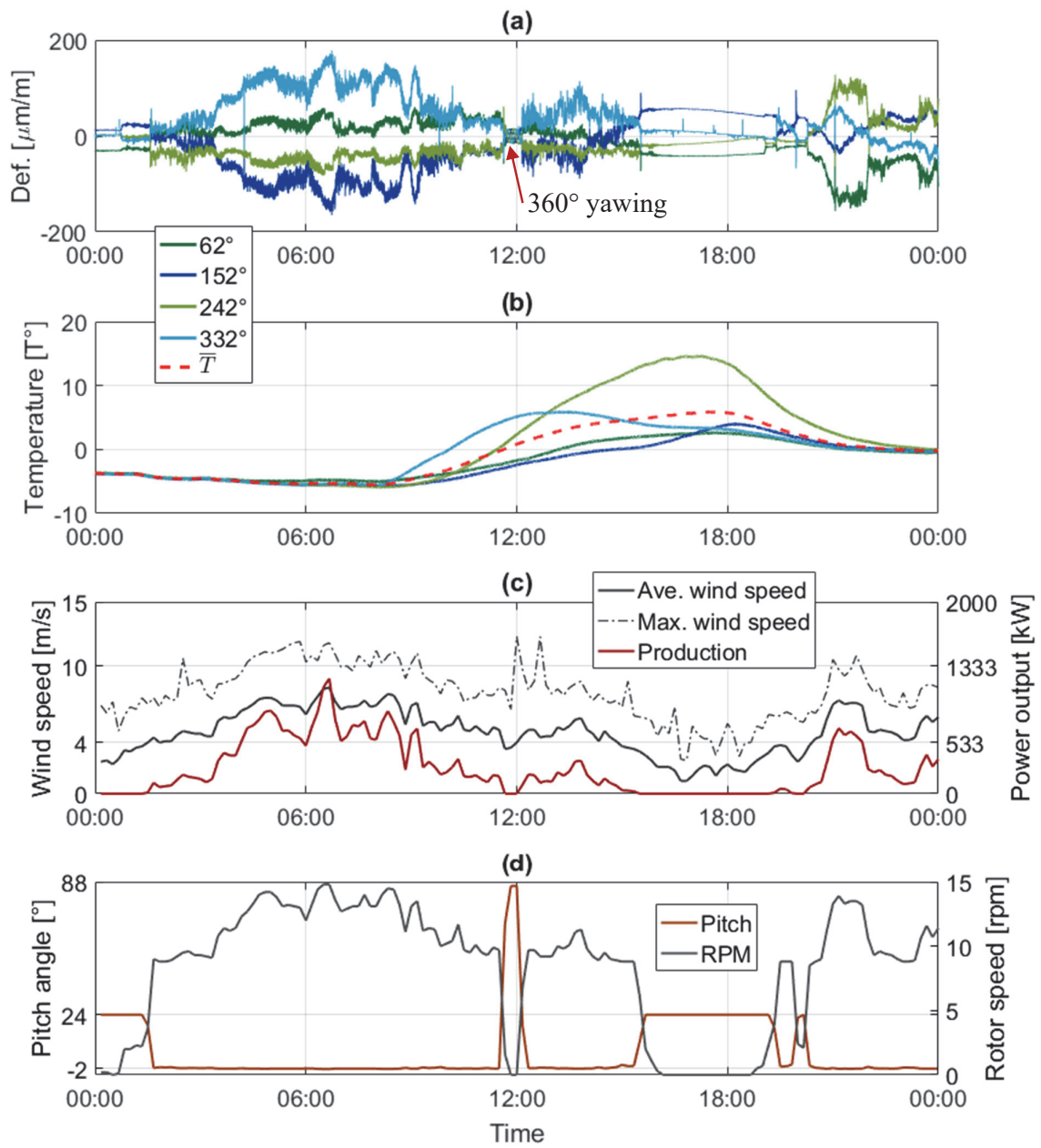
Figure 2-14.Single day (a) strain (zeroed raw signal) and (b) temperature measurements at the bottom section recorded the 25/02/2017 with corresponding SCADA parameters: (c) 10-minute average, maximum wind speed, and production (d) blades pitch angle and rotor speed.
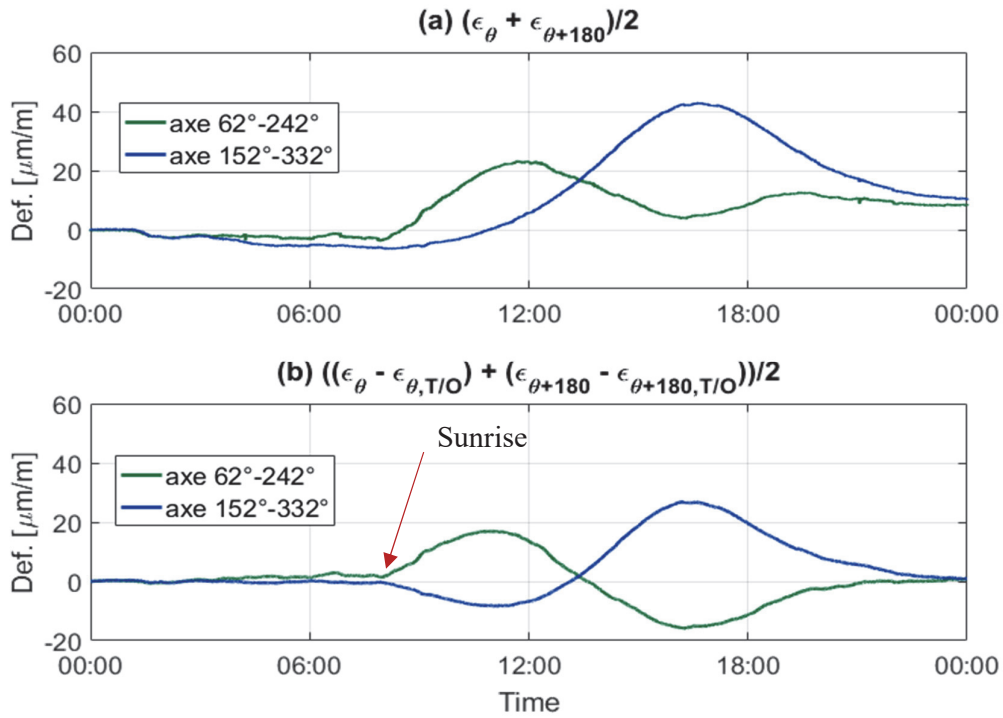
Figure 2-15. Average of two opposite strain gauges at the bottom section (a) raw signal and (b) after compensating the T/O for the 25/02/2017.

Figure 2-15(b) is the indirect measurement of the eigenstresses that develop in the steel tube because of local heating of the structure. The maximum error on the signal is about 25 με for this day. An example of the induced relative error is presented in Figure 2-16 when calculating the maximum bending stress ($\sigma = E\sqrt{\epsilon_{62}^2 + \epsilon_{152}^2}$) in the section. Relative error varies between 5 and 20 % during periods of power production (high stresses) but becomes huge during start-up and shut-down periods (low stresses). The difference is even more pronounced during idling or parking of the turbine (shift of the peak in Figure 2-16(b)).
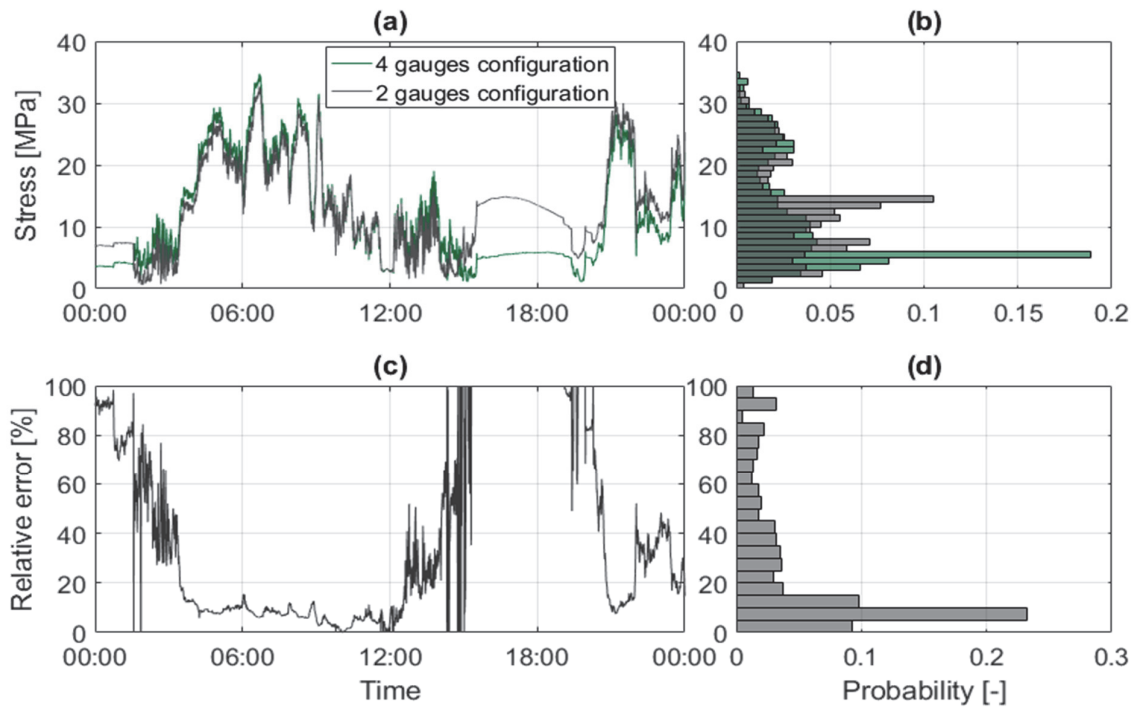
Figure 2-16. Comparison between the two and the four gauges configuration for the 25/02/2017 (1 minute averaged signal). (a) Absolute stress and (b) corresponding histogram (c) relative percentage error and (d) corresponding histogram.

2.8.2 Long-term effects

The long-term effects on strain gauges result in a significant drift of the signal. Over the measurement period, a total of 42 full rotations of the nacelle were observed and used for the calibration process. Figure 2-17 shows all the observed rotations during the measurement period, regardless of the date and Figure 2-18 presents the same data but over the time. There are relatively few rotations during winter, whereas there is a lot in summer. The reason behind this behavior is the slow and very variable wind in summer whereas the wind from West is blowing for longer periods in winter (see in particular the wind direction in Figure 2-4(d) during the 2015/2016 winter).

During the first year, the remaining zero-point error reached about 90 µε and is substantially the same for each sensor at the bottom section, while the final drift measured is of 200 µε for the gauges at the top section. Drift observed during the 2nd and the 3rd years is less important; about 25 µε over almost a year. Figure 2-18 shows the initial strain signal and the final strain signal after the correction process over the measurement period. The final value for zeroing the signal is taken as the mean value of the rotation signals.

Considering the rotation only (*i.e.,* when the two gauge configuration is used), calibration seems straightforward as drift follows a relative linear evolution over time. However, Figure 2-19 shows a rapid drift at an early age and drift that does not vary linearly during the 2nd part of the monitoring.
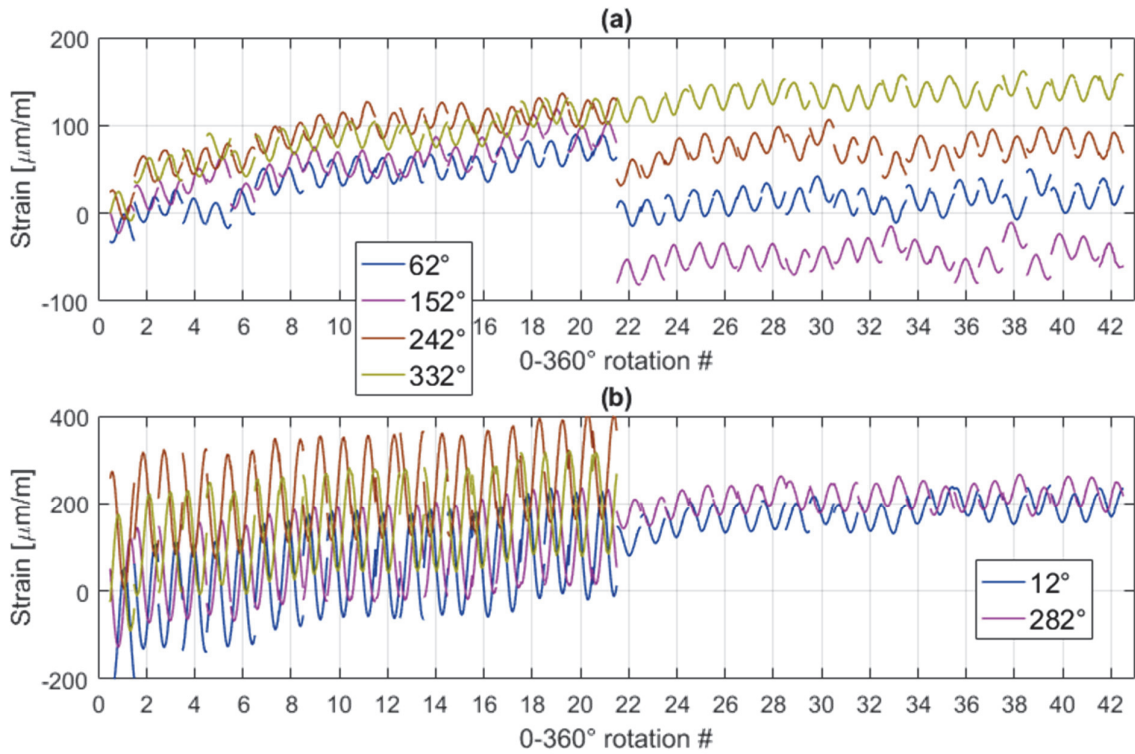
Figure 2-17. Observed strains from 0-360° rotations of the nacelle (a) at the bottom section, (b) at the top (first 21 rotations) and the middle section (last 21 rotations). The sudden change in the 22nd rotation in (a) is a result of the signal zeroing.
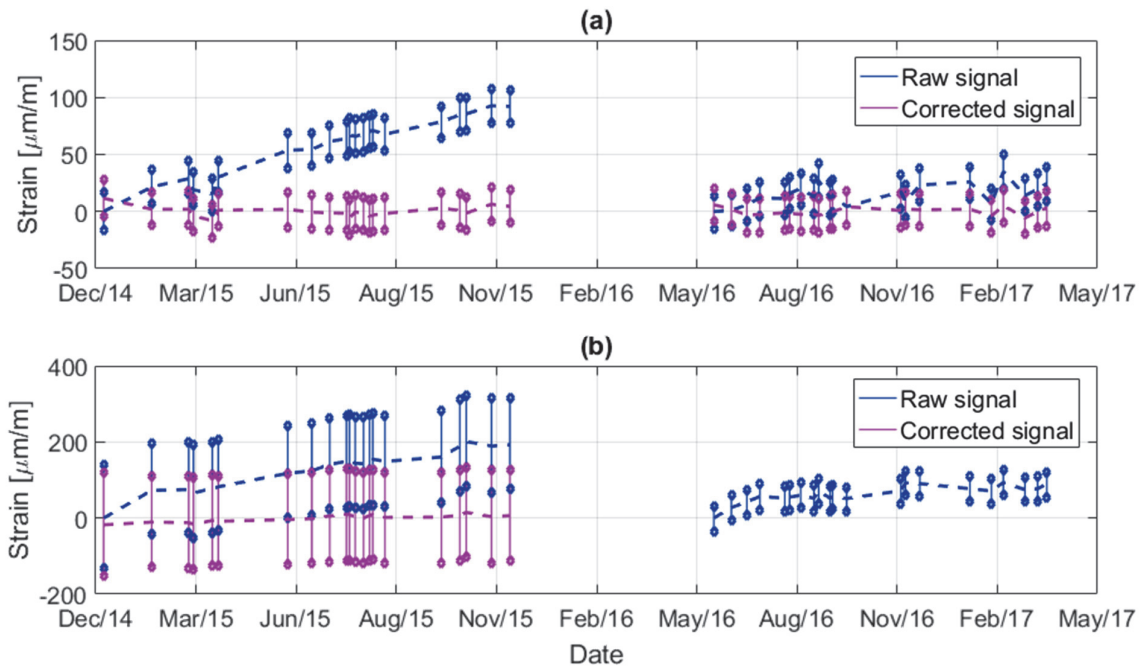
Figure 2-18. Observed strains from 0-360° rotations of the nacelle (a) at the bottom section, and (b) at the top section for the strain gauges at 62° over the measurement period for the measured, and zeroed signal. The measured signal in (b) for 2016-2017 is from the middle section, the gauge at 12°.

37
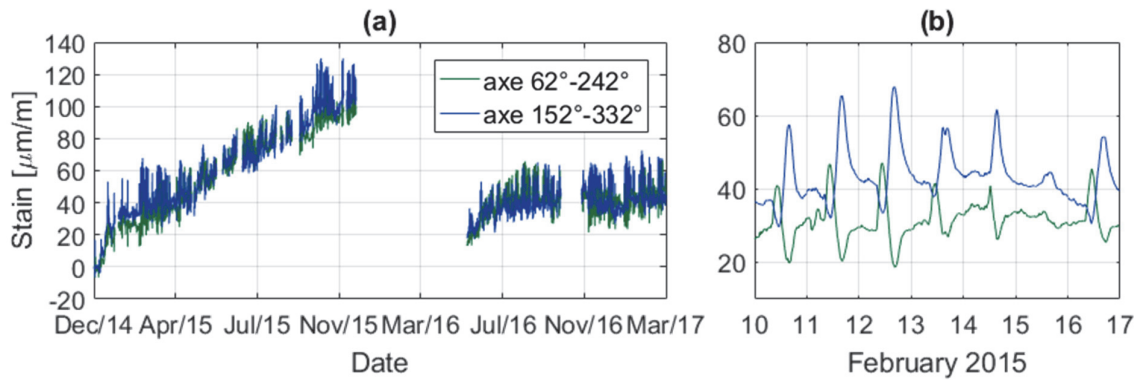
Figure 2-19. Short and long-term variations of remaining zero-point error at the bottom section (a) for the measurement period and (b) 7 days in February 2015.

2.9 Recorded signals and operating condition

The strain recorded at the bottom location is presented in the following figures. By combining the measurement from the SCADA system and the associated clustering of the 10-minute series into different operation condition, the characteristic signal of each specific load case can be showed. The following figures represent different time series according to the specific recorded type of event. In every case, the orange signal corresponds to the fore-aft and the green to the side-to-side strain signals. The data from the nacelle orientation is used to calculate the two strain signals.

2.9.1 Power production

The following graphs in Figure 2-20 show the strain variations for two different turbulence intensity of 10 % and 20 %, and for 3 different wind speeds below the rated speed of 10 m/s. The pitch control system is usually not enabled except when the wind goes beyond the rated wind speed which occurs during turbulent time series. Figure 2-21 shows time series with wind speed in average above the rated speed. During this period, the pitch control system is active. The average wind speed influences the mean strain, whereas turbulence intensity effects the standard deviations of strain amplitudes.
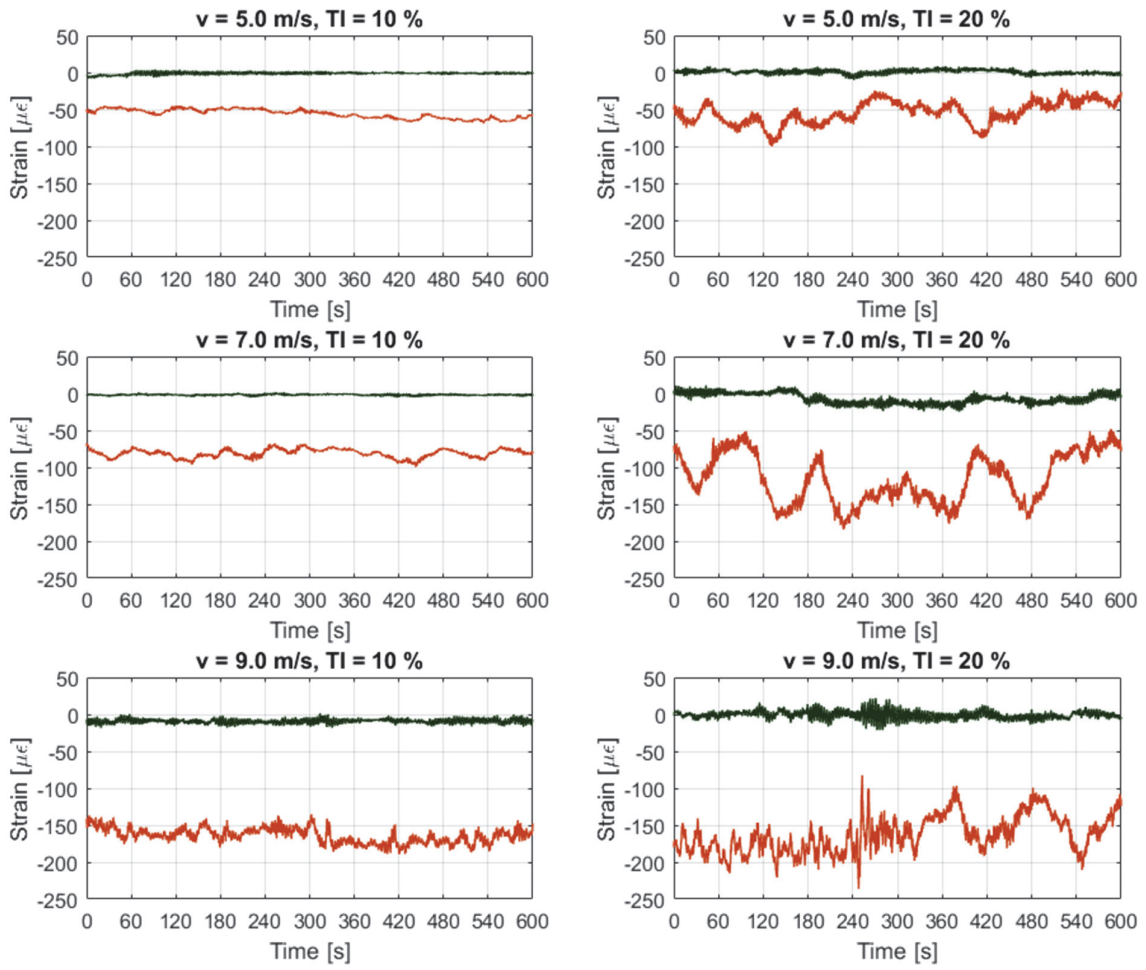
Figure 2-20. Strain variations for average wind speed between the cut-in and the rated speeds for two different turbulence intensities.
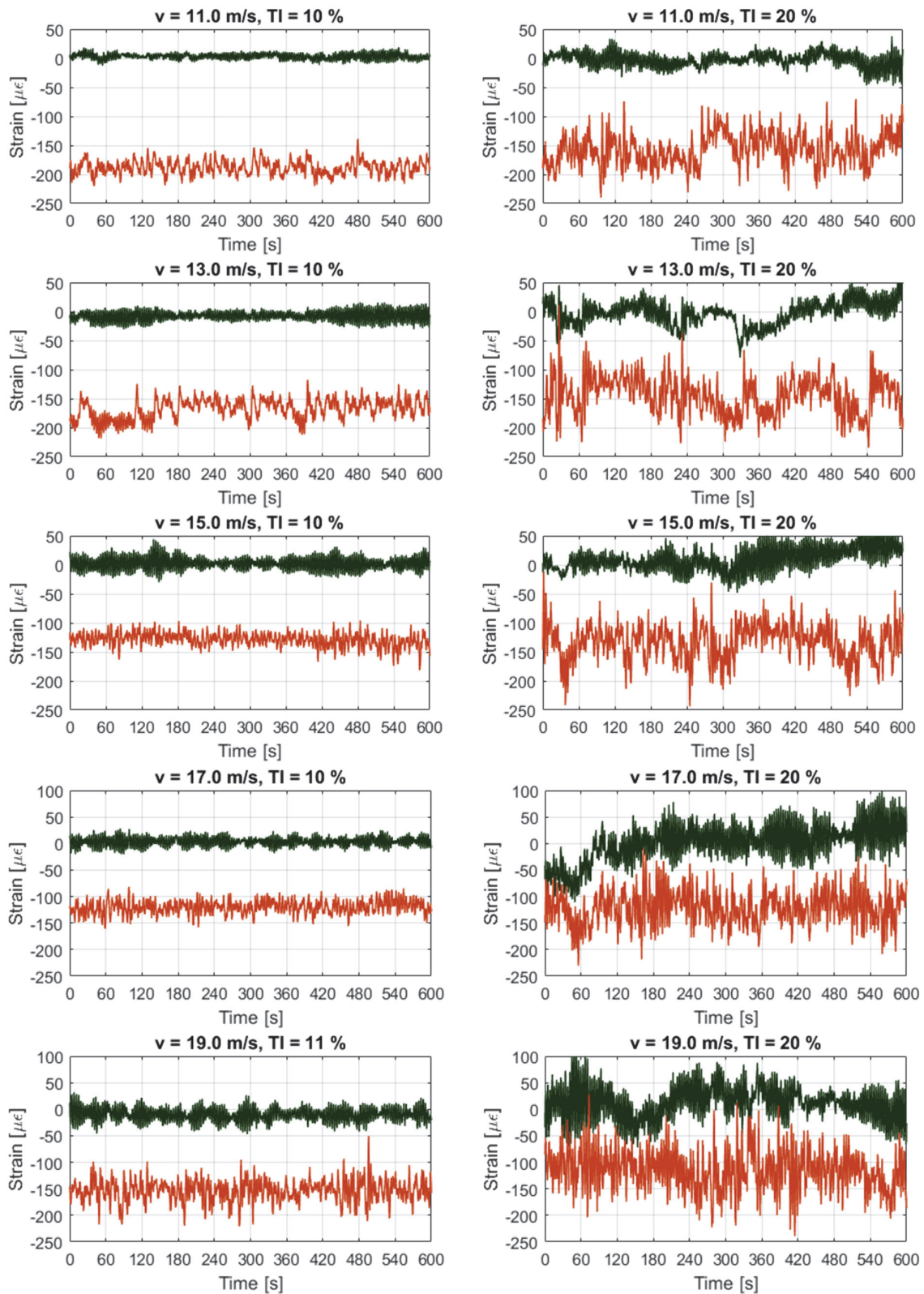
Figure 2-21. Strain variations for average wind speed between the rated and the cut-out speeds for two different turbulence intensities.

2.9.2 Transient events

Figure 2-22 shows two hours of measurement at low wind speed. During this period, the turbine started and stopped two times. The average wind speed is oscillating around 4 m/s.
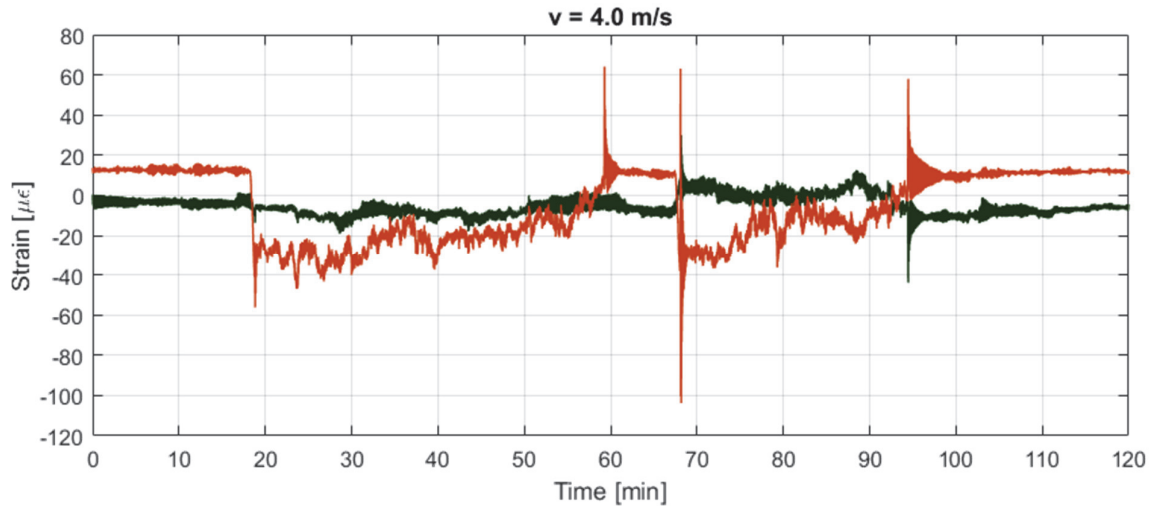
Figure 2-22. Variation of strains during the start-up and shut-down of the turbine around the cut-in wind speed.

Figure 2-23 shows a typical behavior of the turbine when the wind speed reaches the rated wind speed of 10 m/s. Figure 2-23(a) is a one-hour window and Figure 2-23(b) focuses on one single event over a 2-minute window. Without high-frequency SCADA, it is not possible to adequately describe what happened during those events. One reason could be the switching between two operating conditions by the controller. When the wind reaches the rated speed, the lift force responsible for the rotor rotation leads to a rotor speed higher than the rated 15 rpm. To control the rotor speed, the controller quickly increases the blades pitch to a high value to slow down the rotor by reducing the lift. As a result, the thrust force rapidly decreases.
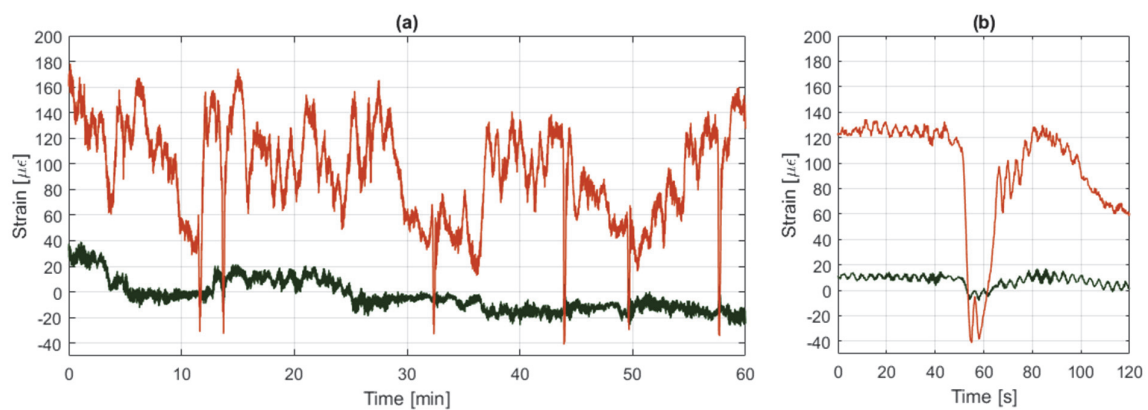
Figure 2-23. Signal variations (a) during a change in operation condition (b) focused on a single event of blade pitch change by controller.

During the first few days of the measurement period in December 2014, an extended episode of icing prevented the turbine from producing power. The characteristic signal of this

phenomenon is illustrated in Figure 2-24(a) for a low wind speed of 5.0 m/s and in Figure 2-24(b) for a higher wind speed of 9.0 m/s. Due to excessive additional mass on the blades, the wind turbine control system starts the rotor and stops it a few minutes later; with two different frequencies for different wind speeds. For low wind speed, the turbine starts/stops every 5 minutes and it is about every two minutes when the wind speed is higher. The control system of the turbine is optimized to maximize the power output, thus resulting in this erratic behavior.
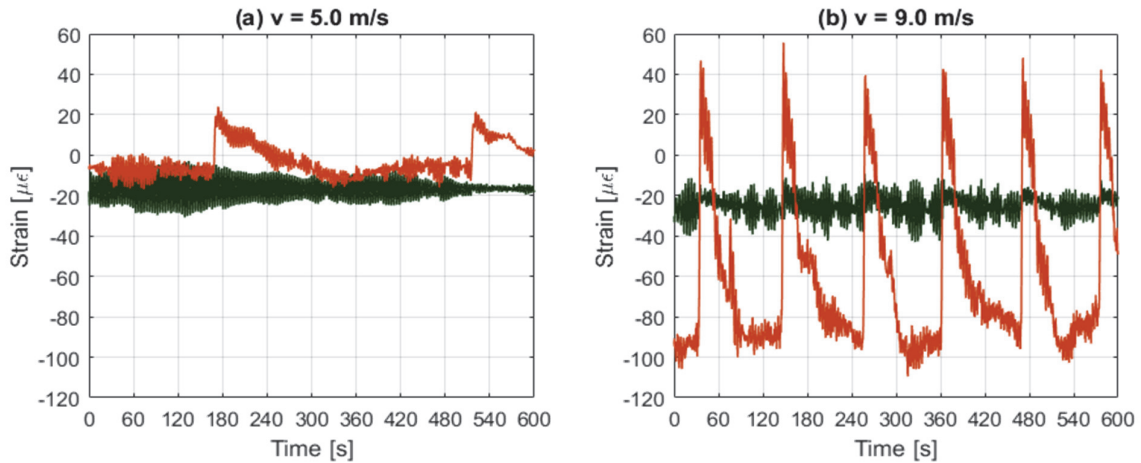
Figure 2-24. Variation of strain during icing of the blades for (a) a wind speed of 5.0 m/s and (b) a wind speed of 9.0 m/s.

Figure 2-25 shows an example of emergency shutdown procedure. It is activated when the wind speed goes beyond 20 m/s. One can see the rapid decrease at about 300 seconds in the fore-aft strain signal until it oscillates around 0 for 4 minutes. Once the wind speed decreases again, blades are pitched back, gradually increasing the wind load on the rotor.
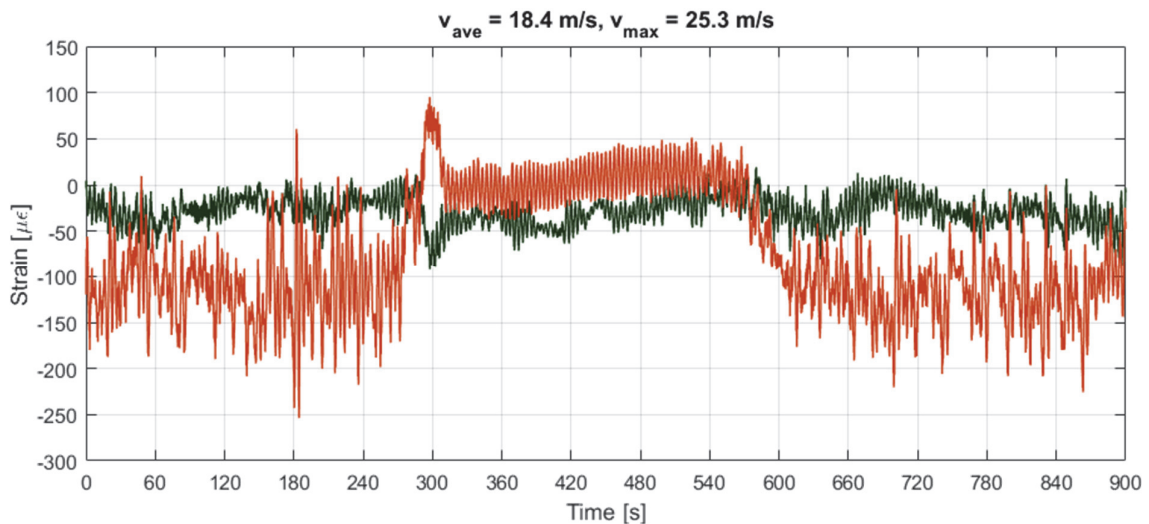
Figure 2-25. Variation of strain during an emergency shutdown procedure.

Figure 2-26(a-b) shows 10 minutes of strain signal during parking conditions (fixed rotor yaw angle and blades pitched at their maximum). When wind speed is below 4.0 m/s, only the strain

42

resulting from the nacelle masse offset is visible. The signal is well zeroed as the side-to-side strain is 0. Figure 2-26(b) was measured during a severe storm. Having an average wind speed above 20 m/s and maximum wind speed close to 120 km/h, the control system parked the turbine. The side-to-side signal (in dark-green) is not oscillating around 0 as the fixed nacelle orientation during this storm was not aligned with the wind speed orientation.
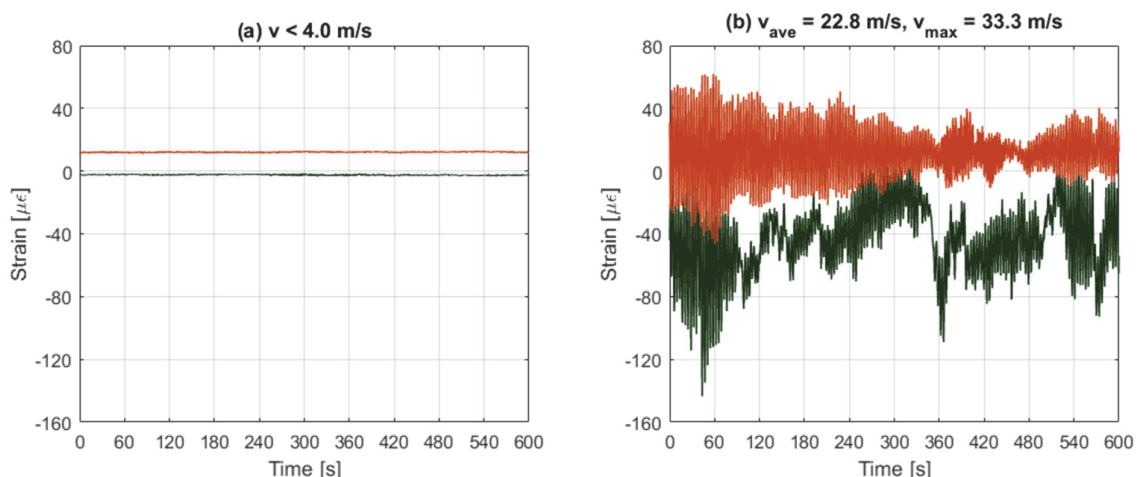
Figure 2-26. Variation of strain during parking condition for (a) a period with wind below the cut-in speed and (b) during a storm.

The Figure 2-27 below represents the idling situation. The blade pitch is set to 24°, and the rotor is free to rotate (usually no more than 3 rpm). The signal variations are a result of small corrections in the nacelle yaw angle. The control system simply orients the nacelle against the wind.
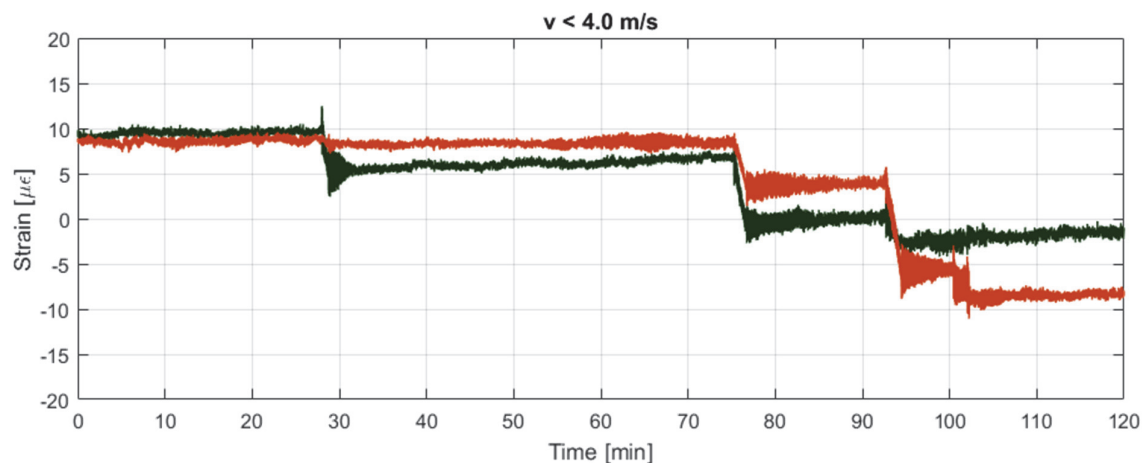
Figure 2-27. Two hours of measurements during idling condition. Variations of the signals are a result of the nacelle orientation.

Finally, an example of two rotations is presented in Figure 2-28.
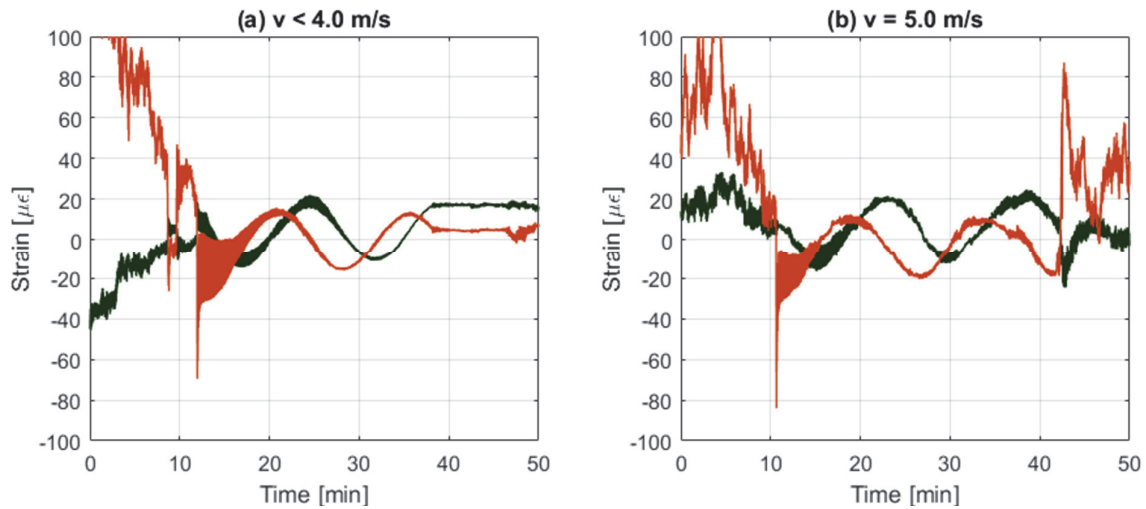
Figure 2-28. Example of nacelle rotation (a) below cut-in wind speed and (b) during low wind speed.

2.10 Acceleration measurements

Accelerometers are often used as a sensing technique for wind turbines as they can provide a wild range of information concerning the dynamic behavior and its evolution over long periods. Data from accelerometers can be used for actively controlling the wind turbine during operation, with the aim of reducing the thrust loads or increasing the power production. Data from accelerometers are also employed to detect changes in the turbine dynamic that could indicate cracks in the concrete foundation and in the bolted connections of the towers. Many advanced techniques using long-term measurement from accelerometers are now used to detect damage. However, since the aim of this thesis was to make safety predictions from direct strain measurements, acceleration data was not extensively studied.

In addition to strain gauges, 3 accelerometers were installed at the top of the wind turbine during the first year of the monitoring period. They were used to validate the finite element model and to choose the sampling rate for strain gauge monitoring. The Power Spectral Density (PSD) of the measured accelerations at the top of the tower yields a first vibration mode of 0.27 Hz. A typical PSD of the accelerometer signals is presented in Figure 2-29 for 20-minute windows over 12 hours of continuous measurement that includes a period of parked time and power production.
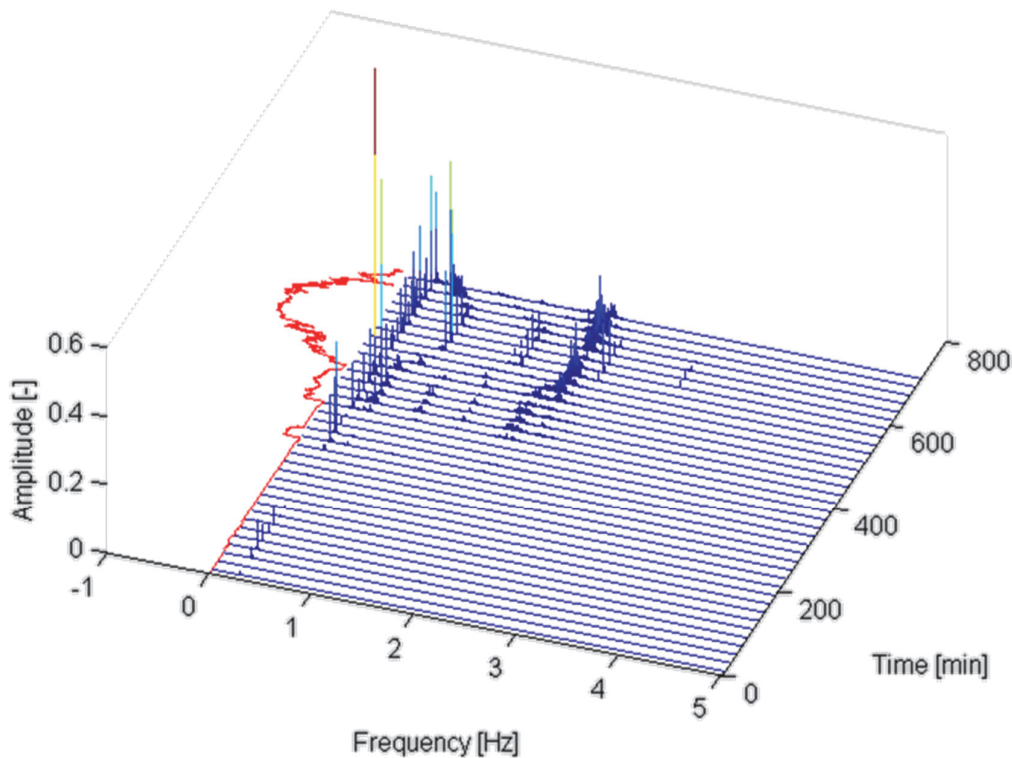
Figure 2-29. 20-minute window PSD along the turbine fore-aft axis for a 12 hours measurement period. The red line shows the normalized average hub force evolution.

The PSD over time shows a stable 1st vibration mode, when higher modes depend mainly on the rotor speed, and thus vary with the wind speed.

2.11 Discussion

2.11.1 Turbine model

Despite being a widespread turbine type, the Vestas V90 remains a relatively simple steel design and its dynamic behavior is relatively well known. Other types of onshore WT may have a very different behavior. This can be the case with prestressed concrete towers and hybrid towers (generally composed of concrete prestressed segments over the first 2/3 of the tower height and a steel top segment). For such designs, the critical detail is certainly the connection between the top concrete ring and the steel connectors, and measuring the effective stains could be less straightforward.

In case of offshore wind turbines, the sensor installation becomes a major limitation, as the critical sections around the mud line are not accessible. The more complex interaction of the tower with the foundation and the water leads to a more complex dynamic behavior.

2.11.2 Sensor technology

Metallic strain gauges used for monitoring suffer from a bad reputation since they are considered as an "old technology" that is not reliable on the long-term (excessive drift) and too exposed to temperature effects that are difficult to compensate. As a result, they are not used

45

for "active monitoring", or they are used only for very short periods (Cooperman and Martinez 2015). Actual monitoring methods oriented towards fatigue and load evaluation aim to develop models based on acceleration measurement. These models are expected to replace the use of conventional strain gauges, although they do not have the same accuracy yet. Additionally, they have no alternatives but to use strain gauges for calibration.

Some of the installed strain gauges experienced defects after some months/year of utilization. At the bottom section, one strain gauge started to indicate overflow values during few milliseconds after a year, and a second strain gauge installed along the other axis showed the same pattern. These artifacts happened rarely and did not influence the final measured strain since only the 10-minute moving average of this two gauges were used. In all cases, carefully installed and protected strain gauges can withstand a full year of measurements without a problem. Nevertheless, a defect resulting from a poor bonding of the glue, welding of the gauge or magnetic interferences would be directly visible on the signal.

Fiber optical sensors for strain measurement is a more recent alternative to conventional strain gauges. Despite its higher cost, this technology is also easily deployable inside a wind turbine tower and is even more robust in aggressive environments (when metallic strain gauges are more subject to corrosion). Despite this advantage, the aim of this thesis was to collect data with a reliable and robust system, and experience previously acquired within our laboratory with metallic strain gauges led us to this choice.

2.11.3 Strain gauge configuration

The monitoring system exclusively uses ¼ bridge configuration for the strain measurement, for the simplicity of its installation and the direct access to the signal of each individual gauge. However, one could have taken advantage of Wheatstone bridge circuit for thermal and drift compensations. During the first phase of the monitoring, two configurations were tested and compared with the ¼ bridge configuration.

A first approach is to install a "dummy" gauge (Figure 2-30(a)) glued to an unstrained piece of steel that has similar properties as the tower steel (a similar thermal expansion coefficient). The non-stress inducing strain resulting from thermal expansion/contraction appears in both the "active" and the "dummy" gauge. Thus, this strain is eliminated by using the proper ½ bridge gauge arrangement. Theoretically and under perfect conditions, the thermal output of both gauges is canceled out since the identical change of resistance do not unbalance the circuit, leaving only the stress-induced strain being recorded by the DAU (Vishay 2007). However, substantial thermal influences can appear from the single wire connecting the two gauges (indicated in Figure 2-30(a)), causing more errors than the expected benefits of this configuration. Microstructural changes in the gauge and the adhesive may also not evolve at the same speed, as the compensation gauge is not subject to any stress.

A second configuration requires the use of a gauge oriented at 90° (glued radially in this case) and a bridge factor adjusted to 1.3 (Figure 2-30(c)). In this case, the second gauge records the radial deformations, perpendicular to the longitudinal bending deformations. Thermal deformations on the other hand – and if the section is free – will also be canceled as they produce

the same electrical resistance. Again, in this scenario, the system would still be affected by transversal strains unrelated to longitudinal bending (e.g., shear strain).
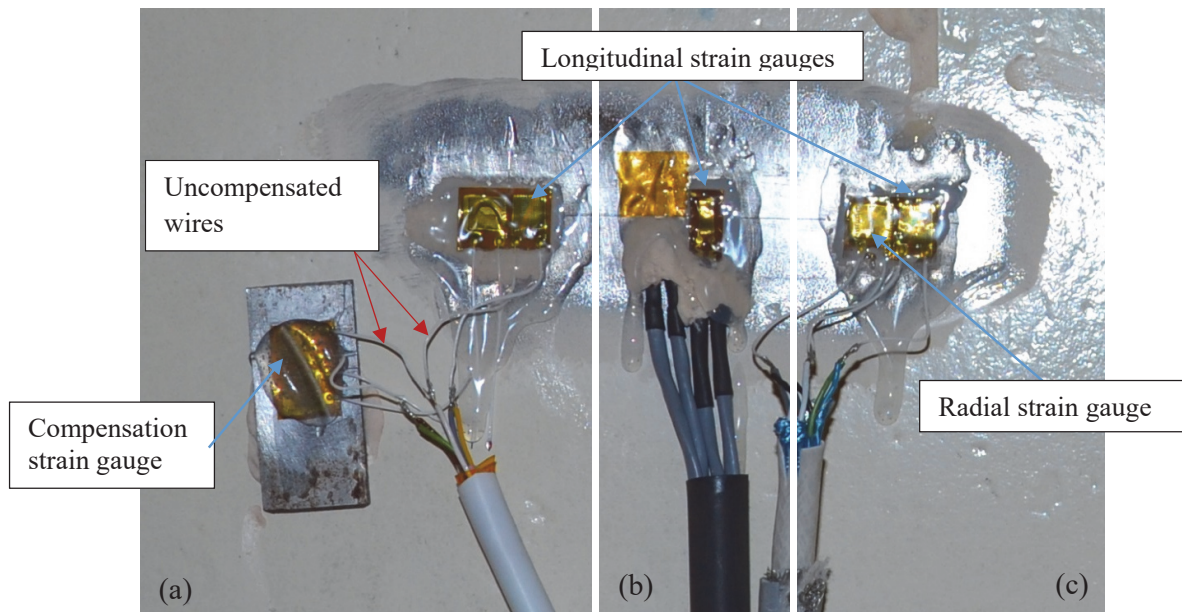
Figure 2-30. Comparison between ¼ bridge (b) and two ½ bridge configurations (a) and (c).

2.12 Conclusions

The following conclusions can be drawn from this work:

1. The SCADA data, despite the low frequencies available in this study, provides useful information regarding the environmental and operational parameters of the monitored wind turbine and is a good alternative to the expansive met mast.

2. The algorithm developed for the classification of the turbine operating conditions will be used later to estimate the remaining service duration.

3. A novel monitoring configuration for measurements of tower mechanical loads was proposed and validated over a period of 3 years. This monitoring scheme is robust, economic and can be rapidly deployed in several wind turbines. Further improvement using automatic data treatment can provide owners with a direct estimation of the wind loads and wind fatigue load history.

4. Direct monitoring allows the assessment of the complex wind turbine behavior under a large variety of wind and operating conditions. It can record short events as well as seasonal variations.

5. The specific problem of temperature and long-term effects (drift) that usually prevent the use of conventional strain gauges for this application was quantified. Accounting for it leads to a drastic decrease in the measurement uncertainties and the post-processing time required for the calibration of the sensors.

6. The in-situ measurement of the tower geometry performed in this study provided essential information – since the design assumptions are often not available due to confidentiality – for the realistic examination of the wind loads and the calibration of FE model.

3 The use of long-term measurement for the evaluation of the wind loading effects and for the fatigue safety verification on wind turbines steel towers

3.1 Introduction

During their service duration of 20 years, wind turbines experience a large variety of loads combined with harsh environments, particularly onshore turbines installed along the ocean coast and offshore turbines. Therefore, wind turbines are designed according to environmental factors of their future locations including specific wind class and turbulence intensity category. In the previous chapter, it was shown that the monitored turbine was situated in a location with average wind speed below the design values. As a result, the effective fatigue loading endured by the wind turbine is likely to be below the design assumptions.

Despite being the major limitations for the design of wind turbines, fatigue is rarely the cause of a complete failure of the tower. Such dramatic events remain exceptional and are the result of negligence during the assembly and bolting of the tower segments. In almost every reported case of tower failure (not resulting from a blade failure), the failure arises from the fatigue of the high strength bolts connecting the tubular sections. This failure mode usually happens rapidly during the early age of the structure and is caused by lack of prestressing in the bolts (Liu and Ishihara 2001). A study of about 15 years on wind farms in Germany shows that 4 % of the encountered malfunctions arises from the structural parts (Hahn, Durstewitz, and Rohrig 2006). Additional fatigue damage can be caused by rotating mass imbalance due to blade damage. Data collected around the world on failure and accidents related to the wind turbine industry indicates an average of 11.4 structural failure per year during the last 10 years. It includes local defects on the nacelle, the tower or the foundation , as well as the complete failure of the turbine (Caithness Windfarm Information Forum 2017). The last reported structural collapse of a tower was a GE 1.7MW on 21/06/2017 in the Shannon Wind Farm, Windthorst, Texas, USA. The turbine was two years old and seemed to have failed at tower mid-height.

The 604 days of high-frequency measurement will be presented in this chapter. The goal is to provide the result of the long-term measurement on the effective wind loading and wind fatigue loading acting on the structure through the realistic examination of the bending strains of the tower. Such approach can provide useful information on the seasonal effects and the impact of storms on the tower structural integrity regarding the acting forces and fatigue loads directly on critical construction details without the need of numerical simulations on generic models. This chapter can also provide valuable information to turbine operator to improve the management of the wind farm.

3.2   Wind Load calculation from strain measurements

The wind turbine is primary subjected to aerodynamic loads including the lift force that drives the rotor rotation and the thrust force responsible for the tower bending moment. Additional loads can arise when the wind flow is not uniformly distributed on the rotor, *e.g.*, wind shear causing an additional moment at the tower top, yaw misalignment. The turbine is also subject to inertial (centrifugal and gyroscopic forces from moving elements) and gravitational forces (rotor and nacelle mass). More detailed information on aerodynamic loads on wind turbines can be found in Hansen's paper (Hansen 2015).

| (a) | (b) |
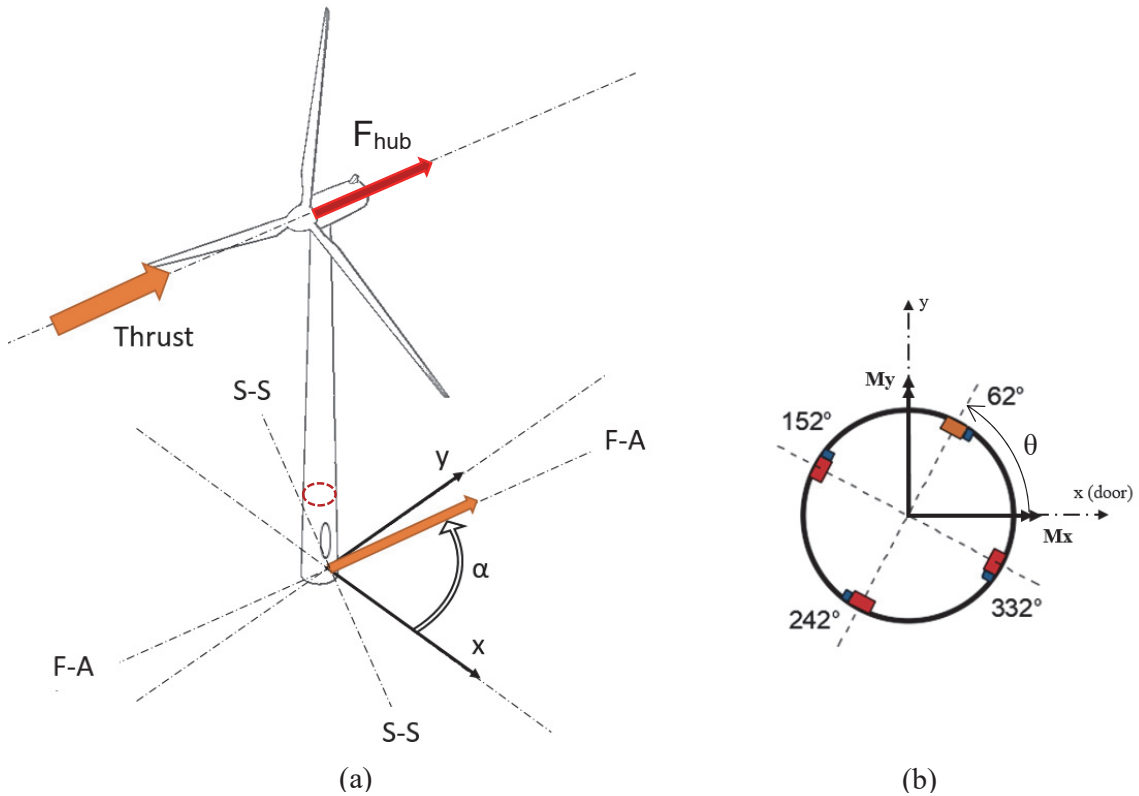
Figure 3-1. (a) Tower coordinate system in which the x-axis is aligned with the door and (b) coordinate system for the tower cross section with sensors position.

Figure 3-1 shows the coordinate system used in this study. Longitudinal strains obtained from the procedure described in Chapter 2 from the position at 62° and 152° are used to calculate the bending moments and the quasi-static force acting at hub height. The nacelle angle defines the fore-aft and the perpendicular side-to-side axis.

According to the theory of linear elasticity and due to the small thickness of the tower walls compared to others dimensions, the perpendicular stresses are considered negligible ($\sigma_{zz} = 0$). Additionally, the plane stress is simplified and the stress-strain relationship for an isotropic material becomes:

$$\begin{bmatrix} \epsilon_{xx} \\ \epsilon_{yy} \\ \epsilon_{xy} \end{bmatrix} = \frac{1}{E} \begin{bmatrix} 1 & -\nu & 0 \\ -\nu & 1 & 0 \\ 0 & 0 & 1+\nu \end{bmatrix} \begin{bmatrix} \sigma_{xx} \\ \sigma_{yy} \\ \sigma_{xy} \end{bmatrix} \tag{3-1}$$

The stiffness matrix for plane stress is obtained by inverting equation (3-1):

$$\begin{bmatrix} \sigma_{xx} \\ \sigma_{yy} \\ \sigma_{xy} \end{bmatrix} = \frac{E}{1 - v^2} \begin{bmatrix} 1 & v & 0 \\ v & 1 & 0 \\ 0 & 0 & 1-v \end{bmatrix} \begin{bmatrix} \epsilon_{xx} \\ \epsilon_{yy} \\ \epsilon_{xy} \end{bmatrix} \tag{3-2}$$

Based on numerical simulations performed on the FEM of the tower, it is shown that the transverse deformations are negligible compared to the high longitudinal deformations caused by the thrust force. Thus, the following equation is used to calculate the axial stress in the tower plates:

$$\sigma_{xx} = E \cdot \epsilon_{xx} \tag{3-3}$$

Considering two orthogonal strain signals ϵ_θ and $\epsilon_{\theta+90°}$ obtained from strain gauges installed at θ and $\theta+90°$ from the x-axis aligned with the door (see Figure 3-1), the stress at any given α and $\alpha + 90°$ angle from the x-axis is calculated with:

$$\sigma(\alpha) = E \cdot (\epsilon_\theta \cdot \cos(\alpha - \theta) + \epsilon_{\theta+90°} \cdot \sin(\alpha - \theta)) \tag{3-4}$$

$$\sigma\left(\alpha + \frac{\pi}{2}\right) = E \cdot (-\epsilon_\theta \cdot \sin(\alpha - \theta) + \epsilon_{\theta+90°} \cdot \sin(\alpha - \theta)) \tag{3-5}$$

Consecutively, the stress calculation from the combined action of two bending moments and an axial compression is given by:

$$\sigma(x,y) = \frac{N}{A} - \frac{M_y}{I_y} \cdot x + \frac{M_x}{I_x} \cdot y \tag{3-6}$$

The measurement of the longitudinal stress at three different locations around the section, usually with three gauges at 120° is required to calculate the normal force N and the two bending moments, M_x and M_y. However, the normal force (resulting from the tower and nacelle weight) cannot be measured as the sensors only provide variation from the initial stress state of the structure. Only vertical vibrations and temporarily added mass could be detected (*i.e.,* ice on blades). The normal force variations are actually very small and can be neglected and the normal stress under self-weight is about 5.0 MPa at the bottom measurement section.

For wind turbines towers, the bending moment along the rotor axis (fore-aft) M_{F-A} and the perpendicular side-to-side moment M_{S-S} are of more interest than the moments along the fixed axis M_x and M_y of the tower. Finally, for a cylindrical section of internal radius R_i and inertia I_c, the two bending moments are:

$$M_{F-A} = -\frac{E \cdot I_C}{R_i} \cdot (\epsilon_\theta \cdot \cos(\alpha - \theta) + \epsilon_{\theta+90°} \cdot \sin(\alpha - \theta)) \tag{3-7}$$

$$M_{S-S} = \frac{E \cdot I_C}{R_i} \cdot (-\epsilon_\theta \cdot \sin(\alpha - \theta) + \epsilon_{\theta+90°} \cdot \cos(\alpha - \theta)) \tag{3-8}$$

where α is the nacelle orientation obtained from the SCADA system and θ the angle of the first sensor.

By convention, the equivalent quasi-static hub force can be calculated with:

$$\begin{bmatrix} F_{F-A} \\ F_{S-S} \end{bmatrix} = \frac{E \cdot I_c}{R_i \cdot h} \cdot \begin{bmatrix} \cos(\alpha - \theta) & -\sin(\alpha - \theta) \\ \sin(\alpha - \theta) & \cos(\alpha - \theta) \end{bmatrix} \begin{bmatrix} \epsilon_\theta \\ \epsilon_{\theta+90°} \end{bmatrix} \tag{3-9}$$

and the absolute hub force is simply given by:

$$F_{hub} = \sqrt{F_{F-A}^2 + F_{S-S}^2} \tag{3-10}$$

The above mentioned calculation of load was combined with the data from the SCADA system to analyze monitoring data. The 10-minute nacelle direction is used for the α angle in previous equations.

3.2.1 Analysis of monitoring results

Hub force measurement

The full temperature compensation on the measured strain signals allows for the accurate estimation of the tower bending moments over the full monitoring period without the need for doing regular calibration tests. Statistical parameters of the wind loading were calculated for each 10-minute series and synchronized with the data from the SCADA system to benefit from the wind speed measurements at hub height and other turbine related parameters.
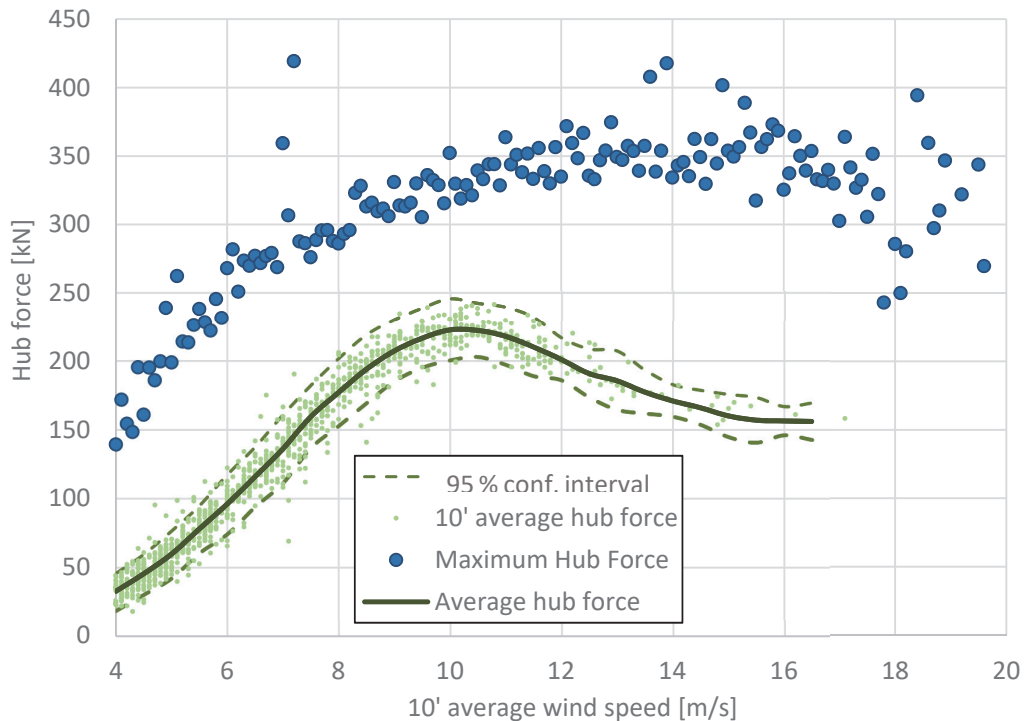
Figure 3-2. Average 10-minute hub force over the first 330 days of the monitoring period.

52

The Figure 3-2 shows the result of load measurement for the first 330 days of monitoring from December 2014 to January 2016. The average hub force and the 95 % confidence interval are presented as a function of the wind speed. The maximum recorded hub forces for each wind speed bin of 0.1 m/s are indicated, as well. Only the average loads recorded during the normal operation of the turbine are presented. The average and 10-minute maximum hub force over the monitoring duration are presented in Figure 3-3 below. The peak at 20 kN on the force histogram corresponds to the parked situation and results from the constant bending moment due to the nacelle mass eccentricity. The stability of the data regarding temperature and drift is confirmed in Figure 3-3(a, c), as no long-term variations are visible. The extreme loading on the structure will be studied in more detail in Chapter 4.
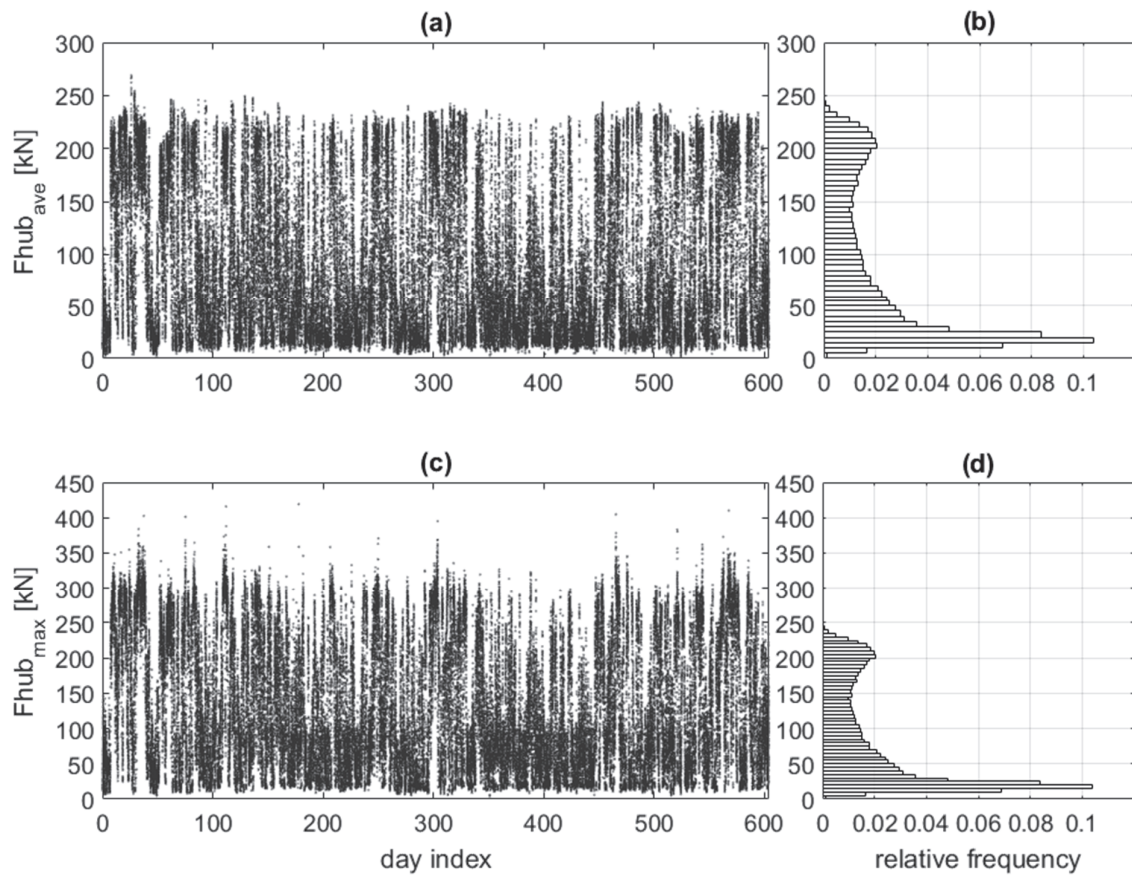
Figure 3-3. Average and maximum hub forces and corresponding histograms.

Effect of operating conditions on the hub force

Using the clustering algorithm presented in paragraph 2.3.2, the 10-minute maximum hub loads are presented for various operating conditions. Figure 3-4 highlights the recorded hub forces (data points in green) from different operating conditions for the 604 days of measurement, when the total set of hub forces are presented in grey.
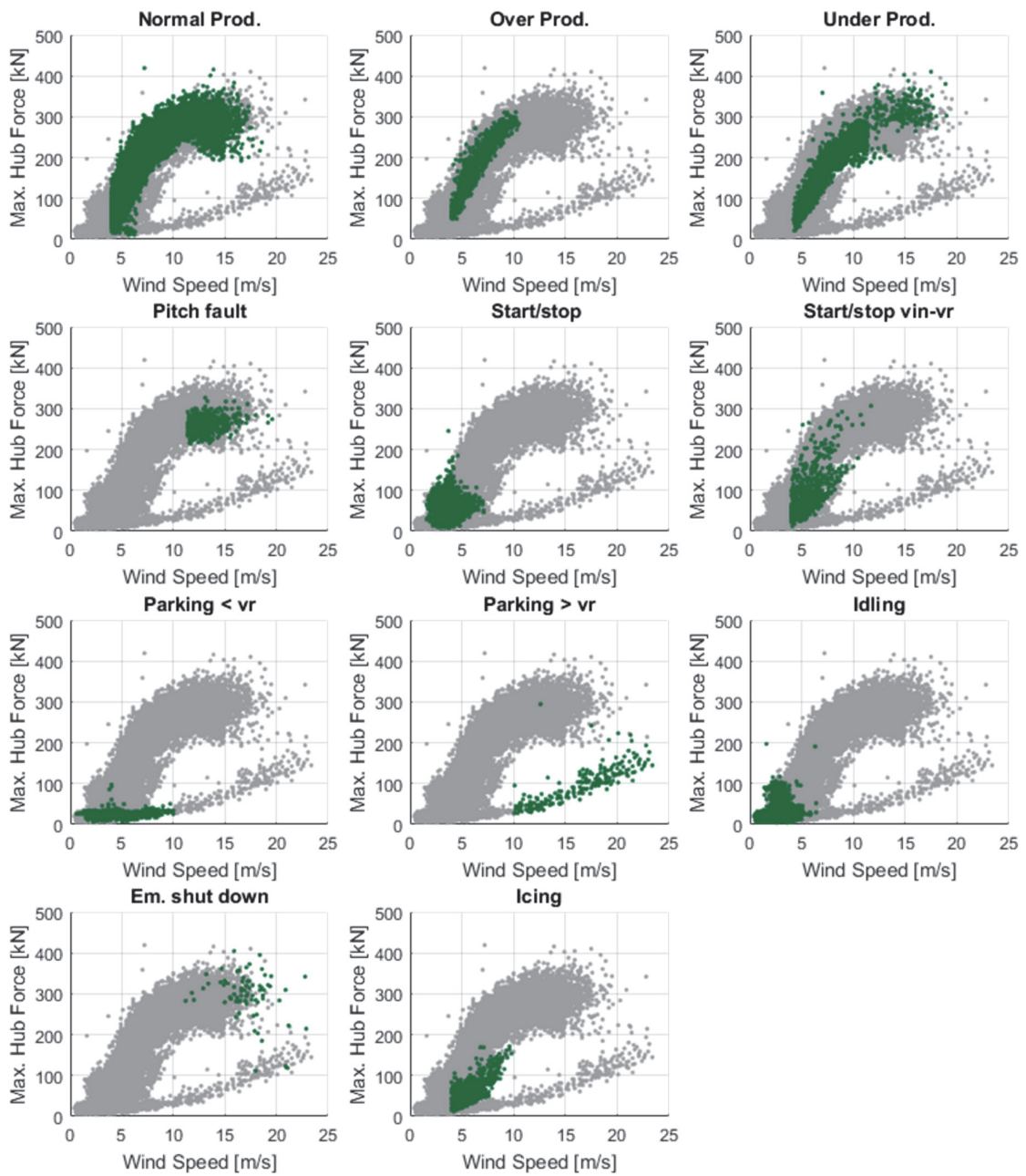
Figure 3-4. Measured hub forces for various turbine conditions.

Figure 3-5 shows the fore-aft and side-to-side hub forces for normal power production (power output within the normal range), power production plus fault (power output higher or much lower than expected for a given wind speed), and parked periods. The average forces for the fore-aft and side-to-side axis are indicated with the green and orange dotted lines, respectively.
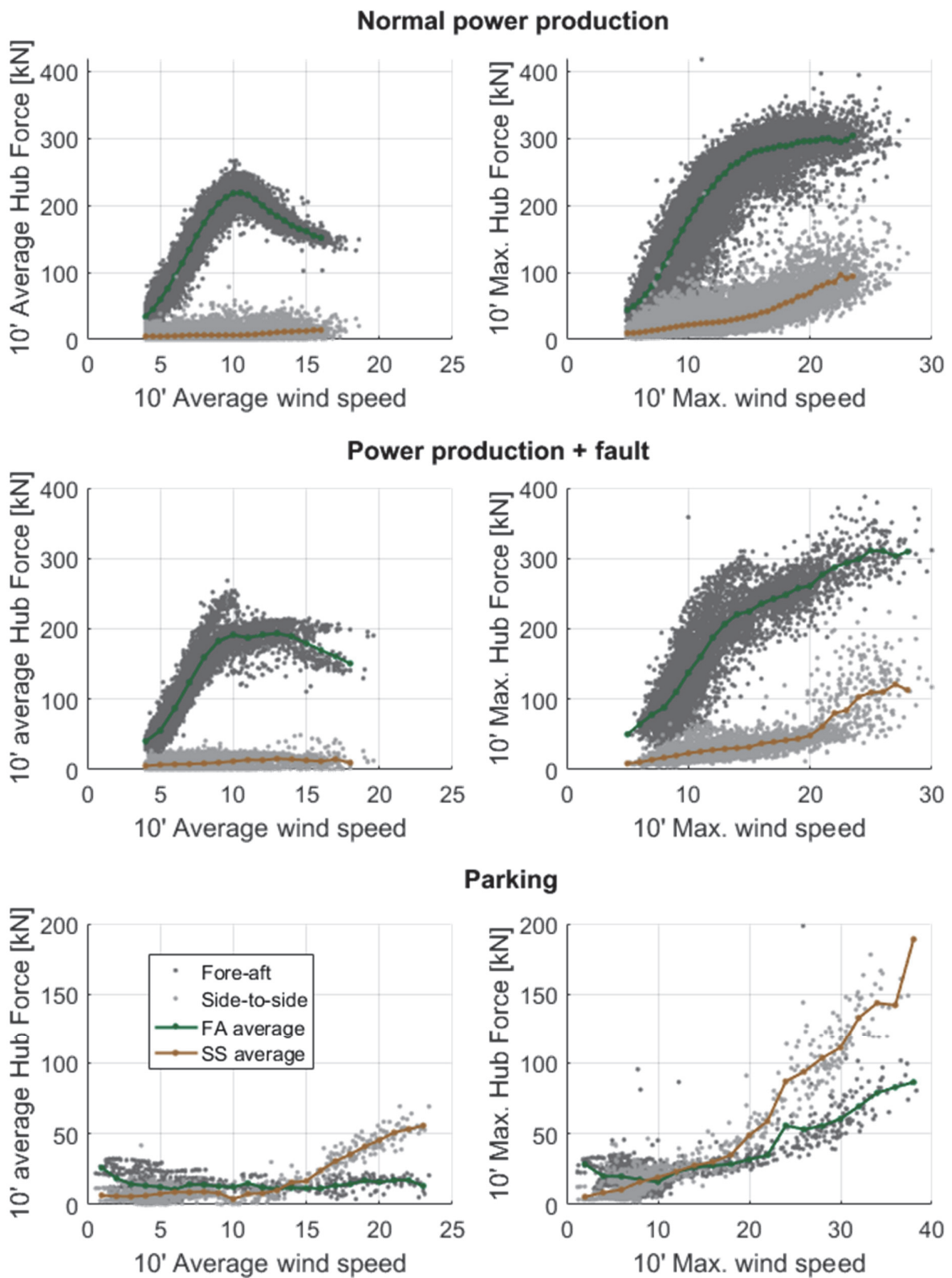
Figure 3-5. 10-minute average (left) and maximum (right) thrust loads with the 10-minute average and maximum wind speed, respectively.

The fore-aft hub force during normal production increases gradually up to the rated speed and decreases when the control system of the turbine enables the pitch control. Meanwhile, the

average side-to-side force is extremely small. Generally, the average forces are relatively small compared to the maximum loads experienced by the turbine. At the rated speed of 10 m/s, the maximum average forces are about 250 kN. The 10-minute maximum forces, on the other hand, are directly resulting from high wind speeds and gradually increase with it following a bi-linear curve. This indicates that the turbine cannot adjust the blade pitch angle fast enough to wind gusts and thus experiences high loads for a few seconds.

Out-of-range power production results in lower than average forces below the rated speed (since an activated pitch at low speed would decrease both lift and thrust) and higher than average forces above rated speed. This is caused by a pitch value lower than usual (see Figure 2-6).

During parking periods, the turbine does not experience any heavy wind loading, and the small residual force is actually the force equivalent to the bending moment resulting from the off-centered mass of the rotor. The turbine experiences higher forces during storms, but they remain lower than the average operational loads and are not a concern if the turbine is safely parked. The side-to-side thrust forces are increasing with the wind speed as the blades offer more surface to wind pressure when they are pitched at 90°. The turbine experienced wind speeds up to 38 m/s under parked condition.

Effect of icing and estimation of the ice mass on blades

The icing on blades impacts greatly the power production efficiency of wind farms situated in cold climate sites. During cold and humid periods, the two major types of ice accretion, precipitation icing, and in-cloud icing, can happen and affect the turbine behavior. The significant added mass to the blades induces mass imbalance, causing a reduced power production and an increase in loads (static and fatigue). The effects of icing on WT fatigue loading are studied by Frohboese and Anders (Frohboese and Anders 2007). Based on the results from simulations they showed that the main loads increase due to the unbalanced rotor, whereas the aerodynamic imbalance seems to have no effects on them. In another study, the determination of the actual mass of ice was studied on a monitored turbine (Brenner 2016). Vibrations measurement was used to detect icing on blades. The blades and rotor natural frequencies tend to decrease in the presence of ice, as the mass increases. The measurement of blade vibration is used for the automatic turbine shutdown and restart. Ice throw has a heavy impact on the drive train due to change of moment of inertia.

Figure 3-6 compares few days of measurement in February and July 2015. The wind conditions are summarized in Table 3-1. The data recorded in July shows a perfect wind turbine operation with a turbine efficiency of 95 % (calculated from the power curve provided by the manufacturer (Vestas 2010)). The 10-minute average hub force presents a very small scatter and the change of control mode at rated speed is clearly visible at 10 m/s. The period recorded in February shows a completely different behavior of the turbine. The scatter in the hub force and the low power production result from too low pitch angle of the blades. From Figure 3-6(c), it appears that the pitch angle is much lower than the normal values (red points), resulting in higher thrust load. The ice on the blade seems to decrease the lift coefficient, so the turbine control will try to set the pitch to a minimum value to keep the rotor speed higher.

Table 3-1. Wind conditions and power productions for two periods.

		03/02-09/02/2015	25/07-29/07/2015
Temperature	[°C]	-5.6	12.3
Wind speed	[m/s]	8.8	8.3
TI	[%]	19	16
Production	[MWh]	137	119
Theoretical Prod.	[MWh]	189	125
Efficiency	[%]	72.5	95.2
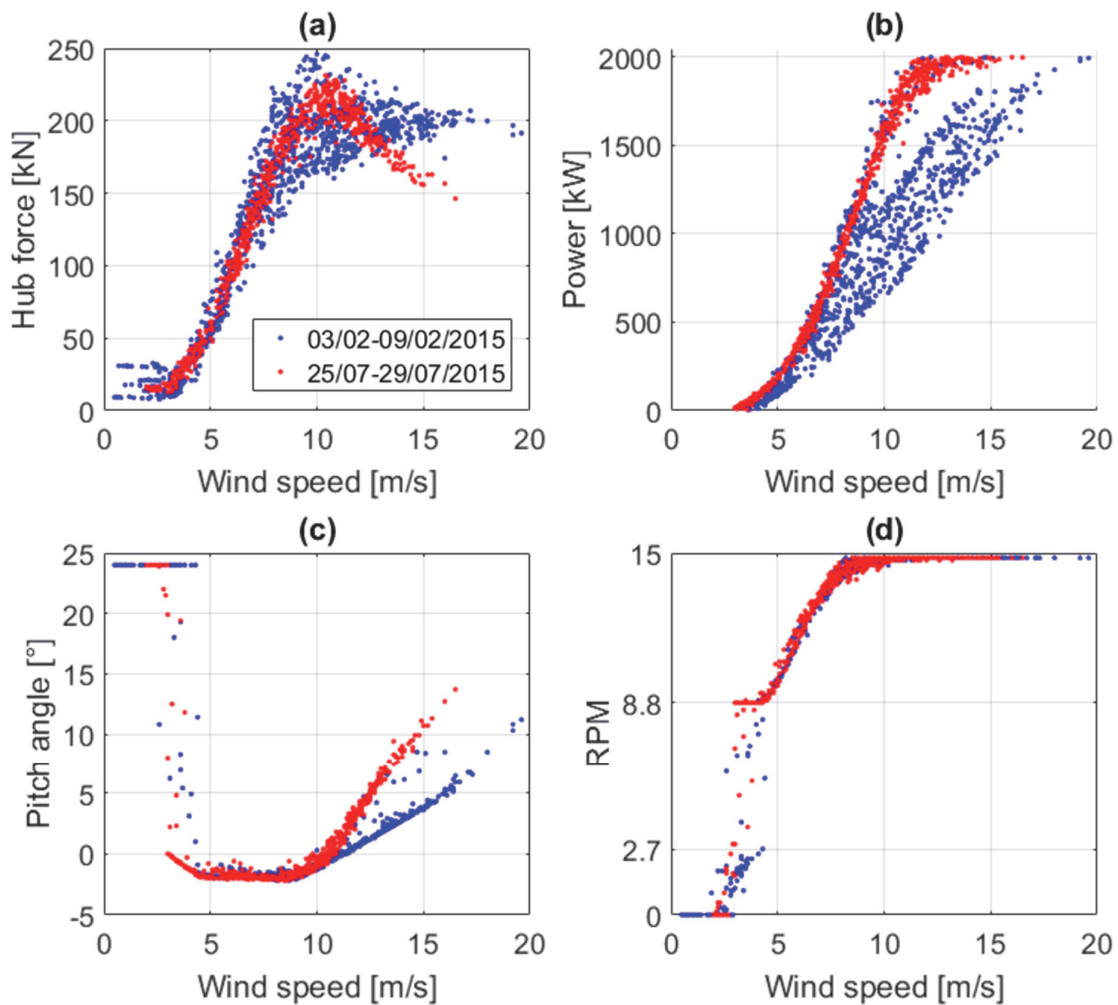
Figure 3-6. Effect of ice on blades. (a) Measured 10-minute average hub forces and (b-d) power, pitch, and rotor speeds as a function of the wind speed.

The added mass on the tower can reach 2-3 % of its self-weight (4 to 6 tons for a 90-m tower height). For the blades, the added mass will depend on the accretion process and the ice density. A maximum of 1.5-2 cm thickness on the outer third of the blade length leading edges is allowed for production (equal to 27 kg of ice for the Vestas V90). A higher amount of ice on the blade

would endanger the structure during production. However, the ice mass on the blades can be significantly higher as shown below.

From the measurements, the eccentricity of the nacelle and the rotor mass can be estimated, as well as the added weight on the blades due to the icing. The total hub mass is known and equal to 106 tons (Vestas 2010) with e_{F_A} being the eccentricity of the hub mass relative to the tower vertical axis:

$$m_{hub}.g \cdot e_{F-A} = -\frac{EI_c}{R_i}\epsilon_{F-A}$$ (3-11)

The center of mass of the added ice is supposed to be at the position of the blades hub (see the figure below), at a distance of 4.6 m from the tower center.

Table 3-2. Parameters used to determine the hub mass eccentricity and ice mass on blades

	Section		Bottom	Middle	Top
	t	[mm]	37.8	22.5	12.4
	D_i	[mm]	4110	3550	2510
	h(z)	[m]	7.8	36	87
	I	[m4]	1.06	0.40	0.08
Normal condition	Strain	[µε]	-14.7	-33.0	-119.8
	Moment	[kN.m]	-1587	-1573	-1566
Icing (10.12.2014)	Strain	[µε]	-16.2		-135.7
	Moment	[kN.m]	-1758		-1775
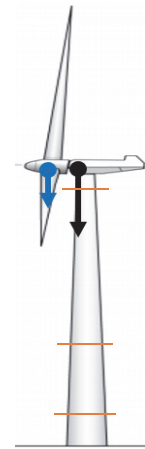
The first recorded 0-360° rotation of the nacelle happened on 10th of December 2014, during a long period of icing. The maximum strain measured at the bottom location during this rotation is only 1.5 µε higher; the difference in more visible on the strains at the top section with an increase of 15.9 µε of the amplitude. The measured constant bending moment along the tower due to the eccentricity of the hub mass is in average 1566 kNm. With the ice on blades, an average bending moment of 1775 kNm is measured with the top and bottom section. Finally, using equation (3-12), an eccentricity e_{F-A} 1.52 m is calculated for the hub mass and a total weight of 4'300 kg of ice on the rotor. This amount of ice corresponds to an ice thickness of about 22 mm (with a blade surface of 80 m² and an ice density of 800 kg/m³).

3.3 Fatigue safety verification using long-term monitored data

3.3.1 Theoretical background

The fatigue assessment of a structure can be performed in different ways. The probabilistic crack initiation and propagation lives can be estimated using Paris' law or a classic approach combining S-N curves (or Wöhler curves) and a rainflow counting algorithm. The S-N curve represents the fatigue resistance of a given detail and is determined from series of fatigue tests on specimens, and can be found in the relevant standards. The rainflow cycle-counting algorithm translates the hysteresis loops experienced by the material during the loading history

into a stress histogram. It gives for a certain stress range, $\Delta\sigma_i$, the number of experienced cycles n_i. The obtained fatigue spectrum is translated into a damage factor D_{tot} according to linear damage accumulation rule of Palmgren-Miner (Miner 1945) for single slope m:

$$D_{tot} = \sum_{i=1}^{k} n_i d_i = \sum_{i=1}^{k} \frac{n_i}{N_i} = \sum_{i=1}^{k} \left(\frac{n_i}{C\Delta\sigma_i^{-m}} \right) \tag{3-12}$$

where C is a constant representing the construction detail category, m is the slope of the corresponding S-N curve and N_i the number of allowable fatigue cycles to failure for a specific stress range σ_i. In order to calculate the realistic total damage experienced by a construction detail, the correct S-N curves with C and m are the key parameters. The structure is assumed failed when the total damage D_{tot} is equal to 1.
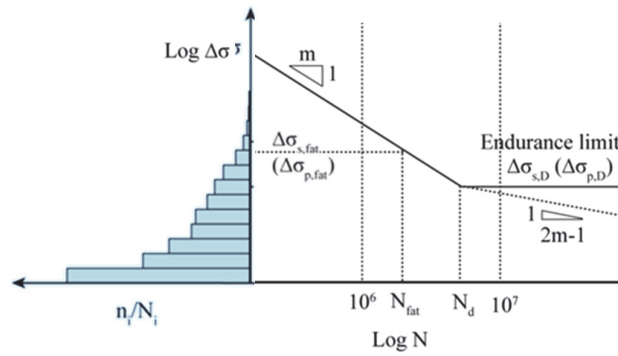
Figure 3-7. Simplified stress histogram and bi-linear S-N curve adapted from (Hirt, Bez, and Nussbaumer 2006) and (SIA 263 2003).

One can also evaluate the equivalent stress difference $\Delta\sigma_E$, which represents the fatigue damaging effect of all the encountered stress differences $\Delta\sigma_i$. Again, the total damage can be expressed as:

$$D_{tot} = \frac{N_{tot}}{C\Delta\sigma_E^{-m}} \tag{3-13}$$

From equations (3-1) and (3-2), $\Delta\sigma_E$ can be explicitly stated as (for single slope m):

$$\Delta\sigma_E = \left(\sum_{i=1}^{k} \Delta\sigma_i^{m} \frac{n_i}{N_{tot}} \right)^{\frac{1}{m}} \tag{3-14}$$

In the field of wind turbines, this equivalent stress difference is called Damage Equivalent Load (DEL) and defined as the hypothetical load with a fixed number of cycles (N_{eq}) that introduces as much damage as the complex load spectrum. Another way of defining the DEL is introduced for studying 10-minute time series during mechanical load measurement. In this case, the 1 Hz Equivalent Damage Load is defined as the amplitude of a load acting at 1 Hz that would create as much damage as the load histogram; and calculated as follow (IEC 61400-13 2001):

$$DEL = \left(\frac{\sum_{i=1}^{k} \Delta\sigma_i^m \, n_i}{600}\right)^{\frac{1}{m}} \qquad (3\text{-}15)$$

The main advantage of the DEL is that being used for a rapid observation of the fatigue loading acting on the structure without considering any particular construction details, such as the C parameter. However, the equation is limited to a single slope S-N curve and no fatigue safety consideration. For the slope of the S-N curve, a value of m = 4 is commonly used, with a fixed number of cycles $N_{eq} = 10^7$ (Weijtens et al. 2016).

According to Eurocode (Eurocode 3 part 1-9 1990), the stress differences $\Delta\sigma_i$ obtained from a load spectrum must be multiplied by a partial safety factor γ_{Ff} (usually equal to 1.0) , and the stress strength $\Delta\sigma_C$ must be divided by another partial safety factor γ_{Mf}. The damage D_d is calculated as follow:

$$D_d = \sum_i \frac{n_{Ei}}{N_{Ri}} \qquad (3\text{-}16)$$

where

$$N_{Ri} = N_C \cdot \left(\frac{\Delta\sigma_C}{\gamma_{Ff} \cdot \gamma_{Mf} \cdot \Delta\sigma_i}\right)^m = 2 \cdot 10^6 \cdot \left(\frac{\Delta\sigma_C}{\gamma_{Mf} \cdot \Delta\sigma_i}\right)^3 \quad for \; \Delta\sigma_i \geq \Delta\sigma_D \qquad (3\text{-}17)$$

$$N_{ri} = N_D \cdot \left(\frac{\Delta\sigma_D}{\gamma_{Ff} \cdot \gamma_{Mf} . \Delta\sigma_i}\right)^m = 5 \cdot 10^6 \cdot \left(\frac{\Delta\sigma_D}{\gamma_{Mf} \cdot \Delta\sigma_i}\right)^5 \quad for \; \Delta\sigma_i < \Delta\sigma_D \qquad (3\text{-}18)$$

Finally, the fatigue verification based on the damage accumulation should meet the criterion:

$$D_d \leq 1.0 \qquad (3\text{-}19)$$

3.3.2   Critical construction details

The fatigue calculation is performed on the L-flange connection detail located at the junction between tube #2 and #3, at about 36 m higher from the tower foundation, where the maximum stresses are predicted by mean of FEM and local measurement with strain gauges (see Chapter 2). The door of the WT is not considered as critical as it consist of an oval opening in a thicker plate, few meters above the foundation. The ladder is connected to the tower with magnets and do not creates any stress concentration, whereas floor are supported with small connectors but no information could be found on this detail.

Despite being the preferred design for the connections of circular tubes and the most widely used in the field of wind turbines, bolted L-flange design results in an eccentrically loaded bolted connection. The eccentricity results in a non-linear relationship between the external

load on the turbine and the tensile forces in the bolt. This non-linear relationship occurs when the loads are high relative to the bolt preload and can rapidly lead to bolt fatigue failure. Various connection designs can be found in the study by Veljkovic (Veljkovic et al. 2011). Different approaches and models are developed to estimate the load transferred into the bolts. For example, some models suggest a bi-linear (Petersen 2013) or a tri-linear relationship (Schmidt and Neuper 1997) and these models can be found in a guideline for the calculation of highly stressed bolt joints (VDI 2230 Blatt 1 2015). In 2001 a comprehensive comparison of the models was performed (Seidel and Schaumann 2001) and a study on the improvement of the design was released recently. (Pedersen 2017). This study concludes that such sections can be optimized by placing the bolts as close as possible to the tower wall to reduce the eccentricity and it was shown that an increase in the flange thickness also help reduce the stresses in the bolds. In any case, the bolts stay prestressed as the R-ratio for large cycles is small (R ≤ 0.1).

Bolts alone are weak components of this construction details, although the actual stress variations inside the prestressed bolts are low during normal operation of the turbine and no opening of the joint is expected with service loads (Rebelo, Veljkovic, Matos, et al. 2012). The inspection of the bolted connection of the monitored turbine showed an optimized detail with bolts situated as close as possible to the tower walls and thick flanges of 95 mm between tube #2 and #3.

Finally, the fatigue of the bolts should not be a concern because the prestressing of the bolts is a necessity for the stiff clamping of the joints and keeping the stress variations below the fatigue limit. Loss of prestressing can be expected, but a correct maintenance program that includes the retightening of the bolts prevents the appearance of any unwanted behavior. As mentioned in the introduction, the only failure that occurs at a bolted connection was a result of a fault during the assembly, causing a premature failure after a few months. The fatigue calculation presented in this chapter will focus on the welded connections between the tower wall and the flange showed in Figure 3-8.
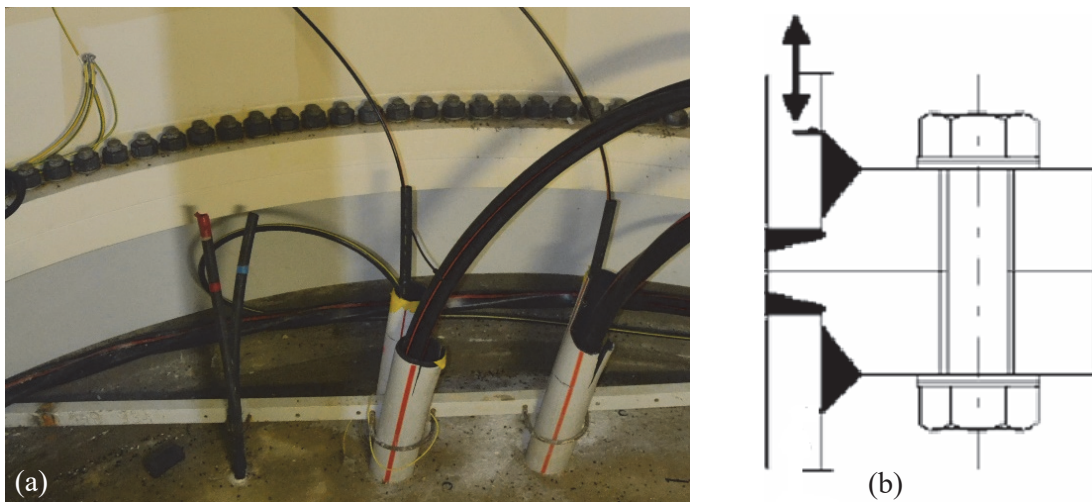
Figure 3-8. (a) Picture of the bottom tube-to-tube bolted connection between the foundation tube and the first tower segment and (b) generic schematic of the construction details adapted from Eurocode (Eurocode 3 part 1-9 1990)

For components predominantly loaded by normal stresses, such as the connection detail studied here, design codes for wind turbine support structure (DNVGL 2016) recommend the use of bilinear S-N curves (Eurocode 3 part 1-9 1990) with slope of $m = 3$ for stress number $N_i \leq 5 \cdot 10^6$ and $m = 5$ for stress number $N_i > 5 \cdot 10^6$. They however do not recommend the use of an endurance limit.

According to Eurocode (Eurocode 3 part 1-9 1990), the fatigue detail shown in Figure 3-8(b) has a detail category of 71 MPa. Therefore, the following limits are considered for the calculation of the damage. The fatigue limit under constant amplitude $\Delta\sigma_D$ defined at $5*10^6$ cycles and the endurance limit $\Delta\sigma_L$ defined at 10^8 cycles are formulated as:

$$\Delta\sigma_D = \left(\frac{2}{5}\right)^{\frac{1}{3}} \cdot \Delta\sigma_C = 0.737 \cdot \Delta\sigma_C \tag{3-20}$$

$$\Delta\sigma_L = \left(\frac{2}{100}\right)^{\frac{1}{3}} \cdot \Delta\sigma_D = 0.549 \cdot \Delta\sigma_D \tag{3-21}$$

The parameters used for the S-N curve are presented in Table 3-3, and Figure 3-9 shows the process for the calculation of the damage. The damage distribution is obtained directly from the measured stress cycles distribution using the corresponding bilinear S-N curve.

Table 3-3. Parameters for S-N curve

	Parameter	Eurocode 3	DNVGL
region I	$\Delta\sigma_C$	71	71
	N_{fat}	$2*10^6$	$2*10^6$
	m	3	3
region II	$\Delta\sigma_D$	53	53
	N_D	$5*10^6$	$5*10^6$
	m	5	5
region II	$\Delta\sigma_L$	29	
	N_L	10^8	
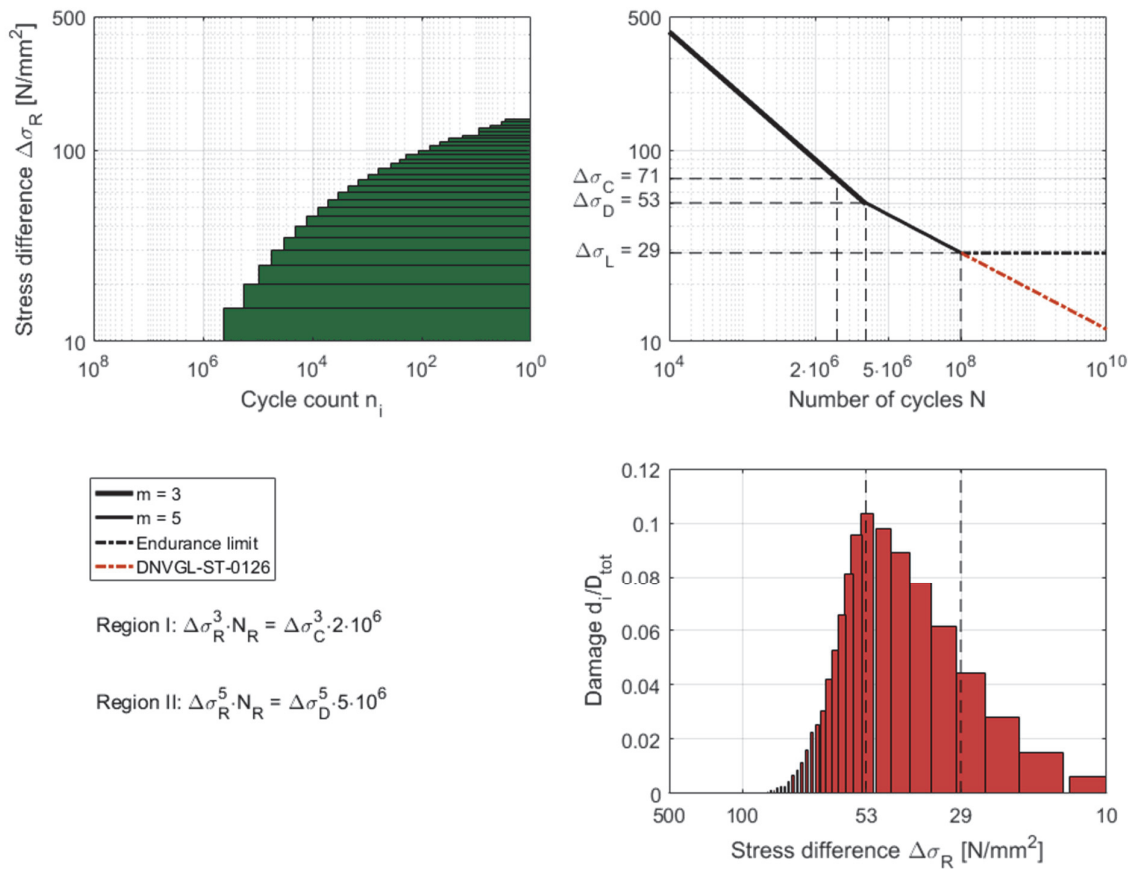
Figure 3-9. The process to estimate the damage based on monitored data and S-N curves.

3.3.3 Damage calculation from monitored data

The damage calculation is performed on the full dataset of 604 days. The first block of 330 days was recorded during a full year from December 2014 to January 2016. The remaining days were recorded from mid-2016 to April 2017. The damage is calculated both from cycles obtained within 10-minute time series and daily time series. The damage is also calculated according to a bilinear S-N curve with and without considering the endurance limit.
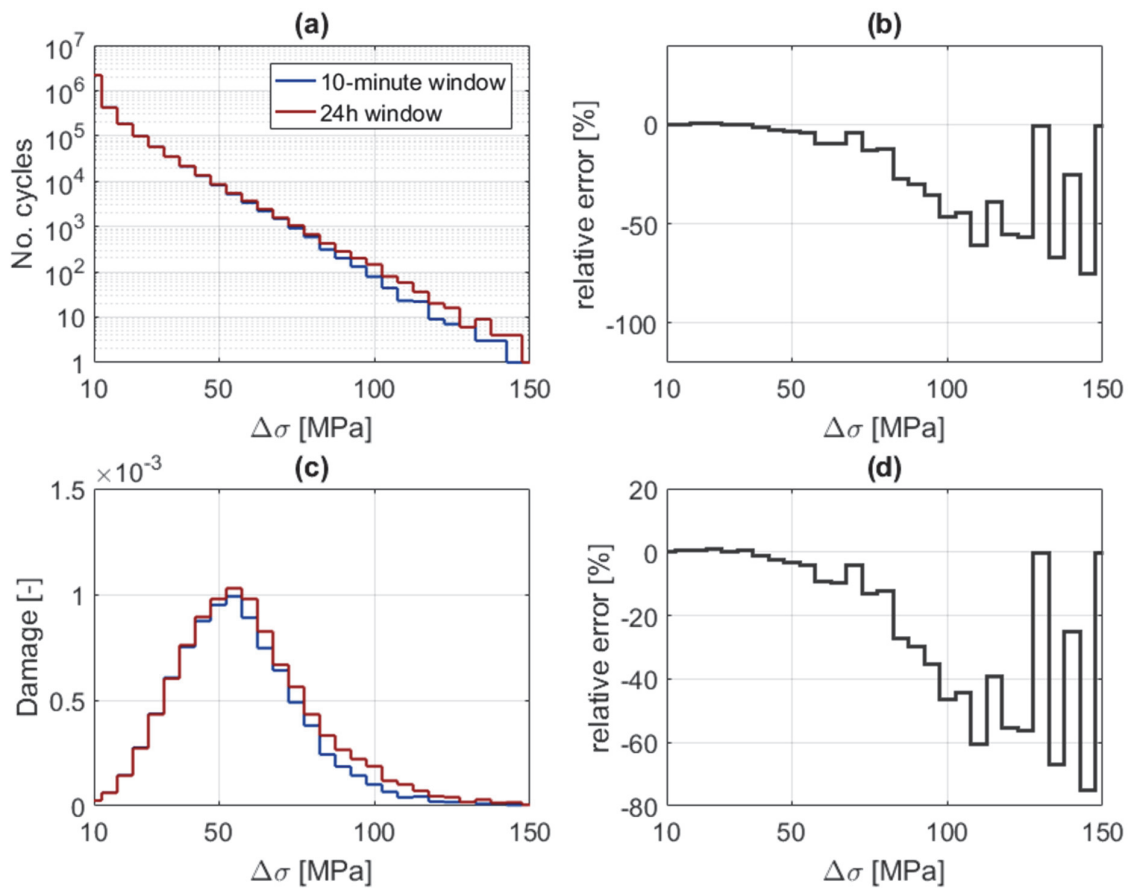
Figure 3-10. (a) Histograms of the stress cycles calculated with two different window lengths and (b) relative errors compared with the histogram from the 24-hour window (c) damage distribution and (d) relative errors for both window length.

The histograms presented in Figure 3-10(a) show the stress cycles obtained from 604 days. The same rainflow algorithm was applied for 10-minute series synchronized with the SCADA system. The following data for every day was recorded. A relatively big difference can be seen between the two curves, especially for the largest stress cycles, starting from 70 MPa. The largest cycles, only detected when the rainflow counting algorithm is performed on full days are resulting from a change of wind directions or start-stop happening during the day. Some larger cycles are not visible here (few between 150 and 200 MPa). When the wind changes direction and follows the other main direction (both main wind directions are along the same axis approximately, see Figure 2-2), the turbine is bent on the opposite direction resulting into a large cycle. Figure 3-10(b) shows the relative error for the 10-minute compared to the 24-hour window. The 10-minute window underestimates the cycles above 70 MPa.
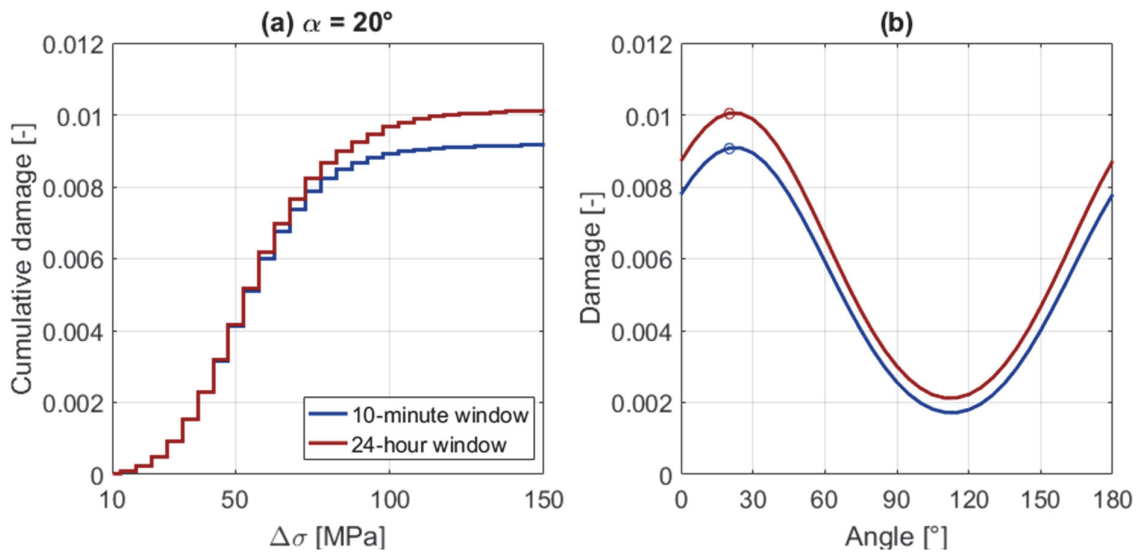
Figure 3-11. (a) Cumulative fatigue damage calculated from the stress histogram at an angle of 20° and (b) damage distributions over the section for 604 days of measurement.

The damage can be estimated over the section by performing the rainflow counting algorithm on the stress signals calculated every 5° along half of the section. The damage at two opposite sides is considered equal, due to the assumption of mean stress not affecting the fatigue damage. Figure 3-11(b) shows the results of the damage calculation from 0° to 180° with 5° intervals based on the full dataset. The damage calculated from the 10-minute time series was found to be 11.2 % and 9.50 % lower than the damage calculated with 24-hour time series for $\gamma_{Mf} = 1.0$ and $\gamma_{Mf} = 1.15$ respectively. The damage is calculated according to (DNVGL 2016) with the bi-linear S-N curve. Figure 3-12 shows the damage for different S-N curves.
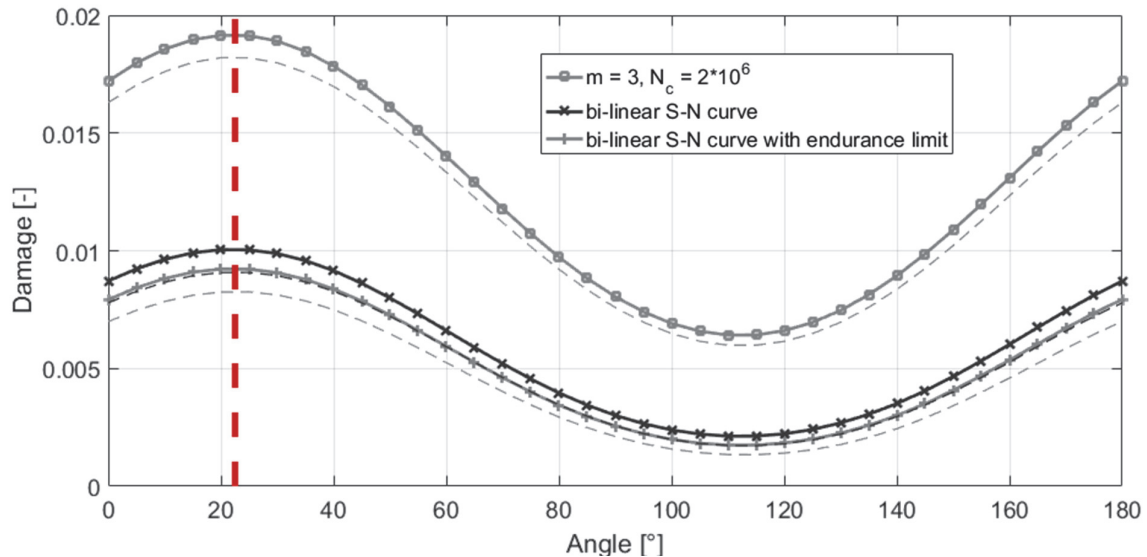
Figure 3-12. Influence of the S-N curve on the damage. The dashed lines are obtained with the 10-minute time series.
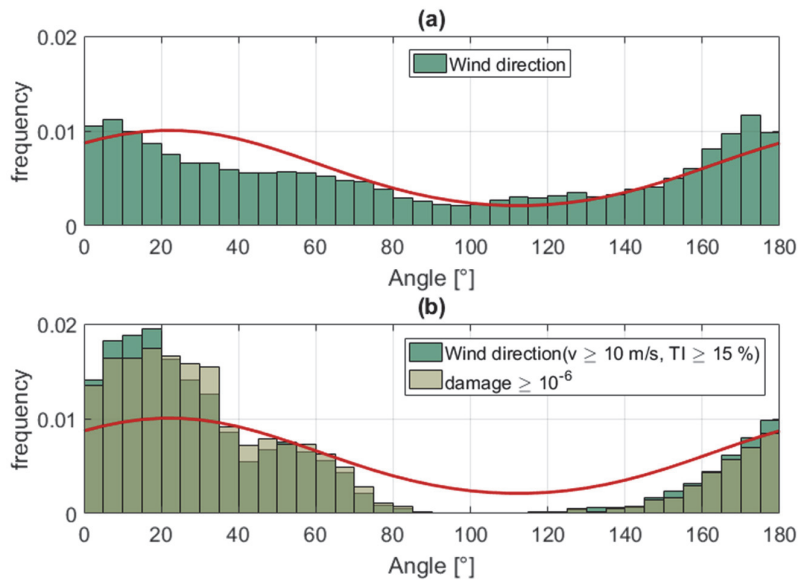
Figure 3-13. Relation between the calculated damage distribution (red line) and (a) the absolute wind direction and (b) 10-minute time series with high damage, high wind speed, and turbulence intensity.

Figure 3-13(a) displays the absolute wind direction from the SCADA system and the damage distribution from 0° to 180°. It is not expected to observe the maximum damage at around 22.5°. Figure 3-13(b) presents the histogram of the 10-minute time series with a damage higher than 10^{-6}, and the distribution of the absolute wind direction restricted to wind speed and turbulence intensity higher than 10 m/s and 15 %, respectively. This clearly indicates the strong effect of storms and high wind speed periods on the accumulated damage.

Based on the 604 days of measurements and the fatigue analysis, it appears that the endured fatigue damage is relatively low compared to what could be expected from design. The difference between the fatigue damage from the bilinear S-N curves with and without the endurance limit is relatively limited. The linear curve with m = 3 gives an upper boundary to the estimated fatigue life with a conservative calculation. For the case of the bilinear curve, an expected service duration of 165 years can be expected before reaching the damage of 1. The results are summarized in Table 3-4. Fatigue verification is performed for a partial safety factor $\gamma_{Mf} = 1.0$ and $\gamma_{Mf} = 1.15$, as the flanges connection and welds in the tower walls are considered to be accessible for inspection (DNVGL 2016; Eurocode 3 part 1-9 1990).

Table 3-4. Summary of damage in the construction detail.

	Time serie length	Single slope method		Bilinear S-N method		Bilinear S-N + endurance limit	
		24-hour	10-minute	24-hour	10-minute	24-hour	10-minute
$\gamma_{Mf} = 1.0$	D	0.0192	0.0182	0.0101	0.009079	0.0092	0.008252
	$D_{av/day}$	3.17E-05	3.01E-05	1.66E-05	1.50E-05	1.53E-05	1.37E-05
	D_{20y}	0.2317	0.2201	0.1215	0.1098	0.1116	0.0998
	n_{year}	86	91	165	182	179	200
$\gamma_{Mf} = 1.15$	D	0.0291	0.0277	0.0173	0.0158	0.0163	0.0148
	$D_{av/day}$	4.82E-05	4.59E-05	2.86E-05	2.62E-05	2.70E-05	2.45E-05
	D_{20y}	0.3519	0.3350	0.2092	0.1911	0.1971	0.1790
	n_{year}	57	60	96	105	101	112

Seasonal influence and monitoring duration

The temperature plays a role in the strain signal but is not responsible for any variation on the damage. A correlation is visible only because the strong wind periods occur in winter. The fatigue damage is found to be highly dependent on the number of high wind events, *i.e.,* storms. The 10-minute damage is presented over the monitoring period in Figure 3-14 below. For better reading, the negative common logarithm of the damage is plotted (-log(D)). The points above the orange dotted line are responsible for 99 % of the total cumulated damage whereas the red dotted line represents the limit for 50 % of it. It appears clearly that the few recorded storms have the biggest impact on the fatigue damage of the structure.
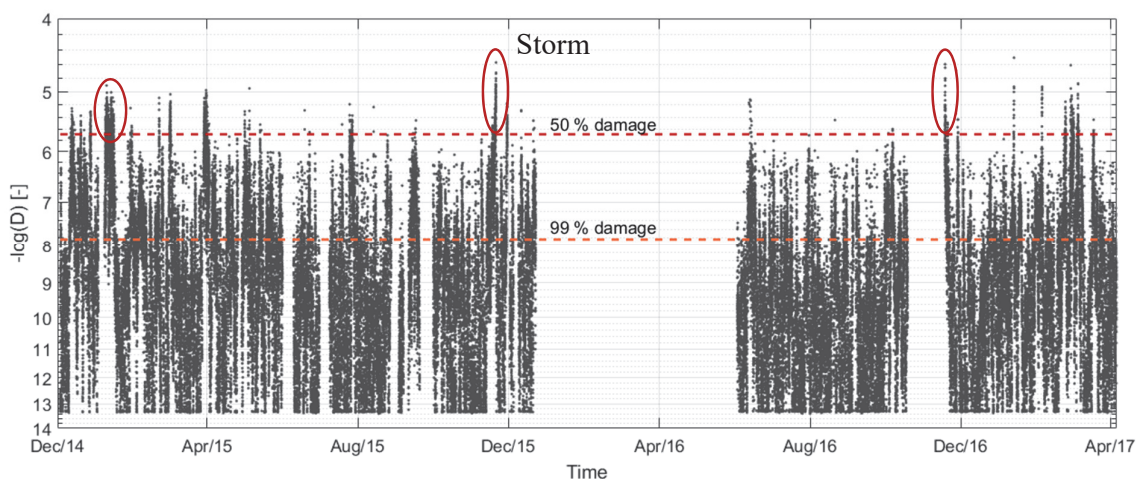
Figure 3-14. 10-minute fatigue damage calculated over the whole set of data for the 20° angle.
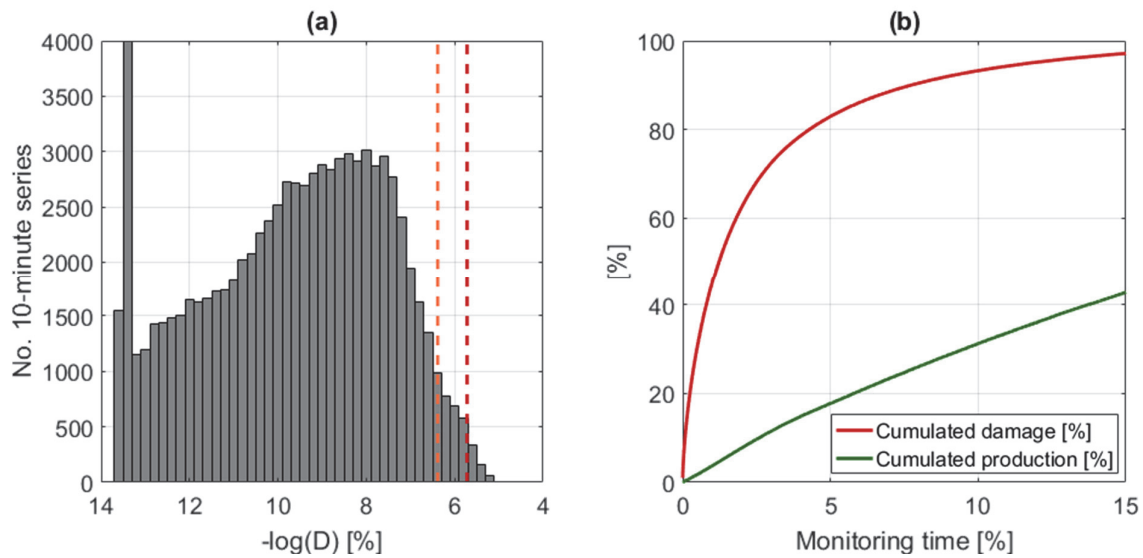
Figure 3-15. (a) 10-minute damage frequency (20° angle) with the 50 % and 99 % limits (red and orange dotted lines) and (b) percentage of the cumulated damage and electricity production as a function of the monitoring time.

Figure 3-15(a) shows the damage distribution for the 20° angle. The peak on the left represents the 10-minute time series without any measured damage (parked situation). The Figure 3-15(b) gives an overview of the percentage of 10-minute time series required to achieve a certain level of damage. For example, 50 % of the damage is reached within 1.29 % of the monitoring duration (1122 10-minute series, 7.8 days of the 604 days of measurement) and 99 % of the damage is reached within 25 % of the time, less than half of the power production time of the turbine. The detection of the few periods causing the major damage on the structure could drastically decrease the total fatigue damage endured, without losing too much electricity production. Based on the data collected over the monitoring period, stopping or decreasing the load on the rotor during 2 % of the time would reduce 1/3 of damage.

Figure 3-16 displays the calculated service duration ($D_d = 1$) for an increasing monitoring duration. The estimated number of years before failure is largely influenced by individual storms and therefore varies a lot during the first weeks. Long periods of relatively low wind speed tend to increase this estimation. An asymptotic behavior is visible towards the end of the monitoring period, indicating a sufficient monitoring duration.
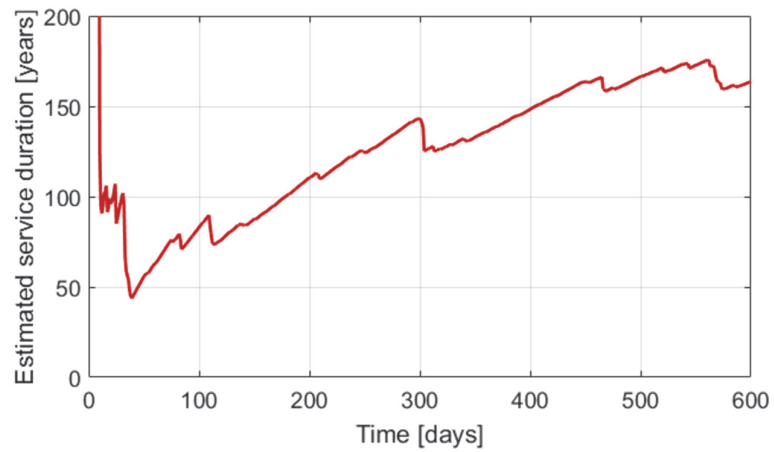
Figure 3-16. Estimated service duration of the turbine as a function of the monitoring duration.

The total number of stress cycles recorded from December 2014 to November 2015 is plotted in Figure 3-17. Not all the days were recorded in each month (due to some power outage). Thus the data was corrected to represent an average of 30 days. The red curve indicates the monthly average number of cycles.
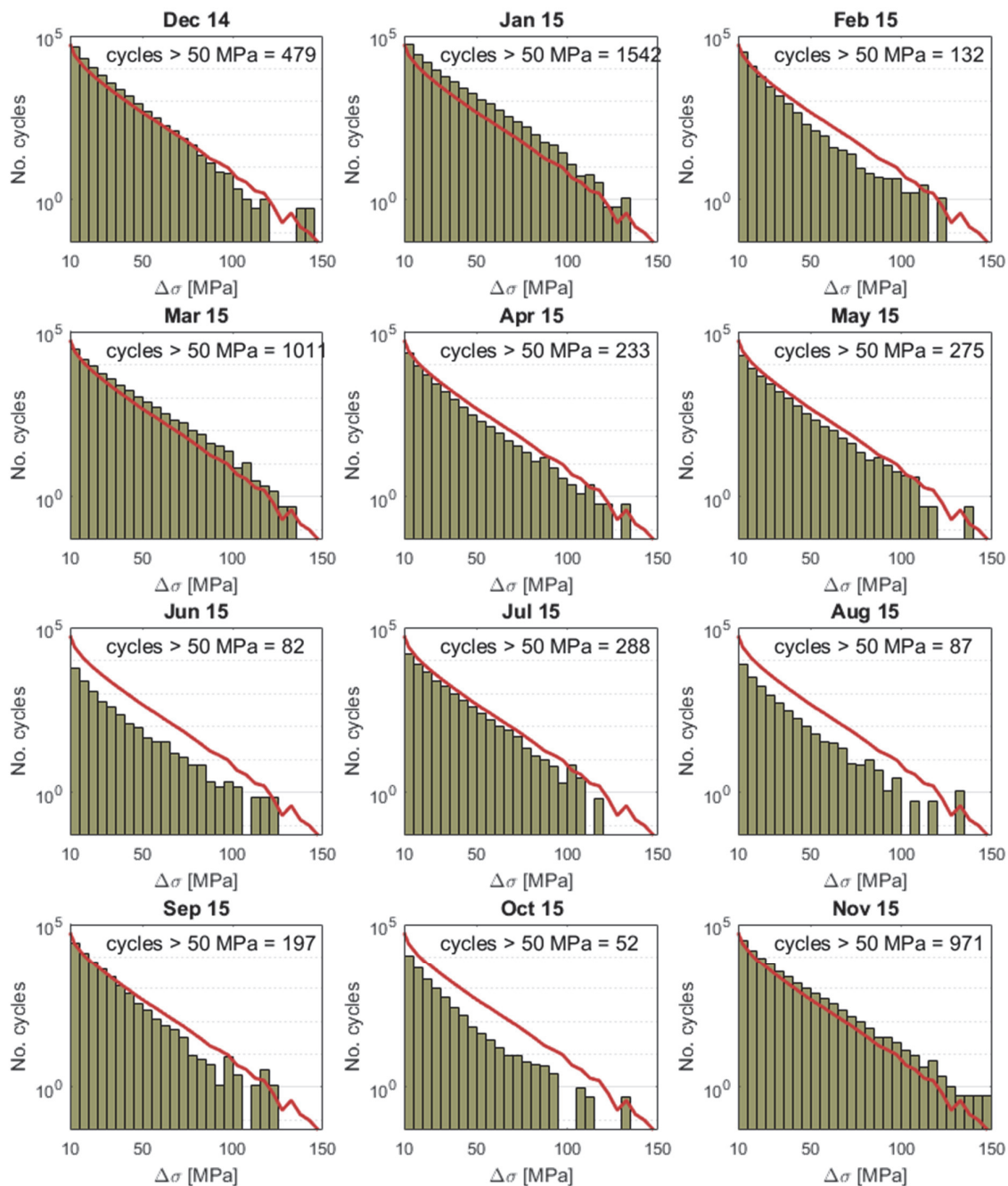
Figure 3-17: Histograms of the stress cycles for the first 12 months of measurement.

The wind distribution varies a lot over the year, and it is clearly shown in the resulting stress histograms. From April to October 2015, the number of cycles recorded was always below the monthly average, with a very low number of cycles exceeding 50 MPa. Figure 3-18 shows the monthly damage from December 2014 to November 2015. A long period of full power production with high wind speed in January 2015 generated a damage three times bigger than the monthly average damage. The monthly damage was found to be very fluctuating, however in average high in winter and extremely low in summer, with wide disparities from one month to the next.
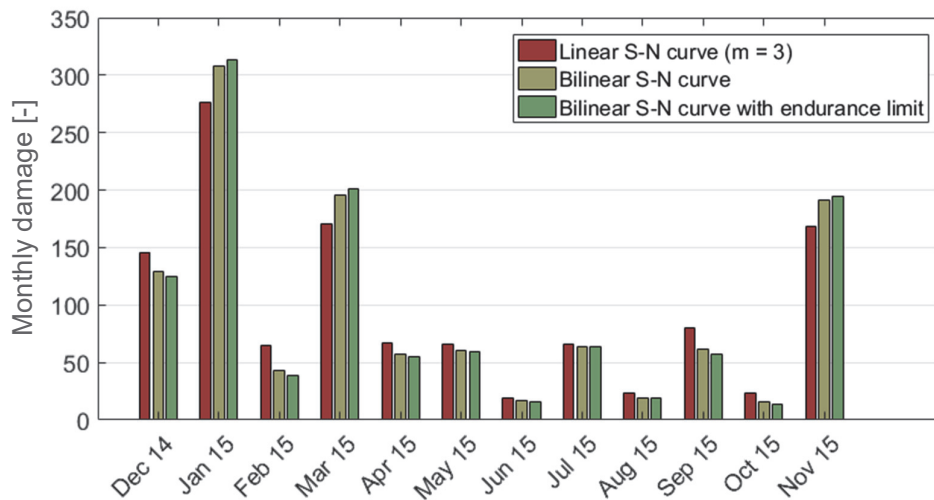
Figure 3-18. Variation of the monthly damage for the first year of measurement.

Influence of the environmental and operational parameters

It was established previously that the damage mainly occurs during the storms and high wind speed periods. To investigate further the reasons for such variations in the damage, the data from the SCADA system was used. The Figure 3-19(a-c) shows the 10-minute damage as a function of the average wind speed, the turbulence intensity, and the wind direction whereas Figure 3-19(d-f) shows the pitch angle, the rotor speed, and the power production. The dashed lines represent the 50 % (red curve), 80 % (orange curve), and 99 % (yellow curve) of the damage.

Figure 3-19(a) shows that almost 80 % of the damage occurs exclusively between V_{rated} and V_{out}. Below rated speed, 20 % of the damage is the accumulation of a very high number of 10-minute series. The turbulence intensity, on the other hand, does not provide any relevant information, except that 80 % of the damage occurs between 10 % and 25 % of TI. The damage as a function of the wind direction confirms the variations presented in Figure 3-13. Figure 3-19(d) indicates the damage when the pitch control is active having pitch values between 0° and 15° which is typical for wind speeds above V_{rated}. Few points above the red dashed line with a pitch higher than 15° indicates emergency shutdowns. Figure 3-19(d-e) confirms that 80 % of the damage occurs above V_{rated}.

71
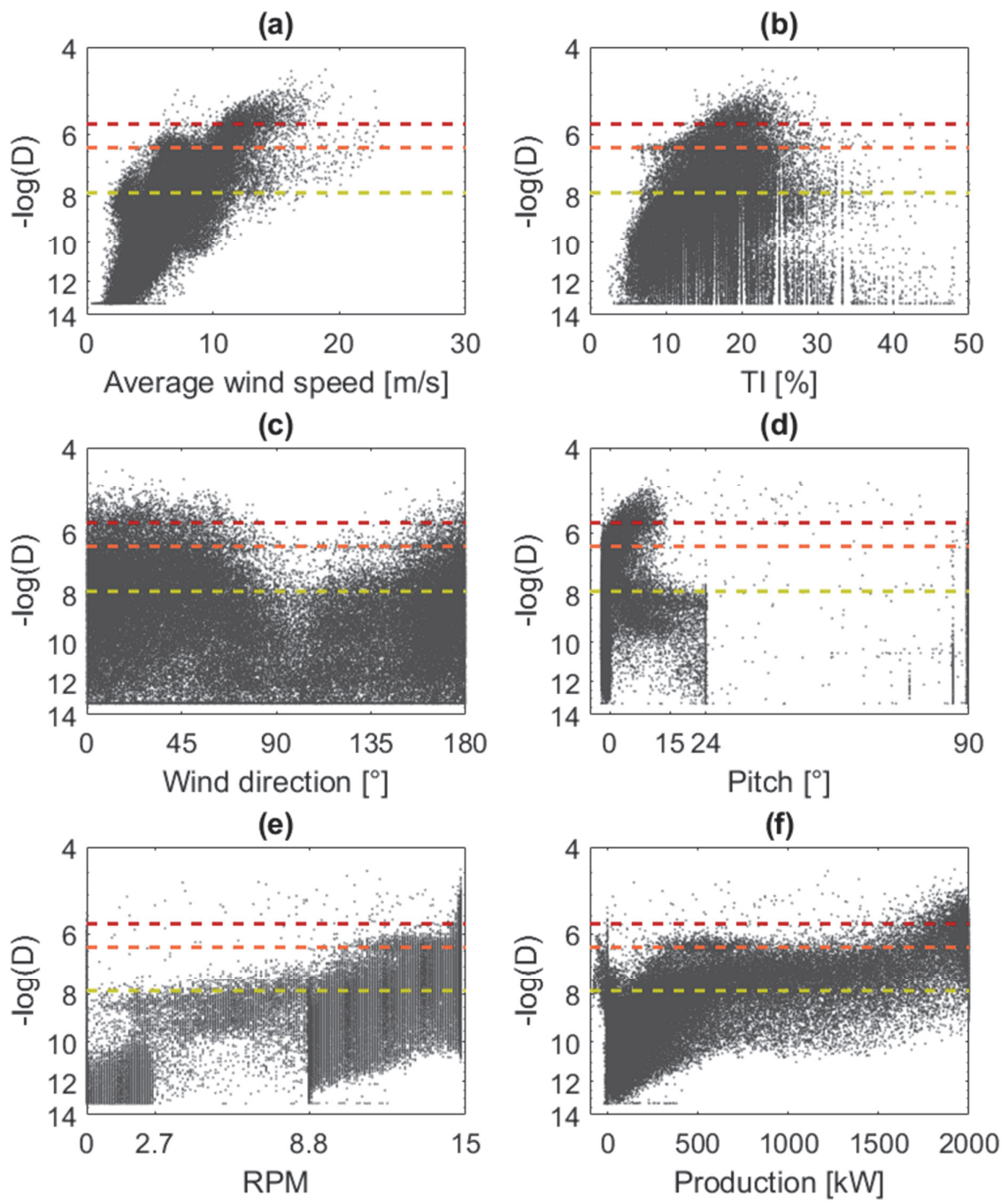
Figure 3-19. 10-minute damage as a function of (a-c) environmental and (d-f) operational parameters.
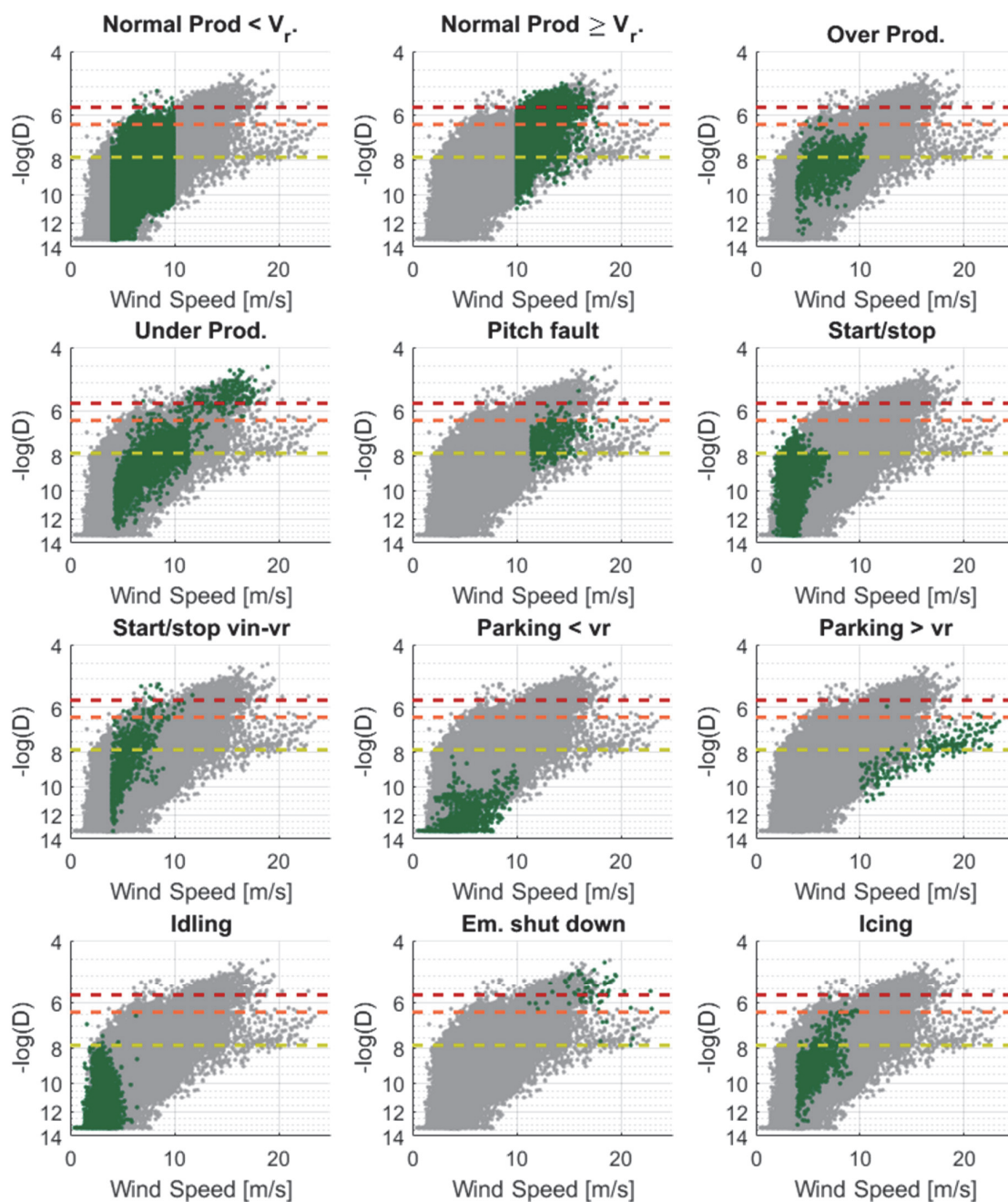
Figure 3-20. Calculated 10-minute damage for various turbine conditions.

Finally, Figure 3-20 and Figure 3-21 summarize the individual effect of each load case generated by the clustering algorithm. Almost all of the damage occurs during power production and 60 % of it occurs above V_{rated}. The relative damage, on the other hand, shows that the emergency shutdowns are the more aggressive situations, followed by the normal production having the pitch control system activated. This indicates that the total damage endured by the wind turbine is closely related to the probability of encountering winds above the rated speed.
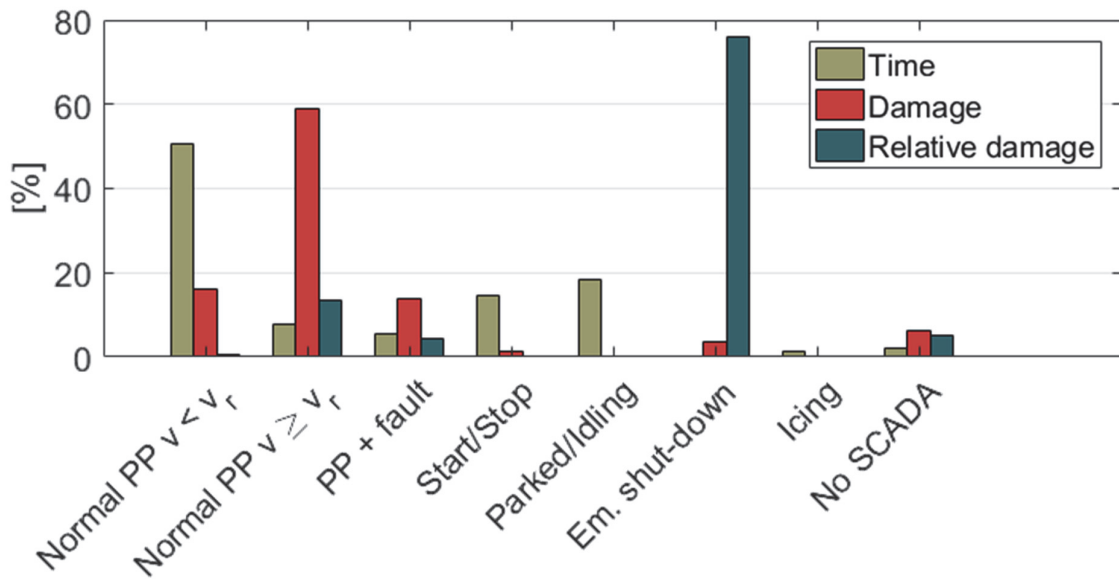
Figure 3-21. Total and relative damages of different turbine conditions.

3.3.4 Relation between hub force and damage

The maximum wind forces happen during storms, so does the damage. Since the fatigue damage is a result of the hysteresis loops experienced by the material, it may be more closely related to variations of the forces rather than the maximum force. The standard deviation of the hub force was computed for the 10-minutes series and is displayed in Figure 3-22 below in logarithmic scale against the damage, for the standard operation load case.
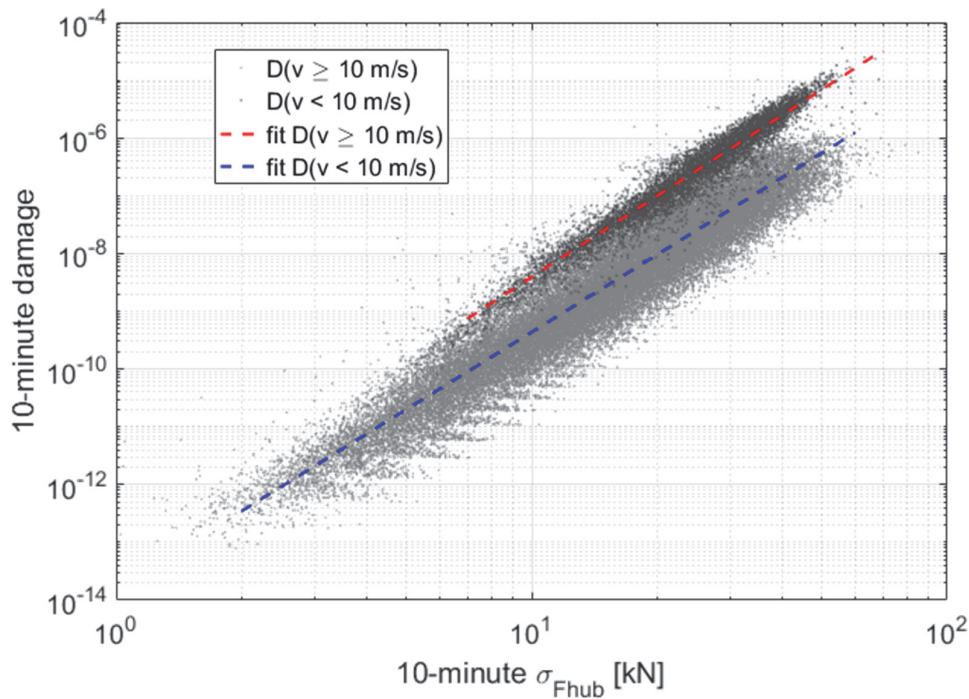
Figure 3-22. Relation between the damage and the hub force standard deviation.

The data was fitted by a linear curve in log scale. For the data above the rated speed, the following equation was obtained with $R^2 = 0.91$:

$$D = 8.73 \cdot 10^{-14} \sigma_{Fhub}^{4.65}, \qquad V \geq V_{rated} \qquad \text{(3-22)}$$

$$D = 1.58 \cdot 10^{-14} \sigma_{Fhub}^{4.44}, \qquad V < V_{rated} \qquad \text{(3-23)}$$

The two sets of data (below and above rated speed) appear to be clearly separated, and the 10-minute damage is significantly higher at high wind speed. For the same value of the hub force standard deviation, the resulting damage could be 10 times higher depending on the turbine control system. Below V_{rated}, the turbine blades are not pitched, and the load acting on the structure will follow the wind speed. With high turbulence intensity, this can result in large variations of the load as the wind speed varies a lot during a 10-minute period, but with a low frequency. When the wind speed is in average above V_{rated}, the turbine control system is enabled and optimizes the rotor speed by pitching the blade and reducing the lift (and the drag at the same time). The turbine will thus be subject to a change of the thrust load but in a much higher frequency, resulting in a higher damage.

3.4 Discussion

3.4.1 Direct monitoring results

The strain gauges located at the bottom section (1st platform above the entrance) of the tower were very effective for the calculation of the mechanical loads, as well as the fatigue loads over a period of almost three years, thanks to the robustness of the system. The combination of the SCADA data with the strain measurements also proved to be an important source of information for the understanding of the wind turbine behavior. Despite being limited by the 10-minute average the operational parameters such as the pitch angle, the rotor speed, and the power, it can shed light on some particular phenomena.

The turbine behavior during the period of blade icing was isolated from the data and compared with standard production. It revealed a reduction of the efficiency of the turbine by 25 % during this period. The turbine control system performed more erratically and generated higher loads in average above the rated speed. The additional two measurement sections provided information regarding the ice mass on the blade. The top section provided more accurate results for the study of mass imbalance, as the measured strains amplitude were larger. The measurement was also not affected by additional ice mass on the tower. A relatively high mass of ice (1.4 t/blade) was estimated which completely prevented the turbine from starting.

The continuous monitoring over a long period increases the probability of capturing rare events in a sufficient amount to be studied and automatically clustered. However, more precise data from the SCADA system is required to detect the short events responsible for the overloading of the structure. Finally, a more detailed measurement of the wind field around the turbine is required for further studies on the wind-structure interaction.

3.4.2 Safety of details

The damage on the structure was precisely computed using the relevant fatigue details and the exact tower geometry. The strong variations between different periods of the year were a result of few high wind speed events (above-rated speed) which were more frequent in winter than in summer. Emergency shut-down is so far the most damaging event, but the extremely low occurrence makes it less significant. Normal operation above the rated speed is responsible for the majority of the damage (60 %) despite representing less than 10 % of the time. The pitch control system is responsible for this increased damage.

Stress variations in the turbine walls were relatively small during normal operation (less than 150 MPa), and only a few higher cycles were neglected as they appeared within weeks (reverse loading of the turbine due to wind direction change). It was estimated that the turbine would likely experience more than $3.7\text{x}10^7$ cycles (higher than 5.0 MPa) during the 20 years of operation. Using the bilinear S-N curve method, it was estimated that the turbine would only reach 12 % of the fatigue life, while a more conservative calculation with a single slope S-N curve would indicate 24 % after 20 years. The damage computed with 10-minute strain series is 10 % lower than the damage computed with 24-hour strain series. The partial safety factor highly influences the estimated damage. For instance, the partial safety factor with a value of $\gamma_{Mf} = 1.15$, increases the damage by 51 % and 71 % for the linear and the bilinear S-N curve, respectively.

Results from the monitoring campaign performed within the research project HISTWIN show similar results (Rebelo, Veljkovic, Matos, et al. 2012). Strain measurements in conventional M36 and M42 class 10.9 bolts show very small stress variations. The overall fatigue verification performed results in a predicted lifetime of 51 years with the most unfavorable situation ($\gamma_{Mf} = 1.35$). With 159 days of measurement, they obtained an average 10-minute damage of D = $7.4\text{*}10^{-4}$.

For relatively low deformations, no failure should be expected from the bolted connections. In case of higher damage to the welded detail, the bolted connections could be checked as well. Regular maintenance and possible bolt replacement keep this detail safe. Finally, it must be noted that the studied wind turbine is located in a relatively non-aggressive environment and is mainly subject to long periods of cold temperatures and icing. For WTs located near the shore or offshore, the problematic of corrosion should be included. The potential corrosion and fatigue corrosion of the bolds as well as the probable deterioration of the concrete foundations should be considered.

3.4.3 Comparison with aero-elastic simulation tools

This study focuses on the monitoring and the use of monitored data. Complete simulation of wind turbines requires the use of complex aero-elastic simulation tools, such as FAST. Simulations were performed using a modified version of a 1.5 MW baseline turbine available in this software, with the correct geometry of the tower. However, the number of unknown parameters is too important to reproduce the measured data successfully. The aerodynamics of blades and more importantly the blade pitch control system are the main parameters affecting

the turbine response. Without any information regarding the blades and the pitch control system, results from the simulation were too biased to offer any proper comparison. In this case, the direct monitoring approach is preferred as it removes the uncertainties from the simulation and gives the real induced action effects.

3.5 Conclusions

This chapter presents the results of a long-term monitoring on a wind turbine for the evaluation of the wind loading effects and for the fatigue safety verification. The following conclusions can be drawn from this study:

1. Results from the measurement campaign clearly demonstrate that WT towers service duration can be extended safely beyond 20 years using a simple, robust, and economic monitoring system. Extending the service duration beyond 20 years allows to continue to safely produce energy with existing wind turbine towers while enhancing the sustainability of the WT.

2. The high reliability of the recorded dataset allowed for the precise evaluation of the wind loading effects on the tower, as temperature and long-term effects were absent from the strain signals.

3. The direct measurement of the strains allowed to the realistic examination of the fatigue damage endured by the wind turbine tower and provided a reliable alternative to aero-simulation tools on generic turbine models which are usually necessary to estimate the fatigue loading.

4. The use of the SCADA data in combination with the monitoring system provided useful information regarding the contribution of environmental and operational parameters on the turbine behavior. In particular, the effect of icing on blades was presented.

5. Most of the damage occurs during normal production above the rated wind speed and storms. Damage could significantly be reduced without loss of power production by improving the emergency shut-down procedure and optimizing the active pitch control algorithm.

6. Monitoring provides a reliable estimation of the endured wind induced action effects and future service duration of WT towers because the *in-situ* wind regime, resonance phenomena, transient, and extreme events, as well as various failures in the control system, are explicitly considered. Actual design codes are too conservative, and the design assumption of a 20 year-service life should be altered.

4 Wind turbine extreme loads and their statistical extrapolation from monitored data

4.1 Introduction

The estimation of extreme wind turbines loadings has been of an increasing interest in recent years, as the current version of the IEC standards (IEC 61400-1 2005) requires statistical extrapolation of loads to predict the 1-year and the 50-year return levels of wind turbine rotor and tower loadings. Nowadays, this statistical extrapolation can be performed on either in-situ measured data obtained from certification measurements or longer monitoring campaigns, but also from simulated data. Measurement campaign performed on research facilities (test field with prototype turbines) remains expansive since they include a large number of sensors distributed on several turbines and met masts. Data can be available for research under restrictive conditions. Researchers must often work with a limited amount of data as the recorded times series are not necessarily of interest for their studies. The quality of the data is also a concern.

Because of the lack of quantity and reliability of in-situ measured data, most of the extrapolation procedures are performed on simulated data. They are indeed readily available with actual simulation capabilities and the relatively easy use of such simulations tools. Again, limitations occur with simulated data, since many assumptions must be made about the wind turbine control system, the blades geometry and aerodynamic profile, and the generated stochastic wind field. Despite the constant improvement and complexification of aeroelastic simulations, errors and biases are numerous. Performing comparison between numerical simulations and in-situ measured loadings is even more complicated, as the number of parameters involved is very high and cannot be entirely satisfied. However, collecting quality data is extremely important to improve aeroelastic models. The Vestas V90 (and similar design) used in this study is widely spread around the globe, and its location in the Juvent SA wind farm is also of interest as many other teams have been studying its structural behavior or its surrounding wind field.

This chapter aims to provide a clear methodology for the extrapolation of extreme values (EV) based on a broad set of reliable data of 604 days of measurement of the tower deformations. The first part of this work gives an update on the methods and procedures related to load extraction with the Block Maxima Method (BMM) and the Peak-Over-Threshold (POT) method. The monitoring period was sufficiently long to provide a measurement of both extreme and accidental loads that are rarely observed outside of specific certification tests. The limitations of the BMM with short-term and long-term extrapolation procedures are evaluated and compared with the POT. The POT method in combination with the Generalized Pareto (GP) distribution is studied in detail, as it provides the most relevant results. The appropriate statistical distribution, fitting method, and goodness of fit criterion are evaluated. Finally, recommendations about the required measurement length for extreme predictions are given.

4.2 Extreme values extrapolation

The IEC standards (IEC 61400-1 2005) require statistical extrapolation of loads to predict the 1-year and the 50-year return levels of wind turbine rotor and tower loads but do not provide a

detailed extrapolation procedure. The designer must select the choice of the extreme loads extraction method, the statistical distribution, and the fitting method. Several studies already compared different fitting methods and various statistical distributions. The overall method for load extrapolation focuses on two approaches: "fitting before aggregation" and "aggregation before fitting".

4.2.1 Extraction of extreme wind loads

Maximum loads are extracted from measured or simulated time series using either BMM or the POT method. The main assumption for the extreme load extrapolation is the statistical independence of the maxima. The BMM is the easiest method as the maximum of each available 10-minute load time series is extracted. These 10-minute intervals can, however, provide maximum values that are statistically dependent. The artificial separation of the 10-minute blocks can give two extreme values from the same event. To avoid such situation, the time separation between two events should be checked, and one of the value can be replaced by another extreme value that does not lie between a selected amounts of rotor revolution.

On the other hand, the POT method extracts all the values that exceed a carefully defined threshold. To ensure the statistical independence of the maxima, a minimum time between two peaks must be respected. Some recent recommendations (IEC 61400-1 2005) suggest a minimum time of 3 response cycles (about 11.1 seconds for the Vestas V90 tower 1st mode) or a certain amount of rotor revolution; *i.e.*, 5 rotor revolutions were found to be a reasonable choice (Freudenreich and Argyriadis 2007; Lott and Cheng 2016). The advantage of the POT is that several peaks can be extracted from a single 10-minute series and sometimes none when the load level is relatively low.

The POT requires an appropriate threshold. This threshold can be set for each wind speed bin or for the complete set of data if the wind speed information is discarded. The threshold must be selected with great care since a too high threshold could lead to an excessively reduced set of data and therefore a significant variance in the estimators, whereas a too low threshold is likely to compromise the wellness of the selected distribution. For each wind speed bin, a similar threshold must be chosen. A convenient way is to compare thresholds based on the mean value of the time series (μ) and a certain number of times the standard deviation (σ). Standards values of $\mu + 1.4\sigma$, $\mu + 2.0\sigma$ et $\mu + 2.5\sigma$ are often selected (Agarwal and Manuel 2008; Lott and Cheng 2016). However, it is recommended to perform a complete evaluation of the threshold impact on the extrapolated values and search for an "optimal" threshold. The threshold is for example defined as a percentage of the maximum recorded load and some goodness-of-fit criterion are evaluated to select the most appropriate threshold (Ragan and Manuel 2008). Finally, another approach makes it possible to visually detect a threshold out of an empirical distribution (Grigoriou 2015).

Figure 4-1 shows an example of the high-resolution wind load of three consecutive 10-minute time series with an average wind speed of 16 m/s and a turbulence intensity of 19 %. On Figure 4-1(a), the 10-minute block maxima and the 1-minute block maxima are highlighted, whereas Figure 4-1(b) shows the extracted peaks according to three different thresholds and a minimum time between peaks of five rotor revolution (5P ~20 s). The number of extracted extreme values

varies a lot depending on the method and the selected threshold. For the BMM, 3 and 30 values are selected for the 10 and 1-minute block, respectively. Meanwhile, the POT method selects 38, 24, and 11 extreme values for thresholds being $\mu + 1.4\sigma = 221.6\ kN$, $\mu + 2.0\sigma = 248.4\ kN$, and $\mu + 2.5\sigma = 270.7\ kN$, respectively. However, this threshold selection method is based on the SCADA values of the 10-minute average wind speed. As already mentioned, the measured wind speed with the turbine anemometer is subject to large uncertainties and could lead to an incorrect selection of the extreme values.
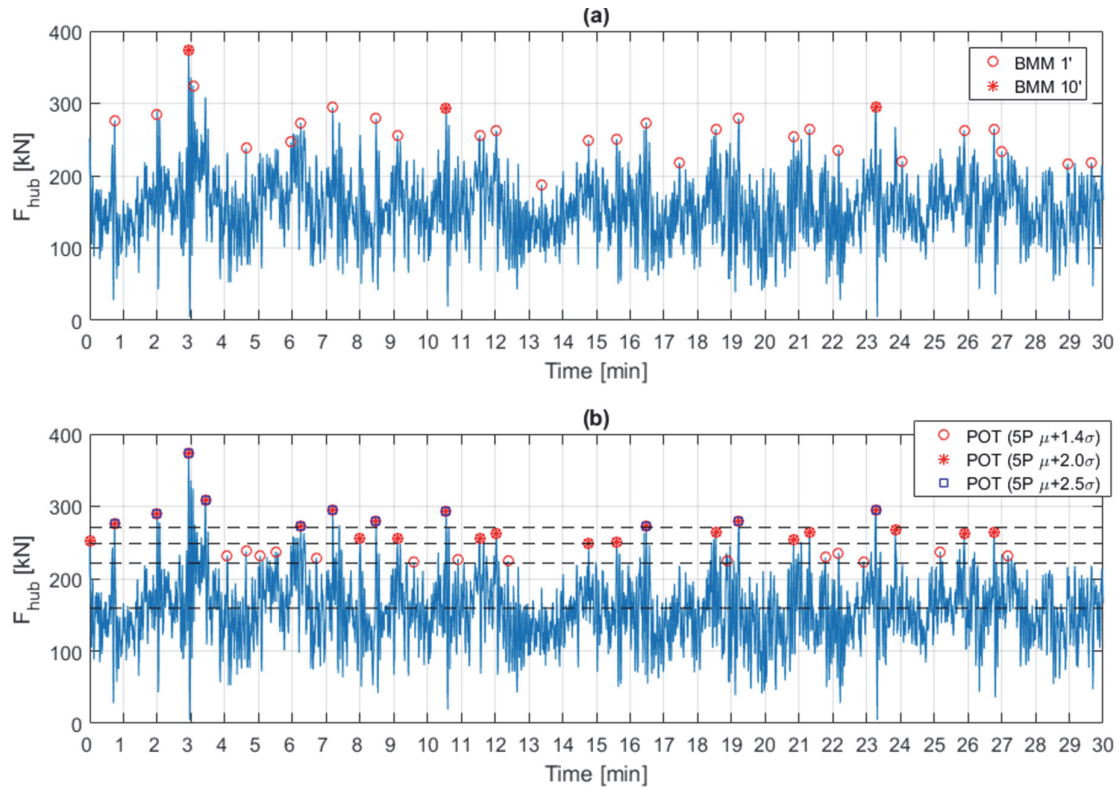
Figure 4-1.Comparison of the extracted extreme loads for the (a) BMM and (b) POT on a 30 minutes hub force signal.

4.2.2 Short-term extrapolation

First, a short-term extrapolation is performed on the dataset. For each binned 10-minute average wind speed (usually a bin of 2.0 m/s is selected), the corresponding 10-minute maximum forces are modeled with a probability distribution. The commonly used distribution for the short-term extreme load distribution $F_{short}(L|v)$ conditional to the wind speed bin v are (Peeringa and Bierbooms 2013):

- Gumbel distribution;
- 3-parameter Weibull distribution;
- Generalized Extreme Value distribution (GEVD);
- Generalized Pareto Distribution (GPD);

81

- Log-Normal distribution;
- Gamma distribution.

The distributions with three parameters are typically defined by a scale parameter σ, a location parameter μ, and a shape parameter ξ. The probability distribution is plotted against an empirical distribution. The maxima of the time series are ordered with the smallest maximum having a value of $i = 1$, the largest with a value of $i = N$, and N being the total number of extracted maximums. The following empirical probability is assigned for the ordered maxima:

$$p_i = \frac{i}{N + 1} \tag{4-1}$$

The extreme data (x_i, y_i) points are plotted on a Gumbel probability paper, where x_i is an arbitrary values vector and the standard extreme variate (SEV) of the inverse Gumbel cumulative distribution (CDF) is given by:

$$y_i = -\ln\left(-\ln\left(F^{-1}(x_i)\right)\right) \approx -\ln(-\ln(p_i)) \tag{4-2}$$

The GEVD is a well-established distribution used to model extreme natural phenomena, such as flood levels and wind gusts. Its CDF is defined as (Coles 2001):

$$F_{GEV}(L|v; \sigma, \mu, \xi) = \begin{cases} \exp\left[-\left[1 + \xi\left(\frac{L-\mu}{\sigma}\right)\right]^{-\frac{1}{\xi}}\right], & \xi \neq 0 \\ \exp\left[-\exp\left[-\left(\frac{L-\mu}{\sigma}\right)\right]\right], & \xi = 0 \end{cases} \tag{4-3}$$

where σ, μ, ξ are the scale, the location and the shape parameters respectively and such as $-\infty < \mu < \infty, \sigma > 0$ and $-\infty < \xi < \infty$. The shape factor ξ defines the GEVD with a type I (Gumbel) when it reaches 0, a type II (Fréchet) when $\xi > 0$, and a type III (reversed Weibull) when $\xi < 0$.

However, studies showed that the Log-Normal, the 3-parameter Weibull, and the gamma distributions give more realistic values when the GEV and the Gumbel distributions seem to lead to too conservative results (Freudenreich and Argyriadis 2007; Ragan and Manuel 2008; Lott and Cheng 2016).

$$F_{Lognormal}(L; \sigma, \mu, \xi) = \begin{cases} \Phi\left(-\frac{\ln(1-\frac{\xi(L-\mu)}{\sigma}}{\xi}\right), & \xi \neq 0 \\ \Phi\left(\frac{\ln(L)-\mu}{\sigma}\right), & \xi = 0 \end{cases} \tag{4-4}$$

Where Φ is the cumulative distribution function of the standard normal distribution.

$$F_{Weibull3}(L|v; \sigma, \mu, \xi) = 1 - \exp\left[-\left(\frac{L-\mu}{\sigma}\right)^{\xi}\right], \qquad L - \mu, \sigma, \xi > 0 \tag{4-5}$$

$$F_{Gamma}(L|v; \sigma, \mu, \xi) = \frac{\gamma\left(\xi, \frac{L}{\theta}\right)}{\Gamma(\xi)} \tag{4-6}$$

Finally, the Generalized Pareto Distribution can be used. It was demonstrated that it is an appropriate distribution for exceedance over a threshold just as the GEV is an appropriate distribution for global maxima. The Generalized Pareto (GP) family and the GEV family are closely related as they share the same shape factor ξ. The CDF of the GPD is defined as (Coles 2001):

$$F_{GPD}(L|v; \sigma, \mu, \xi) = \begin{cases} 1 - \left[1 + \xi\left(\dfrac{L-\mu}{\sigma}\right)\right]^{-\frac{1}{\xi}}, & \xi \neq 0 \\ 1 - \exp\left[-\left(\dfrac{L-\mu}{\sigma}\right)\right], & \xi = 0 \end{cases} \tag{4-7}$$

The case of $\xi = 0$ coincides with a shifted exponential distribution. Scale and shape parameters are defined for $\sigma > 0\ and -\infty < \xi < \infty$, respectively. Despite its strong theoretical foundation, the GPD has not been used to extrapolate structural loads on wind turbines. The 3-parameters Weibull was preferred as it offers one extra parameter that provide a greater fitting flexibility than the GPD.

Finally, for short-term extrapolation, the probability of exceedance of a specific load l conditional to the wind bin v is:

$$P(L > l|v) = 1 - [F_{local}(l|v)^{n(v,T)}] \tag{4-8}$$

with $n(v, T)$ is the average expected number of local maxima during the observed period (i.e. mean crossing rate). In wind energy, the 10-minute period is commonly used for load calculation. Thus:

$$P(L > l|v) = 1 - F_{short}(l|v) \tag{4-9}$$

4.2.3   Long-term extrapolation

After computing the individual short-term distribution for each wind speed bin, the long-term exceedance probability is calculated by integrating the conditional short-term distribution with the wind speed pdf $p(v)$

$$P(L > l) = \int_v P(L > l|v) \cdot p(v)dv \tag{4-10}$$

Finally, when only the extreme loads are considered during production range (between v_{in} and v_{out} so that $F(l|v \leq 4.0\ m/s)$ and $F(l|v \geq 20.0\ m/s)$ are taken equal to 1, Equation (4-10) becomes for the BMM:

$$P(L > l) \approx \sum_{v_{in}}^{v_{out}} \left(1 - F_{short}(l|v)\right) \cdot \frac{p(v)}{\sum_{v_{in}}^{v_{out}} p(v)} \tag{4-11}$$

And the POT method:

$$P(L > l) \approx \sum_{v_{in}}^{v_{out}} \left(1 - [F_{local}(l|v)^{n(v,T)}\right) \cdot \frac{p(v)}{\sum_{v_{in}}^{v_{out}} p(v)} \qquad (4\text{-}12)$$

This procedure is called the "fitting before aggregation". The other option, "aggregation before fitting", is to determine a long-term distribution regardless of the wind speed and only take the maximums wind loads.

Thus the 10-minute SEV of the BMM for a 50-year return period is equal to:

$$Y_{50} = -\ln\left(-\ln\left(1 - \frac{10}{50 \cdot 365.25 \cdot 24 \cdot 60}\right)\right) = 14.8 \qquad (4\text{-}13)$$

4.2.4 Fitting method

After choosing the most appropriates distributions, a fitting method must also be selected as they also influence the extrapolated values. The commonly used methods are the method of moments, the maximum likelihood, and the least squares method. A number of diagnostic checks can then be performed to validate the choice of the distribution. For the evaluation of the goodness of fit, one can, for example, use the Chi-squared or Kolmogorov-Smirnov tests and plot quantiles-quantiles plots (Q-Q-plots) or a similar probability-probability plot (P-P-plots). For Q-Q-plots, the graph of the quantiles of a specific distribution is plotted against the corresponding quantiles of the observed data. If the observations follow the selected distribution, the resulting plot should be close to a straight line. However, a visual inspection is always mandatory to judge the goodness of fit.

4.3 Database for load extrapolation

The measurement campaign carried out on the Vestas V90 n°10 of the Juvent SA wind farm from December 2014 to April 2017 is used in this chapter. A large set of reliable data – 604 days of measurements – of the tower loads is used, which represents a total of 86'976 10-minute series. The resultant hub force is obtained from two strain signals measured at a frequency of 20 Hz in two perpendicular directions at the tower's first platform location, at 7.80 m higher from the foundation. This hub force is proportional to the resultant tower base bending moment; it was preferred to speak of the equivalent wind force that leads to the tower base bending moment.

The measured loads were processed and carefully checked according to the procedure developed in chapter 2. Therefore, the totality of the measured data set is considered as valid and used in this work. The SCADA data is also available. However it contains uncertainties, as the wind speed measurement is affected by the rotor. 2.09 % of the SCADA data are not available over this period.

Figure 4-2(a) shows the maximum hub forces extracted every hour – 10-minute maximum would make an unreadable plot. The corresponding histogram (this time based on 10-minute maximums) of the wind load in Figure 4-2(b) shows some distinct modes. The first peak of 10-30 kN represents the idling/parked state of the turbine in which only the nacelle mass produces

a constant moment over the tower height. This is not strictly speaking a wind load. The second large peak between 30 and 90 kN represents maximum loads occurring mainly during low wind speeds (4-7 m/s). This wind range, despite the fact that it represents the majority of the time, does not produce any extreme loads. While applying the "fitting before aggregation" method, one must be careful that the low wind speed bins do not dominate the extrapolation and that the asymptotic behavior of the selected distribution does not overestimate the long-term extrapolation. The last peak around 280 kN appears because above 10-12 m/s of wind speed (the rated speed), the average maximum load tends to stabilize and the standard deviation tends to increase with the wind speed. This behavior is clearly visible in Figure 4-2(b) when the average wind force decrease after 10 m/s (Figure 4-2 (a)). It is interesting to observe that the collected data do not suffer from any variation through time and idling or parked situations remain in a very close interval, regardless of the seasonal changes or temperature effects. Finally, Figure 4-2(d) focuses on the right tail of the global distribution. This part of the histogram regroups the wind loads with an average wind speeds higher than 10 m/s.
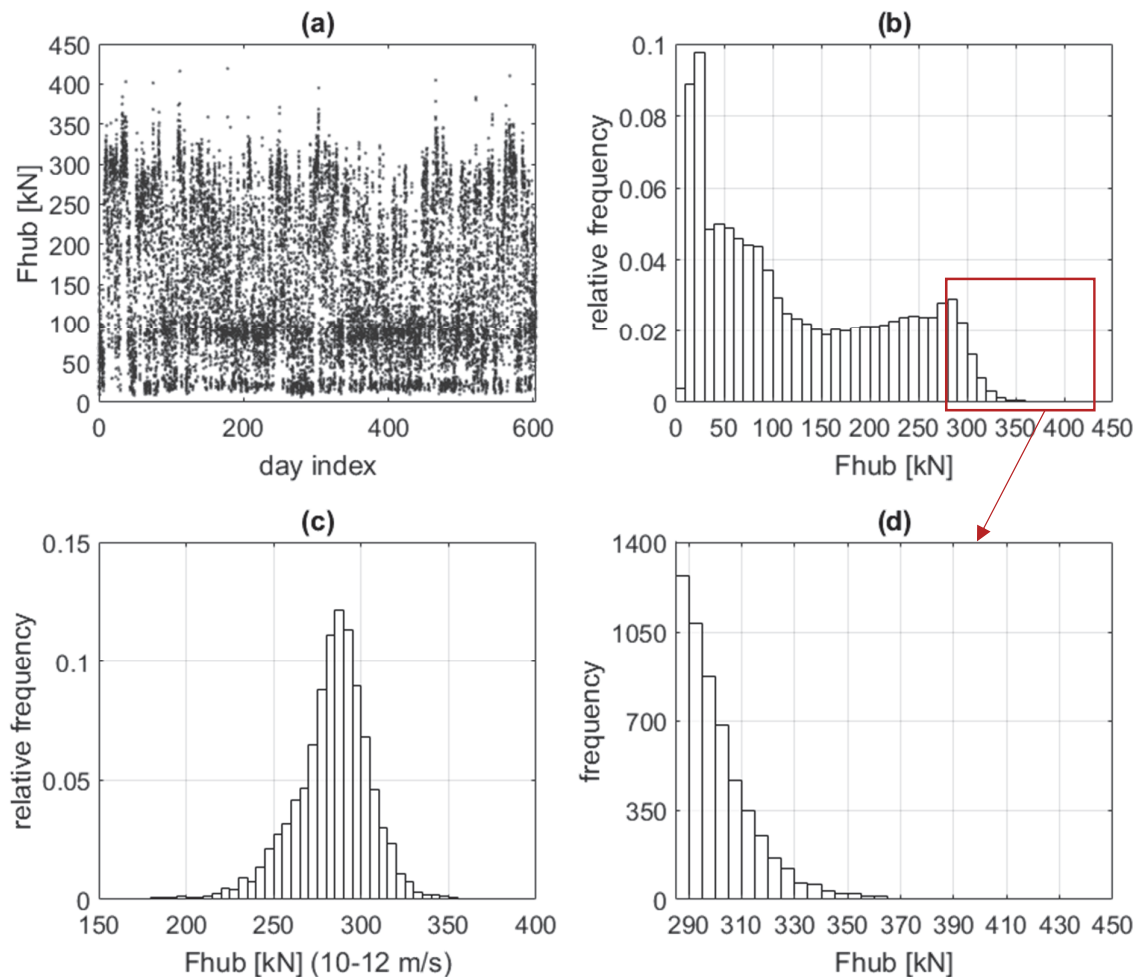
Figure 4-2. (a) 1-hour maximum wind load over the 604 days of measurement. (b) Histogram of the 10' maximum wind load. (c) Subset histogram of the 10-12 m/s mean wind speed bin and (d) zoom on the extreme values region.
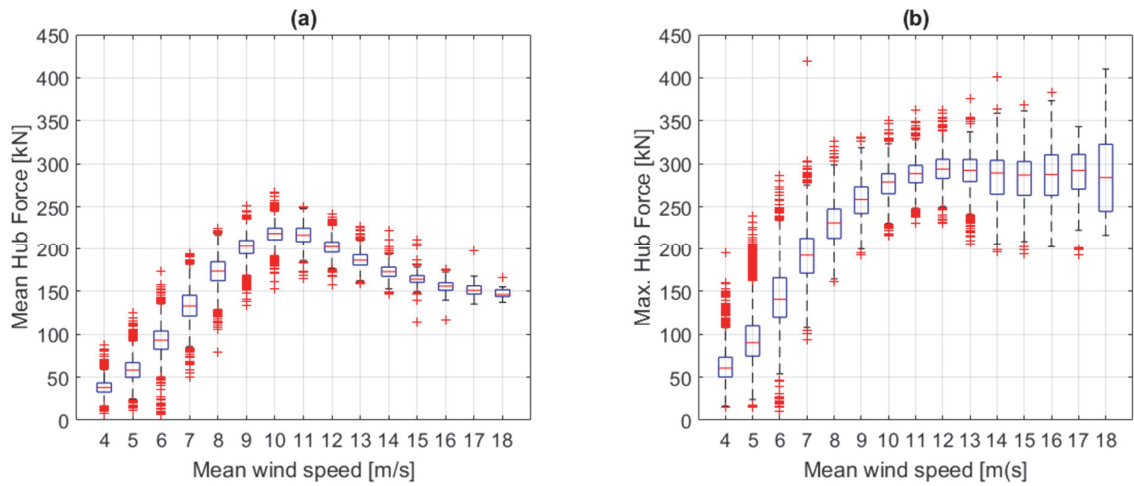
Figure 4-3. Distribution of wind loads as a function of the wind speed during normal production condition. (a) 10-minute average hub force and (b) 10-minute maximum hub force.

The Figure 4-4 below resumes the collected database (using the 10-minute BMM) for load extrapolation according to the binned wind speed. The number of 10-minute series rapidly decreases with the wind speed, down to a point where it becomes problematic to fit a proper distribution.
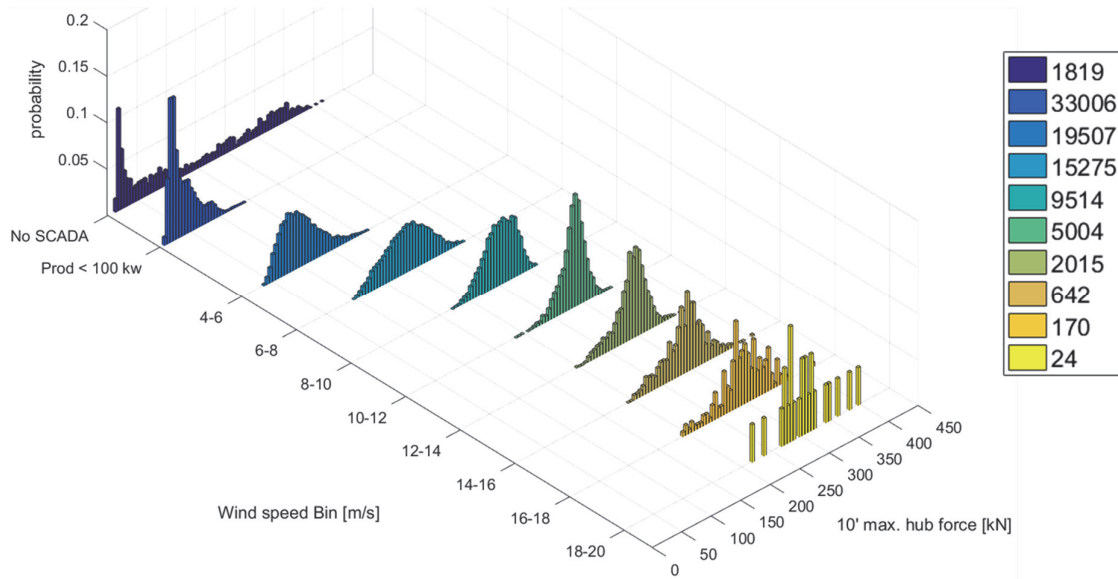
Figure 4-4. Database of the 10-minute resultant hub force binned according to the hub-height 10' average wind speed.

The database created from the POT method and a time separation of 20 seconds between peaks (5 rotor revolutions) is not plotted against the wind speed as it was chosen to be studied without the uncertainties related to wind speed measurements. The few peaks extracted from the same 10-minute window can correspond to a large variety of wind speed that can differ a lot from the average known wind speed. The amount of extracted extreme values is largely superior to the 10-minute BMM since 3 times more data is available above 280 kN (*i.e.,* 24782 with POT

against 6771 with the 10-minute BMM). Figure 4-5 below shows the histogram (in logarithmic scale) of the peaks. Outliers are defined in this case as the few peaks that lies relatively far from the linear fit of the data and are visible on the right side of the graph. The data shows a linear relationship between the hub force and the number of extracted peaks, which indicates that a Generalized Pareto distribution will undoubtedly be the most relevant distribution for the extreme value estimation, as it is closely related to a shifted exponential distribution.
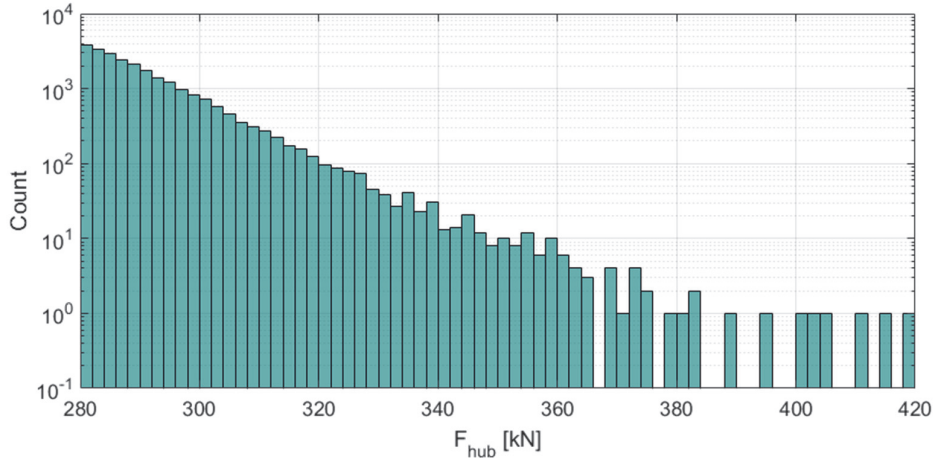
Figure 4-5. Database of extreme values obtained with the POT method.

4.4 Analysis of outliers

Extreme loads on the wind turbine tower are not the necessarily direct result of a high wind speed but rather changes in the operating condition of the wind turbine. Around the rated speed, the turbine control system starts pitching the blades to keep a constant lift force (and thus a constant rotor speed), and results in a lower thrust force (as shown in Figure 4-3(a)). However, alternating wind speeds between below and above the rated wind speed lead the controller to switch between different operating conditions, resulting in temporary higher loads due to a pitch angle lower than expected. Such short phenomena are visible with high-resolution SCADA data (Lott and Cheng 2016) but cannot be detected with only the 10-minute resolution, as these events last for less than 30 seconds.

The Figure 4-6 below shows the 10 and 2-minute windows of the two highest wind loads recorded during the measurement period. Despite having the same amplitude (419 kN measured on 19.06.2015 and 416 kN on 01.04.2015), the variations of loads are significantly different, as well as the wind conditions.

On 01.04.2015 during the event, the average wind speed was around 15 m/s when the wind speed ranged from 7 m/s to over 20 m/s. This high wind speed variation resulted in high variations in the wind loading over the 10-minute signal, between 100 kN and 250 kN. The maximum force occurs after a sudden decrease in the wind load. The amplitude of the wind speed probably decreased before sudden increasing, causing the wind turbine to operate for a small period of time at high wind speeds without the pitch angle enabled, producing the maximum thrust on the rotor. The turbine came back quickly to a normal load level, as the aerodynamic damping is larger at high wind speed. This kind of event happens regularly, but

the large peak, in this case, could be explained by the tower top displacement. Just before the large peak, the nacelle comes back to its initial position and the combined effect of the wind load with the nacelle inertia resulted in such a large tower bending.

The event recorded on the 19.06.2015 shows an entirely different story. The wind load (between 150 and 200 kN) is stable before the event and indicates a wind speed between 7.5 and 9.0 m/s, which is in agreement with the SCADA that displays wind speeds between 5.0 to 10 m/s and an average of 7.0 m/s during this period. However, the turbine suddenly enters in a period of large vibrations for about 70 seconds resulting in the maximum bending moment observed. The erratic behavior of the turbine can be the result of a fault of the controller during a wind gust. This event leads to the temporary shut-down of the turbine (visible between 5 to 7 minutes), as the internal turbine sensors measured unacceptable acceleration. The accelerations recorded by the accelerometers located at the tower top indicated peaks of 0.13 g on 01.04.2015 and 0.17 g on 19.06.2015.
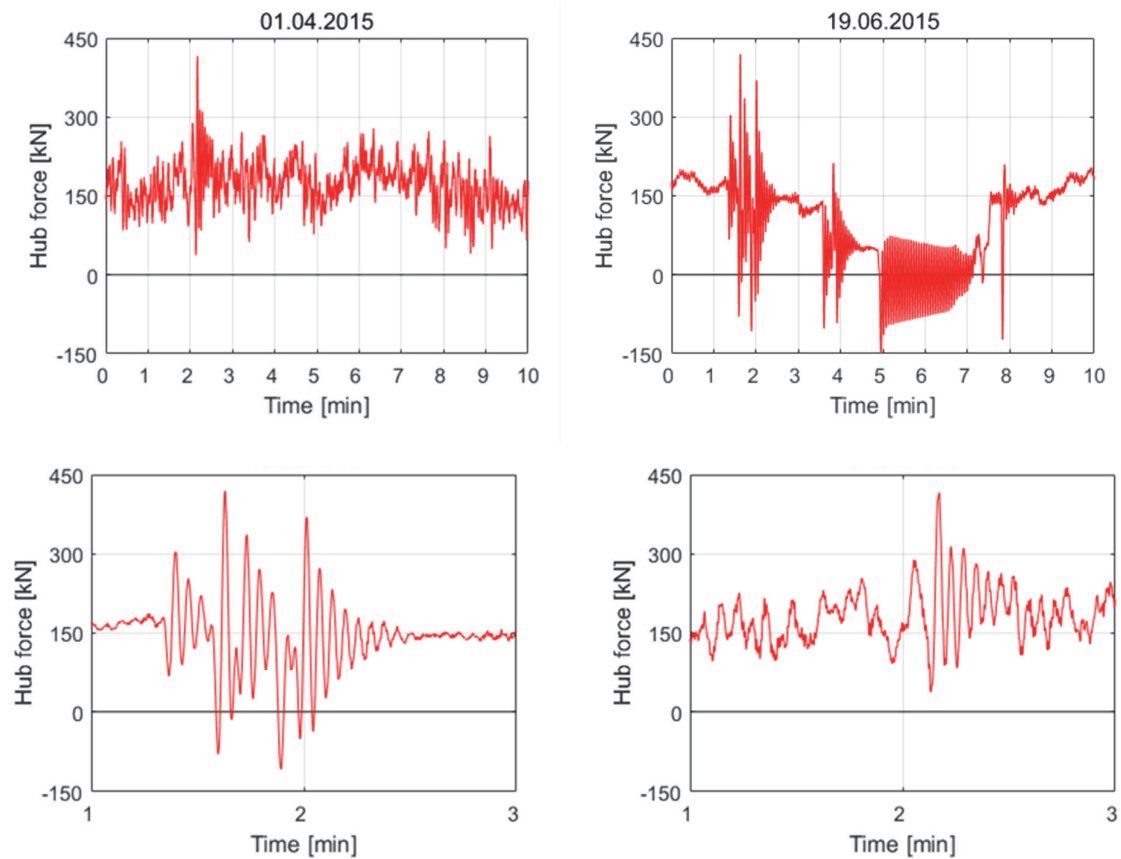
Figure 4-6. Comparison of the two most extreme events recorded during the monitoring period.

For the short-term extrapolation based on wind speed binning of the extreme forces, these two events are discarded from the dataset as the recorded load lies largely outside of the usual range of other extreme loads. This has obviously an impact on the extrapolated loads with this method.

Such events could also be shifted to another wind speed bin. However, without any high-resolution data for the wind speed, this cannot be performed in this case. For the long-term extrapolation, the maximum event occurring on 19.06.2015 will be included regardless of the wind speed.

4.5 Extreme wind load extrapolation from monitored data

4.5.1 Short-term extrapolation with Block Maxima Method

Dealing with measured data for the short-term extrapolation requires an extensive pre-processing. A first review of the database is performed to exclude outliers that do not lie in the correct wind speed bin. This is valid for high loads but also low loads that lie significantly below the usual extreme loads. Only 10-minute series with power production exceeding 100 kW are included but still for low wind speed bins some low values may remain. Figure 4-7 shows the database before and after removing the outliers. Removed low values are particularly visible for the 6-8 m/s wind speed bin.

Such out-of-range low values also affect the maximum likelihood estimator of the location parameter μ. The 3-parameter Weibull density function is positive only for $L > \mu$, which implies that the location parameter must be smaller than the minimum sample value of the dataset of the wind speed bin. Keeping low values in the data would result in an artificially shifted distribution towards zero, and consecutively minimizing the extreme values.
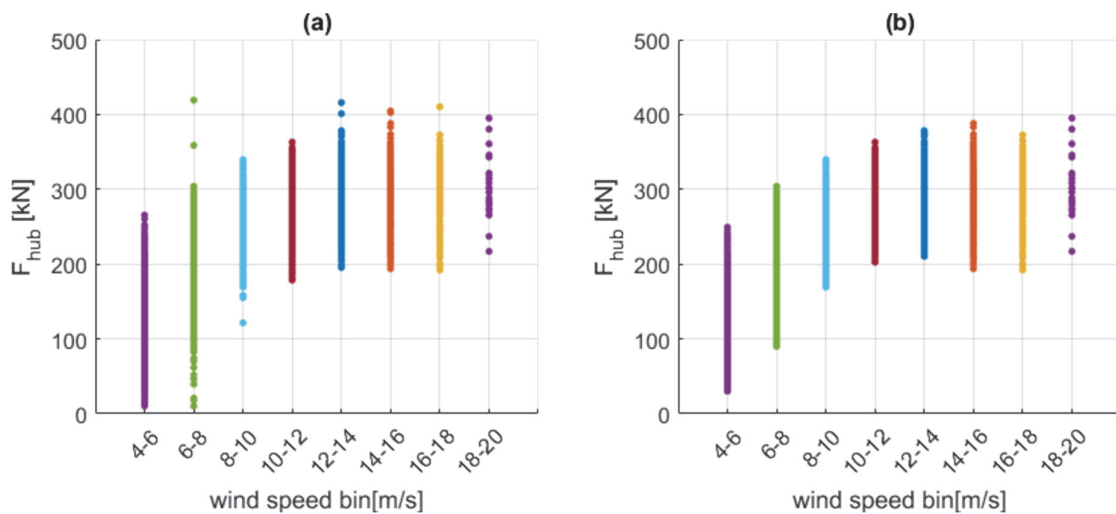
Figure 4-7. (a) Database of the tower hub force with outliers and (b) after outliers removed.

For the short-term extrapolation, three distributions are selected based on recommendations found in various studies and fitted on the 8 wind speed bins ranging from 4 to 20 m/s. The Generalized Extreme Value, the 3-parameter Weibull, and the Gamma distribution are fitted using maximum likelihood estimates (MLE). The Maximum Likelihood Method is often recommended to provide the best approximation of the measured data. Figure 4-8 shows the return level plot of each wind speed bin to the 50-year return period using the whole set of data

(604 days of measurement). The horizontal dashed line represents the 50-year SEV calculated with equation (4-13).

The first observation drawn from Figure 4-8 is that the distribution greatly influences the 50-year return value and it appears clearly that the GEV distribution is not suited for extrapolation. Except for the 4-6 m/s wind speed bin, the return level curve from the GEV distribution is asymptotic and leads to a finite value as a consequence of a negative estimator of the shape parameter ξ. Therefore, this distribution cannot be used for the 50-year extrapolation. The 3-parameter Weibull and the Gamma distribution provide a good fit, but not in every case. The 3-parameter Weibull offers a good fit for the below rated wind speeds and for the 16-18 m/s wind speed bin. On the other hand, the Gamma distribution gives a good fit for above rated speeds (10 to 16 m/s). For the last wind speed bin where only 24 peaks are available, the Gamma distribution tends to give a high value (519 kN) when the 3-parameter Weibull gives a relatively low value of 458 kN for the 50-year return value.

The evaluation process was performed for various monitoring periods and various monitoring durations. The selected distribution for each wind speed bin and monitoring duration are resumed in Table 4-1. The two 120-day periods that take place in winter (1-120 and 481-600) are similar and provide a clear distinction between wind speeds below rated and above rated with Weibull3 being preferred for below 10 m/s and the Gamma distribution for above. Except for the first period of 120 days, the 18-20 m/s wind speed did not gather enough points to fit a distribution. Between day 121 and 480, measurement was mostly performed during summer with a lower average wind speed. The stability of the extreme estimates is proportional to monitoring duration. However, starting measurement in summer would lead to different results and lower return values.

Table 4-1. Selected short-term distributions depending on the wind speed bin and the monitoring period and duration.

Wind speed Bin [m/s]	120 days monitoring periods					Increasing monitoring durations				
	1-120	121-240	241-360	361-480	481-600	120	240	360	480	600
4-6	Wbl3	Wbl3	GEV	Gam.	Wbl3	Wbl3	Wbl3	Wbl3	Wbl3	Wbl3
6-8	Wbl3	Wbl3	Wbl3	GEV	Wbl3	Wbl3	Wbl3	Wbl3	Wbl3	Wbl3
8-10	Wbl3	Gam.	Wbl3	Gam.	Wbl3	Wbl3	Wbl3	Wbl3	Wbl3	Wbl3
10-12	Gam.	Gam.	Gam.	Gam.	Gam.	Gam.	Gam.	Gam.	Gam.	Gam.
12-14	Gam.	Gam.	Wbl3	Gam.	Gam.	Gam.	Gam.	Gam.	Gam.	Gam.
14-16	Gam.	Wbl3	Wbl3	Wbl3	Gam.	Gam.	Gam.	Gam.	Gam.	Gam.
16-18	Gam.	Gam.	Wbl3	Gam.	Wbl3	Gam.	Gam.	Gam.	Wbl3	Wbl3
18-20	Gam.	-	-	-	-	Gam.	Gam.	Gam. Wbl3	Gam. Wbl3	Gam. Wbl3
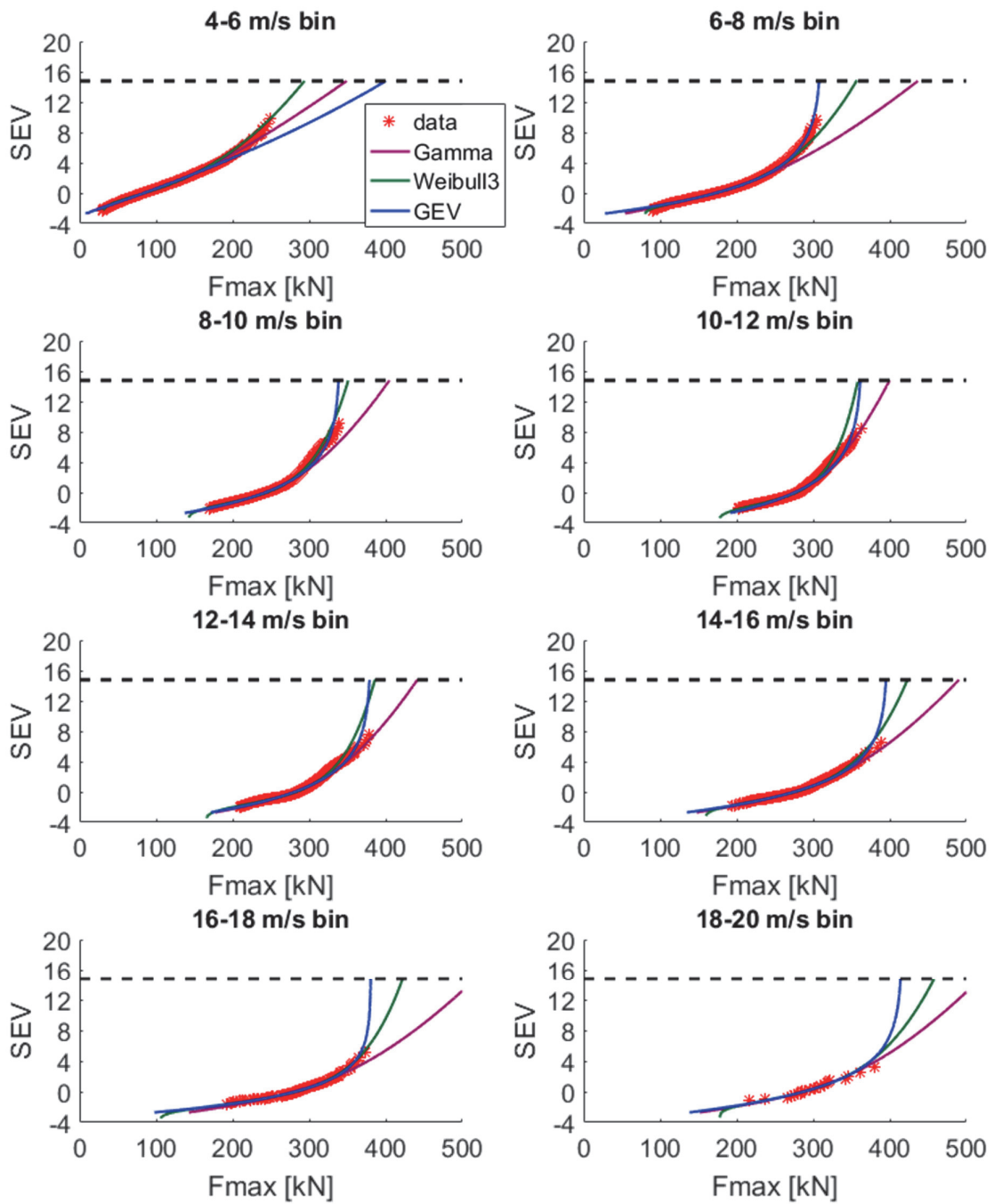
Figure 4-8. Gamma, 3-parameter Weibull, and GEV distribution fit 10-minute block maxima for different wind speed bins and for the 50-year return period extrapolation (dashed horizontal line) based on 600 days of measurement and removed outliers.

91

4.5.2 Long-term extrapolation with Block Maxima Method

The long-term extrapolation with the BMM is performed using the selected best short-term distributions (Table 4-1) for the various scenarios. The results from periods of 120 days vary between 419 kN for the 2nd period and 492 kN for the 4th period. This is surprising as the probability density function (pdf) of both periods is quite similar, and the selected distributions are identical. The difference comes from the 16-18 m/s wind speed bin. For the 2nd period (121-240 days) the 50-year return value for the Gamma distribution is 380 kN when it reaches an unrealistically high value of 642 kN during the 4th period (631-480 days). Considering the effect of the monitoring duration, between the first 120 days and the full period only an increase of 5 % is noted. This is exclusively due to the first period being recorded during an average high wind speed time. The 50-year value decreases slightly with two consecutive periods of low wind speeds before reaching the final value of 463 kN.
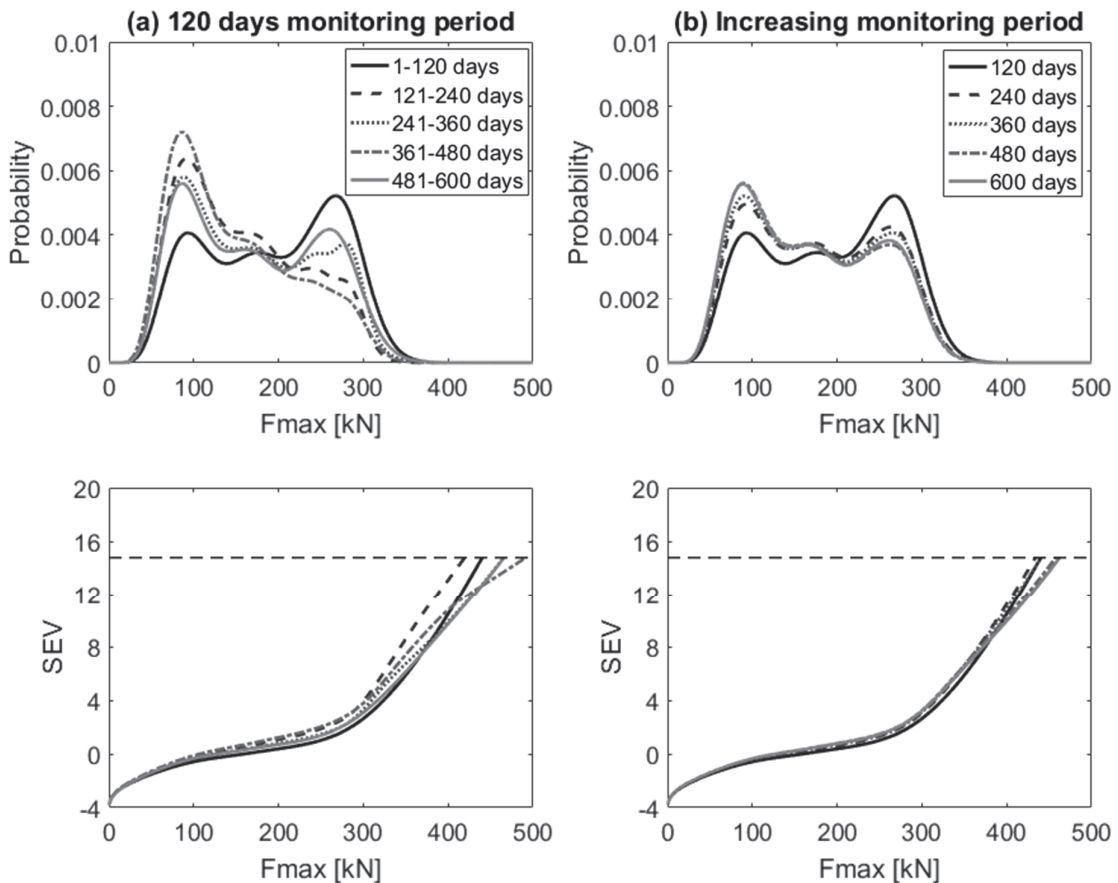
Figure 4-9. Aggregated long-term pdf and extrapolation to the 50-year return level for (a) various 120 days monitoring periods and (b) increasing monitoring period.

Figure 4-10 shows the effect of the most extreme values on the extreme value estimates in more detail. The 50-year return value is estimated every two days starting from day 15 with the best combination of distribution. Values are normalized with the maximum load ever recorded (419 kN on day 178). During the first two weeks of measurement, the wind farm was subject to a long period of icing that resulted in only low wind loads, as the turbine never really started.

After 37 days of measurements, the maximum cumulative load reached 96 % of the maximum measured load. However, the EV estimate is extremely high (around 1.4 times the maximum recorded load), mostly due to the lack of peaks in the high wind speed bins. It is only after 120 days that the EV estimate reaches a more stable value and varies between 1.02 and 1.06 of the maximum recorded load.
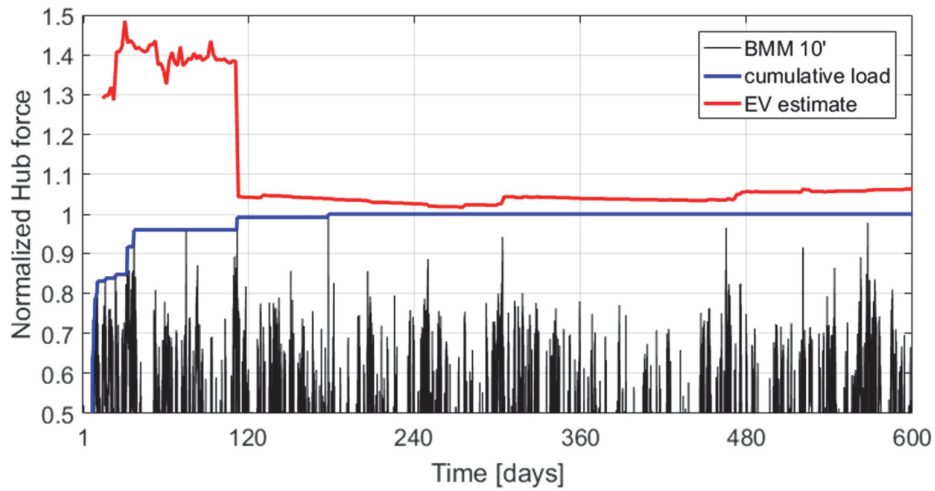
Figure 4-10. Evolution of the 50-year load extrapolation with the best combination of distributions over the monitoring length.

The effect of the outliers is also compared in Figure 4-11. For the selected distributions, the 50-year extrapolated load is only 1.3 % lower than with the outliers included. The difference is more significant in particular for the GEV and the 3-parameter Weibull (6-7 % less without outliers). Table 4-2 resumes the 50-year extrapolated loads from long-term distributions and Block Maxima Method. Employing the best combination of distributions, the extrapolated load is 9 % higher than the maximum measured load. Choosing only the 3-parameter Weibull would give the maximum measured load as the 50-year return load.
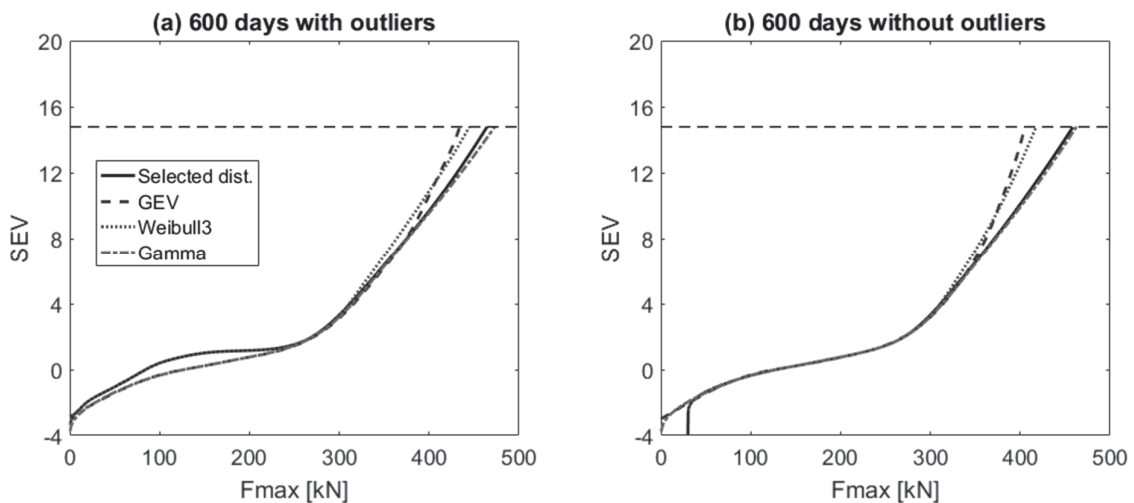
Figure 4-11. Long-term extrapolation with the "fitting before aggregation" method and BMM.

Table 4-2. 50-year extrapolated loads from long-term distributions and Block Maxima Method compared with the maximum observed normalized load.

Distributions	Outliers included		Outliers removed	
	[kN]	[-]	[kN]	[-]
Best combination	464.5	1.11	458.5	1.09
GEV	434	1.04	405	0.97
Weibull3	444.5	1.06	417.5	1.00
Gamma	473	1.13	462.5	1.10

Finally, Table 4-3 shows the probability that the extrapolated 50-year load arises from a certain wind speed bin. Results seem consistent, as high loads mostly arise from wind speed between 14 and 20 m/s. Even though the low wind speeds (< 12 m/s) were observed during 67 % of the time and the high wind speeds only 1.2 %, the probability that the 50-year return load arises from this small amount of time is more than 98 % for the best combination of selected distribution.

Table 4-3. Probability of occurrence $p(v)$ of different wind speed bins (based on a Gamma distribution) and probability that the extrapolated 50-year load arises from a certain wind speed bin.

Wind speed bin [m/s]	$p(v)$ (Gamma – MLE)	Best combination	GEV	Weibull3	Gamma
4-6	0.301	0.000	0.013	0.000	0.000
6-8	0.206	0.000	0.000	0.000	0.035
8-10	0.110	0.000	0.000	0.000	0.000
10-12	0.050	0.000	0.000	0.000	0.000
12-14	0.021	0.015	0.014	0.000	0.009
14-16	0.008	0.364	0.467	0.249	0.267
16-18	0.003	0.603	0.048	0.164	0.470
18-20	0.001	0.018	0.458	0.586	0.218

Despite the uncertainties related to the wind speed measurements, realistic estimation was obtained with BMM method under the condition that the distribution is adequately selected. The GEV distribution, in this case, results in lower than measured predictions, whereas the 3-parameter Weibull distribution alone can lead to unexpected values if the low outliers are not correctly removed from the dataset. High wind speed bins also suffer from insufficient extreme loads and a proper fitting cannot be performed. Due to the lack of high-frequency wind speed measurements, the POT method is not applied.

4.5.3 Long-term extrapolation with Peak-Over-Threshold Method

An improvement from the BMM and the "fitting before aggregation" method can be obtained by using the POT method regardless of the wind speed. Extreme loads extrapolation cannot be performed for each wind speed, but an overall 50-year return load can be estimated for the monitored turbine. The POT has the advantage of including more extreme values during time series with higher loads while less relevant loads are discarded. Estimating an extreme value without considering the wind speed benefits of few high loads that occur at high wind speed (no distribution can be fitted with confidence otherwise).

The major drawback of the POT approach is the selection of a threshold, a process that requires an iterative process. The selected threshold will depend on the amount of data (i.e., the measurement period) and influence the extreme value estimate. The goal here is to select a threshold that is not too low since it could violate the asymptotic basis of the model and lead to biased estimations. The threshold should not be too high either, where too few extreme values could lead to a high variance. For this study, only the Generalized Pareto distribution will be studied as it provides strong theoretical foundations. The 3-parameter Weibull distribution could also be used, but it lacks the theoretical justification. The only argument for its utilization is the extra location parameter that can, in some cases, take into account the skewness of the sample data.

Once a GP distribution with a selected threshold is fitted, one can estimate the return level of an exceedance probability. If a GP distribution with parameters σ and ξ is a suitable model for an exceedance of a threshold μ by a load L, then for $l > \mu$,

$$P(L > l) = \varsigma_u \left[1 + \xi \left(\frac{L - \mu}{\sigma} \right) \right]^{-\frac{1}{\xi}} \tag{4-14}$$

where $\varsigma_u = P(L > \mu) = \frac{k}{n}$ the probability of an individual load exceeding the threshold μ, with n being the number of measured10-minutes series, in this case n = 86'976 for 604 days. The exceedance on average once every m observations is the solution of:

$$\varsigma_u \left[1 + \xi \left(\frac{L - \mu}{\sigma} \right) \right]^{-\frac{1}{\xi}} = \frac{1}{m} \tag{4-15}$$

and gives,

$$x_m = \begin{cases} \mu + \dfrac{\sigma}{\xi} \left[(m\varsigma_u)^{\xi} - 1 \right], & \xi \neq 0 \\ \mu + \sigma \log(m\varsigma_u), & \xi = 0 \end{cases} \tag{4-16}$$

where $m = N \cdot n_y$, with n_y the number of observation per year and N the N-year return level.

Thus, the SEV of the POT for a 50-year return period is not constant, and depends on the probability of exceeding the threshold:

$$Y_{50} = -\ln\left(-\ln\left(1 - \frac{10}{50 \cdot 365.25 \cdot 24 \cdot 60} \cdot \frac{n}{k} \right) \right) \tag{4-17}$$

Figure 4-12 below shows the return level plot for an increasing threshold for the complete set of data (604 days, outliers included). The dashed lines represent the 95 % confidence intervals obtained with MLE. A large amount of relatively small extreme values resulting from the selection of low threshold results in a biased distribution with an unrealistically low confidence interval. Such thresholds can directly be excluded since they do not estimate a large amount of measured extreme values. On the other hand, high thresholds lead to high variance, resulting in a diverging upper confidence limit. For this set of data, visual inspection indicates that acceptable thresholds lie between 290 and 310 kN. The final threshold selection is based on diagnostic plots. The optimal threshold is chosen in this case as the value for which the sum of the mean squared error (MSE) of the Q-Q plot is minimal. It must be remembered, however, that an increasing threshold automatically leads to a lower number of data and therefore a lower sum of MSE.
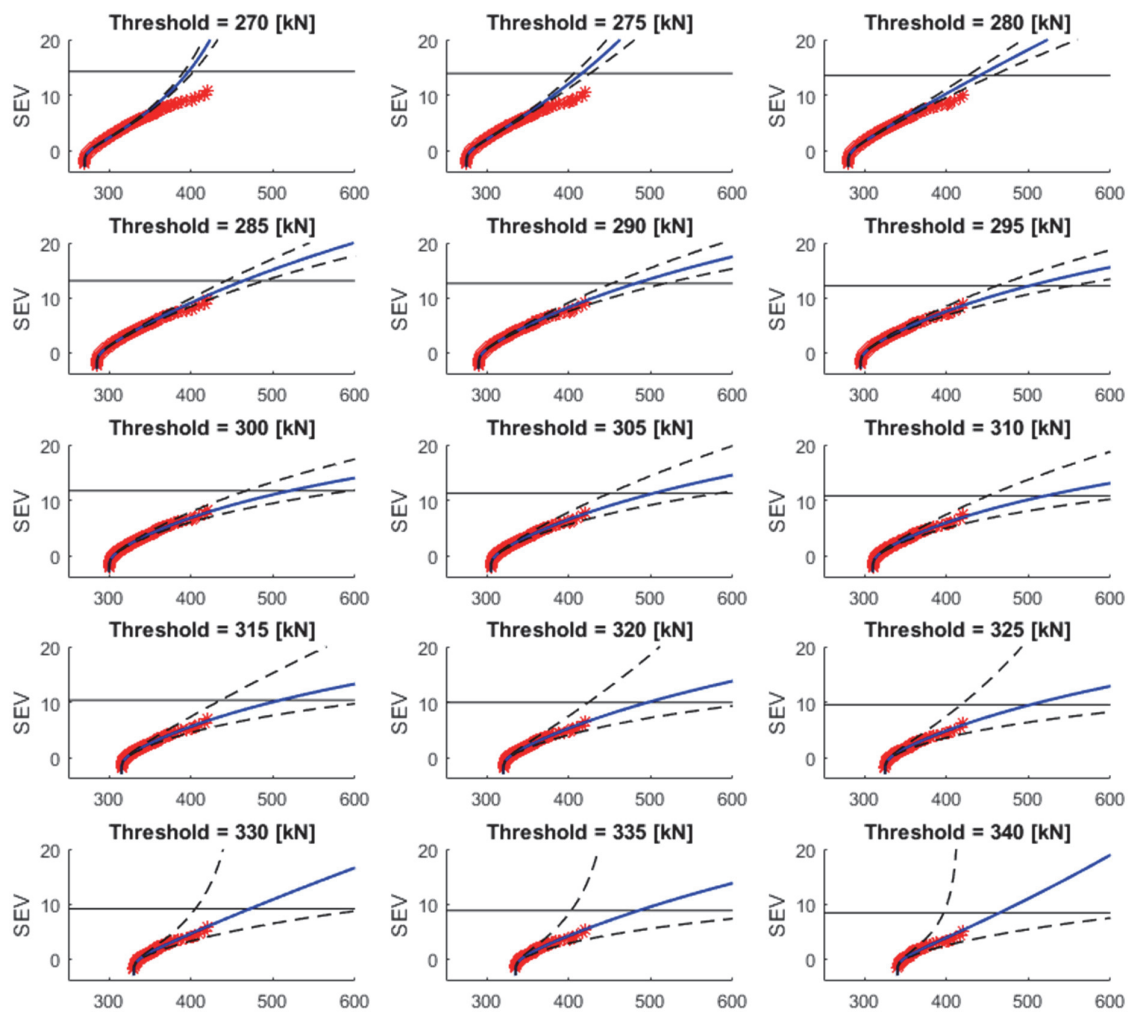
Figure 4-12. Return level plots of the GPD for various thresholds with confidence intervals and the two largest extreme events included.

96
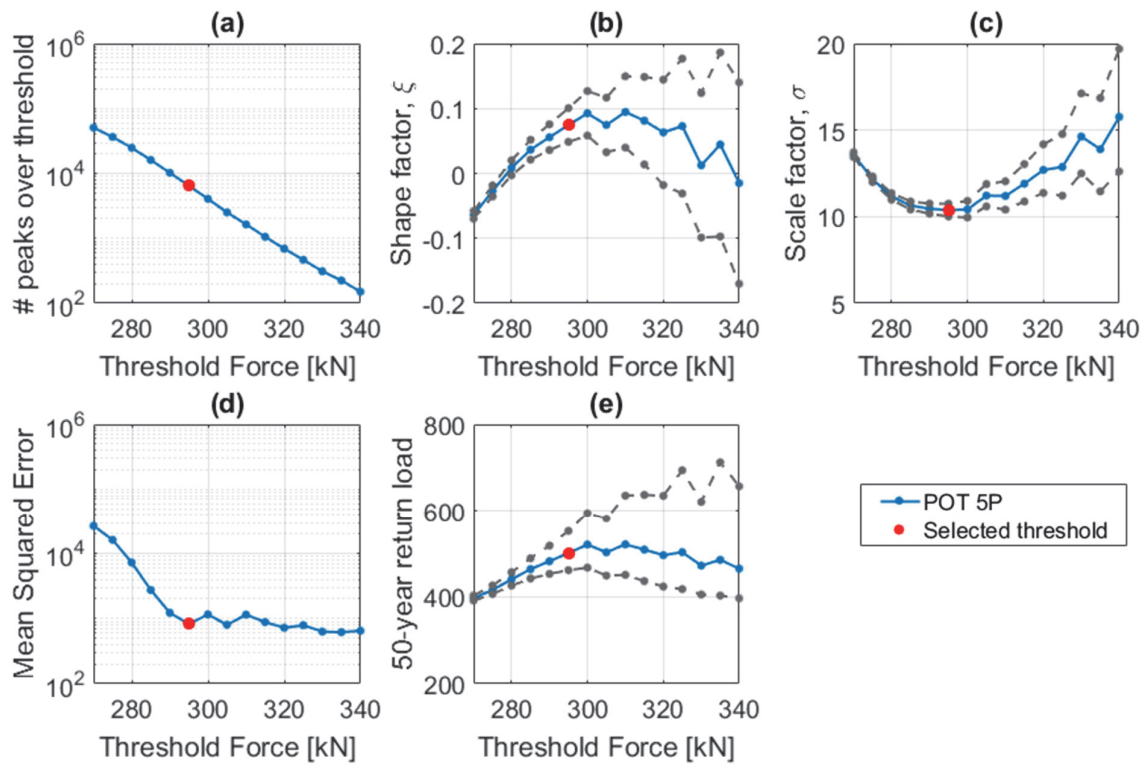
Figure 4-13. Summary of parameters for GP distribution fits with the 95 % confidence interval for the shape and scale parameters and the 50-year estimate for various thresholds.
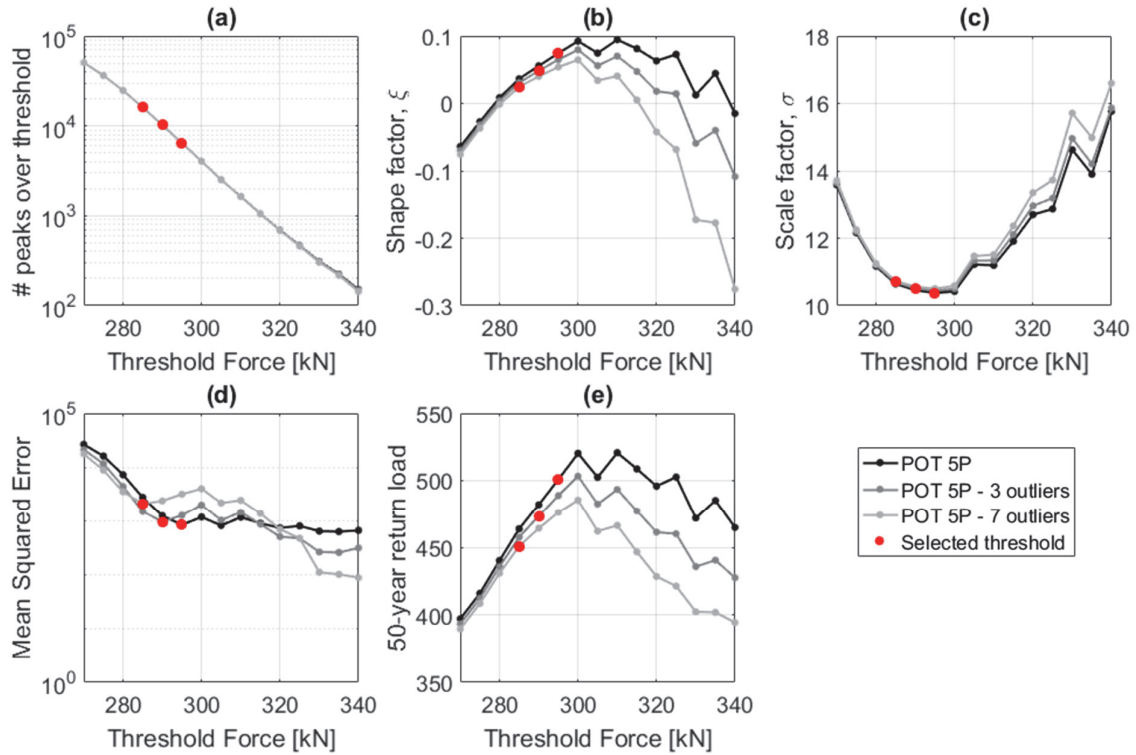
Figure 4-14. Summary of parameters for GP distribution fits for various thresholds and the effect of outliers on the threshold selections and extreme value estimates.

The evolution of the sum of the MSE for the full monitoring period is shown in Figure 4-13(d). The optimal threshold is selected as being the first local minimum of the sum of the MSE, 295 kN. Lower minimums are discarded based on the width of the confidence interval of the 50-year return values (Figure 4-13(e)) that suddenly increase. Figure 4-13(a) indicates the number of peaks over the threshold. Figure 4-13(b-c) shows the scale and shape estimates and the 95 % confidence interval.

Influence of extreme outliers on predicted extremes

Figure 4-14, on the other hand, shows the effect of the extreme values on the 50-year load extrapolation. Three scenarios are evaluated based on the POT histogram (see Figure 4-5). Two clusters of data can be easily separated from the entire population of events: the three major peaks that belong to the 410-420 kN bin and the four other peaks between 395 and 405 kN. Results clearly point a high dependency of the model to very high loads. Table 4-4 resumes the GP parameters estimates and the 50-year return values for the full sample and samples with removed extreme outliers. The sum of the MSE is calculated for data points over 320 kN to ensure a valid comparison between the three different sets of data. The selected threshold of 295 kN seems to be a robust choice, as its influence is small (less than 2 %) compared to the outliers which play a major role in the extreme value estimate.

However, there is no particular reason to remove the outliers from all data set except for the maximum event of 419.2 kN which could actually be considered as an accidental load as it clearly lies outside of its wind speed and the normal operation (see Figure 4-6).

Table 4-4. Comparison of the 50-year load extrapolation with POT and GP distribution and the effect of outliers.

	Full sample	3 outliers removed		7 outliers removed	
Threshold [kN]	295	295	290	295	285
# data points	6447	6444	10206	6440	16102
Shape, ξ	0.075	0.065	0.049	0.054	0.025
Scale, σ	10.37	10.43	10.51	10.50	10.73
$\sum$(MSE > 320 kN)	824	1248	940	3144	2073
L_{50} [kN]	500.9	488.9	473.4	476.0	450.8
normalized L_{50}	1.19	1.17	1.13	1.14	1.08

Figure 4-15 and Figure 4-16 present the diagnostic plot for the POT method for the full sample and the sample with 7 extreme outliers removed. The fit for the full sample is excellent for the GP distribution as the probability (P-P) and quantile (Q-Q) pots are linear, except a slight deviation for the highest load (the residual histogram is truncated and do not show the error of this extreme point). All of the most extreme points are included in the 95 % confidence interval.
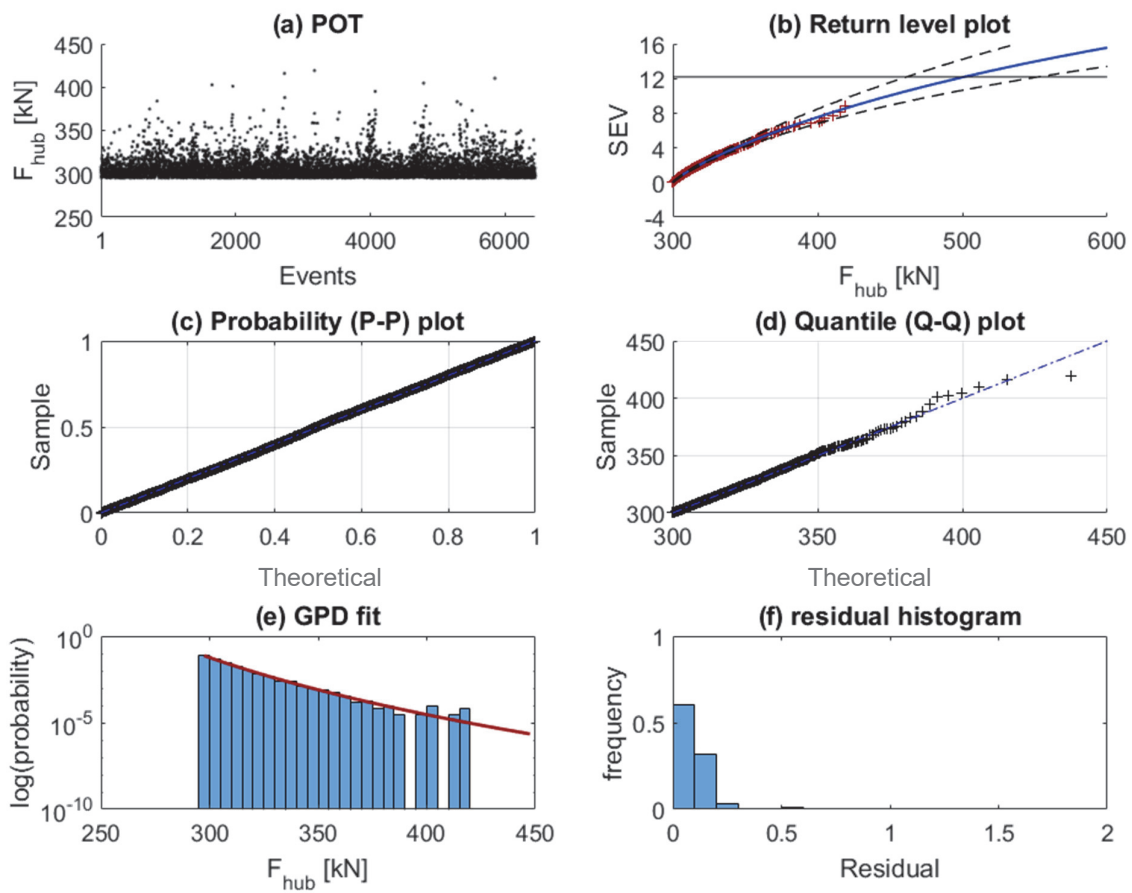
Figure 4-15. Diagnostic plots for the 50-year return value from 604 days of measurement using POT method and a threshold of 305 kN.

The diagnostic plot for the sample without the 7 most extreme recorded loads (Figure 4-16) is quite different despite having a reasonable GPD fit. The Q-Q plot shows a divergence from the linearity for the highest loads and the relatively small confidence interval is resulting from a lower threshold. This shows the singificant influence of outliers on the model.
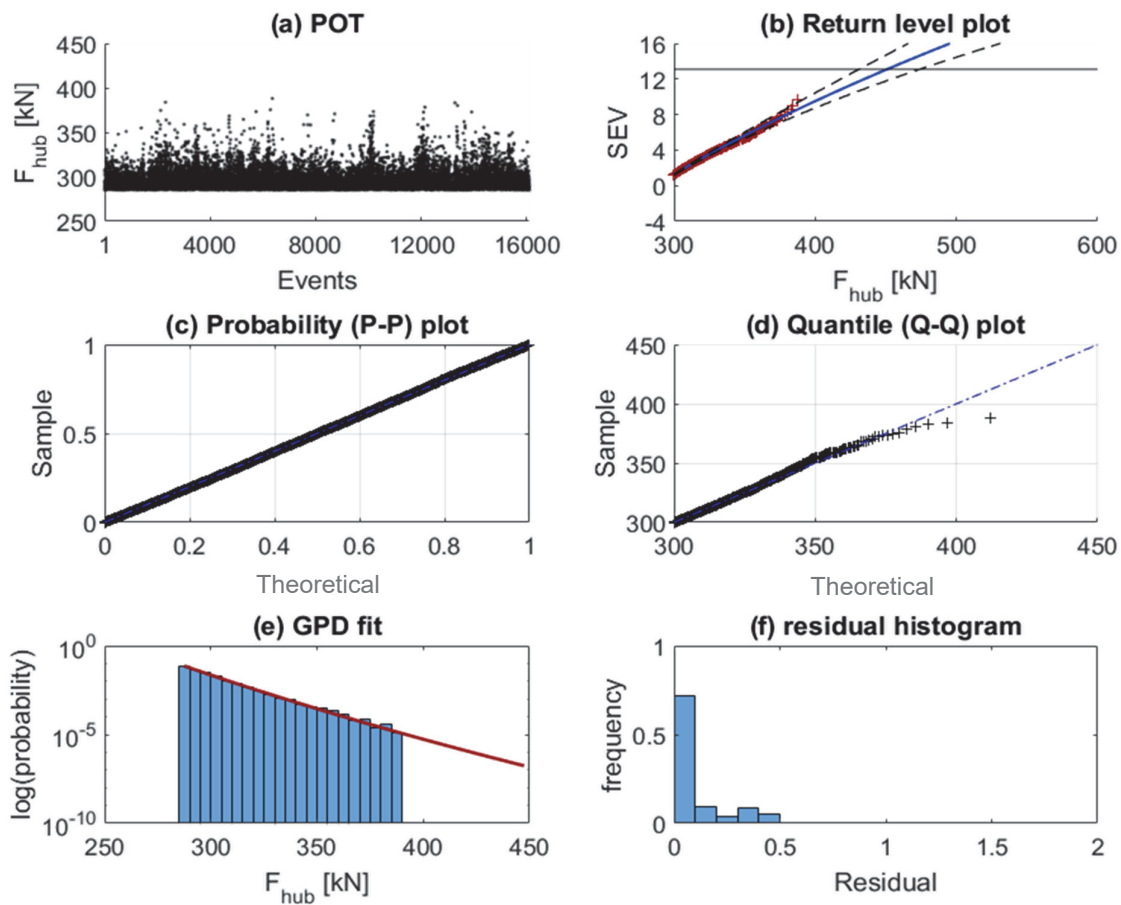
Figure 4-16. Diagnostic plots for the 50-year return value from 604 days of measurement using POT method and the 7 highest outliers removed and a threshold of 285 kN.

Influence of monitoring period and duration on predicted extremes

The monitoring period and duration can have an important effect on the load extrapolation as the environmental conditions vary over the year and high loads are more likely to be recorded during storms. The variation of the measurement period is presented in Figure 4-17. The 50-year return value is calculated for the fixed threshold of 295 kN since it seems to be the most robust value. The effects of storms or high wind speed events are easily identifiable as the number of peaks suddenly increases. The first reasonable load estimation occurs only after 38 days, as the turbine experienced icing during the first part of the measurement period and could not properly produce electricity and thus experienced normal wind loads. The fact that the measurement period started in winter strongly influenced the early age estimates. Despite the icing during the first month, the following days directly lead to a 50-year return value close to the calculated one with 600 days of measurement. However, the 95 % confidence interval width (red curve in Figure 4-17(b)) is high and will continually decrease with the increasing number of peaks (Figure 4-17(a)). The high wind speed episodes, *i.e.*, storms, induce a significant increase in the 50-year return value. The following periods of relatively low wind smoothen the 50-year estimate because the monitoring length increases without recording any new peaks.

100
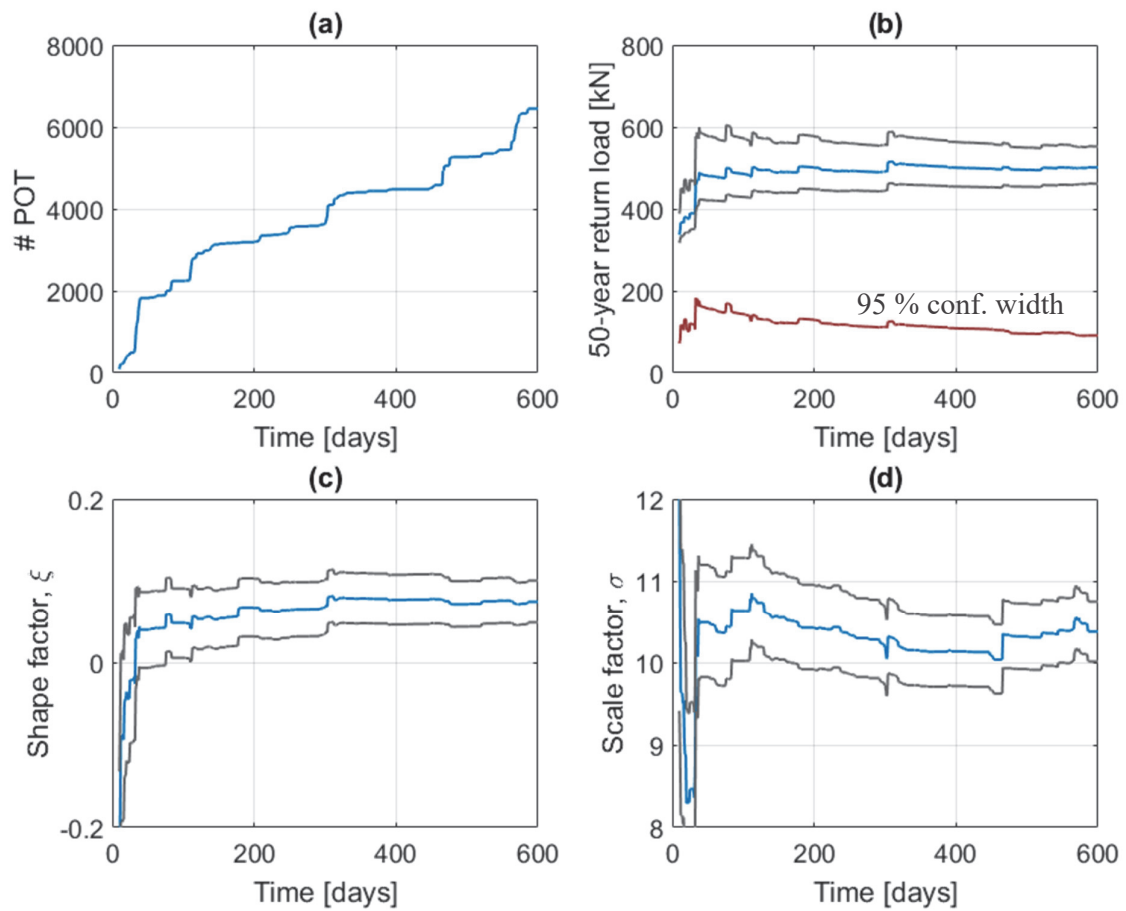
Figure 4-17. Evolution of the GPD parameters and extreme value estimates with an increasing monitoring period for the full data set with a threshold of 295 kN.

To demonstrate the effect of the monitoring period and duration, the 50-year estimate and the 95 % confidence interval width are calculated for individual periods. Figure 4-18 shows the results for periods of 15, 30, 60, and 120 days compared with the full period of 600 days. It is clear that the period duration and seasonal changes greatly affect the extrapolation. For short periods of 15 to 30 days, the 50-year return can be 20 % lower, and up to 50 % higher than the maximum load and in most cases, the confidence interval does not have an upper boundary. Monitoring periods of 4 months show close estimates for the first two periods and the last one. However the 95 % confidence interval width varies a lot between these three periods. The strong winter happening during the first period of 120 days leads to the closest final estimations.
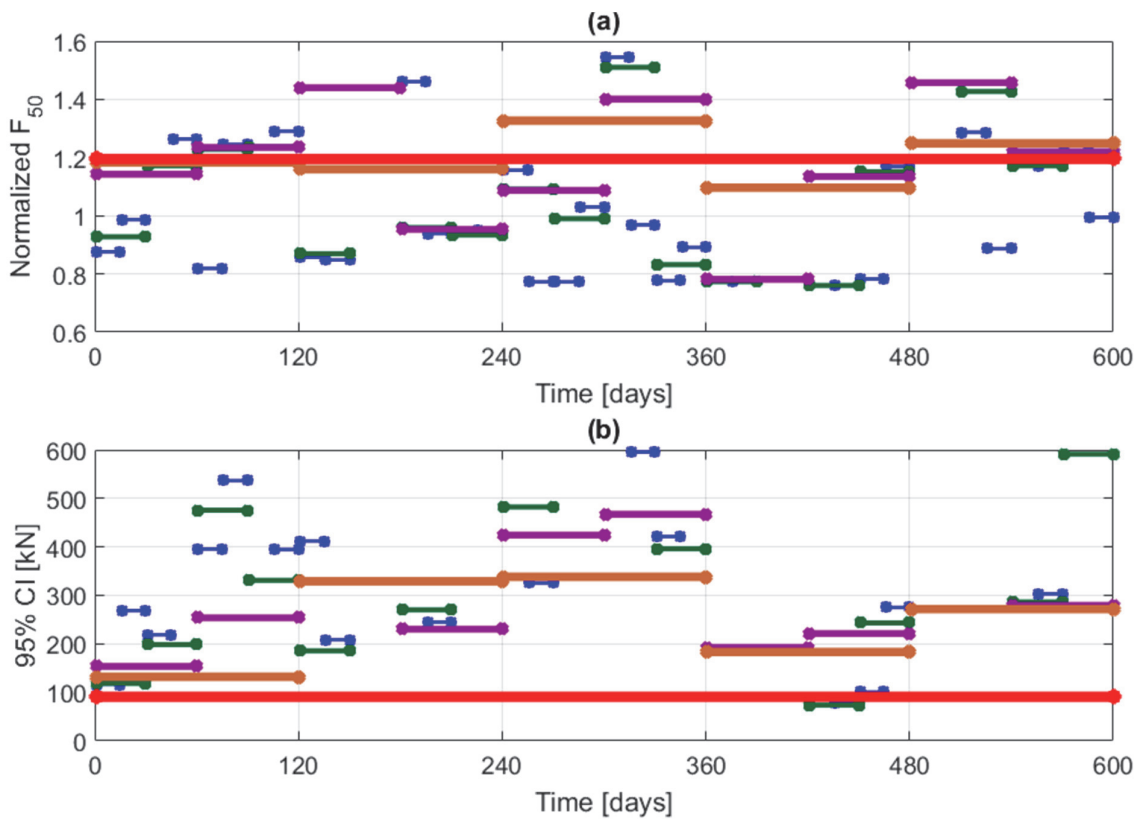
Figure 4-18. Effect of the monitoring period and duration on (a) the normalized 50-year extrapolation and (b) the 95 % confidence interval for 15 (blue), 30 (green), 60 (violet), 120 (orange) days and red being for the 600 days full period.

4.5.4 Discussion

Extrapolation from in-situ measurement

Regardless of the method used for the extreme load prediction, working with in-situ monitored data from a 2.0 MW wind turbine placed in a relatively low wind speed area is still a challenge. Results will always bring a higher variety of wind conditions and turbine behaviors than simulated data. However, measured data used for load extrapolation is subject to a certain amount of uncertainties, arising from both the strain measurements and the wind speed measurements. The long-term extrapolation of the wind effects on the turbine tower is shown to be strongly impacted by storms. Additionally, the frequency and intensity of such events are very variable from year to year. In the specific case of the monitored wind turbine, it was shown that variations between winters and summers are so important that few days of measurement during a storm can quickly lead to a relatively reasonable estimate, but with still large uncertainties. Each additional storm tends to increase the confidence in the extrapolated loads. The 2nd recorded winter (2016-2017) did not influence the estimated values, as much as the two maximum loads were recorded during the first recorded winter-spring period (2014-2015). The two maximum loads were recorded after 113 and 178 days.

102

Simulations from numerical tools, on the other hand, can quickly generate a set of data, but it will always include a certain bias (due to uncertainties in the wind turbine geometry, materials, modeling hypothesis, *etc.*). More importantly, the very high loads and their probabilities to occur (for example the fault of the controller) are difficult to estimate.

Comparison between the BMM and POT

Both approaches studied in this chapter, BMM with a long-term distribution integrated from short-term distribution for all wind conditions and the POT method with a distribution independent from the wind conditions, provide a good fit to the recorded sample, confirmed by diagnostics plots and visual inspections.

Despite the high uncertainty regarding the wind speed measurement and the limitation of the first method (exclusion of extreme values that lie in high wind speed bins due to lack of peaks), the extreme wind loads value extrapolation was found to be 10 % higher than the maximum recorded wind load. Extrapolated values mostly arose from high wind speed bin, between 14 and 20 m/s, and not necessarily from the rated speed where the controller change between different operating conditions. Higher wind speed bin cannot be included as not enough peaks are available. Again, the major disadvantage of this method is the lack of consistency in the wind speed (the 10-minute wind speed from the turbine anemometer is far from being reliable), which fully conditions the extrapolated values. Therefore, the POT method was not applied to this set of data, as it would increase the probability of peaks being categorized in the wrong wind speed bin. The threshold selection based on the average and standard deviation of the wind load is also dependent on the proper wind speed measurement. It was also showed that a single distribution could not be used for each wind speed bin and thus required more time to correctly analyze every wind speed bin.

The suggested approach with POT regardless of wind speed bin overcomes those difficulties by including all the highest loads. The GP distribution was preferred instead of a 3-parameter Weibull distribution as it provides a stronger theoretical foundation and it showed a good fit of the measured sample. The threshold selection based on the sum of the MSE offers a robust and reliable estimation. Significantly low thresholds were easily discarded with the Q-Q plots and the SEV plots (highest peaks systematically outside of the confidence interval) when the too high threshold was resulting in a sudden increase in the confidence interval width. The robustness of this threshold selection method was demonstrated, as the 50-year extrapolated value was stable for a +/- 5 kN threshold variation.

Minimum monitoring duration for extreme load extrapolation

The Juvent wind farm located in the Swiss Jura mountains experienced in average the highest wind loads in winter with an average higher power production during this period. The number and intensity of storms are therefore not evenly distributed over the year and even vary annually. For this study, the monitoring was started in December, at the beginning of the high wind season and the 50-year estimate rapidly reached the value obtained with 600 days of measurement. However, over time the effect of each storm becomes less significant for the 50-year return

value. Only the 95 % confidence interval width keeps decreasing as more and more peaks are included in the model.

For the POT method with the GP distribution, a stable value is reached after one year of measurements (for the continuous period from December 2014 to January 2016). The second part of the monitoring, from June 2016 to March 2017 do not change the 50-year estimate. The decision on the minimum measurement period in terms of a narrowed confidence interval (proposed by Treacy 2014) is a good indication, and it validates the measurement period of one full year as a minimum monitoring duration for extreme load extrapolation.

For the BMM with a combination of 3-parameter Weibull and Gamma distributions, a stable value of the 50-year extrapolation is reached suddenly after approximately 120 days and then changed slightly over the rest of the monitoring period. It should be noted that this extreme value extrapolation is very sensitive to the one or two most relevant wind speed bins. Although the distributions fit the data in a similar manner, they can significantly deviate for the higher return periods. Therefore, extreme values are highly dependent on the choice of the model.

Structural safety of the tower

The maximum recorded strain over the monitoring period corresponding to the 419 kN hub force is of 338 $\mu\varepsilon$ at the bottom sections. The corresponding strain at the critical location between the tube #2 and #3 is of 527 $\mu\varepsilon$. This is equivalent to 111 MPa (with a value of 210'000 MPa for the Young's Modulus). For the 50-year extrapolation from the POT method, the maximum estimated stress is 132 MPa, significantly below the yield stress.

4.5.5 Conclusions

This study presented the results of the load extrapolation from a 2.0 MW existing wind turbine from the long-term measurement of the tower bending loads in combination with the wind speed measured by the SCADA system. Two different approaches were investigated: the Block Maxima Method with the "fitting before aggregation" method and the POT method with the "aggregation before fitting". For the BMM, three distributions were tested: the GEV, the Gamma, and the 3-parameter Weibull distributions, whereas only the GP distribution was used for the POT. For the POT, the threshold selection was detailed with diagnostic plots and the confidence interval. Finally, the effects of "extremes of extremes", as well as the monitoring period and duration were studied in detail. The following conclusions can be drawn from this study:

1. Extreme load extrapolation from long-term monitoring of the tower bending moments is only possible with strain gauges fully compensated for drift and temperature since such errors will influence the maximum loads distribution and result in a meaningless extrapolation. The wind speed measured by the WT anemometer at hub height can have high uncertainties at high wind speed.
2. The single maximum recorded load can undoubtedly be categorized as an accidental load resulting from a fault of the control system. This event was easily detected as it

clearly lies out of its wind speed range. However, its single effect has a limited impact on the extrapolation.

3. The extrapolation method with BMM and "fitting before aggregation" results in lower 50-year extreme loads and requires a considerable amount of work in terms of data processing and quality control of the sample. It is very likely that the 50-year extreme value arises from the highest wind speed bins, for which a sufficient number of peaks is not always available.

4. Not all of the short-term distributions were fitted with a single distribution. A combination of 3-parameter Weibull and Gamma distribution was necessary to ensure the proper fit of the highest wind bins. The wind speed distribution was fitted with a Gamma distribution.

5. The extrapolation method with POT method and a GP distribution results in higher 50-year extreme loads. The threshold selection combining quantile-quantile plots and the confidence interval width provides a robust and objective method. Therefore, a stable extrapolation value is rapidly reached.

6. The measurement period and duration play a significant role in the extrapolation values. A minimum period of few months in winter is recommended to get a realistic value. A full year leads to stable data, as the 4 months of the 2nd winter had no impact on the 50-year return value (and gives similar results as the 1st winter).

7. The maximum stress prediction remains 34 % below the yield stress for the turbine tower and is not a concern for the Ultimate Limit State.

5 The use of SCADA data for the extension of wind turbine service duration

5.1 Introduction

Wind turbines are designed for a service duration of 20 years and subject to a heavy loading that is significantly dependent on the wind conditions. The data collected and analyzed in Chapter 3 shows the importance of the high wind speed distribution on the total accumulated damage. Additionally, a number of storms and their durations have a significant effect on the damage in which they should be considered individually. As a result of the variations in wind conditions, the effective endure damage by the turbine will be fluctuating. The overall availability (downtime and maintenance) of the turbine plays an important role in the fatigue life and must be considered, as a higher downtime than considered in the design will directly affect the remaining service duration (i.e. increase it).

The simulation tools available for the verification of existing structures are subject to a numerous amount of uncertainties and need the real wind conditions as input, the same that was used for the design. Changes in the wind farm configuration also need to be taken into account (*i.e.,* installation of new turbines that can locally increase the wake and affect the damage of existing turbines). The direct measurement of wind turbine tower can accurately measure the fatigue loads and gives an estimation of the damage accumulated over the monitoring period.

This chapter aims to extend the estimation of the damage prior to and after the monitoring period, using the already available data from the SCADA system. The realistic damages calculated at the critical details are first clustered into various load cases described in Chapter 2. The 10-minute damage values are stored in a database that will be used later for the estimation of the damage according to the environmental and operational parameters. This method is based on Monte-Carlo simulation for the long-term estimation of the endured damage.

A few approaches are available in the literature and focus on the SCADA data for the extrapolation of the fatigue damage. The 1-second SCADA data can be used for the estimation of the quasi-static hub force (by mean of learning algorithms) and combined with vibration measurement to reconstruct the fatigue loading (Noppe et al. 2016b). The SCADA data is also used to estimate the damage in an entire wind farm from two instrumented wind turbines (Weijtens et al. 2016). Previously, Heilmann (Heilmann et al. 2014) presented a monitoring concept based on short-measurement of a 600 kW turbine for the reconstruction of the endured load spectrum again employing SCADA data.

5.2 Model for the extrapolation of the damage based on monitored data

The model presented in this chapter combines a long-term measurement of the strain with the SCADA data of the concerned wind turbine. The 10-minute damages obtained from direct measurement are binned according to the corresponding wind speed and turbulence intensity. The final goal is to estimate the occurred damage at a given angle along the tower section using only a few data from the SCADA system: wind speed, turbulence intensity, and nacelle

orientation. For a defined critical angle (20° from the door axis in the case of the monitored n°10 Vestas V90 turbine), the damage is estimated from the maximum recorded 10-minute damage.

Once validated, this model can be employed for the monitored turbine to estimate the damage that occurs prior to and after the monitoring period, until the end of the service duration. Based on the assumption that similar turbines (same model and controller system) have the same behavior in the wind farm, the damage matrix obtained from one turbine can be used for the rest of the turbine wind farm. Figure 5-1 illustrates the methodology.
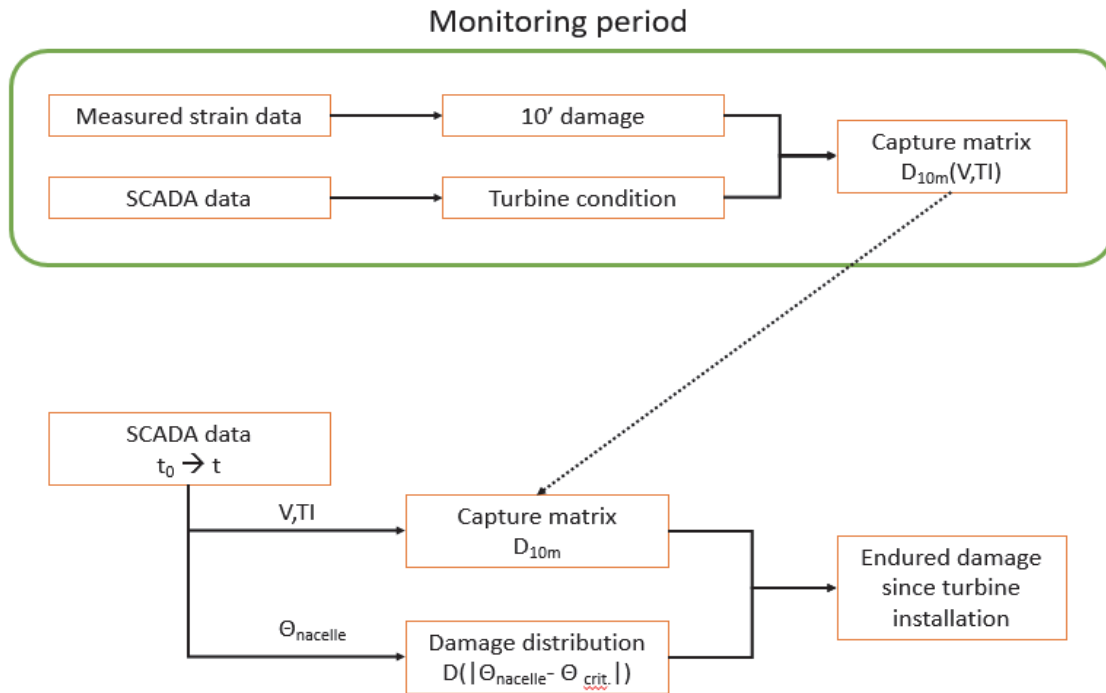
Figure 5-1. Illustration of the methodology for the reconstruction of the endured fatigue damage

The use of the SCADA data for the estimation of the endured damage follows this procedure:

1. The damage from the 10-minute recorded time series is computed using the appropriate S-N curve. Minimum monitoring period of 1 year is recommended.
2. The 10-minute maximum damages are stored in a capture matrix according to the wind speed and the turbulence intensity of the power production condition. The damage reduction coefficient C_D is fitted on the damage distribution.
3. According to the main direction of the high wind speeds (typically above the rated speed), the critical angle θ_{crit} for the damage calculation is chosen along the tower perimeter.
4. For each 10-minute series, a damage value is randomly picked from the capture matrix bin according to the wind speed and turbulence intensity. This value is multiplied by the damage reduction factor accounting for the angle difference between the calculated angle and the nacelle angle.
5. Step 4 is repeated multiple times to obtain a damage distribution.

5.2.1 Capture matrix

The two perpendicular strain signals measured at the bottom section of the turbine are used to calculate the stress of or on critical location. The 10-minute damage is then estimated using the appropriated S-N curve (See Chapter 3). Meanwhile, the environmental and operational parameters are used to define the proper clustering for the damage (*e.g.,* power production, emergency shut-down). The different turbine conditions are defined in Chapter 2. to evaluate the power production conditions; the 10-minute damage is stored in a capture matrix defined by the wind speed and the turbulence intensity, based on the similar approach described in (IEC 61400-13 2001). Turbine conditions that do not generate any relevant fatigue damage (parked situation and idling), the damage is discarded and accounted for downtime.

In this chapter, the damage will be assumed employing a bilinear S-N curve and a partial safety factor $\gamma_{Mf} = 1.0$. The turbulence intensity is derived from the SCADA data and calculated according to equation 2-1. Despite the possible unreliability of the wind turbine anemometer to accurately determine the wind speed, the absence of a meteorological mast near the turbine imposes to use the available data. The measured wind turbine, due to its localization in the wind farm, is not directly in the wake of a neighboring turbine along the main wind direction. There is then no need to classify the damage according to the turbulence intensity and the wind sector. In case of large offshore wind farms, the variation of the turbulence intensity with respect to the wind sector must be taken into account for the damage estimation (Weijtens et al. 2016).

The following capture matrixes account for 63.7 % of the monitoring duration and 89.0 % of the total damage endured by the turbine. For this study, the damage collected for load cases 1.1 to 1.4 (normal power production and faults, respectively) is considered as a single load case counting for power production higher than 100 kW and wind speed below the cut-out wind speed. Figure 5-2 shows the number of recorded 10-minute values for each wind speed bin and turbulence intensity bin. The majority of the recorded data is situated below the rated wind speed. After 604 days of measurement, some bins remain empty, as some combinations of wind speed and turbulence intensities have not occurred yet, and are not likely to occur during the entire service duration of the turbine, especially wind speeds above 18 m/s. A large number of bins only accounts for few time series. Figure 5-3 displays the associated damage for each wind speed and TI bin. The negative common logarithm (base 10) of the 10-minute average damage is indicated. The damage increases with both wind speed and turbulence intensity. Finally, the combinations of the number of recorded series and the average damage are shown as the map of the total damage in Figure 5-4.

	Wind speed [m/s]																	
Turbulence Intensity [%]	4	5	6	7	8	9	10	11	12	13	14	15	16	17	18	19	20	Σ
4	42	23	25	10	8	2	2											112
6	83	305	349	230	213	143	75	17	15	4	4	5						1443
8	293	924	995	720	561	378	235	163	65	31	28	12	3	3				4411
10	749	1419	1111	951	658	440	287	209	131	64	45	20	13	2	1			6100
12	1080	1462	1228	1007	780	733	470	341	209	116	47	28	6	3			1	7511
14	933	1966	1386	1202	1142	830	644	387	256	98	50	31	16	7	2	3		8953
16	883	1698	1463	1395	1046	883	622	438	278	154	66	35	20	13				8994
18	805	1773	1215	893	807	696	554	448	270	191	105	46	33	13	4			7853
20	682	1129	912	648	466	344	284	295	249	158	110	66	33	9	4	1		5390
22	268	585	473	320	242	157	151	175	135	84	55	40	17	7	1	1		2711
24	104	222	193	148	76	80	62	58	63	33	26	18	7	3				1093
26	113	129	84	51	32	21	26	32	18	8	2	5	2					523
28	26	46	29	15	10	11	10	6	6	2	4	1	1					167
30	18	21	14	11	3	3	2	5	1	2	1		1					82
32	6	13	5	2	2	2												30
34	2	3	4	1				1										11
36	1	4			2													7
38	3					1												4
40	1																	1
Σ	6092	11722	9486	7604	6048	4724	3424	2575	1696	945	543	307	152	60	12	5	1	

Figure 5-2. Capture matrix of the number of recorded 10-minute time series.

	Wind speed [m/s]																	
Turbulence Intensity [%]	4	5	6	7	8	9	10	11	12	13	14	15	16	17	18	19	20	D_{ave}
4	12	12	11	11	9.8	9.7	9.5											10
6	9.7	10.2	9.8	7.6	7.8	8.1	9.4	9.0	7.8	8.5	8.7	8.4						8.2
8	11	9.6	9.6	7.7	7.9	8.8	8.6	8.1	7.4	7.5	7.6	7.4	7.3	8.0				7.8
10	10	9.4	8.6	7.5	7.6	8.0	8.0	7.4	6.9	7.0	7.0	7.1	7.1	7.1	6.9			7.3
12	9.9	9.0	8.2	7.4	7.4	7.7	7.5	6.8	6.5	6.6	6.7	6.8	6.6	6.5			6.2	6.8
14	9.5	8.6	7.8	7.1	7.3	7.3	7.1	6.5	6.2	6.2	6.2	6.1	6.1	5.9	6.5	6.3		6.4
16	9.1	8.3	7.6	7.0	7.0	7.0	6.8	6.3	6.0	5.8	5.9	5.8	5.8	5.6				6.1
18	8.9	8.0	7.3	6.9	6.9	6.9	6.6	6.1	5.8	5.7	5.6	5.6	5.5	5.3	5.4			5.8
20	8.7	7.9	7.1	6.8	6.8	6.7	6.4	6.1	5.7	5.6	5.5	5.4	5.2	5.2	5.0	5.1		5.6
22	8.4	7.7	6.9	6.7	6.7	6.5	6.3	6.0	5.7	5.5	5.4	5.3	5.1	5.0	5.6	4.4		5.3
24	8.3	7.5	6.7	6.5	6.5	6.4	6.1	5.9	5.6	5.4	5.3	5.3	5.2	4.8				5.5
26	8.1	7.3	6.5	6.4	6.4	6.2	6.1	5.7	5.5	5.5	5.7	4.9	4.8					5.5
28	8.1	7.2	6.4	6.2	6.3	6.1	6.0	5.9	5.6	5.4	5.3	4.9	4.6					5.4
30	7.8	7.0	6.4	6.2	6.3	6.2	6.4	5.7	5.4	5.4	5.3		5.0					5.6
32	7.9	7.1	6.1	6.5	5.7	5.9												6.2
34	8.4	6.6	6.2	6.3				7.4										6.6
36	6.6	7.4			6.0													6.4
38	7.3					6.2												6.4
40	6.7																	6.7
D_{ave}	7.5	7.4	6.7	6.6	6.5	6.5	6.5	6.1	5.8	5.7	5.6	5.4	5.2	5.4	5.5	4.8	6.2	

Figure 5-3. Capture matrix of the 10-minute average damage [-log(D)].

110

Turbulence Intensity [%]	Wind speed [m/s]																	D_{ave}
	4	5	6	7	8	9	10	11	12	13	14	15	16	17	18	19	20	
4	10	11	9.6	9.7	8.9	9.4	9.2											9.4
6	7.8	7.7	7.3	5.2	5.5	6.0	7.5	7.8	6.6	7.9	8.1	7.7						6.1
8	8.8	6.7	6.6	4.8	5.1	6.3	6.3	5.8	5.6	6.0	6.2	6.3	6.9	7.5				5.7
10	7.5	6.3	5.6	4.5	4.7	5.3	5.6	5.1	4.8	5.2	5.4	5.8	6.0	6.8	6.9			5.2
12	6.9	5.8	5.1	4.4	4.5	4.8	4.9	4.3	4.2	4.5	5.0	5.4	5.8	6.0			6.2	4.7
14	6.5	5.3	4.7	4.0	4.2	4.3	4.3	3.9	3.8	4.2	4.5	4.6	4.9	5.1	6.2	5.8		4.4
16	6.1	5.1	4.4	3.9	4.0	4.1	4.0	3.7	3.5	3.6	4.1	4.3	4.5	4.5				4.0
18	6.0	4.8	4.2	4.0	4.0	4.0	3.8	3.5	3.4	3.4	3.6	3.9	4.0	4.2	4.8			3.8
20	5.8	4.8	4.1	4.0	4.1	4.2	4.0	3.6	3.3	3.4	3.4	3.6	3.7	4.3	4.4	5.1		3.8
22	6.0	4.9	4.3	4.2	4.3	4.3	4.1	3.7	3.6	3.6	3.6	3.7	3.9	4.1	5.6	4.4		4.0
24	6.3	5.2	4.4	4.3	4.6	4.5	4.3	4.1	3.8	3.9	3.9	4.0	4.3	4.4				4.2
26	6.0	5.2	4.6	4.7	4.9	4.9	4.7	4.2	4.2	4.6	5.4	4.2	4.5					4.6
28	6.7	5.6	5.0	5.0	5.3	5.1	5.0	5.1	4.8	5.1	4.7	4.9	4.6					5.0
30	6.5	5.7	5.3	5.1	5.8	5.7	6.1	5.0	5.4	5.1	5.3		5.0					5.3
32	7.1	5.9	5.4	6.2	5.4	5.6												5.7
34	8.1	6.1	5.6	6.3				7.4										6.1
36	6.6	6.8			5.7													6.1
38	6.8					6.2												6.4
40	6.7																	6.7
D_{ave}	6.4	5.3	4.7	4.4	4.5	4.6	4.4	4.0	3.8	3.9	4.1	4.2	4.3	4.5	5.0	4.8	6.2	

Figure 5-4. Capture matrix of the total damage [-log(D)].
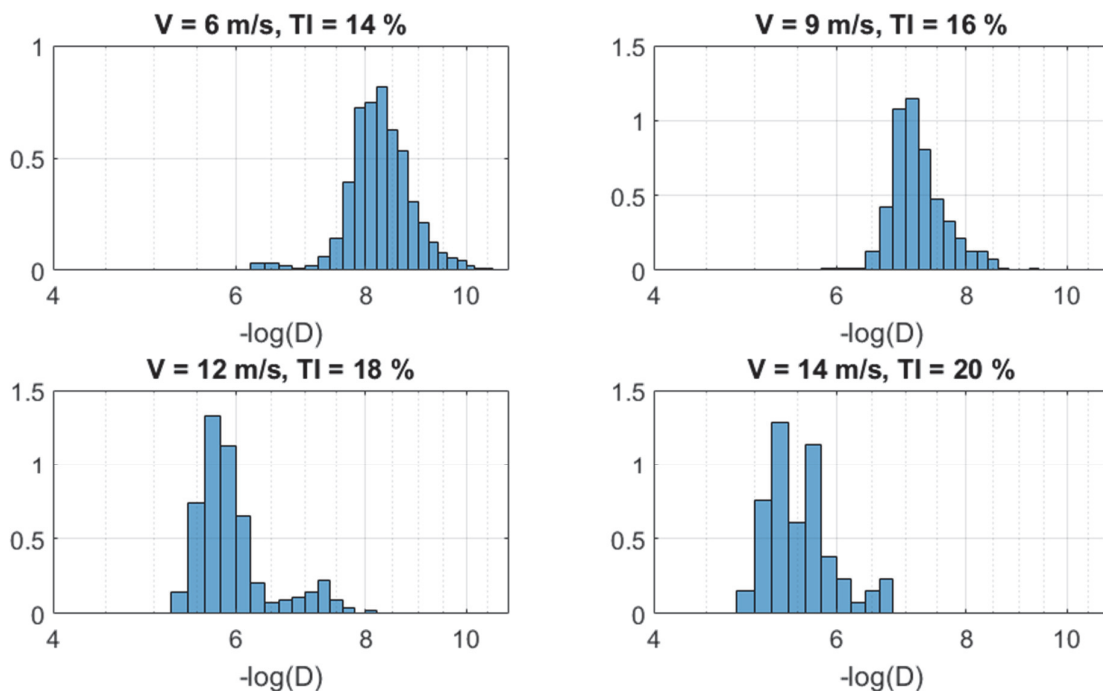
Figure 5-5. Damage distribution within four different wind speed and turbulence intensity bins.

The probabilistic damage assessment requires knowing the damage distribution for each wind speed and turbulence intensity bin. However, the lack of data in the high wind speed bin is a limitation to this approach. Additionally, the distribution of the damage does not seem to follow

111

standard distributions. Figure 5-5 displays the damage histograms for four different bins. Finding a proper statistical distribution that can fit well all wind speeds bins is not possible, as small discrepancies in the high damage region (towards the left tail of the histogram) would lead to unrealistic damage.

To overcome this limitation, the measured 10-minute damage will be used as a database of damage values, and the probabilistic damage assessment will be performed through multiple simulations.

5.2.2 Damage distribution over the section

The damage matrix is computed using the maximum damage recorded over the turbine section rather than the damage occurring at the critical angle of the monitored turbine. Therefore, the capture matrix is independent of the specific wind condition of the monitored turbine and can be used for other similar turbines.

In order to not overestimate the damage, the actual damage occurring at a specific location depends on the angle between the critical angle θ_{crit} and the nacelle orientation $\theta_{nacelle}$.

$$\Delta\theta = |\theta_{nacelle} - \theta_{crit}| \tag{5-1}$$

Figure 5-6 below shows the damage distribution for 1'000 of 10-minute time series. The minimum damage along the section is perpendicular to the fore-aft direction and close to 0. Small variations occur due to the small lateral vibrations of the tower. The damage reduction is fitted with a cosine function with two parameters; a stands for the minimum damage level and b the steepness of the slope. The damage reduction coefficient is calculated as:

$$C_{D(\Delta\sigma)} = a + (1 - a) \cdot \cos(\Delta\theta)^b \tag{5-2}$$
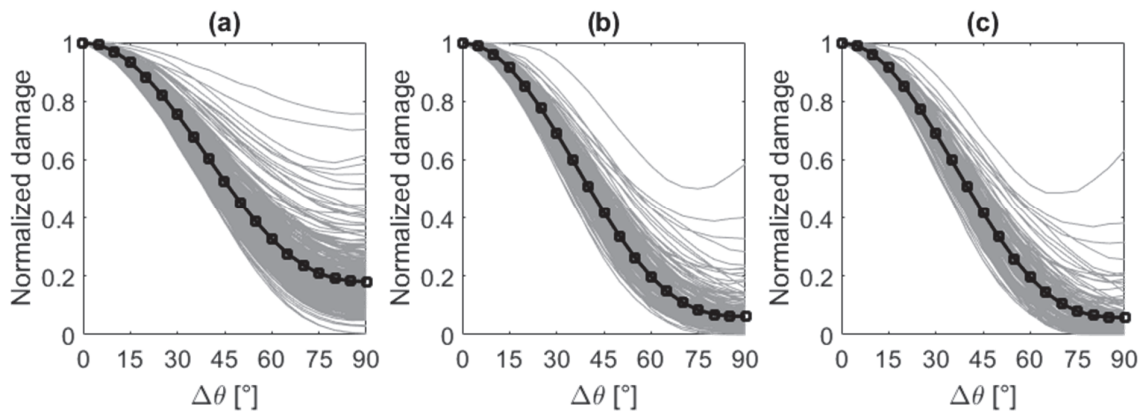
Figure 5-6. Distributions of the normalized damage for 1'000 time series of 10 minutes for (a) a linear S-N curve, (b) a bilinear S-N curve, and (c) bilinear S-N curve with endurance limit.

For the power production case and a bilinear S-N curve (Figure 5-6(b)), the fitted coefficients are a = 2.78 and b = 0.062.

5.2.3 Model validation

The first run of the model is performed on the monitoring period and using the synchronized data from the SCADA system. Figure 5-7 below shows the results from the simulation for the 604 days of the monitoring period. The vertical bars of the estimated red curve indicate two standard deviations. The model is capable of predicting the damage with fidelity around the critical angle. The total damage can then be corrected by a factor in which the cycles excluded from the 10-minute series are taken into account. The amplification factors can be found from the full damage assessment summarized in Table 3-4 and it is approximately equal to 1.10 for the bilinear S-N curve without endurance limit.
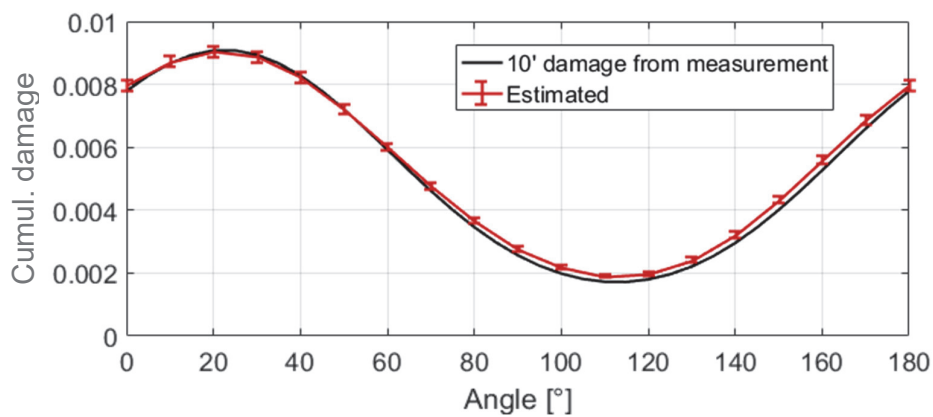
Figure 5-7. Validation of the model over the monitoring period.

Through the monitoring duration, the number of recorded events increases in every bin of the capture matrix, leading to a more stable estimation of the damage. Figure 5-8 below shows the calculated damage over the 604 days of the monitoring period with an increasing database. The first estimations with less than a full year of measurement lead to a damage 12 % to 7 % lower than measured. Starting the monitoring in summer would have led to a much lower damage with short-monitoring periods.
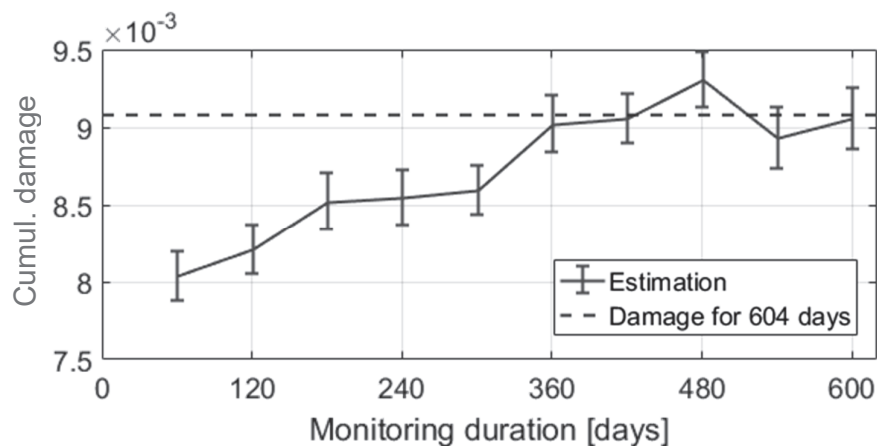
Figure 5-8. Impact of the monitoring duration on the estimated damage over the full monitoring period with an indication of two standards deviations.

113

5.3   Reconstruction of the endured damage

The monitored turbine was installed in 2010 during the first repowering of the wind farm along with seven other 2.0 MW Vestas V90. The SCADA data for this turbine has been available since 1st of January 2012. The average wind speeds measured by the turbine anemometer is presented in Figure 5-9(a). The red curve shows the 30-day moving average. Both high and low wind periods are easily observable. The SCADA data was available until May 2017. The total dataset represents a total of 282'454 series.

The average results from 1'000 simulations are presented in Figure 5-9(b). The 10-minute damage and its 30-days moving average are displayed, as well. The higher damage occurring in winter, the different wind periods and their durations are clearly visible.
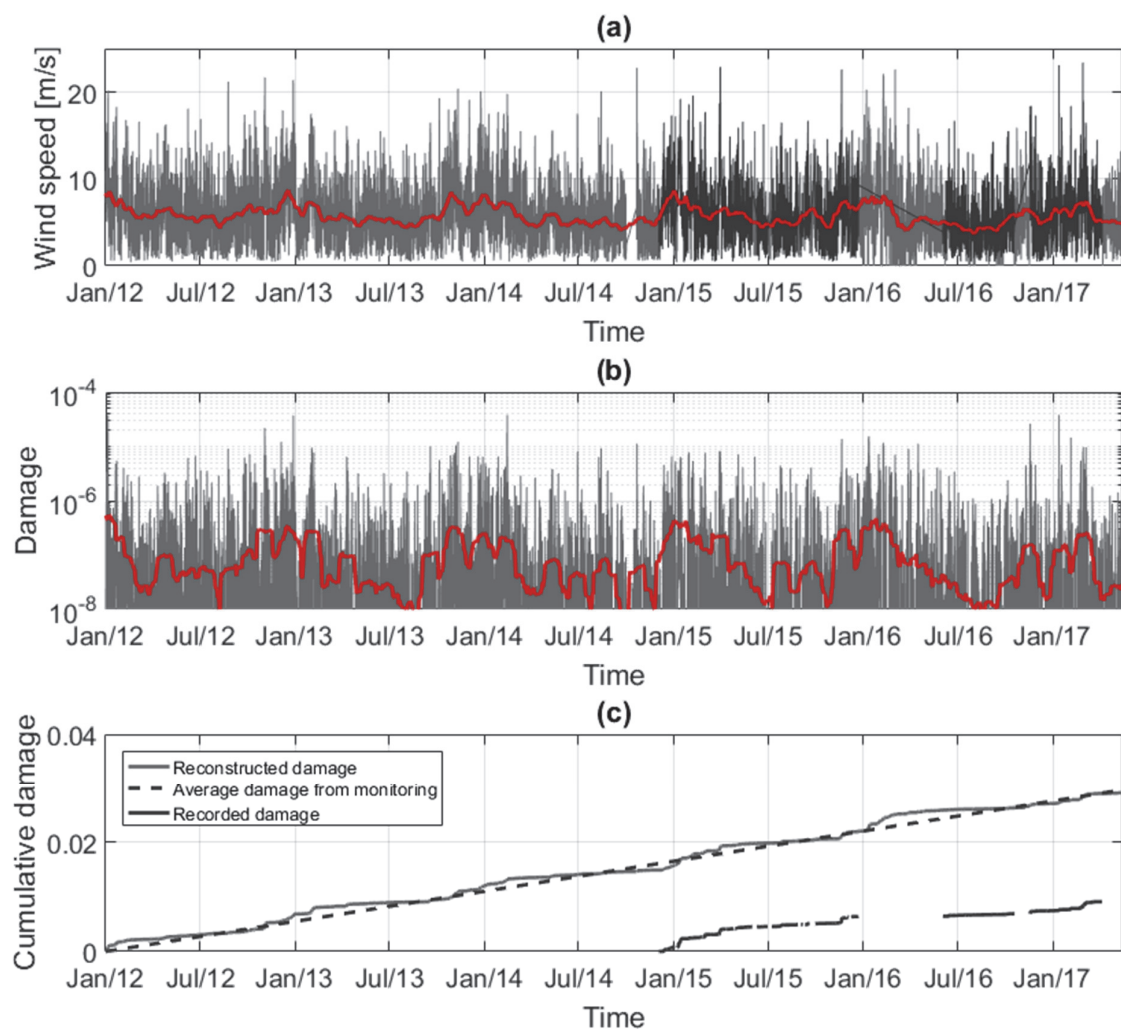
Figure 5-9. (a) Wind speed variations since the installation of the turbine (the monitored period is highlighted) and (b) reconstructed 10-minute damage (the red curves are the 30-day running average). (c) Cumulative damage.

Figure 5-9(c) presents the cumulated estimated damage based on the SCADA data. The importance of measuring in winter between November and April is indicated here. The wind condition seems somewhat similar to the estimated daily average damage is almost equal to the one calculated during the monitoring period. It can be seen that winter 2017 was less windy than the previous winters and affected the predicted damage from the measurement.

Finally, the original dataset was modified by artificially increasing the average wind speed over the entire period. Two scenarios are compared with the original case: an overall increase of 15 % of the average wind speed and an increase of 30 % to provide a set of data with an average wind speed of 7.5 m/s. This average wind speed of 7.5 m/s corresponds to the wind class III (IEC 61400-1 2005), which was used for the design of the Vestas V90.

Average results from the simulations are presented in Figure 5-10 and show the evolution of the damage for three different scenarios. With an increase of 15 % of the average wind speed, the calculated damage after 5.4 years increases by 71 %, whereas the damage for the design wind conditions is 256 % higher. The damage distribution observed from the 1'000 simulations are shown in Figure 5-11 for the three scenarios.
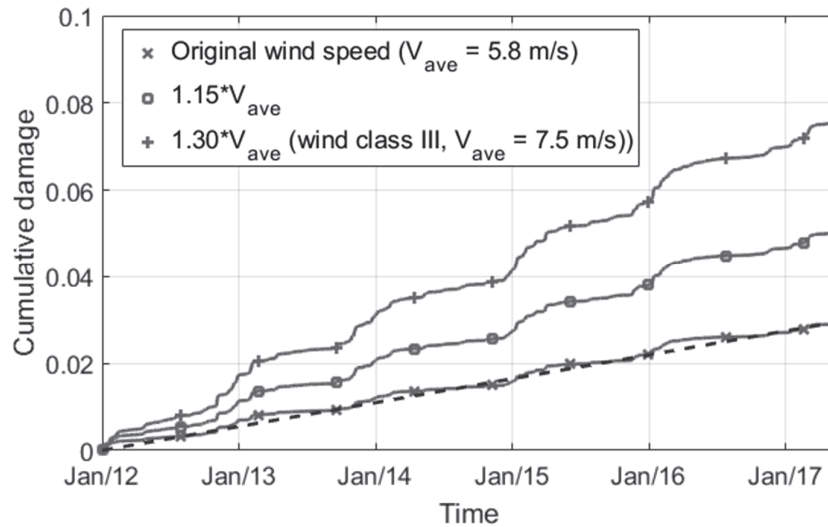
Figure 5-10. Results of the cumulative estimated damage from 3 scenarios.
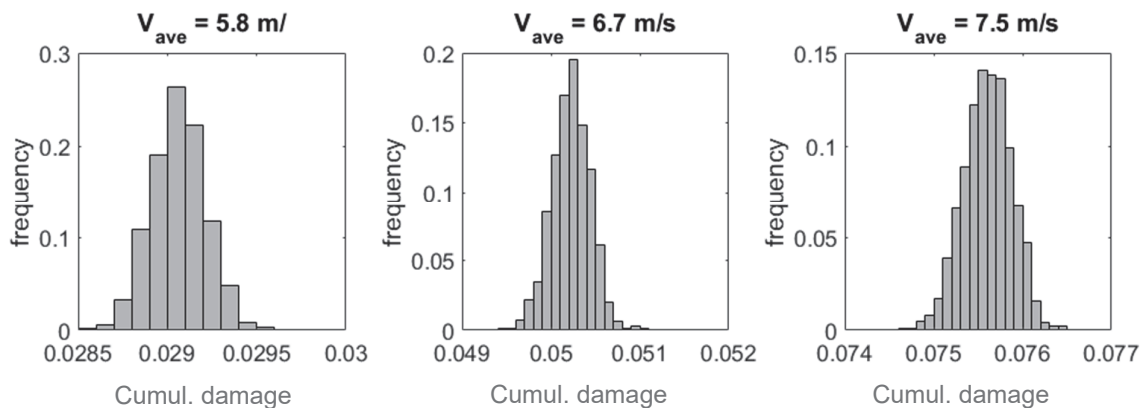
Figure 5-11. Cumul. damage (5 years) distributions obtained from 1'000 simulations.

5.4 Discussion

The results obtained using the model presented in this chapter are closely linked to the wind conditions and the location of the wind turbine in the wind farm. The relatively low wind speeds observed at this location (30 % below the wind class value) resulted in an incomplete capture matrix. Lack of a sufficient amount of data in the high wind speed bins leads to possible large uncertainties. Additionally, the turbine anemometer is likely to underestimate the wind speed, and proper measurements with a Lidar-based system would provide correction factors to the SCADA data.

The first results on a modified wind distribution show a drastic increase in the damage. The choice of the monitored turbine was, in 2014, driven by the direct availability of the SCADA data. The rest of the turbines were not equipped for the automatic export of the data. In the hypothesis of monitoring a second turbine support structure in the Juvent S.A. wind farm, the turbine undergoing the most severe wind conditions has to be selected. Another possibility would be to select a turbine situated in the wake of the currently monitored turbine to estimate the effect of neighboring turbines directly.

The method was only applied to the available SCADA data from the monitored turbine. A first validation was performed over the measurement period. The method should be extended to the neighboring wind turbines and validated with an additional short-term measurement.

5.5 Conclusions

The following conclusions can be drawn from this study:

1. A method for the reconstruction of the fatigue damage endured by a wind turbine base on long-term measurement and simultaneous recording of environmental and operational data through the SCADA system is presented. Based on the classification of the turbine conditions and the previous work on the fatigue damage presented in Chapter 3, the damage endured by the wind turbine is estimated even with a limited number of parameters.
2. The uncertainties highly depend on the measurement duration and period. A minimum duration of one year is required with a focus on winter season to ensure the recording of high wind speeds, when the majority of the damage occurs.
3. The annual average wind speed strongly impacts the total endure damage by the turbine support structure. The simulations based on artificially increased wind speeds lead to a higher damage. However, with an annual average wind speed corresponding to the wind class III for design, the service duration of the turbine support structure could still be enhanced.
4. A short-term monitoring with a reduced set of sensors (4 strain gauges at the bottom section) should be installed in either the turbine experiencing the stronger winds in the wind farm or a wind turbine adjacent to the one currently measured for the validation of the method.

6 Compressive fatigue strength of Ultra-High Performance Fibre Reinforced Cement-based Composite (UHPFRC)

6.1 Introduction

Reducing the cost and the environmental footprint of wind turbines can be achieved by developing taller turbines that last more than the actual 20 years suggested by the design codes. Concepts using steel could be designed for an extended service life, yet marine environment would cause serious durability concerns of such structures in terms of steel corrosion. Concrete towers can also provide an alternative to steel, but the increase in size and weight reduces the possibilities of transportation and installation of such designs. A new material, the Ultra High Performance Fibre Reinforced Cement-based Composite (UHPFRC), could overcome this restriction and allow for a more economical and durable solution for both onshore and offshore wind turbines. Some concepts were already introduced and showed the efficiency of this material combined with prestressing (Werner et al. 2013; Jammes, Cespedes, and Resplendino 2013; Sritharan and Schmitz 2013; Wu, Yang, and Mpalla 2013). In order to validate these concepts, the fatigue behavior of the UHPFRC in compression needs to be known, and the fatigue strength determined, as offshore wind turbine towers are supposed to withstand 10^8 to 10^9 of load cycles.

UHPFRC is a high-strength cementitious material characterized by a very dense matrix reinforced with 3-9 % by volume of fine steel fibres. The compact matrix has almost zero capillary pores that make the UHPFRC highly impermeable to gases and liquid solutions (Charron, Denarié, and Brühwiler 2007). The cracking behavior of the material is controlled by fine fibre reinforcement, and it gives UHPFRC its high strength, strain-hardening behavior, ductility, and fracture energy properties. UHPFRC exhibits high mechanical properties with compressive strength above 150 MPa and tensile strength above 7 MPa. UHPFRCs typically have elastic modulus between 40 and 60 GPa. The typical compressive behavior of UHPFRC cylinders is shown in Figure 6-1 for heat treated and untreated cylinders. The ductility of the relatively brittle matrix is increased by the steel fibres. The heat treated UHPFRC exhibits higher strength at early age, and the ratio between the elastic limit and the ultimate strength increases (Graybeal 2007).
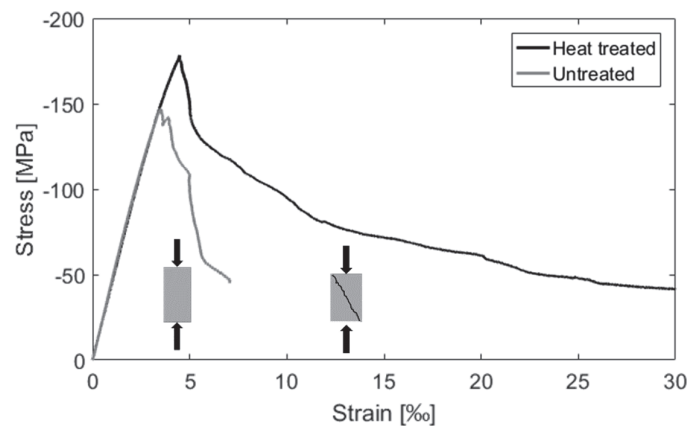
Figure 6-1. Typical stress-strain relation of UHPFRC.

The objective of this chapter is to describe the compressive fatigue behavior of UHPFRC thin plates for its utilization in future wind turbine support structure. The experimental program consists of two parts – static tests to evaluate the compressive strength of UHPFRC plates and compressive fatigue tests under constant amplitude.

6.2   Literature review

The fatigue behavior of UHPFRC was intensively investigated under constant amplitude tensile fatigue by Makita (Makita and Brühwiler 2014). Tests were performed on plates, and endurance limits were determined for the three domains. The solicitation level (S-level) with respect to 10 million cycles $S = \frac{\sigma_{max}}{f_{ck}}$ was found to be 0.70, 0.60, and 0.45 for the elastic domain, the strain hardening domain, and the strain-softening domain, respectively. Tests on plates reinforced with steel rebars showed an endurance limit for S = 0.54 with respect to 10 million cycles. Finally, the endurance limit of a reinforced UHPFRC layer on a reinforced concrete beam was determined as S = 0.5.

Several studies were also performed on bending specimens (Parant, Rossi, and Boulay 2007; Farhat et al. 2007; Behloul et al. 2005; S Lappa, René Braam, and C Walraven 2017). The general outcome is that different types of UHPFRC exhibit good performance under bending fatigue. Little damage was observed on test specimens, and scatter in the results usually results from poorly oriented fibres. The fatigue resistance in compression was however never studied (but no damage in compression was observed).

Results from the experimental and theoretical investigation of high-performance concrete with compressing strength up to f_{ck} = 200 MPa (Lohaus, Oneschkow, and Wefer 2012) were presented and included in the concrete code (FIB 2010) although the concrete grades are still limited to C120.

A study on the fatigue behavior of UHPFRC was presented recently (Tapsoba et al. 2017). Tests showed that UHPFRC under compressive loading could withstand up to 10 million cycles with an upper S-level of 0.6 and a lower S-level of 0.1. Specimens were not tested further, and the static tests carried after showing no deterioration and no effects on the compressive strength.

The thermal treatment has an influence on the behavior of cementitious materials, as it provides higher resistance at a young age. An interesting advantage of the thermal treatment is that the shrinkage becomes negligible because it fully develops at an early age (Richard and Cheyrezy 1995). The creep of UHPFRC, close to that of High-Performance Concrete and smaller than for Normal Concrete, is also largely reduced by thermal treatment, down to a coefficient of 0.2 for a CEM I up to 25% of f_{Uc} (Kamen 2007). This property is very interesting for highly prestressed UHPFRC elements. In compression, the thermal curing affects the linear elastic domain, and 80 to 90 % of the compressive strength is reached before diverging from the linear elastic behavior (Graybeal 2007).

This literature review reveals the lack of high cycles fatigue tests on UHPFRC for the specific application for the turbine towers. To do that, tests need to be extended further than 10 million cycles.

6.3 Experimental campaign

6.3.1 Specimen preparation

The chosen UHPFRC for this experimental campaign is the Holcim 707 (H707), an industrial premix containing 3.8 % by volume of 13 mm long straight steel fibers with a diameter of 0.175 mm. To take into account the future possible application of the UHPFRC for wind turbine, it was chosen to test thin plates of 450 mm long with a cross-section of 100 mm x 30 mm. The cross-section area was chosen so that the fatigue tests could be performed at a relatively high frequency within the testing machine capacity.

Specimens were cast vertically into wooden forms to reproduce the effect of the casting procedure used for precasting concrete tower elements (LaNier 2005). A sock made of plastic was used to control the flow of UHPFRC into the formworks and reduce the entrapped air (Figure 6-2(a) and Figure 6-3). For each batch, 6 specimens of 500 mm long and 200 mm wide were cast simultaneously. The cross-section area of such specimens are too big for the testing machine capacity, and they were actually used to produce the pair of sub-specimens. Initial plates were cut with a concrete saw within the Laboratory of Soil Mechanics (LMS) facilities according to Figure 6-2(b). One of the two samples thus obtained was tested under a quasi-static compressive test, and the other one was tested under constant amplitude fatigue compressive stresses. This method provides a better estimate of the ultimate resistance of the sample tested to fatigue.

(a)   (b)
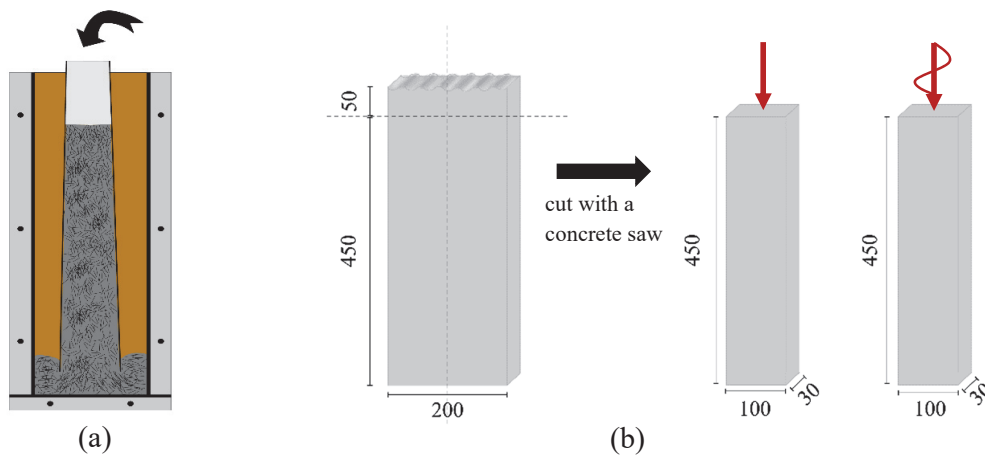
Figure 6-2. (a) Schematic of the casting procedure with a sock and (b) pair of specimens obtained from a single plate.

The specimens were unmolded 48 hours after the casting and heat treated for the next 48 hours. They were stored in closed plastic boxes, and a sufficient amount of water was added to ensure a 100 % relative humidity (RH) to atmosphere around the UHPFRC plates. The boxes containing the UHPFRC plates were put into a climatic chamber, and the following procedure for the thermal curing was then followed. The temperature was linearly increased from room temperature to 90 °C in 4 hours, kept constant for the next 40 hours (with a regular check of the water level in the plastic boxes), and finally linearly decreased. Subsequently, the specimens were stored in the testing hall in a controlled environment. The thermal curing ensures for each

of the specimens to reach its final resistance and thus remove potential uncertainties associated with long-lasting fatigue tests.

Figure 6-3. Specimen fabrication: (a) vertical casting of the fresh UHPFRC and (b) details of the forms.

6.3.2 Test set-up and instrumentation

Specimens were instrumented with a total of 6 Linear Variable Differential Transducers (LVDTs). Two 200 mm-long LVDTs were set on both sides of the specimen to measure the central deformation and four 125 mm-long LVDTs were installed on the top and bottom of the plate, two in the front and two in the back (Figure 6-4). By doing that, the deformations were continuously measured along the specimen, and the deformation measured in the central zone were not affected by the boundary conditions. This system was particularly important for the setting up of the specimens in the machine.

The specimens are required to be perfectly aligned in between the two steel plates of the machine. Due to the impossibility to use a hinge to compensate the defect of parallelism of the support surface (inherent to the formwork precision and the cutting surface), another method was employed to ensure alignment. Aluminum plates were placed on the contact surfaces to compensate for small irregularities, and a high strength glue was put in between aluminum plates and the contact surface to compensate the default of parallelism. A small force was then applied by the machine during the curing of the glue. The correct positioning of the specimen was checked by applying a small force on the specimen and by inspection of the displacement obtained from the 6 LVDTs. Once the glue was cured, the specimen stayed in the machine under a minimum load of 2 kN until the beginning of the test.
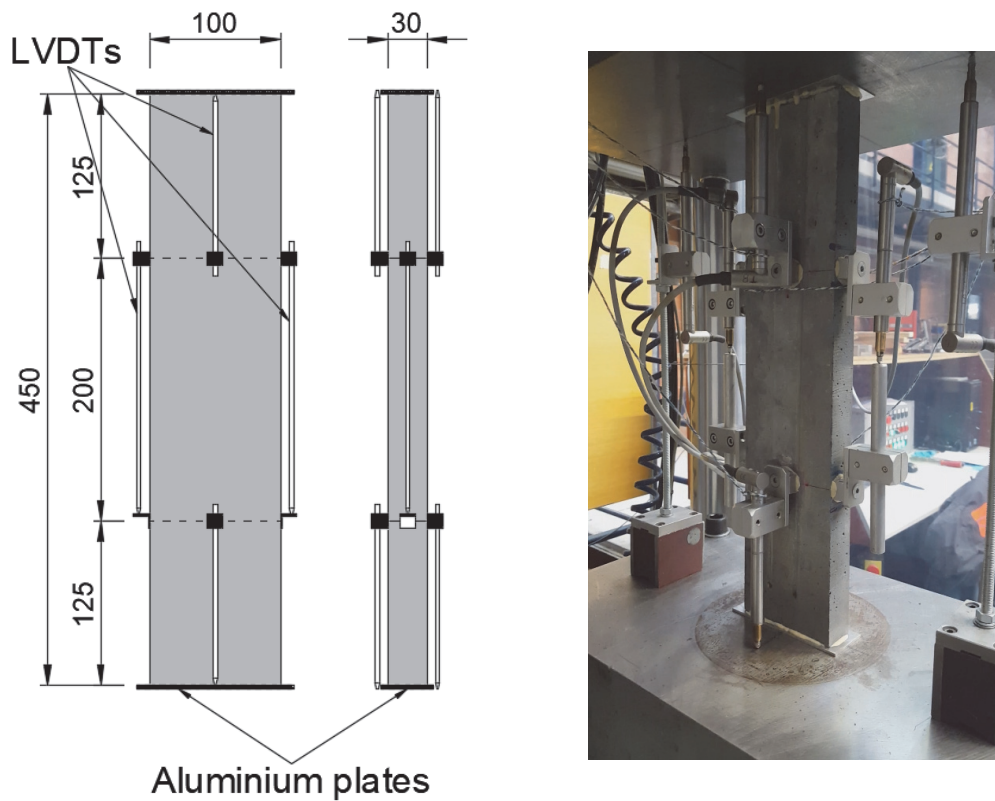
Figure 6-4. Specimen geometry, measuring devices, and testing set-up.

6.3.3 Testing procedure

The force was measured by the load cell of the 1'000 kN servo-hydraulic testing machine. Static tests were performed under displacement control through the use of two additional LVDTs situated on both sides of the specimen. For the constant amplitude fatigue tests, the machine was force controlled. When the testing machine was force controlled, a set of displacement limits were imposed to forbid any damage might happen to the sensors. Due to the slenderness of the specimen and the high stresses, the failure was explosive. The area around the machine was always protected by Plexiglas walls during testing.

For the static tests, three preload were performed under force control up to approximately 30 % of the ultimate resistance. A minimum load of 30 kN (10 MPa) was maintained to ensure that the specimen would not move due to a too low force. The specimen was loaded until failure at 0.05 mm/min (0.07 MPa/s) and the data were recorded at 5 Hz. The typical scheme of the static test is presented in Figure 6-5(a).
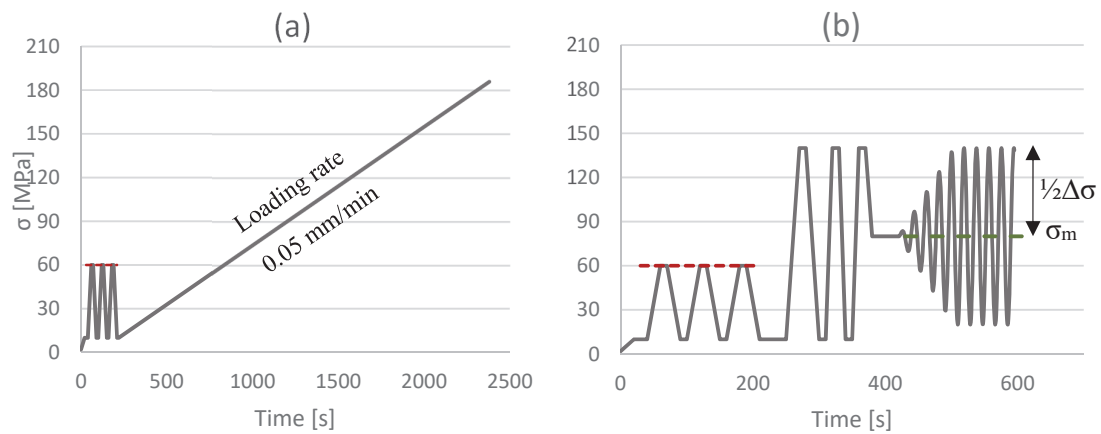
Figure 6-5. Loading procedure for (a) the static tests and (b) the fatigue tests.

For the fatigue tests, a similar pre-load was applied to the specimen to check the proper alignment and the absence of eccentricity. A second loading was then applied to the specimens up to the high stress level, $S_{c,max}$. After the 3rd loading, the average force F_m was reached, and the sinusoidal loading between $S_{c,min}$ and $S_{c,max}$ started (Figure 6-5(b)). A transition period of 10 seconds between the quasi-static and the constant amplitudes cycle stress was needed to ensure a proper loading of the specimens.

A total of 18 specimens was tested under constant amplitude compressive fatigue stress at various imposed stress levels. The minimum S-level was set between 0.05 and 0.1 of the ultimate strength, and maximum stress level varying from 0.6 to 0.9. One specimen was tested at a low maximum stress level of 0.48. The tests were performed at various frequencies depending on the maximum force and the force amplitude. The goal was to conduct tests up to 20 million cycles within a reasonable time frame by increasing the frequency up to the testing machine dynamic capacity. Tests with maximum stress level up to 0.6 were conducted between 10 Hz and 15 Hz, whereas tests at a maximum stress level of 0.8 to 0.9 were conducted at 2 Hz. A test of up to 20 million cycles at 10 Hz requires 23 days of machine operating.

In this chapter, the endurance limit is defined as a stress level below which no fatigue failure occurs up to 10 million cycles. But tests were pushed up to 20 million cycles when the time was available since this is already considered as the very high cycle fatigue domain (Sadananda, Vasudevan, and Phan 2007). When a specimen was declared "run-out", the test was either continued at a higher stress level or stopped to perform a quasi-static test.

6.3.4 Determination of the ultimate strength

A total of 16 quasi-static tests was conducted to determine the quasi-static specimen behavior, as well as the ultimate strength. The value obtained for a specimen was used to calculate $S_{c,max}$ of the "twin" specimen coming from the same initial plate. The Figure 6-6 below presents the characteristic stress-strain curves observed with the thin plates and the histogram of the ultimate resistance. An average compressive strength of 186.8 MPa with a standard deviation of 8.7 MPa was obtained.
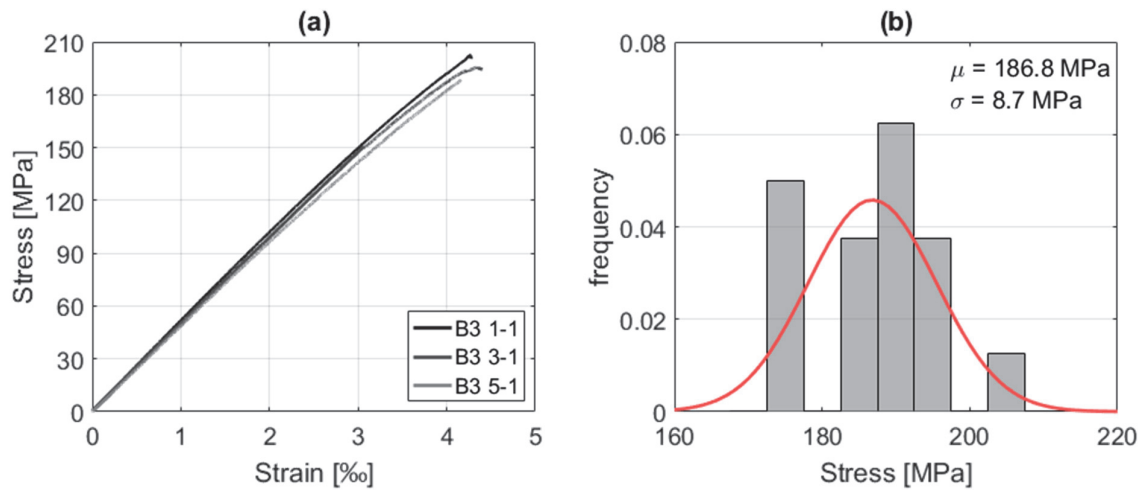
Figure 6-6. (a) Stress-strain curves for three quasi-static tests from the 3ʳᵈ batch and (b) histogram of the compressive strength of heat treated UHPFRC plates.

6.4 Results of the fatigue tests

6.4.1 Fatigue strength and endurance limit

Overview of the results

The results of the compressive fatigue tests on UHPFRC plates are summarized in Table 6-1. The specimens were considered as run-out when they reached the value of 20 million cycles. When a significant crack developed in the specimen, the failure occurred brutally. Therefore, it was not necessary to define a value for maximum allowable deformation.

Due to logistic reasons, specimens B2 4-2 and B3 6-2 were stopped at 17.7 and 15.6 million cycles, respectively. Subsequently, B3 6-2 was continued at a higher load level. Specimen B4 3-2 was stopped at 2 million cycles, and the load was increased.

Table 6-1. Results of compressive tests on UHPFRC plates.

Series	Test No.	f_{Uc} [MPa]	$S_{c,min}$ [-]	$S_{c,max}$ [-]	log N	Remarks
B2	1.2	-188.0	0.25	0.72	7.16	
	2.2	-173.0	0.49	0.90	2.82	
	3.2	-196.4	0.28	0.66	7.30	run-out
	4.2	-191.3	0.09	0.64	7.25	run-out
	5.2	-174.8	0.11	0.48	7.30	run-out
B3	1.2	-202.5	0.10	0.65	6.79	
	2.2	-183.7	0.10	0.88	4.11	
	3.2	-195.4	0.10	0.83	4.21	
	4.2	-191.4	0.10	0.79	4.84	
	5.2	-188.4	0.10	0.71	5.35	
	6.2	-185.7	0.10	0.66	7.19	run-out
		-185.7	0.10	0.82	2.85	load increase
B4	1.2	-173.8	0.05	0.80	3.77	
	2.1	-195.8	0.04	0.63	6.71	run-out
	2.2	-195.8	0.10	0.80	3.53	
	3.2	-183.0	0.05	0.67	6.30	run-out
		-183.0	0.04	0.76	4.71	load increase
	4.2	-189.1	0.10	0.80	3.63	
	6.1	-175.0	0.05	0.70	5.62	
	6.2	-175.0	0.05	0.70	5.14	

The results from the fatigue tests are presented in an S-N diagram (Wöhler diagram). For cementitious materials, the ratio of the maximum applied fatigue stress to the compressive strength is often used to normalize the load level and eliminate the variations of material composition, specimen geometry, and testing setup. The number of cycles to failure is displayed in logarithmic scale.

Figure 6-7 shows the data from the 14 tests that result in a fatigue failure. The 6 run-out tests are displayed differently. The fatigue strength of the UHPFRC plates tested in this study can be expressed by a linear relation between the maximum stress level $S_{Uc,max}$ and log N. A linear regression line was determined (without including the run-out) with a coefficient of determination of $R^2 = 0.67$, indicating a good dependency between the two variables.

$$S_{Uc,max} = \frac{\sigma_{c,max}}{f_{Uc}} = -0.044 \cdot logN + 0.981 \qquad (6\text{-}1)$$

By including the run-out tests, the endurance limit is estimated to be at an S-level of 0.65 (horizontal dashed line in Figure 6-7).
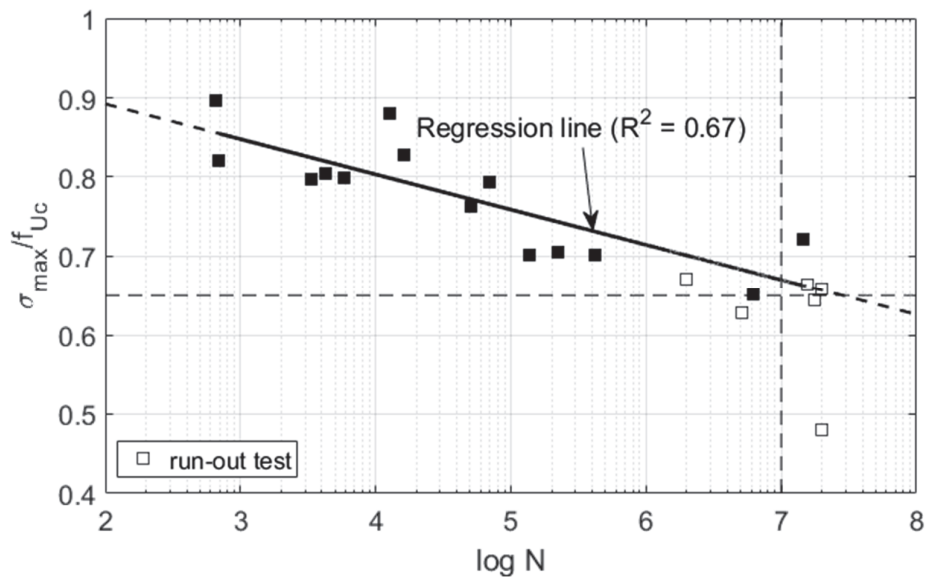
Figure 6-7. S-N diagram obtained from compressive fatigue tests on UHPFRC plates.

Influence of the ultimate strength

One of the substantial uncertainty on the S-N diagrams is the calculated fatigue stress indicator S. The larger scatter observed in Figure 6-8(b) compared to Figure 6-8(a) is due to a slightly too low or too high estimated ultimate limit strength. Using an average value for the compressive strength results in a relatively poor coefficient of determination ($R^2 = 0.44$) in comparison with the ultimate resistance obtained from the 2nd plate of the initial specimen ($R^2 = 0.67$).
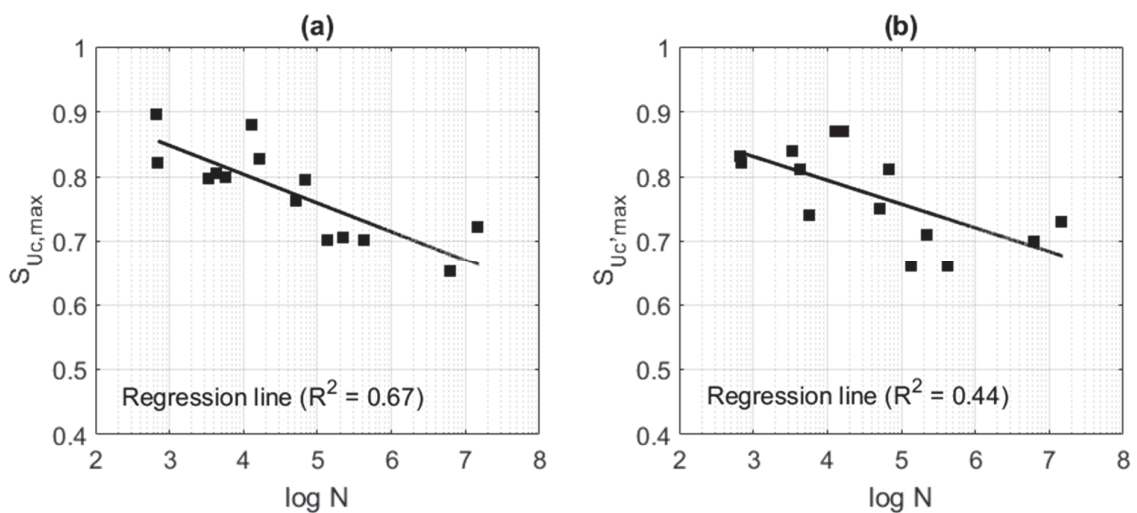
Figure 6-8. Comparison of the S-N diagrams obtained with ultimate strength f_{Uc} (a) from the specimens pair and (b) from the average of the static tests.

6.4.2 Fatigue deformation behavior

The compressive fatigue tests were performed at constant maximum and minimum stresses and the evolution of the specimen deformation was recorded as a function of the number of applied cycles.

Depending on the maximum stress level, the failure mode of the UHPFRC plates is different. For high maximum stress level, the failure is related to a quasi-static failure whereas low maximum stress level induces a damage at the top or the bottom of the plate at the load introduction.

Specimen subject to low maximum stress level

When the maximum stress level in the specimen is low and far below the elastic limit of the UHPFRC in compression (about 80 % of the compressive strength for heat treated UHPFRC), it is doubtful that damage will occur in the specimen. However, due to the testing conditions, higher stresses can appear at the interface between the specimen and the steel plates of the testing machine. The small irregularities of the contact surface will lead to higher stresses, especially on the outer edge of the contact area. During the tests, dust and small crushed matrix particles were observed around the specimen. Thin parts of the surface would crush and over time, the overall stress near the interface would increase.

The Figure 6-9 shows the evolution of the strain measured by the LVDTs at the top, center, and bottom sections of the specimen B3 1-2 which withstood 6.2 million cycles ($S_{c,max} = 0.65$). From the beginning of the test, a higher deformation was observed at the top part of the specimen. At around 200'000 cycles, the deformation increased slightly more in the top than the bottom of the specimen, and the strain started to grow faster in the top but the specimen still accumulated 6 million cycles before the final failure.
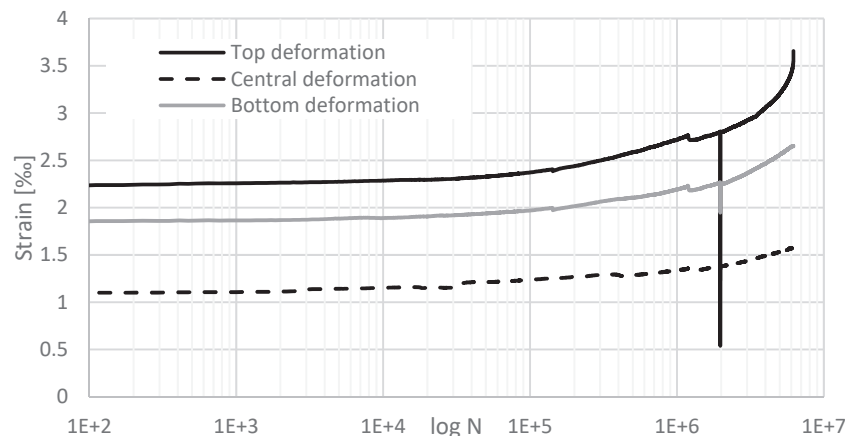
Figure 6-9. Strain growth curves for the top, the center, and the bottom of the B3 1-2 specimen.

Figure 6-10 shows the fracture of the specimen. The delamination of the top surface in the picture (b) was probably the cause of the rupture. The slightly reduced cross-section increased the stress at the interface and lead finally to a fracture initiated from one of the corners. The two

parts of the specimen were still together due to the high amount of fibres. In this case, a redistribution of the stresses was possible on the contact surface since the overall applied stresses were small.
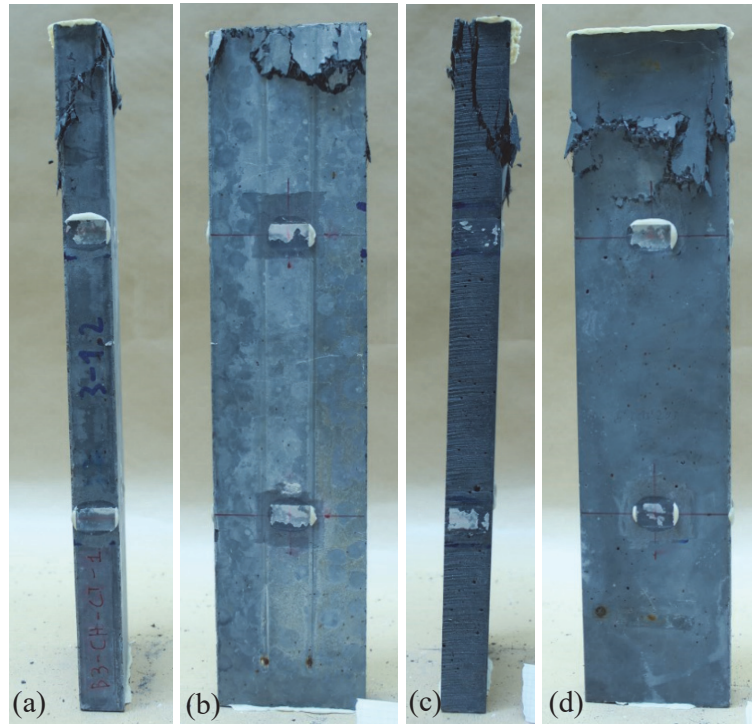
Figure 6-10. Specimen B3 1-2 (failure at 6'213'225 cycles)

Specimens subject to high maximum stress level

Employing maximum stress level above 0.75, the UHPFRC will experience the cycles in non-linear domain of the stress-strain behavior. In Figure 6-11, the deformation growth curves of the B3 3-2 ($S_{Uc,max} = 0.83$, N = 16'200) and the B3 5-2 ($S_{Uc,max} = 0.71$, N = 222'623) are presented. Both the average and maximum global deformation are displayed as a function of the number of cycles. The behavior is similar in both specimens and shows a constant increase in the deformation since the beginning of the fatigue tests. The failure is relatively brutal and follows a rapid acceleration in the deformation.
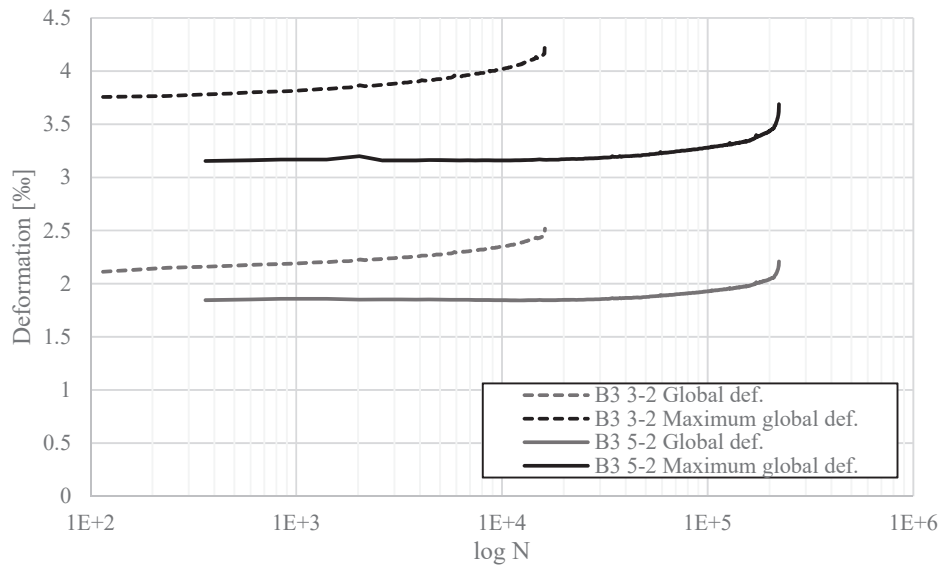
Figure 6-11. Deformation growth curves of the B3 3-2 and B3 5-2 tests

The final fracture of the specimen is a shear crack inclined at 60° (Figure 6-12). Local stress concentration due to a defect (air bubble or a weak zone without fibres) initiates a crack that suddenly propagates through the specimen. Tests were performed on the remaining intact parts of specimens and revealed the same compressive strength as carried out from static tests.
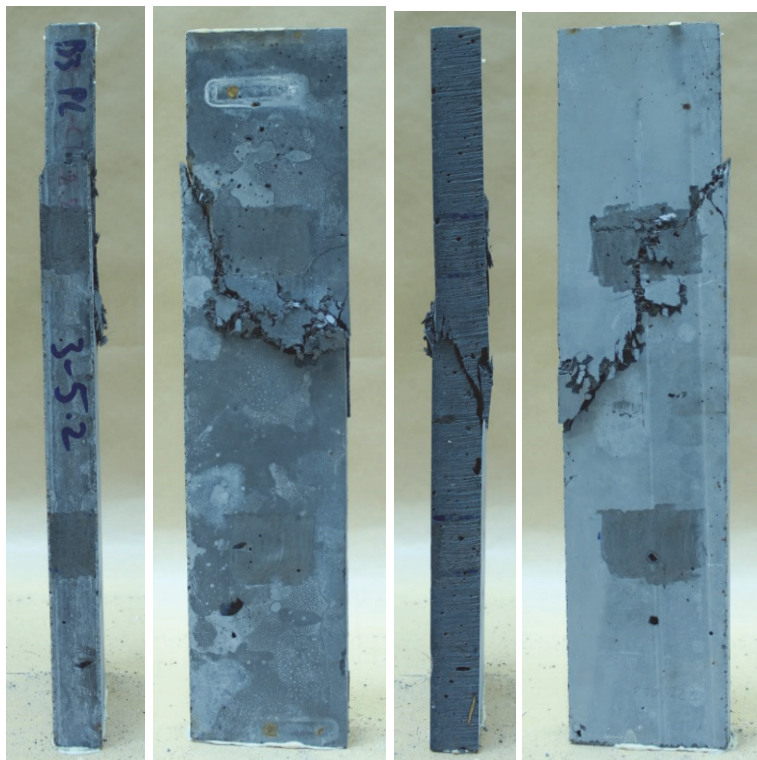
Figure 6-12. Specimen B3 5-2 (failure at 222'623 cycles)

128

6.5 Conclusions

The following conclusions can be drawn from the fatigue behavior of Ultra-High Performance Fibre Reinforced Cement-based Composite (UHPFRC) under constant amplitudes compressive stresses:

1. Quasi-static and fatigue tests were successfully performed on a rather unusual specimen geometry. The very thin and slender specimen geometry was chosen to prove the potential use of thin precast elements under high compressive stresses.
2. An endurance limit with respect to 10 million cycles was obtained for UHPFRC plates at a solicitation level of $S = 0.65$, S being the ratio between the maximum fatigue stress and the compressive strength of UHPFRC. Performing the quasi-static test and the fatigue test on two sub-specimens from the same initial plate helped in providing a more accurate solicitation level.
3. The thermal curing (48 hours at 90 °C and 100 % RH) plays an important role in the fatigue strength of UHPFRC since it increases the compressive elastic limit.
4. The fatigue test campaign was conducted at high S-level and very high number of cycles and showed promising results for the use of UHPFRC for future wind turbines support structures.

7 Conclusions

7.1 Introduction

This thesis aims to develop approaches to extend the service duration of existing wind turbine towers based on fatigue safety evaluation. Data acquisition from direct monitoring of wind turbines was combined with environmental and operational data to be able to provide a scheme for fatigue verification. In the meantime, this work investigates another solution to the short design life and durability concern of offshore wind turbines. The fatigue performance under compressive stresses of a more robust composite material was investigated, with the purpose of using it in the construction of future wind turbine support structures.

7.2 Response to research questions

The main contributions of the thesis to the field and how the results are correlated with the original research questions are stated in this chapter.

7.2.1 Wind turbine monitoring

Unlike the tests performed within the controlled environment of the structural laboratory, the monitoring campaign of operating wind turbines is more challenging. Careful planning and coordination between the turbine owner and the technicians are required. A structural monitoring system for the tower of the n°10 wind turbine of the Juvent S.A. wind farm was designed, continuously ran for over one year and extended for two more years. Modifications and updates on the system were made during the monitoring period to obtain additional data during short-measurement periods on specific locations. A minimal set of sensors was finally kept inside the tower to test the limits of the measurement setup, while still collecting the most relevant data.

The monitoring showed itself relatively economical and long-lasting. Placements of the strain gauges at specific angles on the inner side of the tower were carefully chosen to balance any perturbation on the data due to unwanted thermal effect. Including even the installation period of the strain gauges, this monitoring system did not disrupt power production of the wind turbines. Therefore, wind turbine owners do not need to intervene with the system, which contributes to the robustness of the system. The in-situ measurement of the tower geometry performed in this study provided essential information since the design assumptions were not available due to confidentiality

The monitoring system initially supplied a dataset up to 1 GB per day with all the sensors, but the reduced system produces only 100 MB per day. An optimal solution would be to trigger the measurement only when the turbine is in operation and to integrate the drift and temperature compensation procedure within the acquisition software.

7.2.2 Methodology for data processing

The drawback from collecting continuous data from multiple sensors for such an extended period is the accumulation of a massive amount of recorded data (approximate 200 GB) that

required an efficient and automated methodology. The raw data cannot be processed by conventional softwares such as Excel and Matlab. Therefore the first treatment (data reduction, temperature and drift compensation, and filtering) was performed in the powerful DIAdem software from National Instrument employing and upgrading Visual Basic commands initialy developed by former MCS Ph.D. students. Subsequently, Matlab was employed for the more detail processing of the data. The SCADA data was automatically available via an FTP server, however combining two datasets coming from different sources was intricate.

A framework for the data treatment was finally successfully created. The raw data from a numerous number of channels was collected and processed to automatically remove any temperature and long-term effects, and the resulting reduced set of data was stored and used as input data for both fatigue analysis and extreme loads prediction. The SCADA data coming directly from the turbine system was inspected and finally synchronized with the strain measurement. The stability and robustness of this methodology shows its capacity to be directly implemented on the DAU to reduce the storage requirements.

7.2.3 Fatigue safety and extension of the service duration

Service duration of the wind turbines is expected to be 20 years based on their design codes. However, the design codes are too conservative and need to be altered to be able to indicate more reliable timescale. Here, we used a direct monitoring approach to evaluate the service duration of an operating wind turbine in which strain gauges were used to record occurred strains histories. Results from the measurement campaign clearly demonstrate that WT towers service duration can be extended safely beyond 20 years, and it allows to continue to safely produce energy with existing wind turbine towers while enhancing the sustainability of the WT.

Direct monitoring of the wind turbines for long-term (604 days) provides accurate data for the evaluation of wind loading effect on the wind turbine, since the effects of temperature and long-term effect (drift of the signals) are excluded. By doing that, this monitoring approach bypasses all the uncertainties of commercial conventional simulation tools used for the design of turbines. It allowed to the realistic examination of the fatigue damage endured by the wind turbine tower because the *in-situ* wind regime, resonance phenomena, transient, and extreme events, as well as various failures in the control system, are explicitly considered and recorded. It was showed that most of the damage occurs during normal production above the rated wind speed and storms. Damage could significantly be reduced without loss of power production by improving the emergency shut-down procedure and optimizing the active pitch control algorithm.

In order to consider the effect of environmental and operational parameters on the turbine behavior, the monitoring data was combined with SCADA data that was already available for the wind turbine monitored. In particular, the effect of icing on blades was presented. The combination of strain measurements and SCADA data is used for the reconstruction of the fatigue damage endured by the wind turbine even with a limited number of parameters. However, a long-term (minimum a year) monitoring is a prerequisite to take into account high wind speeds which happens mostly in winter and account for the vast majority of the damage.

7.2.4 Extreme value behavior of wind action effect

The long-term monitoring provided a tremendous amount of data on the realistic wind load effects and continuous measurements allowed to record extreme and even accidental events. The SCADA data was used as a replacement for an expansive met mast. The current approach to evaluate the extreme loading of the turbine based on the wind speed distribution shows its limitation with the lack of high wind speed. Indeed, the extrapolation method with BMM and "fitting before aggregation" results in lower 50-year extreme loads and requires a considerable amount of work in terms of data processing and quality control of the sample. It is very likely that the 50-year extreme value arises from the highest wind speed bins, for which a sufficient number of peaks is not always available.

The direct approach is suggested as an alternative to provid more information, since the total dataset was used. The extrapolation method with POT method and a GP distribution results in higher 50-year extreme loads. The threshold selection combining quantile-quantile plots and the confidence interval width provides a robust and objective method. Therefore, a stable extrapolation value is rapidly reached. The confidence in the extrapolated values was sufficient after one year of measurement and confirmed that the turbine remains in an elastic state even under the 50-year return load as the maximum stress prediction remains 34 % below the yield stress for the turbine tower and is not a concern for the Ultimate Limit State.

The uncertainties were considered in the model and were used to establish the minimum monitoring duration necessary for the robust estimation of the 50-year return value. Impact of the monitoring period and duration were studied in detail. A minimum period of three to four months in winter is recommended to get a realistic value. A full year leads to stable data, as the 4 months of the 2nd winter had no impact on the 50-year return value. Both measured winter periods led to similar results.

Finally, unlike simulated data, it was shown that, despite the reduced uncertainties compared to aero-elastic simulations, the processing and verification of the monitored data requires a lot of time and work.

7.2.5 Fatigue test on UHPFRC

The investigation of the fatigue behavior and fatigue strength of UHPFRC plates subject to a high number of cycles was performed and showed an endurance limit under constant amplitudes compressive fatigue stresses with respect to 10 million cycles. The fatigue endurance limit was determined to be at a solicitation level of $S = 0.65$. Under this limit, no damage could be observed on run-out specimens.

The thermal curing of the specimens was essential to provide results based on specimens with a fully developed resistance. Performing the quasi-static test and the fatigue test on two sub-specimens from the same initial plate helped in providing a more accurate solicitation level.

The tests were performed on rather unusual specimen geometry with the objective of a future application of thin precast towers segments for future wind turbines made of highly prestressed UHPFRC. The fatigue test campaign was conducted at high S-level and very high number of

cycles and showed promising results for the use of UHPFRC for future wind turbines support structures.

7.3 Future work

7.3.1 High-resolution wind field measurement

The development of new techniques in the measurement of the wind field near the wind turbine, such a drone-mounted LIDAR system, in combination with the existing strain monitoring system could provide much more reliable data at a higher frequency, to study the wind-structure interaction. Reliable data from both the wind field and the structure behavior could help to improve the actual numerical models.

7.3.2 Assessment of wind farms

The monitoring system, by its simplicity and low cost, could be extended to multiple turbines into the wind farm and synchronized to assess the effect of neighboring turbines and the complex topography of the site. Therefore, the disparities between similar turbines within the same wind farm could be accurately established. The model for the estimation of the endured damage could be validated and improved by combining multiple measurements.

With multiple monitoring system installed on several turbine, the amount of data collected will quickly be important. When new mining algorithms related to the big data could be used, the automation of the data treatment process could be used to reduce the collected data to its minimum by still extracting the most relevant information.

7.3.3 Large-scale testing of precast UHPFRC elements

The results obtained from the fatigue testing campaign showed the possibility of using the UHPFRC for support structure of new turbines. However the tests were limited to constant compressive fatigue. Future researchers should focus on larger scale tests on precast assembled elements and on the variable fatigue loading happening in real structures. Also in the near future, construction companies which are already active in the development and utilization of UHPFRC, should push towards the fabrication of a full-scale tower prototype, even in the absence of interest and collaboration from wind turbine manufacturers.

7.4 Perspectives

The wind turbine support structure monitored during this work clearly has the potential for service extension, mainly because the wind speed assumptions are much below the design values. However, many of the mechanical parts of the turbine (*e.g.* the blades, the load bearings) have a limited life and could not be extended in the same proportion as the tower. One could argue that the constant evolution and improvement of turbines make old turbines less relevant since a single new turbine can produce more energy than four 10-year old turbines together.

Many regulations restrain the installation of new onshore turbines, and in the case of Switzerland, the total height of the turbine is limited to 150 m. This limit was reached in 2010 in the Juvent wind farm with the installation of the 2.0 MW Vestas V90. More powerful turbines

installed in 2016, the 3.3 MW Vestas V112, have a bigger rotor diameter and consequently a smaller tower. The idea behind is the reusability of the existing towers with state-of-the-art rotors. The adaptation of the height of the last segment to the new rotor could be a solution to decrease the overall footprint and cost of wind turbines towers.

The use of a more durable and efficient material is becoming a requirement for the future infrastructures, especially for improving the robustness and longevity of necessary energy converter. The tests performed within this thesis and the now large literature on UHPFRC clearly show that this exceptional material can be used as a more economical and sustainable solution for tall wind turbine towers since such structures could be designed for a service life of 100 years with the use of precast elements built in-situ with local materials.

http://www.juvent.ch/photos.html

References

Agarwal, Puneet, and Lance Manuel. 2008. "Extreme Loads for an Offshore Wind Turbine Using Statistical Extrapolation from Limited Field Data." *Wind Energy* 11 (6):673–84. https://doi.org/10.1002/we.301.

Beganovic, Nejra, and Dirk Söffker. 2016. "Structural Health Management Utilization for Lifetime Prognosis and Advanced Control Strategy Deployment of Wind Turbines: An Overview and Outlook Concerning Actual Methods, Tools, and Obtained Results." *Renewable and Sustainable Energy Reviews* 64 (Supplement C):68–83. https://doi.org/10.1016/j.rser.2016.05.083.

Botz, Max, Stefan Oberlaender, Manuel Raith, and Christian U. Grosse. 2016. "Monitoring of Wind Turbine Structures with Concrete-Steel Hybrid-Tower Design." *Bilbao*.

Brenner, Daniel. 2016. "Determination of the Actual Ice Mass on Wind Turbine Blades." In *Proceedings of the Winterwind, International Wind Energy Conference, \AAre, Sweden*, 9–10.

Caithness Windfarm Information Forum. 2017. "Summary of Wind Turbine Accident Data to 30 September 2017." 2017. http://www.caithnesswindfarms.co.uk/accidents.pdf.

Charron, J.-P., E. Denarié, and E. Brühwiler. 2007. "Permeability of Ultra High Performance Fiber Reinforced Concretes (UHPFRC) under High Stresses." *Materials and Structures* 40 (3):269–277.

Coles, Stuart. 2001. *An Introduction to Statistical Modeling of Extreme Values*. Springer Series in Statistics. London: Springer London. https://doi.org/10.1007/978-1-4471-3675-0.

Cooperman, Aubryn, and Marcias Martinez. 2015. "Load Monitoring for Active Control of Wind Turbines." *Renewable and Sustainable Energy Reviews* 41 (January):189–201. https://doi.org/10.1016/j.rser.2014.08.029.

Dai, Juchuan, Wenxian Yang, Junwei Cao, Deshun Liu, and Xing Long. 2017. "Ageing Assessment of a Wind Turbine over Time by Interpreting Wind Farm SCADA Data." *Renewable Energy*, March. https://doi.org/10.1016/j.renene.2017.03.097.

DNVGL. 2016. "DNVGL-ST-0126 - Support Structures for Wind Turbines." http://rules.dnvgl.com/docs/pdf/dnvgl/ST/2016-04/DNVGL-ST-0126.pdf.

Eurocode 3 part 1-9. 1990. "Eurocode 3: Calcul Des Structures En Acier - Partie 1-9 : Fatigue."

EWEA. 2016. "European Wind Energy Association. Wind in Power - 2015 European Statistics; 2016. - Google Search." 2016. https://www.google.ch/search?q=European+Wind+Energy+Association.+Wind+in+power+-+2015+European+statistics%3B+2016.&oq=European+Wind+Energy+Association.+Wind+in+power+-+2015+European+statistics%3B+2016.&aqs=chrome..69i57.194j0j7&sourceid=chrome&ie=UTF-8.

Freudenreich, K., and K. Argyriadis. 2007. "The Load Level of Modern Wind Turbines According to IEC 61400-1." *Journal of Physics: Conference Series* 75 (1):012075. https://doi.org/10.1088/1742-6596/75/1/012075.

Frohboese, Peter, and Andreas Anders. 2007. "Effects of Icing on Wind Turbine Fatigue Loads." *Journal of Physics: Conference Series* 75 (1):012061. https://doi.org/10.1088/1742-6596/75/1/012061.

Graybeal, Benjamin A. 2007. "Compressive Behavior of Ultra-High-Performance Fiber-Reinforced Concrete." *Materials Journal* 104 (2):146–152.

Grigoriou, Vasileios. 2015. "Advanced Fatigue Theory and Structural Response Monitoring for Safety Verification of Existing RC Slabs Subject to Railway Traffic." Lausanne: EPFL. http://dx.doi.org/10.5075/epfl-thesis-6847.

Häckell, Moritz W., and Raimund Rolfes. 2013. "Monitoring a 5MW Offshore Wind Energy Converter—Condition Parameters and Triangulation Based Extraction of Modal Parameters." *Mechanical Systems and Signal Processing* 40 (1):322–43. https://doi.org/10.1016/j.ymssp.2013.04.004.

Hahn, Berthold, Michael Durstewitz, and Kurt Rohrig. 2006. "Reliability of Wind Turbines Experiences of 15 Years with 1,500 WTs." Institut für Solare Energieversorgungstechnik (ISET).

Hansen, Martin O. L. 2015. *Aerodynamics of Wind Turbines*. Routledge.

HBM. n.d. "Strain Gauges and Accessories." Accessed October 6, 2017. https://www.hbm.com/fileadmin/mediapool/hbmdoc/technical/s1265.pdf.

Heilmann, Christoph, Anke Grunwald, Michael Melsheimer, Robert Liebich, and René Kamieth. 2014. "Reconstruction of a Wind Turbine's Endured Load Spectrum Using a Short-Time Load Measurement and Operational Data." *Proceeding of EWEA 2014*. http://www.kup.tu-berlin.de/fileadmin/fg68/Dokumente/Publikationen/Rene_Kamieth/EWEA_140310_R econstruction_of_a_wind_turbine__s..._Kamieth_Seite1.pdf.

Hirt, Manfred A., Rolf Bez, and Alain Nussbaumer. 2006. *Construction métallique: notions fondamentales et méthodes de dimensionnement*. PPUR presses polytechniques.

Hoffmann, Karl. 1989. *An Introduction to Measurements Using Strain Gages*. Hottinger Baldwin Messtechnik Darmstadt. http://www.academia.edu/download/44775005/An_Introduction_to_Measurements_us ing_Strain_Gages.pdf.

Hu, Wei-Hua, Sebastian Thöns, Rolf Günter Rohrmann, Samir Said, and Werner Rücker. 2015a. "Vibration-Based Structural Health Monitoring of a Wind Turbine System. Part I: Resonance Phenomenon." *Engineering Structures* 89 (April):260–72. https://doi.org/10.1016/j.engstruct.2014.12.034.

———. 2015b. "Vibration-Based Structural Health Monitoring of a Wind Turbine System Part II: Environmental/Operational Effects on Dynamic Properties." *Engineering Structures* 89 (April):273–90. https://doi.org/10.1016/j.engstruct.2014.12.035.

IEC 61400-1. 2005. "IEC 61400–1 Ed. 3. Wind Turbines – Part 1: Design Requirements." International Electrotechnical Commission (IEC).

IEC 61400-13. 2001. "IEC 61400–13. Wind Turbine Generator Systems – Part 13: Measurement of Mechanical Loads." International Electrotechnical Commission (IEC).

Iliopoulos, Alexandros, Christof Devriendt, Patrick Guillaume, and Danny Van Hemelrijck. 2014. "Continuous Fatigue Assessment of an Offshore Wind Turbine Using a Limited Number of Vibration Sensors." In *EWSHM - 7th European Workshop on Structural*

Health Monitoring, edited by Vincent Le Cam, Laurent Mevel, and Franck Schoefs. Nantes, France: IFFSTTAR, Inria, Université de Nantes. https://hal.inria.fr/hal-01020445.

Iliopoulos, Alexandros, Wout Weijtjens, Danny Van Hemelrijck, and Christof Devriendt. 2016. "Full-Field Strain Prediction Applied to an Offshore Wind Turbine." In *Model Validation and Uncertainty Quantification, Volume 3*, 349–57. Conference Proceedings of the Society for Experimental Mechanics Series. Springer, Cham. https://doi.org/10.1007/978-3-319-29754-5_34.

Jammes, François-Xavier, Xavier Cespedes, and Jacques Resplendino. 2013. "Design of Offshore Wind Turbines with UHPC." In *Proceedings of International Symposium on Ultra-High Performance Fiber-Reinforced Concrete. Marseille, France*, 443–452.

Kamen, Aicha. 2007. "Comportement Au Jeune âGe et Différé d"un BFUP Écrouissant Sous Les Effets Thermomécaniques." Lausanne: EPFL. https://infoscience.epfl.ch/record/104117.

Karlina-Barber, Sarah, Sebastian Mechler, and Mario Nitschke. 2016. "The Effect of Wakes on the Fatigue Damage of Wind Turbine Components over Their Entire Lifetime Using Short-Term Load Measurements." *Journal of Physics: Conference Series* 753 (7):072022. https://doi.org/10.1088/1742-6596/753/7/072022.

Keil, Stefan. 1988. "The Thermal Output of a Strain Gage." *Reports in Applied Measurement* 4 (1):15–17.

Krug, Florian, and Bastian Lewke. 2009. "Electromagnetic Interference on Large Wind Turbines." *Energies* 2 (4):1118–29. https://doi.org/10.3390/en20401118.

Lachmann, Stefan. 2014. "Kontinuierliches Monitoring Zur Schädigungsverfolgung an Tragstrukturen von Windenergieanlagen." Ruhr Universität Bochum. http://www-brs.ub.ruhr-uni-bochum.de/netahtml/HSS/Diss/LachmannStefan/diss.pdf.

LaNier, M. W. 2005. "Lwst Phase I Project Conceptual Design Study: Evaluation of Design and Construction Approaches for Economical Hybrid Steel/Concrete Wind Turbine Towers; June 28, 2002 -- July 31, 2004." NREL/SR-500-36777. National Renewable Energy Lab., Golden, CO (US). https://doi.org/10.2172/15011444.

Liu, Yin, and Takeshi Ishihara. 2001. "Fatigue Failure Accident of Wind Turbine Tower in Taikoyama Wind Farm."

Lott, Sarah, and Po Wen Cheng. 2016. "Load Extrapolations Based on Measurements from an Offshore Wind Turbine at Alpha Ventus." *Journal of Physics: Conference Series* 753 (7):072004. https://doi.org/10.1088/1742-6596/753/7/072004.

Lu, Kung-Chun, Heng-Chu Peng, and Yu-Shu Kuo. 2014. "Structural Health Monitoring of the Support Structure of Wind Turbine Using Wireless Sensing System." In *EWSHM-7th European Workshop on Structural Health Monitoring*.

Martinez-Luengo, Maria, Athanasios Kolios, and Lin Wang. 2016. "Structural Health Monitoring of Offshore Wind Turbines: A Review through the Statistical Pattern Recognition Paradigm." *Renewable and Sustainable Energy Reviews* 64 (Supplement C):91–105. https://doi.org/10.1016/j.rser.2016.05.085.

"Mesureur de Grosseur PCE-TG 200." n.d. Accessed October 10, 2017. http://www.pce-france.fr/fiches-mesureurs/mesureur-grosseur-metaux-pce-tg200.htm.

Miner, M.A. 1945. "Cumulative Damage in Fatigue." *Journal of Applied Mechanics* 12 (3):159–64.

Mittelmeier, Niko, Tomas Blodau, and Martin Kühn. 2017. "Monitoring Offshore Wind Farm Power Performance with SCADA Data and an Advanced Wake Model." *Wind Energy Science* 2 (1):175–87. https://doi.org/https://doi.org/10.5194/wes-2-175-2017.

Noppe, N., A. Iliopoulos, W. Weijtjens, and C. Devriendt. 2016a. "Full Load Estimation of an Offshore Wind Turbine Based on SCADA and Accelerometer Data." *Journal of Physics: Conference Series* 753 (7):072025. https://doi.org/10.1088/1742-6596/753/7/072025.

Noppe, N, A Iliopoulos, W Weijtjens, and C Devriendt. 2016b. "Full Load Estimation of an Offshore Wind Turbine Based on SCADA and Accelerometer Data." *Journal of Physics: Conference Series* 753 (September):072025. https://doi.org/10.1088/1742-6596/753/7/072025.

Noppe, N, W Weijtjens, and C Devriendt. 2015. "Reliable Empirical Analysis of Effects of Turbulent Air in an Operating Wind Farm Based on Unreliable SCADA-Data." Poster presented at EAWE PhD Seminar, Stuttgart, September 22. http://www.owi-lab.be/sites/default/files/Reliable%20empirical%20analysis%20of%20effects%20of%20turbulent%20air%20in%20an%20operating%20wind%20farm%20based%20on%20unreliable%20SCADA-data%20%281%29.pdf.

OFEN. 2016. "Atlas Des Vents de La Suisse: Moyenne Annuelle Modélisée de La Vitesse et de La Direction Du Vent." Office fédéral de l'énergie. http://www.bfe.admin.ch/geoinformation/05061/06675/index.html?lang=en&dossier_id=06606.

Pedersen, Niels Leergaard. 2017. "On Analysis and Redesign of Bolted L-Flanged Connections." *Wind Energy* 20 (6):1069–82. https://doi.org/10.1002/we.2080.

Peeringa, J. M., and WAAM Bierbooms. 2013. "Extreme Loads Using Measured and Calculated Responses for Offshore Applications." *Wind Energy* 2012:2011.

Petersen, Ch. 2013. "Nachweis Der Betriebsfestigkeit Exzentrisch Beanspruchter Ringflanschverbindungen." *Stahlbau* 67 (3):191–203. https://doi.org/10.1002/stab.199800690.

Ragan, Patrick, and Lance Manuel. 2008. "Statistical Extrapolation Methods for Estimating Wind Turbine Extreme Loads." *Journal of Solar Energy Engineering* 130 (3):031011-031011-15. https://doi.org/10.1115/1.2931501.

Rebelo, Carlos, Milan Veljkovic, Rui Matos, and Luís Silva. 2012. "Structural Monitoring of a Wind Turbine Steel Tower - Part II: Monitoring Results." *Wind and Structures* 15 (July). https://doi.org/10.12989/was.2012.15.4.301.

Rebelo, Carlos, Milan Veljkovic, Luís Silva, Rui Simões, and José Henriques. 2012. *Structural Monitoring of a Wind Turbine Steel Tower - Part I: System Description and Calibration*. Vol. 15. https://doi.org/10.12989/was.2012.15.4.285.

Rohrmann, Rolf Günter, Sebastian Thöns, and Werner Rücker. 2010. "Integrated Monitoring of Offshore Wind Turbines – Requirements, Concepts and Experiences." *Structure and Infrastructure Engineering* 6 (5):575–91. https://doi.org/10.1080/15732470903068706.

Schlechtingen, Meik, and Ilmar Ferreira Santos. 2014. "Wind Turbine Condition Monitoring Based on SCADA Data Using Normal Behavior Models. Part 2: Application

Examples." *Applied Soft Computing* 14 (Part C):447–60. https://doi.org/10.1016/j.asoc.2013.09.016.

Schmidt, H., and M. Neuper. 1997. "Zum Elastostatischen Tragverhalten Exzentrisch Gezogener L-Stoesse Mit Vorgespannten Schrauben." *STAHLBAU -BERLIN-* 66 (3):163–68.

Seidel, M., and P. Schaumann. 2001. "Ermittlung Der Ermüdungsbeanspruchung von Schrauben Exzentrisch Belasteter Flanschverbindungen." *Stahlbau* 70 (7):474–86. https://doi.org/10.1002/stab.200101660.

SIA 263. 2003. "SIA 263 - Construction En Acier."

Smarsly, Kay, Dietrich Hartmann, and Kincho H. Law. 2013. "An Integrated Monitoring System for Life-Cycle Management of Wind Turbines." *International Journal of Smart Structures and Systems* 12 (2):209–33.

Smorgonskii, Aleksandr. 2016. "Advanced Methods for the Evaluation of Lightning Incidence over Large Areas, Wind Turbine Parks and Tall Towers." https://infoscience.epfl.ch/record/217933.

Spiridonakos, Michael, Yaowen Ou, Eleni Chatzi, and Ulrich Reiter. 2015. "Wind Turbines Structural Identification Framework for the Representation of Both Short- and Long-Term Variability." In *SHMII 2015 - 7th International Conference on Structural Health Monitoring of Intelligent Infrastructure*. International Society for Structural Health Monitoring of Intelligent Infrastructure, ISHMII. https://www.research-collection.ethz.ch/handle/20.500.11850/119223.

Sritharan, Sri, and Grant M. Schmitz. 2013. "Design of Tall Wind Turbine Towers Utilizing UHPC." In *Proceedings of the RILEM-Fib-AFGC International Symposium On Ultra-High Performance Reinforced Concrete, Eds: F. Toutlemoude, J. Resplendino, RILEM Publications SARL, Bagneux, France*, 433–442.

Sun, Peng, Jian Li, Caisheng Wang, and Xiao Lei. 2016. "A Generalized Model for Wind Turbine Anomaly Identification Based on SCADA Data." *Applied Energy* 168 (April):550–67. https://doi.org/10.1016/j.apenergy.2016.01.133.

Thöns, Sebastian. 2011. *Monitoring Based Condition Assessment of Offshore Wind Turbine Support Structures*. Zurich: Eidgenossische Technische Hochschule Zurich.

Treacy, Mark Anthony. 2014. "The Use of Monitored Data in the Verification of Structural and Fatigue Safety of Existing Post-Tensioned Concrete Highway Bridges." Lausanne: EPFL. http://dx.doi.org/10.5075/epfl-thesis-6207.

Van Bussel, G. J. W., and M. B. Zaayer. 2001. "Reliability, Availability and Maintenance Aspects of Large-Scale Offshore Wind Farms, a Concepts Study." *MAREC 2011: Proceedings of the 2-Day International Conference on Marine Renewable Energies, Newcastle, UK, 27-28 March 2001*. http://resolver.tudelft.nl/uuid:602dec1f-0861-4268-83bb-4ab85baeac1f.

VDI 2230 Blatt 1. 2015. "VDI 2230 Blatt 1 - Systematic Calculation of Highly Stressed Bolted Joints - Joints with One Cylindrical Bolt." VDI-Gesellschaft Produkt- und Prozessgestaltung. //nc/guidelines/vdi_2230_blatt_1-systematische_berechnung_hochbeanspruchter_schraubenverbindungen_zylindrische_/.

Veljkovic, Milan, M Feldmann, J Naumes, Daniel Pak, Luís Silva, da Silva, and Carlos Rebelo. 2011. "Wind Turbine Tower Design, Erection and Maintenance." In , 274–300. https://doi.org/10.1533/9780857090638.2.274.

Vestas. 2010. "General Specification V90–1.8/2.0 MW 50 Hz VCS." Vestas Wind Systems A/S.

Vishay. 2007. "Strain Gage Thermal Output and Gage Factor Variation with Temperature." *Technical Note: TN-504-1*. http://www.vishay.com/docs/11054/tn504.pdf.

VTI. n.d. "Practical Strain Gage." Accessed October 6, 2017. http://www.vtiinstruments.com/catalog/technotes/technote11.pdf.

Weijtens, Wout, Nymfa Noppe, Tim Verbelen, Alexandros Iliopoulos, and Christof Devriendt. 2016. "Offshore Wind Turbine Foundation Monitoring, Extrapolating Fatigue Measurements from Fleet Leaders to the Entire Wind Farm." *Journal of Physics: Conference Series* 753 (9):092018. https://doi.org/10.1088/1742-6596/753/9/092018.

Werner, Sobek, Markus Plank, Björn Frettlöhr, Jochen Röhm, and Dominique Corvez. 2013. "Conceptual Design of an UHPFRC Tower Structure in Segmental Construction for Offshore Wind Turbines." In *Proceedings of the RILEM-Fib-AFGC International Symposium On Ultra-High Performance Reinforced Concrete, Eds: F. Toutlemoude, J. Resplendino, RILEM Publications SARL, Bagneux, France*, 423–32. http://demo.webdefy.com/rilem-new/wp-content/uploads/2016/10/65560237dd659e13b11b7b19b272fa22.pdf.

Wu, Xiang-Guo, Jiang Yang, and Issa Brown Mpalla. 2013. "Innovative Post-Tensioned Hybrid Wind Turbine Tower Made of Ultra High Performance Cementitious Composites Segment." In . Jeju, Korea.

Wymore, Mathew L., Jeremy E. Van Dam, Halil Ceylan, and Daji Qiao. 2015. "A Survey of Health Monitoring Systems for Wind Turbines." *Renewable and Sustainable Energy Reviews* 52 (Supplement C):976–90. https://doi.org/10.1016/j.rser.2015.07.110.

Zaher, A., S.d.j. McArthur, D.g. Infield, and Y. Patel. 2009. "Online Wind Turbine Fault Detection through Automated SCADA Data Analysis." *Wind Energy* 12 (6):574–93. https://doi.org/10.1002/we.319.

Zendehbad, M., N. Chokani, and R. S. Abhari. 2017. "Measurements of Tower Deflections on Full-Scale Wind Turbines Using an Opto-Mechanical Platform." *Journal of Wind Engineering and Industrial Aerodynamics* 168 (September):72–80. https://doi.org/10.1016/j.jweia.2017.05.011.

Ziegler, Lisa, Elena Gonzalez, Tim Rubert, Ursula Smolka, and Julio J. Melero. 2018. "Lifetime Extension of Onshore Wind Turbines: A Review Covering Germany, Spain, Denmark, and the UK." *Renewable and Sustainable Energy Reviews* 82 (Part 1):1261–71. https://doi.org/10.1016/j.rser.2017.09.100.

Christophe Thierry LORAUX

Date of birth: 28.01.1990
Nationality: Swiss and French
Address: Chemin du Couchant 34, 1007 Lausanne, Switzerland
Email: chris.loraux@gmail.com

Education

10.2013 – present	Laboratory of Maintenance and Safety of Structures (MCS), Swiss Federal Institute of Technology in Lausanne (EPFL)
	Doctoral Candidate in Civil Engineering
09.2011 – 07.2013	Swiss Federal Institute of Technology in Lausanne (EPFL)
	Master of Science MSc in Civil Engineering
09.2008 – 07.2011	Swiss Federal Institute of Technology in Lausanne (EPFL)
	Bachelor of Civil Engineering

Professional Experience

07.2012 – 09.2012	Internship at ZS Ingénieurs Civil SA, Engineering Office, Geneva, Switzerland. Pre-design of steel and concrete structures.
07.2011 – 09.2011	Internship at INDUNI & CIE SA, Construction Company, Geneva, Switzerland. Work site management and supervision of interior work for four residential buildings.

Teaching

10.2013 – 07.2016	Teaching assistant for courses in Existing Structures and Structural Safety & Reliability at the School of Architecture, Civil and Environmental Engineering (ENAC) of EPFL.
09.2011 – 07.2013	Student assistant for courses in Static I & II, Structural Safety and Reliability, Existing Structures I: Security and durability at the School of Architecture, Civil and Environmental Engineering (ENAC) of EPFL.
10.2013 – 10.2017	Supervision of numerous master and undergraduate projects at EPFL.

Skills

Languages: French (mother tongue), English (Advanced)
Engineering software: MATLAB, DIAdem, DIANA and Cubus-6 (Statik, Cedrus, and Fagus)

Publications

- Loraux, C. & Brühwiler, E (2015, July). Comportement à la compression et à la fatigue d'un BFUP écrouissant. 16e édition des Journées scientifiques du Regroupement francophone pour la recherche et la formation sur le béton (RF)^{2}B, July 9-10 2015, EPFL, Lausanne, Suisse.
- Loraux, C. & Brühwiler, E. (2015, September). Realistic examination of the fatigue life of a wind turbine tower using data from long term monitoring. IABSE Conference, September 23-35 2015, Geneva, Switzerland.
- Mayencourt, P., Robeller, C., Weinand, Y., Loraux, C. & Brühwiler, E. (2015, September). CNC-fabricated formwork for UHPFRC thin folded plate arch. IABSE Conference, September 23-35 2015, Geneva, Switzerland.
- Loraux, C. & Brühwiler, E. (2016, October). The use of long term monitoring data for the extension of the service duration of existing wind turbine support structures. TORQUE 2016 Conference, October 5-7 2015, Munich, Germany.
- Loraux, C. & Brühwiler, E (2016, July). Renforcement des phares en mer à l'aide de Bétons Fibrés Ultra Performants. 17e édition des Journées scientifiques du Regroupement francophone pour la recherche et la formation sur le béton (RF)^{2}B, July 7-8 2016, IFSTTAR, Marne-la-Vallée, France

Extracurricular Commitments

2016   EPFL finalist in 'My thesis in 180 seconds'
              https://www.youtube.com/watch?v=tLsqwhf4e6A